Multi-dimensional analysis of the reflection matrix for quantitative ultrasound imaging

Flavien Bureau

PSL
UNIVERSITÉ PARIS

THÈSE DE DOCTORAT
DE L'UNIVERSITÉ PSL

Préparée à l'École Supérieure de Physique
et de Chimie Industrielles de la ville de Paris

Multi-dimensional analysis of the reflection matrix for quantitative ultrasound imaging

Analyse multi-dimensionnelle de la matrice de réflexion pour l'imagerie ultrasonore quantitative

Defended by
Flavien Bureau
July 3rd 2023

Doctoral school n°564
Ecole Physique en Île-de-France

Speciality
Physics

Prepared at the
Institut Langevin (UMR 7587)

Composition of the jury:

Olivier COUTURE Research director, CNRS	*Chair of the jury* *Examiner*
Jeremy DAHL Associate Professor, Stanford Unversity	*Reviewer*
Jean PROVOST Associate Professor, Polytechnique Montréal	*Reviewer*
Juliette PIERRE Research scientist, CNRS	*Examiner*
Mathias FINK Professor, ESPCI Paris	*Thesis supervisor*
Alexandre AUBRY Research director, CNRS	*Thesis supervisor*

ESPCI PARIS | PSL

Contents

Acknowledgements

Tout d'abord, je tiens à exprimer ma sincère gratitude envers mes deux directeurs de thèse. Alex, je te remercie chaleureusement pour la vision que tu m'as apportée tout au long de mon doctorat. Ton exigence de rigueur nous pousse à clarifier nos idées parfois encore confuses. Je me souviens encore de tes yeux écarquillés lorsque j'ai déclaré en réunion : *"Le réflecteur virtuel, c'est un peu comme une tache gaussienne, non ?"*. C'est sûrement à ce moment-là que j'ai réalisé que la thèse était un peu comme l'apprentissage d'un nouveau langage. Quel plaisir d'entendre un *"Bravo !"*, signe d'une honnêteté infaillible, que nous avions franchi une étape à célébrer. Enfin, j'aimerais tout particulièrement te remercier pour ta disponibilité, malgré tes nombreuses sollicitations, et du temps que tu prends à relire chacune de nos productions scientifiques. Je me rends compte que c'est bel et bien un privilège d'avoir autant de retours constructifs pour nous pousser à rehausser nos exigences. En bref, merci infiniment pour le temps que tu nous accordes et pour ton mentorat exceptionnel. Ensuite, je tiens à exprimer ma profonde reconnaissance envers mon co-directeur, Mathias. Tu transmets passionnément tes connaissances et fait preuve d'un enthousiasme constant pour les résultats que nous présentons. Je te remercie pour la grande implication que tu portes pour vulgariser de la meilleure manière nos travaux. C'est un privilège d'entendre tes anecdotes et de percevoir la continuité de nos recherches, telle une histoire écrite par nos prédécesseurs.

En second lieu, je tiens à exprimer ma gratitude envers les membres du jury qui ont accepté d'évaluer mon travail. Un grand merci à Jean, Jeremy, Juliette, Gabriel et Olivier pour vos remarques pertinentes concernant mon manuscrit, ainsi que pour la conversation dynamique que nous avons eue à la suite de ma présentation.

Je tiens également à remercier chaleureusement mon comité de suivi de thèse. Fabrice, je ne peux que me sentir privilégié de t'avoir eu en TP de physique *"Ok c'est super important ça : plus un signal est bref, plus il contient de fréquences ! Donc si on va encore plus loin, la TF d'un Dirac, c'est une constante !"* Ce genre de discussion devant un oscilloscope qui marque les esprits ! Et Pierre, il va sans dire que c'est une chance de pouvoir débriefer du labo pour rapidement dériver sur des conseils musicaux.

Vient maintenant la team *"Reminiscence"*, à la croisée entre imagerie optique, sismique, radar et échographique. Je tiens à exprimer ma gratitude envers William, avec qui j'ai pu apprendre les bases de l'imagerie matricielle. Mes remerciements vont également à Cécile, qui travaillait sur des sujets similaires et qui m'a aidé à comprendre de nombreux concepts avec une bienveillance remarquable. Je tiens également à remercier chaleureusement Justine, qui est arrivée à un moment idéal pour me redonner le goût des manips. Je te remercie d'avoir été un modèle, pleine de conseils et pour ta constante bonne humeur. Je ne peux pas oublier Arthur, sans qui j'aurais probablement mis plusieurs mois supplémentaires pour mettre au point les séquences d'acquisitions, et qui contribue, au quotidien, à dissiper de nombreux doutes. Je tiens également à remercier Elsa pour nos nombreuses discussions : *"Il vaut mieux corriger en profondeur ou en temps à ton avis ? Je comprends plus rien, c'est pas la même chose ? Attends, je vais demander à Alex."* Antton, venu tout droit du Canada et du Pays Basque, et avec qui il est si simple d'aborder tout sujet scientifique aussi bien au labo qu'au bar. Également, Rita, avec qui j'ai pu établir des liens entre les domaines des ultrasons et de la sismologie. J'en profite pour remercier

(et encourager) ceux qui poursuivent les travaux au sein de l'équipe : Thibaud Vernier, Gatien Clément, et enfin Emma Brenner, avec qui c'est un réel plaisir d'échanger au quotidien. Merci à Paul de m'avoir fait comprendre en quelques secondes le formalisme de la matrice distorsion : *"Attends, je vais t'expliquer, quand on parle de soustraire la composante géométrique, c'est l'étoile dans le G^*."* Et à Victor, qui débite ses paroles presque aussi rapidement que ses idées : *"J'ai commencé à examiner la taille de la RPSF, mais je pense que rien ne vaut le signal confocal pour optimiser."* Je suis ravi de rejoindre leur aventure pour construire le microscope du futur, ou *"Matriscope"*. Peut-être que *"Discovery"* ça sonne mieux quand même, surtout quand on connaît les précédents qui ont utilisé ce nom pour leur deuxième album.

Je tiens également à remercier les différentes équipes de recherches avec qui j'ai eu l'occasion de collaborer. En premier lieu, l'équipe de Patrick Tabeling, avec Ugur et Pedro, avec qui j'ai eu l'occasion d'appliquer l'imagerie matricielle à un sujet annexe pour la caractérisation des microbulles. Cette tâche, qui s'est révélée plus ardue qu'il n'y paraissait, a bel et bien porté ses fruits, non seulement pour mieux comprendre certains détails techniques, mais plus généralement pour ma meilleure compréhension de la physique des bulles. Je souhaite ensuite adresser des remerciements spéciaux à Olivier Couture et Antoine Coudert, avec qui nous avons mené une collaboration à la fois passionnante et fructueuse. Cela a notamment été l'occasion de confronter notre méthode d'imagerie matricielle à des problématiques plus appliquées, en l'occurrence l'imagerie de super-résolution du cerveau. Cela a constitué une véritable étape dans mon travail puisque cela a notamment confirmé que l'imagerie matricielle pouvait relativement simplement se combiner à d'autres modes d'imagerie. Enfin, j'aimerais remercier toute l'équipe ultrason de Supersonic Imagine avec qui les quelques échanges se sont avérés passionnants pour découvrir une autre dynamique de travail avec des objectifs plus industriels.

De manière plus générale, j'aimerais remercier l'ensemble des personnes constituant l'Institut Langevin : Nathalie, Christelle, Catherine et Emmanuel ; le pôle informatique avec Romain et David ; et bien évidemment les chercheurs, post-docs et doctorants dont les recherches ne sont rien de moins qu'une source d'inspiration. Je tiens à exprimer ma reconnaissance particulière envers Claire, Ignacio, Xiaoping et Arnaud T., qui m'ont ouvert les portes du laboratoire au cours de différents stages. Ils ont constitué mes premiers pas vers cette aventure. J'aimerais également exprimer ma profonde gratitude envers Arnaud Derode. Ta manière si propre à toi d'échanger constitue un réel atout dans l'ambiance du labo. J'aimerais tout particulièrement te remercier d'avoir généreusement mis à ma disposition certains de tes équipements pour que je puisse commencer à expérimenter.

Un remerciement plus lointain va à Monsieur Olivier, mon professeur de physique en classe de Maths Spé. Il demeure sans doute le meilleur enseignant que j'ai eu la chance de rencontrer tout au long de mon parcours académique. Sa manière passionnée de transmettre son savoir a indubitablement joué un rôle majeur dans l'éveil de mon intérêt pour la physique.

Je souhaite maintenant exprimer une reconnaissance plus amicale envers les membres de mon bureau à l'Institut Langevin. Je tiens premièrement à remercier Ulysse Najar, avec qui j'ai traversé les premiers moments de ma thèse lorsque le formalisme matriciel nous semblait encore obscur. Benjamin Apffel, pour m'avoir fait comprendre que le bruit à la surface de l'eau n'était pas du speckle mais bien de la turbulence d'ondes ! Hussam, dont les schémas fait de traits partant dans toutes les directions, ne montrent que l'évidence d'un travail acharné ! Un ringraziamento speciale a Claudia per il suo impeccabile ma silenzioso francese... Jérôme Don Jayamane, dit Jay-Di, dont les nombreuses anecdotes rythment notre quotidien. Et comment ne pas évoquer Guillaume Noetinger, dit Noet. S'il ne fallait citer qu'un seul moment : *"Eh mec, je crois que je suis plus limité par la diffraction. En théorie, si j'itère, je peux être résolu à l'infini."* À confirmer... Enfin, je tiens à saluer Romain Monsarrat, qui, bien qu'il ne soit pas membre du bureau, est si fréquemment présent qu'il laisse presque planer le doute. Merci pour

tes questions excentriques de théoricien chevronné : *"Est-ce qu'il y a quelqu'un ici qui a déjà régularisé une équation différentielle d'ordre 4 avec des tenseurs d'ordre 3 ?"* Merci également à Alexandre Delory pour ta patience face à mon (trop) grand optimisme pour parler de choses (pas si) inutile : un GUI par exemple...

J'aimerais également remercier mes amis : Lucas, Marie, Martin, Alice S., Louis, Vincent. Une pensée spéciale pour l'équipe du Pérou (Thomas, Alice B. et Étienne), qui m'a permis de démarrer ma thèse dans les meilleures conditions. Je tiens également à mentionner ceux qui ont partagé mes journées en visio pendant le confinement : Gabriel, Antonin et Baptiste. Une légère nostalgie pour évoquer finalement la *"lunch team"* : Maxime et sa passion refoulée pour les mathématiques, Léa et son légendaire retard, Victor et son amour pour la pétanque, Renaud et ses envies de tennis à 8h du matin, et Théo, parti bien trop tôt du côté de la région Grand Est.

Enfin, je tiens à exprimer une profonde reconnaissance envers ma famille, une présence constante dans ma vie. À mon père, qui me parlait de logique pendant nos vacances, *"p implique q donc non q implique non p", "oui, oui, papa".* À ma mère et à mon frère, qui, malgré leur médecine, n'ont vraiment saisi les applications de mes recherches qu'au moment de ma soutenance. Et enfin, à Léa, j'ai tout tenté pour soutenir plus tôt que toi, mais j'admets ma défaite.

En conclusion, merci à beaucoup de monde. La recherche, bien que solitaire, est loin de se faire toute seule.

Glossary

Symbol	Meaning
$\mathbf{R}$	Reflection matrix
$\mathbf{R}_{\mathcal{M}}$	Reflection matrix in a common midpoint basis
$\mathbf{R}_{\mathcal{D}}$	Reflection matrix in a de-scan basis
$\mathbf{\Gamma}$	Reflectivity matrix
$\mathbf{G}$	Propagation matrix
RPSF	Reflection Point Spread Function
$\mathbf{T}$ and $\hat{\mathbf{T}}$	Transmission matrix and its estimator
$\mathbf{D}$	Distortion matrix
$\mathbf{C}$	Correlation matrix
$\delta\mathbf{C}$	Perturbation of $\mathbf{C}$
$\|\|\delta\hat{\mathbf{T}}\|\|^2$	Bias intensity of $\mathbf{T}$-matrix estimator
$\mathbf{i}$	Input basis coordinate
$\mathbf{o}$	Output basis coordinate
l_{c}	Confocal filter size
ITR	Iterative Time Reversal
IPR	Iterative Phase Reversal
$\mathbf{W}^{(n)}$	Wave-front of the ITR process at iteration n
$\mathbf{r}_{\mathrm{m}}$	Common midpoint
$\mathbf{r}_{\mathrm{p}}$	Central point of a spatial window
$\mathbf{r}_{\mathrm{c}}$	Confocal point
$\mathbf{\Delta\rho} = \boldsymbol{\rho}_{\mathrm{out}} - \boldsymbol{\rho}_{\mathrm{in}}$	Distance between input and output focusing points
$\mathcal{D}(\mathbf{\Delta\rho})$	De-scan window function

Table 1: **List of symbols for matrix imaging.**

Symbol	**Meaning**
$\times$	Matrix product
$\circ$	Hadamard product
$\circledast$	Convolution product
$\dagger$	Transpose conjugate of a matrix
$\top$	Matrix transpose
$\hat{}$	Estimator of a physical quantity
SVD	Singular Value Decomposition
$\mathbf{U}^{(i)}$	i^{th} right singular vector of a matrix
$\mathbf{V}^{(i)}$	i^{th} left singular vector of a matrix
σ_i	i^{th} singular value of a matrix
$\langle ... \rangle$	Ensemble average
$\langle ... \mid ... \rangle$	Scalar product

Table 2: **Mathematical symbols.**

Symbol	Meaning
$\mathcal{I}$	Image
$\mathbf{H}$	Point Spread Function matrix
$\mathbf{r} = (x, y, z)$	Focal point
$\boldsymbol{\rho} = (x, y)$	Transverse coordinate
λ_{c}	Wavelength at the central frequency
f_{s}	Sampling frequency
c_0	Speed-of-sound hypothesis
$\mathbf{u} = (u_x, u_y, 0)$	Transducer position
$\delta\rho_0$	Transverse ideal resolution
t	Time
γ	Medium reflectivity
$\boldsymbol{\theta}/\mathbf{k}$	Plane wave/Fourier basis
N_u	Number of transducers
f_{c}	Central frequency
β	Antisymmetric rate of a matrix
$\theta_{\max}$	Directivity of transducers
$\delta\theta$	Plane wave sampling
$\boldsymbol{\Delta}\mathbf{u} = (\Delta u_x, \Delta u_y)$	Probe dimension
C	Coherence factor
f_c	Central frequency
$\mathcal{A}_{(-3dB)}$	Area above 1/2 on RPSF amplitude
$\delta\rho_{(-3dB)}$	RPSF resolution
$\mathcal{C}$	RPSF contrast
α_{S}	Single scattering rate
α_{M}	Multiple scattering rate
α_{N}	Electronic noise rate
$\mathcal{W}$	Spatial average window function
$N_{\mathcal{W}}$	Number of resolution cells in $\mathcal{W}$
$\mathbf{w} = (w_x, w_y, w_z)$	Dimension of $\mathcal{W}$
τ	Time-of-flight
$\Delta\tau$	Time delay
A	Apodization term of synthetic aperture

Table 3: **List of general symbols.**

General Introduction

Our ability to see is the oldest imaging system, in which the eye focuses optical light reflected from objects onto the retina. Subsequently, various imaging systems have emerged that go beyond what the human eye can see.

In the specific case of medical imaging, there are several modalities with their respective advantages and drawbacks. Optics suffers from lack of penetration, but offers sharp resolution down to the nanometer range. Computed X-ray tomography is invasive, but provides detailed internal images of the body. Magnetic resonance imaging is generally considered as the holy grail of medical imaging because it is noninvasive, and its resolution is limited only by the strength of the magnetic field. However, it is a quite expensive and voluminous apparatus. Moreover, the object under examination must remain static during a long imaging sequence, and it often requires the injection of a contrast agent.

In this context, ultrasound imaging offers a number of advantages thanks to its noninvasive nature and flexibility. Indeed, it is one of the best-resolved clinical imaging modalities, capable of providing real-time images to a depth of several centimeters with a relatively inexpensive and portable system. Mimicking the biological radar used by dolphins or bats, an ultrasound image is generated by echolocation. From this image, other tissue parameters such as blood velocity or tissue stiffness can be extracted. Recently, thanks to a super-resolution technique, namely Ultrasound Localization Microscopy (ULM), it has even become possible to generate images of the vascular network with a resolution of a few micrometers by intravenous injection of microbubbles. This approach is considered as a real breakthrough for functional imaging.

The construction of an ultrasound image is essentially based on two hypotheses: (i) a global constant speed of sound in the medium and (ii) a single scattering assumption. For *in vivo* imaging, they are approximately valid for most applications. However, in scenarios where these assumptions do not hold, the quality of image reconstruction in terms of contrast and resolution is severely compromised by several factors. First, the spatial variations in the speed of sound distort the wave fronts as the wave propagates through the medium, reducing the quality of the focusing process and thus the resolution of the image. These aberrations can hamper the ultrasound diagnosis. In addition, multiple scattering, usually neglected in ultrasound, can drastically degrade the image contrast, especially at large depths.

Thanks to the growing capacities of data storage and computation, a matrix approach to wave propagation has emerged over the years. In the specific case of imaging, it is based on the acquisition of the medium's reflection matrix, which contains the impulse response between each transmitter and each receiver of the multi-element technology used to illuminate and receive the backscattered wave-field under study. This matrix contains all the information of a static

medium in reflection, so that any adaptive focusing experiment can be performed numerically in post-processing without having to repeat a time-consuming physical process. This approach is very general and applies not only to ultrasound, but also to optical microscopy, radar or seismic imaging. Only the experimental acquisition differs from field to field.

This work targets the building block of image generation by an ultrasound scanner. It therefore precedes image processing tools that can be further used to highlight certain parameters of an already generated image. While the generation of an ultrasound image is based on a process of simultaneous focusing at input and output on each point of the image, matrix imaging consists in decoupling the input and output focal points in order to scan aberrations and multiple scattering.

Mathematically, this can be done by the projection of the reflection matrix onto a focused basis. Physically, it consists in the synthesis of virtual transmitters and receivers located inside the medium. In the specific case of ultrasound imaging, this matrix can be used to compensate for aberrations, resulting in a close to ideal image in terms of resolution and contrast. In experiments with linear transducer arrays, the method has been successfully validated to compensate aberrations *in vivo* [Lambert, 2022a; Bendjador, 2020; Chau, 2019] and also to quantify multiple scattering [Lambert, 2020b; Lambert, 2022b].

Nevertheless, because these results were obtained with 1D ultrasound probes for 2D imaging applications, they provide only a one-dimensional field control, limiting the benefits of aberration compensation. The richness of the reflection matrix lies in the use of the largest possible number of degrees of freedom. Therefore, the goal of this work is to extend the study of the reflection matrix along several dimensions. First, it is transposed from 2D to 3D imaging, thereby allowing a much finer compensation of aberrations, with applications to transcranial imaging whether it be in a standard or ULM imaging mode. Second, the temporal degrees of freedom are exploited to characterize the acoustic response of the scatterers, paving the way towards quantitative ULM imaging. Finally, the spatio-temporal degrees of freedom offered by the focused reflection matrix are exploited to optimize focusing parameters such as the focal length or the speed of sound model to: (i) compensate for axial aberrations (defocus) in ultrasound images; (ii) map the speed of sound and obtain a quantitative image of biological tissues. The speed-of-sound is for instance a relevant bio-marker for a certain number of liver diseases.

In Chapter 1, the basics of ultrasound imaging are presented. First, wave propagation and, in particular, focusing are described using Fourier analysis. The main limitations of ultrasound imaging and the strategies to overcome them are examined.

Chapter 2 introduces the general matrix formalism of wave propagation, which goes beyond conventional imaging. In particular, it has been successfully used in previous work to quantify focusing quality and local multiple scattering in ultrasound imaging. In addition, a method for correcting aberrations *in vivo* is presented based on the results of previous work.

In Chapter 3, this framework is extended from 2D to 3D imaging using a matrix array of transducers. Experimental results are presented, and images with enhanced contrast and close to ideal resolution are presented, even in the difficult case of transcranial imaging. Finally, it is shown that the gain in image quality for aberration correction is larger when the correction can

be performed in both dimensions of the imaging probe, which is the case with 3D imaging.

In Chapter 4, we show how matrix imaging can be fruitful for other imaging modalities by considering the example of transcranial ULM. On the one hand, it allows a fine compensation of aberrations induced by the skull to improve the contrast and eliminate artifact of ULM images. On the other hand, it exploits the temporal degrees of freedom of the reflector to make ULM quantitative by tracking the resonance frequency of micro-bubbles, a quantity that is related, in principle, to local pressure in vessels. In particular, we show that our matrix imaging framework can be easily combined with other ultrasound modalities and demonstrate this claim with Ultrasound Localization Microscopy in a transcranial *in vivo* experiment in sheep. Furthermore, we show that microbubbles can also be a promising tool for tracking intra-arterial pressure by using matrix imaging to track their resonance frequency. All the results presented in this chapter are the results of two fruitful collaborations with other academic teams, the groups of Olivier Couture and Patrick Tabeling.

In Chapter 5, we exploit the spatio-temporal degrees of freedom of the reflection matrix to tackle axial aberrations which affect ultrasound images. The reflection matrix actually provides an auto-portrait of the focusing process. Using the extreme sensitivity of the Gouy phase shift at the focusing plane, we exploit this physical phenomenon for a sharp estimation and compensation of defocus at any point of the medium. We first show the advantages of this technique in multi-layered media before turning to *in vivo* imaging.

In Chapter 6, a similar approach is used to map the speed of sound inside the medium, resulting in an image freed from for axial aberrations, on which distances can be accurately measured. Beyond conventional ultrasound imaging, the speed-of-sound is a potential bio-marker for a certain number of disease. Its mapping therefore opens a route towards quantitative ultrasound matrix imaging.

Chapter 1

Ultrasound Imaging

Objectives

Ultrasound imaging is a non-invasive imaging technique that uses ultrasound waves to examine an unknown medium. By physically or numerically **focusing the waves** at any point in the field of view, an image of the reflectivity of the medium can be obtained. Basic principles from echolocation to conventional ultrasound imaging are presented, with emphasis on a Fourier analysis applied to wave propagation. Finally, the fundamental limitations affecting the quality of an image and the current strategies to overcome them are presented.

Contents

1 Introduction

Following Paul Langevin's research on echolocation [Langevin, 1920], ultrasound imaging is an imaging technique that emerged in 1942 [Dussik, 1942] and is currently widely used in the clinic to investigate and diagnose pathologies based on the generation of an ultrasound image. Even though it offers a relatively low resolution ($\sim 0.1 - 1$ mm), it is still an undeniable imaging modality for radiology, mainly because of its real-time capability and portability. Another major advantage is that this imaging technique is non-invasive, relying only on the propagation of ultrasound waves throughout the body.

Basically, an unknown medium is first insonified with ultrasonic waves. The spatial variations in the density and speed-of-sound of the medium inside the body result in secondary scattered and/or reflected waves that propagate back to the probe. However, the reflected wave field recorded by an ultrasonic probe does not provide a direct image of the medium. Usually, an inverse problem is formulated to select the appropriate echoes for a given point by calculating the time-of-flight of the wave from the probe to that point, assuming a constant speed-of-sound in the medium. An image of the reflectivity of the medium is obtained, taking into account both the contribution of speed-of-sound and density. In other words, an anatomical image of a particular body part can be created, which can be used to study medical pathologies. In addition, various other ultrasound imaging modalities can be derived from such a map to characterize, for example, blood flow velocity (Doppler) or tissue stiffness (elastography).

The generation of a conventional ultrasound image is mainly based on two hypotheses: (i) a constant background speed-of-sound in the medium and (ii) a single scattering assumption. However, these two strong hypotheses are generally not true for *in vivo* imaging, because successive tissue layers can cause spatial variations in the speed-of-sound and also multiple scattering events. In other words, as the ultrasound wave propagates, it experiences spatial variations in the speed of sound that distort its wavefront, resulting in a degradation of the image resolution. This detrimental effect is referred to as **aberration**. This is the case, for example, when a thick layer of fat results in a poorly resolved and low-contrast image because the speed of sound varies between the fat and the target organ [Zhang, 2018]. In addition, the signal-to-noise ratio is drastically reduced due to the attenuation of layers such as the skull, which makes the feasibility of transcranial imaging in adult subjects an active research topic from a clinical perspective. Finally, the axial dimension displayed in a medical ultrasound scanner is nothing more than an estimate based on the assumption of the speed-of-sound. Therefore, distance measurements used to monitor the size of malignant tumors or to detect chromosomal abnormalities during pregnancy [Nicolaides, 1992] may be highly biased in such cases.

This first chapter introduces the basic principle of echolocation from pulse-echo detection to ultrasound imaging applications and its evolution over the years. Then, some notes on Fourier analysis of wave propagation are given to describe the fundamental limitations of ultrasound imaging, the key idea being that ultrasound imaging is based on a focusing process of waves. Finally, all factors affecting the quality of ultrasound imaging are examined, and current techniques to circumvent their effects are presented.

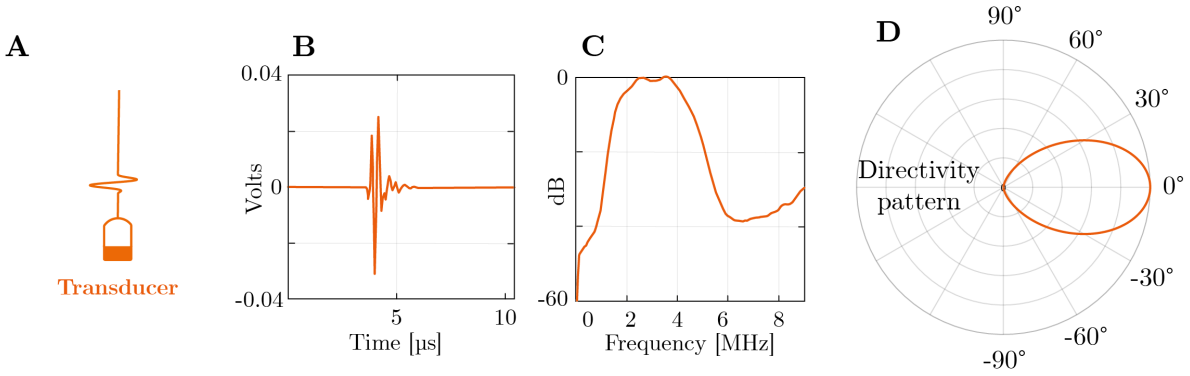

Figure 1.1: **Properties of a piezoelectric transducer.** (**A**) Sketch of a single transducer excited by an electrical pulse. Example of a (**B**) time response and its corresponding (**C**) frequency spectrum of a matrix array of transducers [see Table 3.1], as specified by the manufacturer (Vermon). (**D**) Numerical simulation of the directivity pattern for a transducer of size $\delta u = 0.5$ mm with a central frequency $f_c = 3$ MHz, assuming a speed-of-sound $c = 1540$ m/s.

2 Conventional ultrasound imaging

In this first section, we introduce the building blocks of conventional ultrasound imaging. After describing the key physical properties of a piezoelectric transducer that allow an ultrasonic wave to insonify an unknown medium and record the corresponding backscattered reflected wavefield, we introduce the principle of echolocation, which was originally introduced in underwater acoustics for sonar imaging to detect submarines [Langevin, 1920] and then extend it to the use of an ultrasonic probe to produce an image of the reflectivity of an unknown medium.

2.1 Piezoelectric transducer

A piezoelectric transducer, usually made of lead zirconate titanate (PZT) in medical imaging, is the most important element of any ultrasound imaging device, as it enables the conversion of an electrical signal into a pressure change and inversely thanks to the piezoelectric effect. In other words, it is both a transmitter and a receiver, so it allows not only the generation of ultrasound waves, but also the recording of the time dependence of the pressure wave field at a given point. It is characterized by the following key parameters:

- its spectral responses [Fig. 1.1C], characterized by its central frequency f_c, which is directly related to the thickness of the piezoelectric crystal [Szabo, 2004], and its spectral bandwidth Δf, which defines the minimum and maximum available frequencies. In medical ultrasound imaging, its value ranges from 1 to 20 MHz;
- its directivity pattern [Fig. 1.1D], which is related to its size. The smaller the transducer compared to the wavelength, the more it radiates in all directions, resulting in an isotropic directivity pattern. Conversely, a large transducer radiates in a specific direction.

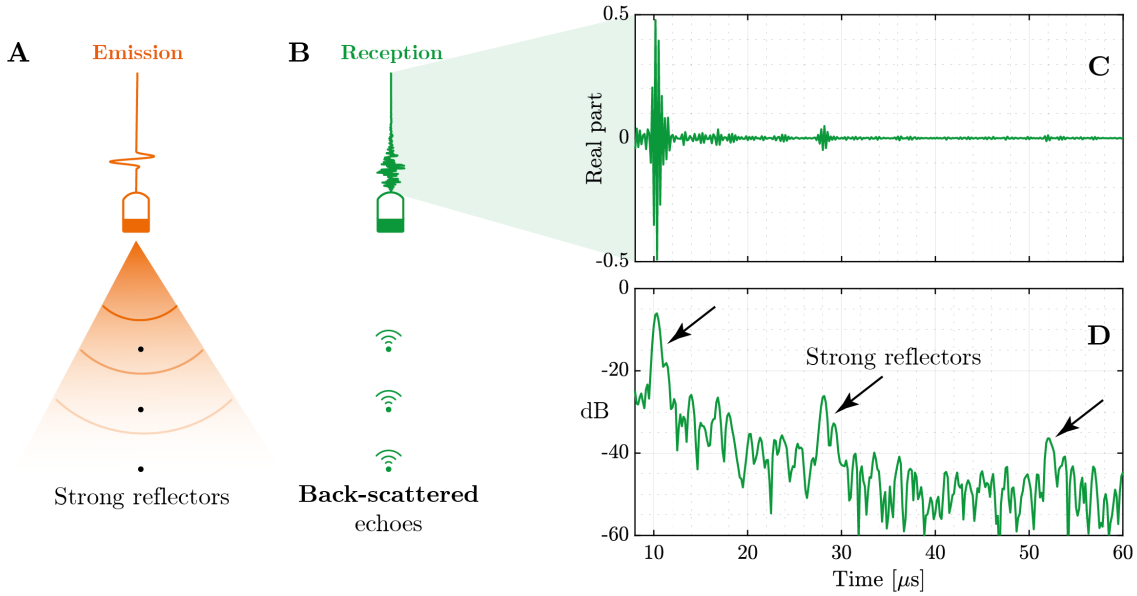

Figure 1.2: **Pulse-echo detection.** (**A**) A single transducer transmits a diverging wave into a medium containing three strong reflectors (nylon rod). (**B**) When the wave interacts with a strong reflector, a secondary scattered wave is generated that propagates back to the transducer, where the time dependence of the pressure wave field is recorded. (**C, D**) Real part and intensity of the recorded wave field, respectively. Three peaks can be seen, clearly indicating the presence of the strong reflectors. The attenuation in the medium explains the decrease in the energy trough time. The experiment is investigated in a tissue mimicking phantom (CIRS, Model 054GS).

2.2 Pulse-echo detection

The simplest way to gain information about an unknown medium is to use a plane transducer that emits a short pulse [Fig. 1.2A], which ideally can be described by the Dirac distribution $\delta(t)$, where t is time. In practice, however, the pulse has a finite duration [Fig. 1.1B], which is directly inversely proportional to the spectral bandwidth $\delta t_{\text{pulse}} = 1/\Delta f$. This electrical pulse is converted into a pressure pulse, so that a diverging wave is generated, provided that an impedance match between the transducer and the medium is ensured. This is done, for example, with ultrasound gel when examining human soft tissues.

When the wave encounters a reflector [Fig. 1.2B], *i.e.* a change in the density and/or speed-of-sound of the medium, a secondary diverging waves is generated. Some examples of acoustic impedance values defined by the product of density and sound velocity of the medium can be found in [Table. 1.1]. The transducer thus allows the echoes backscattered by the medium heterogeneities recorded in the so-called Radio Frequency (RF) signal [Fig. 1.2C]. To reduce the dynamic range of such a signal and make its tiny fluctuations more visible, it is usually displayed on a logarithmic scale [Fig. 1.2D]. In this simple experiment, three echoes are clearly visible, so three reflectors can be detected. This is the principle of echolocation introduced by Paul Langevin in underwater acoustics to detect enemy submarines [Langevin, 1920].

Tissue/Material	**Speed-of-sound** [m/s]	**Density** [kg.m^{-3}]	**Impedance** [Mrayls]
Human tissues			
Breast	1510	1020	1.54
Liver	1578	1050	1.657
Skull/bone	3000	2310	3.9
Ultrasound phantom			
Zerdine gel	1540	1000	1.54
Nylon	2600	1114	2.3
Other materials			
Water (at 20 °C)	1480	1000	1.483
Water (at 60 °C)	1550	1000	1.55
PZT-5A	4350	7.75	33.71

Table 1.1: **Ultrasound properties of various human tissues and materials.** Values are extracted from [Duck, 1990; Fry, 1978; Ogawa, 2013].

2.3 Ultrasound probe

Even though the above method is characterized by a good temporal resolution directly related to the duration of the pulse, it suffers from a poor signal-to-noise ratio (SNR). A strategy to improve this ratio could be to use a convex transducer to increase the energy deposited in the focal point. To increase flexibility, this simple method can be implemented with an ultrasound probe consisting of multiple transducers [Fig. 1.3A] regularly spaced that can be controlled independently of each other, as described in [Fig. 1.3B]. A converging wave that focuses on the desired focal point can be generated by applying time-delays to each transducer of the probe [Fig. 1.4A]:

$$\underbrace{\Delta\tau(\mathbf{u}_{\text{in}}, \mathbf{r}, c_0)}_{\text{Time-delay}} = \underbrace{\tau(\mathbf{u}_{\text{in}}, \mathbf{r}, c_0)}_{\text{Time-of-flight}} - \frac{z}{c_0} = \frac{\sqrt{(x-u_x)^2 + (z-u_z)^2}}{c_0} - \frac{z}{c_0}, \tag{1.1}$$

where $\mathbf{u} = (u_x, u_y, u_z)$ denotes a transducer, $\mathbf{r} = (x, y, z)$ refers to the target focal point, c_0 is the speed-of-sound hypothesis of the medium and the subscript "in" denotes the propagation of the transmitted wave.

This approach is much more flexible because we can focus at any point of the medium. The improvement in SNR depends directly on the number of transducers N_u. This number ranges from 128 or 256 for conventional 1D probes to 1024 for matrix arrays of transducers. In addition, 1D ultrasonic probes usually use an acoustic lens [see blue part in Fig. 1.3C] to focus at a certain depth in the elevation plane (y-plane) such that propagation remains constrained in a plane, thus increasing the energy of wave propagation in that imaging plane (x, z). In addition, the geometry of the probe can be adapted to a specific anatomical part. Convex probes, for example, are characterized by transducers that are aligned along a specific radius, greatly increasing the field-of-view and allowing imaging of relatively large organs such as the liver.

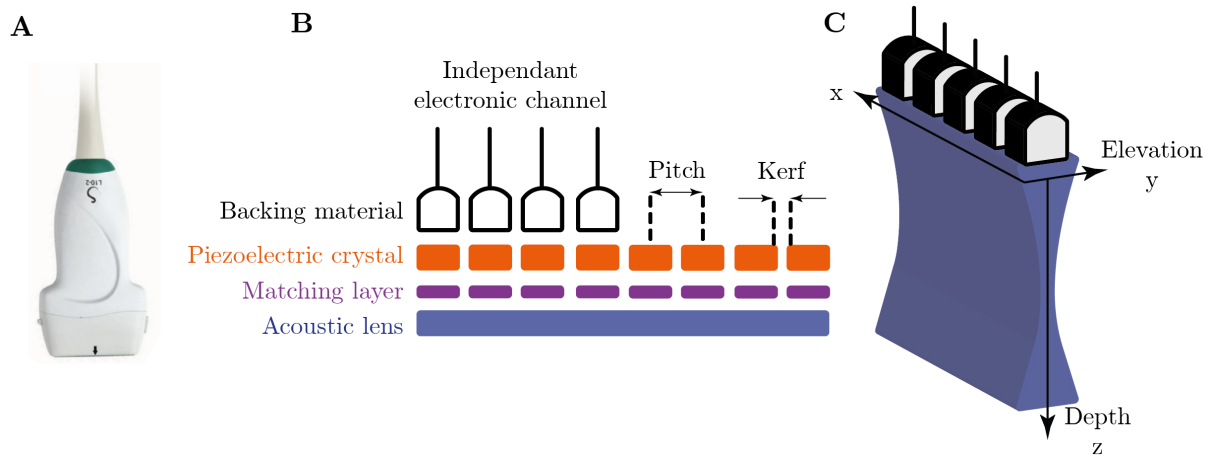

Figure 1.3: **Sketch of a linear ultrasound probe.** (**A**) Commercial linear probe [*Extracted from* Hologic website]. (**B**) Sketch of the main components of an ultrasound probe. (**C**) Three-dimensional view. The acoustic lens enables the study of wave propagation in a plane with a resolution called the elevation plane.

2.4 Numerical focusing

Interestingly, the reflected wavefronts contain much more information that can be combined to further increase the signal-to-noise ratio at the focal point. Assuming that we focus at a given point $\mathbf{r}$ and that we have recorded the reflected wavefront at each transducer in time, this wealth of information can be stored in a matrix $\mathbf{s} = [s(\mathbf{u}_{\text{out}}, t)]$. The propagation time-of-flight to go from $\mathbf{r}$ to $\mathbf{u}_{\text{out}}$ is also given by (Eq. 1.1). Thus, the received channels [Fig. 1.4B] can be delayed to align the recorded wavefronts associated to the focal point [Fig. 1.4C]. By summing the individual channels [Fig. 1.4D], the signal emanating from this point is significantly amplified. Mathematically, this can be expressed as follows:

$$s'(\mathbf{r}, t, c_0) = \sum_{\mathbf{u}_{\text{out}}} s(\mathbf{r}, \mathbf{u}_{\text{out}}, t + \Delta\tau(\mathbf{u}_{\text{out}}, \mathbf{r}, c_0)), \tag{1.2}$$

where s' is the delayed and summed signal. Assuming that the origin of time $t = 0$ is set when the transmitted wave is generated, so that the transmitted wave reaches the focal point at z/c_0. The value of $\mathcal{I}$ at the ballistic time ($t = 2z/c_0$) directly holds an estimation of the reflectivity at this very point [Fig. 1.4E]:

$$\mathcal{I}(\mathbf{r}, c_0) = s'(\mathbf{r}, t = 2z/c_0, c_0) \tag{1.3}$$

$$= \sum_{\mathbf{u}_{\text{out}}} s(\mathbf{r}, \mathbf{u}_{\text{out}}, \tau(\mathbf{u}_{\text{out}}, \mathbf{r}, c_0)), \tag{1.4}$$

where $\mathcal{I}$ is the image of the reflectivity.

2.5 Reflectivity map

To create an image, this process can be repeated for each focal point. However, this is a time-consuming process because a physical focusing process is required for each point of the

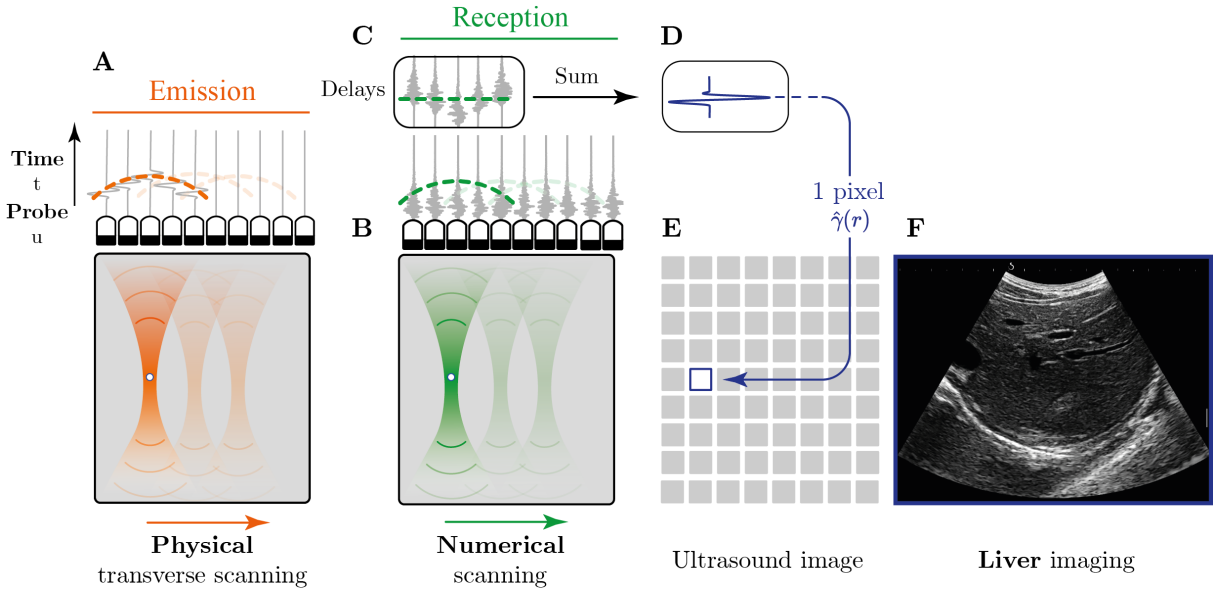

Figure 1.4: **Conventional *B-mode* in ultrasound imaging.** (**A**) A focused beam is generated for emission by appropriately delaying the individual transducers of the probe. The focusing process here is physical. (**B**) The backscattered wavefronts are recorded on each transducer of the probe. (**C**) A numerical focusing process is performed by applying the same appropriate time delays to align the wavefront coming from the targeted focal point. (**D**) A coherent sum is then performed whose value at the ballistic time corresponds to one pixel of the image. (**E**) Each pixel is thus a complex value containing both phase and amplitude information. (**F**) Example of a liver ultrasound image of a healthy volunteer. The intensity of the image is displayed in a logarithmic scale. The brightest part corresponds to the interface of the liver.

medium and the assumption of a static medium may not be guaranteed, resulting in possible motion artifacts. However, it is possible to take advantage of the finite size of the field of view created by the focusing process, which distributes energy not only at the focal spot $\mathbf{r}_{\text{in}}$ but also above and below the focal depth; this is the so-called depth-of-field. Using appropriate time delays $\tau(\mathbf{r}_{\text{in}}, \mathbf{r}, c_0)$, an image can thus be obtained from focused beams. Iterative scanning in the transverse direction, called B-mode imaging, with few input focal spots thus enables the recovery of real-time imaging capabilities. Such data can be stored in a new matrix $\mathbf{R} = [R(\mathbf{r}_{\text{in}}, \mathbf{u}_{\text{out}}, t)]$, that we will refer to the reflection matrix in the following. Thus, the previous equation becomes:

$$\mathcal{I}(\mathbf{r}, c_0) = \sum_{\mathbf{r}_{\text{in}}} \sum_{\mathbf{u}_{\text{out}}} R(\mathbf{r}_{\text{in}}, \mathbf{u}_{\text{out}}, \underbrace{\tau(\mathbf{r}_{\text{in}}, \mathbf{r}, c_0)}_{\text{Input focusing}} + \underbrace{\tau(\mathbf{u}_{\text{out}}, \mathbf{r}, c_0)}_{\text{Output focusing}}). \tag{1.5}$$

The intensity of the ultrasound image is then usually displayed on a logarithmic scale to reduce the dynamic range and make the structures more visible. An example of a liver image in a normal subject is shown in [Fig. 1.4F]. The vessels are associated with dark areas in the image because they contain scatterers that are much less echogenic compared to the soft tissues of the liver, meaning that they exhibit lower impedance fluctuations.

The imaging process is thus the result of a double focusing process, namely **confocal imaging**, in which the waves are focused either physically or numerically at the same point at emis-

sion and at reception. It is clear that the reconstructed image depends directly on the constant speed-of-sound hypothesis c_0. In order to quantify the fundamental limitations of this method, especially in terms of contrast and resolution, it is necessary to introduce some basics of wave propagation that can be well described by a Fourier analysis.

3 Fourier analysis of wave propagation

To better understand the fundamental limits of the reconstructed image $\mathcal{I}$, it is necessary to recall some memories of wave propagation. In particular, we will see that the Fourier analysis is an indispensable tool for describing wave propagation.

A wave can be defined as the propagation of a perturbation of a field through space ($\mathbf{r}$) and time (t). In this way, the spatio-temporal dependence of a particular parameter of the medium is studied. In ultrasound imaging, the field under consideration is the pressure field, which can be considered as a scalar value, unlike other wave fields such as the electromagnetic or elastic waves, where the vector nature of the wave must be taken into account.

The pressure perturbation oscillates in the longitudinal direction, *i.e.* in the direction of propagation, which is characteristic of compressional waves.

3.1 The d'Alembert equation

Assuming a homogeneous medium, the propagation of ultrasonic waves is described by the d'Alembert equation:

$$\Delta p(\mathbf{r},t) - \frac{1}{c^2}\frac{\partial^2 p(\mathbf{r},t)}{\partial t^2} = S(\mathbf{r},t), \tag{1.6}$$

where p is the scalar pressure field, Δ is the Laplacian operator, c is the speed of sound of the medium and S a source term. This equation underlies fundamental physical properties. First, its second order derivative with respect to time makes it **invariant by time reversal** [Fink, 1992]. Second, we can use the Green's formalism to show that the self-adjoint property of the Laplacian operator implies the **spatial reciprocity** of wave propagation. Indeed, the Green's function $G(\mathbf{r},\mathbf{r}_A,t)$ is the solution of the d'Alembert equation when the source is a unique point located at $\mathbf{r}_A$ emitting an infinitely short pulse, *i.e.* $S(\mathbf{r},t) = \delta(\mathbf{r}-\mathbf{r}_A)\delta(t)$. The roles of the transmitter and a receiver located at $\mathbf{r}$ can be reversed: The signal recorded from $\mathbf{r}_A$ to $\mathbf{r}$ is the same as the signal recorded from $\mathbf{r}$ to $\mathbf{r}_A$.

Without any source term, a solution of the wave equation is the monochromatic plane wave, which can be expressed as follows:

$$p(\mathbf{r},t) = A_0.\exp(-i\underbrace{(\omega t + \mathbf{k}.\mathbf{r} + \phi_0)}_{\text{Phase}}), \tag{1.7}$$

where A_0 is the amplitude, $\omega = 2\pi f$ is the pulsation, $\mathbf{k}$ is the wave vector, and ϕ_0 is a phase reference. The norm of the wave vector is given by $2\pi/\lambda$, where λ is the wavelength defined by the ratio between the speed of sound and the frequency $\lambda = c/f$. Considering a biological tissue composed mainly of water ($c \sim 1540$ m/s), the associated wavelength for a frequency of $f_c = 3$

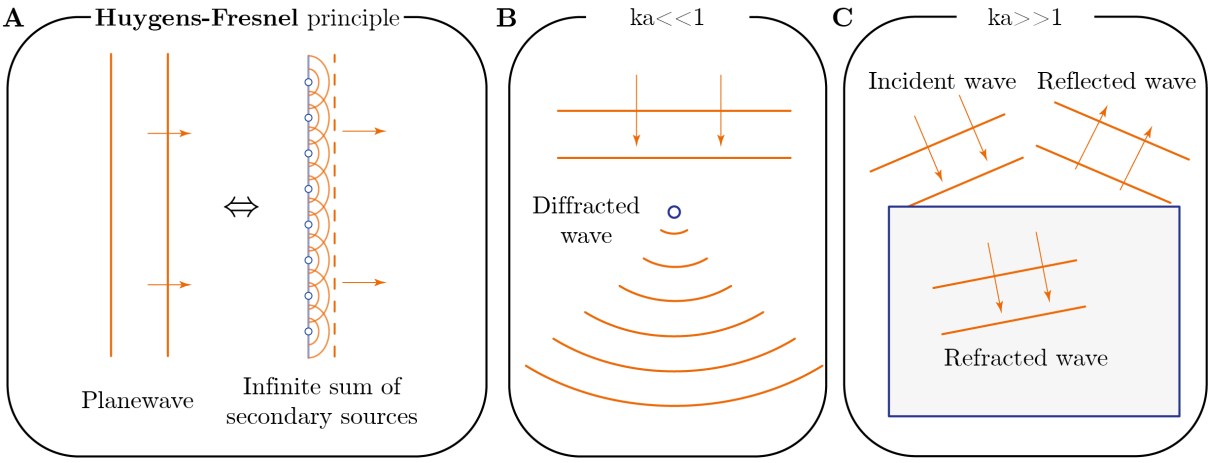

Figure 1.5: **Huygens-Fresnel principle and diffraction theory.** The Huygens-Fresnel principle states that the propagation of a wave can be considered as an infinite sum of secondary waves at any instant. (**A**) Example of a plane wave decomposed into a sum of aligned virtual secondary sources. (**B**) The Huygens-Fresnel theorem can be used to explain the diffraction of a plane wave by an object whose size is on the order of the wavelength. (**C**) Snell-Descartes' laws apply to interfaces between two media, *i.e.* objects whose size is much larger than the wavelength. An incident plane wave results in a tilted transmitted wave (refraction) and a reflected wave whose wavevector points in the opposite direction.

MHz is about 0.5 mm. Spatial and temporal oscillations of a plane wave can be linked by the dispersion relation $\|\mathbf{k}\| = \omega/c$.

3.2 Huygens Fresnel principle

Another important feature of the d'Alembert equation is **linearity** and the resulting superposition principle. Originally formulated as the Huygens-Fresnel principle, it states that a wave can be decomposed into an infinite sum of secondary waves. In other words, each instant of wave propagation can be viewed as the emission of an infinite number of diverging waves lying on the wavefront of the propagation, as shown in [Fig. 1.5A] for the particular case of a plane wave.

This remarkable view of wave propagation explains why, on the one hand, a small scatterer (or a pinhole) whose size is smaller than the wavelength diffracts, radiates, or scatters in all directions of space [Fig. 1.5B]. On the other hand, if we consider a boundary surface, *i.e.* an object whose shape is much larger than the wavelength, the wave is reflected in a single direction [Fig. 1.5C]. Moreover, the transmitted wave is diffracted according to the Snell-Descartes law. Thus, there are different scattering regimes depending on the size of the objects under consideration, where λ is the relevant observable to be compared.

3.3 Fourier analysis

Combing linearity with (Eq. 1.7), each solution of the d'Alembert equation can be expressed as follows:

$$p(\mathbf{r},t) = \int\int \mathrm{d}\omega\mathrm{d}\mathbf{k} p_{\mathcal{F}}(\mathbf{k},\omega)\exp(-j(\omega t + \mathbf{kr})), \tag{1.8}$$

where $p_{\mathcal{F}}$ is the spatio-temporal Fourier transform of the pressure field p. Thus, Fourier analysis seems to be a suitable tool for describing wave propagation. Mathematically, it is a change of basis that projects experimental data into an abstract space, that provides a different view on experimental data.

A first use of the Fourier transform can be made when considering the Dirac distribution whose Fourier transform is a constant. In other words, a perfect pulse results in a flat response in the Fourier domain and is thus associated with an infinite frequency range. However, the wave generated in ultrasound imaging has a finite duration, reducing the available frequencies in the so-called spectral bandwidth, such that $\Delta f = 1/\delta t_{\text{pulse}}$. Using the dispersion relation and assuming a constant speed of sound in the medium, this quantity thus defines the axial resolution δz_0 of an ultrasound image:

$$\delta z_0 = c_0 \delta t_{\text{pulse}} = c_0/\Delta f. \tag{1.9}$$

Such signals are called **broadband** because they represent a sum over a certain frequency range.

3.4 Coherence and interferences

The key concept behind the Huygens-Fresnel principle is wave **coherence**, which describes the ability of two waves to interfere with each other. Mathematically, this property can be described by considering two waves p_1 and p_2 and looking at the intensity of the wave field:

$$|p_1(\mathbf{r},t) + p_2(\mathbf{r},t)|^2 = \underbrace{|p_1(\mathbf{r},t)|^2 + |p_2(\mathbf{r},t)|^2}_{\text{Incoherent}} + \underbrace{p_1(\mathbf{r},t)p_2^*(\mathbf{r},t) + p_1^*(\mathbf{r},t)p_2(\mathbf{r},t)}_{\text{Coherent}}, \tag{1.10}$$

where $p_n(\mathbf{r},t) = A_n \exp(j\phi_n(\mathbf{r},t))$ is the pressure wave-field associated to the wave of subscript "n" with A_n its amplitude and ϕ_n its phase.

The resulting intensity is not only the result of the two intensities, namely the incoherent term, but also the contribution of a coherent term describing the interference between the two waves. In other words, the phase of the wave field is determinant, since it can lead to constructive interference when two waves are in phase ($A_1^2 + A_2^2 + 2A_1A_2$), or to destructive interference when two waves are out of phase ($A_1^2 + A_2^2$).

In contrast to optical imaging, where coherence is only guaranteed under certain conditions (coherent source such as laser, or secondary sources like in the experience of Young's slits) and thus applies to a spatially and temporally limited coherence length, ultrasonic sources are characterized by a much larger coherence length, which we will consider infinite in the following.

3.5 Random wave-field and speckle pattern

When considering a random wave field, this property of interference leads to random patterns. In ultrasound imaging, these so-called **speckle patterns** generally form the background of the ultrasound image, since the medium consists of a random distribution of unresolved scatterers that can be modelled by a random reflectivity $\gamma(\mathbf{r})$.

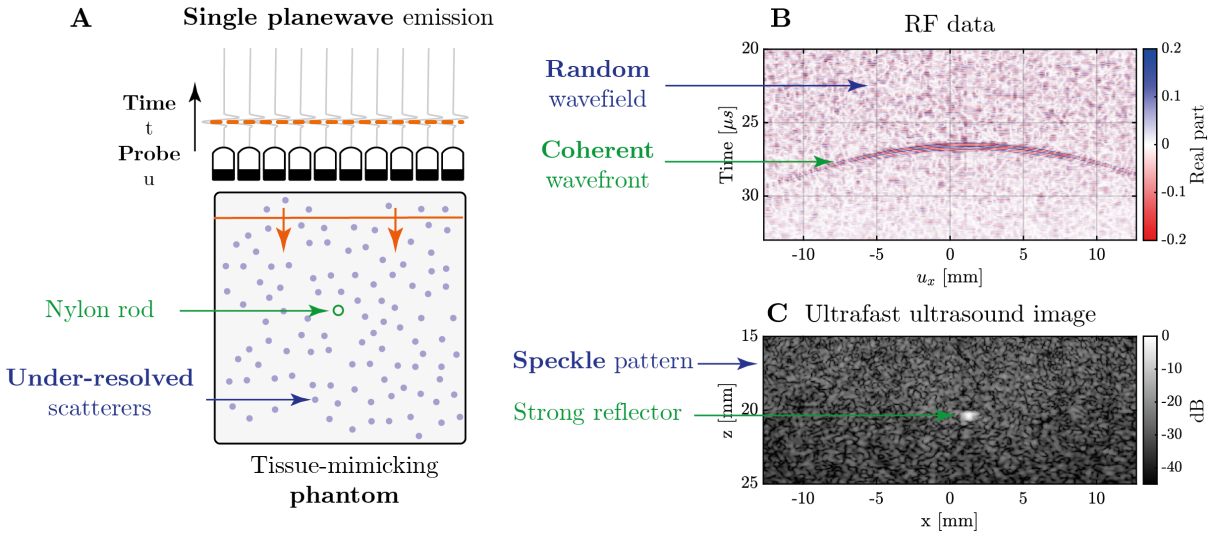

Figure 1.6: **Ultrafast imaging in a random medium.** (**A**) A single plane wave insonifies a tissue-mimicking phantom made of randomly distributed and under-resolved scatterers. (**B**) Real part of the raw radio-frequency (RF) signals. A coherent wavefront appears clearly and is associated with the nylon rod. (**C**) Corresponding ultrasound image. A random wave-field results in a random pattern, called *speckle*.

We will now consider the generation of a speckle pattern by a tissue-mimicking phantom insonified by a partial plane wave [Fig. 1.6A]. This can be done by emitting a pulse simultaneously with each transducer of the probe [Bruneel, 1977; Lu, 1997; Sandrin, 1999]. Albeit simple, it was considered as a real breakthrough at that time because it allows a much larger field of view with a smaller number of insonifications compared to previously focused beams, resulting in an ultrafast frame rate of several kHz.

The ultrasound phantom consists of an ultrasound gel composed of unresolved scatterers and some bright targets made of nylon rods. The backscattered reflected wavefronts are recorded on each transducer of the ultrasound probe and shown in [Fig. 1.6B].

Two features stand out clearly in [Fig. 1.6B]. First, a coherent wavefront associated with a bright reflector appears. Second, the background wave-field shows random fluctuations due to the random reflectivity of the medium. After beamforming, an ultrasound image can be obtained. Thus, the background corresponds to a random speckle pattern, and the bright target can be detected with a sharp resolution [Fig. 1.6C].

3.6 The focusing process

This experiment can be used to better illustrate the numerical focusing process described earlier. When the wave reaches the reflector, a secondary wave propagates back to the probe, and its corresponding wave-field is captured by the ultrasonic probe. The corresponding wavefronts are shifted in time with respect to each channel of the probe due to the geometry. The numerical focusing process consists of applying appropriate time-delays (or equivalent phase shifts at the central frequency) to realign the wavefronts with respect to each channel. Doing so, a **coherent sum at the ballistic time** results in a strong amplification of the signal emanating from

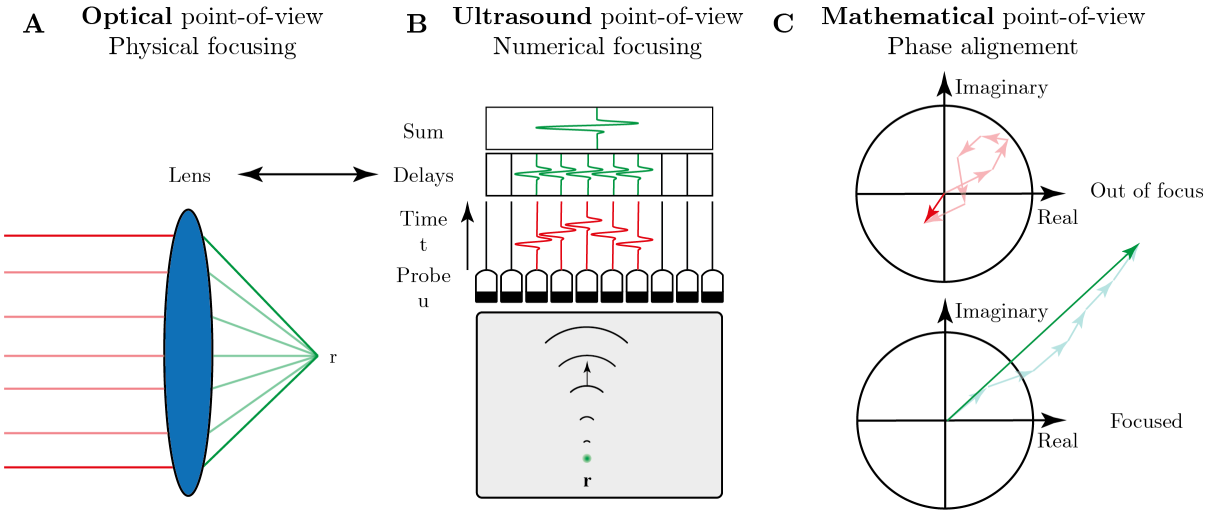

Figure 1.7: **The focusing process.** (**A**) A plane wave light passing through an optical lens results in a focused wave at the output due to the radius curvature of the lens. (**B**) This process is very similar to the time delay of echoes coming from a single targeted focal point and recorded on each transducer of an ultrasound probe. (**C**) Mathematically, the focusing process consists of aligning the phases of all partial wave, which are combined to form the total wave.

that point. This principle is called beamforming in ultrasound imaging and can be viewed as a numerical focusing process in which a wave is not physically focused in the medium, but is virtually focused in post-processing.

The geometric time-delays to be applied [Fig. 1.7B] are very similar to the radius of curvature of an optical lens, which causes an optical path difference such that a plane wave passing through a lens gives rise to a converging wave that focuses in the so-called focal plane [Fig. 1.7A]. Thus, the focusing process can be regarded as a Fourier transform connecting the far-field (plane wave basis or **k**-space) and the focal plane (real space). Mathematically, the focusing process corresponds to the phase alignment of each individual partial wave recorded by each transducer [Fig. 1.7C] to maximize the energy at a particular time and point, called the focus. The focusing process, whether physical or numerical, is at the heart of ultrasound imaging to maximize the signal emanating from any focal point in the field-of-view.

However, the amplification of the focusing process is inherently limited by the so-called isochronous volume [Mallart, 1994]. It is defined as the spatial area from which echoes, that will contribute to the acoustic signal at a given time-of-flight, come from. For a given source-receiver couple, the isochronous curve is an arc of ellipse whose foci are the source and the receiver and whose width is $c_0\delta t$ [Fig. 1.8A]. The corresponding isochronous volume follows the shape of this ellipse, with a thickness δz_0. When considering the focused beamforming process, the acoustic signal will result from echoes coming from each individual isochronous volume associated with each transmitter-receiver couple [Fig. 1.8B]. Thus, instead of summing only the contribution of the targeted focal point where all isochronous volumes overlap, one pixel of the ultrasound image results from the summation of echoes coming from each isochronous volume at the ballistic time, thus reducing the gain in signal-to-noise ratio provided by the beamforming process.

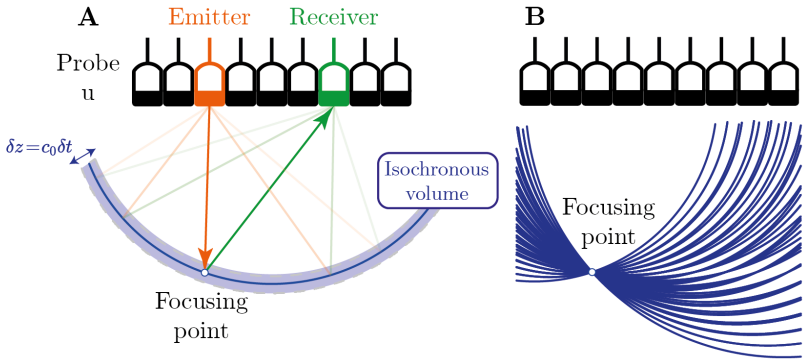

Figure 1.8: **Isochronous volume.** (**A**) Isochronous volume associated to a single emitter (orange), receiver (green) and a focal point. The associated ballistic time has multiple solutions that describes an ellipse. (**B**) Complete set of isochronous curves, $\mathcal{V}$, associated with all the emitters & receivers and the same time echo. *Inspired from* [Mallart, 1994].

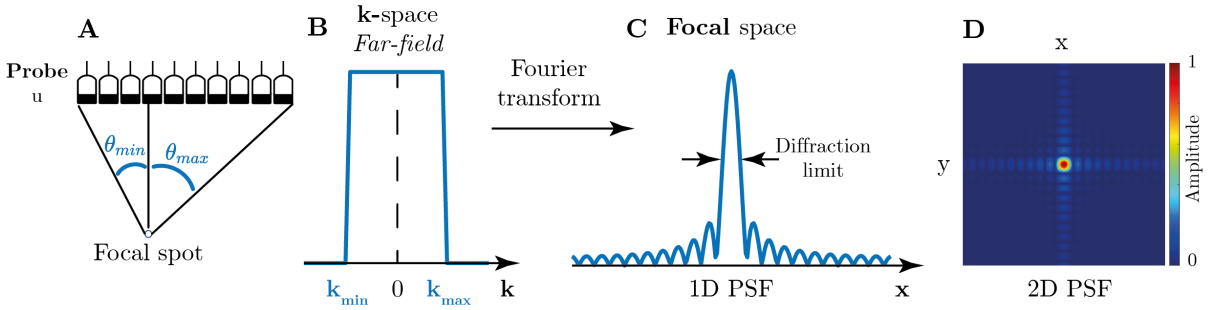

Figure 1.9: **Numerical aperture and Point Spread Function (PSF).** (**A**) The aperture of an imaging system defines the maximum angle of insonification that reaches the targeted focal point. (**B**) Flat aperture function in $\mathbf{k}-$space. This space can be considered as a plane wave basis or a far-field basis. (**C**) The Fourier transform of the aperture function defines the Point Spread Function of the system, which determines the transverse resolution of the imaging system. In other words, it defines the limit of the system for distinguishing two points. The most common method of defining resolution is the Rayleigh criterion, *i.e.* the full width at half maximum. (**D**) Point Spread function in 3D imaging.

3.7 Resolution and Point Spread Function (PSF)

The observed size of the bright target in [Fig. 1.6C] does not correspond to the actual size of the object, but to the resolution of the imaging system. In the axial direction it is limited by the duration of the emitted pulse, while in the transverse direction it is limited by the wavelength and the size of the imaging system, more precisely by its **numerical aperture**.

The angular aperture refers to the angular range $\Delta\theta = \theta_{min} + \theta_{max}$ observed from a given focal point, as described in [Fig. 1.9A]. Thus, the angular aperture function is rectangular in the k-space [Fig. 1.9B], where the transverse wave vector k_x is related to the angle of a plane wave according to the relation $k_x = \|\mathbf{k}\| \sin(\theta)$. Interestingly, the focal plane ($\mathbf{r}$) and the far-field ($\mathbf{k}$), are related by a spatial Fourier transform. Thus, the Fourier transform of the angular aperture is a cardinal sinus in the focal plane that defines the impulse response of an imaging system, better known as the **Point Spread Function (PSF)** [Fig. 1.9C]. Its size determines the transverse

resolution of an imaging system, defined by its ability to distinguish two point-like objects at the same depth. The transverse resolution of an imaging system δx_0 is thus given by the first zero of the cardinal sinus function:

$$\delta x_0 = \frac{\lambda}{2NA} = \frac{\lambda}{2\sin(\Delta\theta/2)}. \tag{1.11}$$

Using a matrix array of transducers, the PSF of a 3D imaging system is thus the product of two cardinal sinuses, as depicted in [Fig. 1.9D].

In a paraxial approximation, *i.e.* for a point located far away from the probe ($z \gg \lambda$) and along the propagation axis, and the previous equation can be simplified as follows:

$$\delta x_0 \approx \frac{\lambda z}{\Delta u_x}, \tag{1.12}$$

where Δu_x is the size of the probe and z is the depth of the focusing point. It is important to note that only the focusing process at the output was considered here, with a single transmitted plane wave at the input.

Conversely, the size of the transducer implies a certain range of spatial frequencies (or angles) that defines its pattern of directivity. Thus, a transducer of size λ emits in all directions [blue curve in Fig. 1.10A, D], while a transducer of size 20λ emits preferentially in one direction and thus generates a quasi-plane wave [green curve in Fig. 1.10B, D].

3.8 Shannon criterion & aliasing effect

The considerations in the previous section refer to the continuous access to real space. However, the use of an ultrasound probe leads to a spatial sampling of the wave-field in the transducer plane, which also corresponds to a sampling of the **k**-space. Mathematically, the aperture function of an ultrasound probe is the convolution of a Dirac comb that accounts for the regular position of each transducer, known as the pitch and noted δu, and a rectangular window that accounts for the size of each transducer $\delta u' = \delta u - \kappa$, where κ is the spacing distance between two elements. Mathematically, the aperture function $\mathcal{A}$ of a finite probe made of N transducers can be written:

$$\mathcal{A}(x) = \underbrace{\Pi_{\delta u'}(x)}_{\text{Transducer size}} \overset{x}{\circledast} \underbrace{\left(\sum_{n}^{N} \delta(x - n\delta u)\right)}_{\text{Sampling}}, \tag{1.13}$$

where $\Pi_{\delta u'}$ is a rectangular window function of size $\delta u'$ and $\overset{x}{\circledast}$ denotes a spatial convolution. Thus, the maximum spatial frequency k_x that can be correctly detected according to the Shannon's criterion must satisfy the following expression:

$$2\left(\frac{k_x}{2\pi}\right) \leq \frac{1}{\delta u}. \tag{1.14}$$

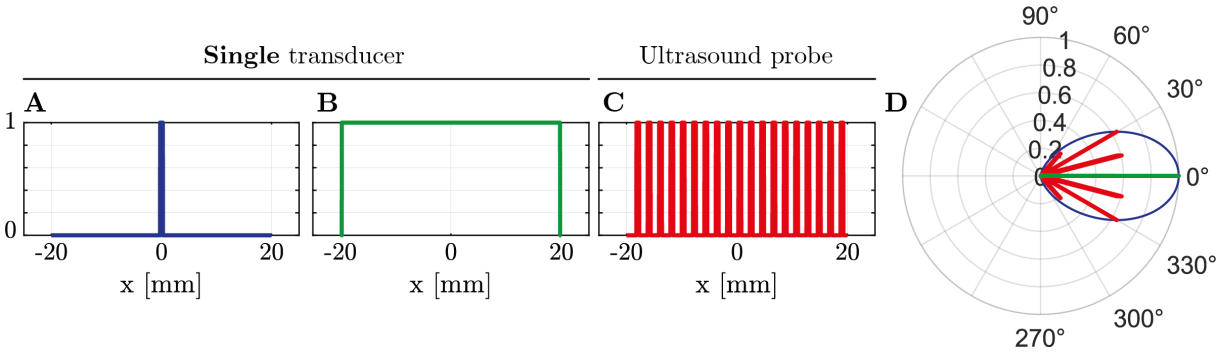

Figure 1.10: **Grating lobes and aliasing effect.** (**A, B**) Aperture function of a single transducer of size λ and 20λ, respectively. (**C**) Aperture function of an ultrasound probe. (**D**) Directivity pattern in each case. These are numerical simulations obtained with a central frequency $f_c = 7.5$ MHz, $c = 1540$ m/s.

Assuming a central wavelength $\lambda_c = c/f$ such that $k_x = 2\pi/\lambda_c \sin(\theta)$, it can be reformulated as follows:

$$\sin(\theta) \leq \frac{\lambda_c}{2\delta u}. \tag{1.15}$$

Thus, this condition is always satisfied if $\delta u \sim \lambda_c/2$ which is the case for phased-array probes. Phased-array probes are thus characterized by a small aperture, with a large angular field-of-view. They are particularly suitable for trans-costal imaging, where bones should be avoided as much as possible. However, for linear probes characterized with a pitch of $\delta u \sim \lambda_c$, Shannon's criterion cannot be always satisfied, and grating lobes may appear. For example, if a plane wave is transmitted with an angle of 30°, energy at $\theta = -30°$ is also transmitted. Such grating lobes are shown in [red curve in Fig. 1.10D].

Spectral aliasing can also occur in the time domain. To satisfy the Shannon criterion, the most naive approach is to set the sampling frequency f_s to at least twice the maximum frequency of the transducers' spectral bandwidth. However, there are some strategies to reduce the sampling frequency of a recording system in order to reduce the amount of data. In the specific case of ultrasound imaging, one technique is IQ modulation (see Appendix 7) [Kirkhorn, 1999]. Briefly, this can be used to demodulate the RF signal so that the spectrum is shifted to the zero frequency as follows:

$$s_{\mathrm{IQ}}(t) = s_{\mathrm{RF}}(t).\exp(-2i\pi f_c t). \tag{1.16}$$

After applying a low-pass filter, the signal can be down-sampled at a sampling frequency equal to the spectral bandwidth, drastically reducing the amount of collecting data. In this way, the signals from IQ demodulation are directly complex values containing both phase and amplitude information. One strategy for accessing the complex information in the real RF signals is to keep only the positive frequency. In the following, we will only consider complex signals.

4 Ultrasound imaging today

Originally, ultrasound imaging used focused beams to physically scan an unknown medium, namely *B-scan*. Although ultrasound imaging is the fastest clinical imaging modality, its conventional frame rate is limited because it requires multiple focused ultrasound beams distributed over a limited portion of the field of view to image the medium. Therefore, it is not sufficient to capture the rapid fluctuations of biological tissue.

4.1 Ultrafast imaging

The ability to generate an ultrasound plane wave was introduced to increase the frame rate [Bruneel, 1977; Lu, 1997; Sandrin, 1999], namely *ultrafast ultrasonic imaging* [Tanter, 2014]. This increased frame rate of about a thousand frames per second represented a paradigm shift at the time because, in conjunction with fast parallel processing [Delannoy, 1979], it can reveal previously hidden information about tissue and blood motion. In particular, this new technology paved the way for ultrafast Doppler imaging [Hansen, 2009; Bercoff, 2011; Osmanski, 2012b; Ekroll, 2013; Yiu, 2013] and ultrafast contrast imaging [Couture, 2009; Couture, 2011; Couture, 2012], but also for new ultrasound imaging modalities such as functional ultrasound imaging of brain activity [Macé, 2011; Mace, 2013] or even shear wave elastography [Bercoff, 2003; Bercoff, 2004]. The latter is based on tracking the tissue displacement induced by a shear wave in the medium to extract the shear wave velocity, which can eventually be converted into a shear modulus map to characterize the stiffness of tissues.

4.2 Synthetic focusing

Moreover, it is possible to use the total number of available spatial degrees of freedom at the input, which is nothing else than the number of transducers N, associated with the same number of available plane waves. Therefore, it is possible to use successive series of plane wave insonifications [Fig. 1.11A] that forms a basis in the **k**-space and focus them synthetically, *i.e.* numerically, on a given point [Fig. 1.11C] [Montaldo, 2009]. It should be noted that the angle of the plane waves depends on the medium speed of sound (see. Appendix 8). An example is shown in the carotid artery of a healthy volunteer. This is the principle of *coherent compounding*, which corresponds to a numerical focusing process at the input and thus produces a large contrast enhancement, as shown in [Fig. 1.11D]. Note that there is always a tradeoff between contrast and frame rate: The contrast of the ultrasound image scales as the number N_{in} of plane wave insonifications, while the frame rate scales as $1/N_{\text{in}}$.

4.3 Confocal imaging

Coherent compounding leads not only to a large contrast enhancement, but also to an improvement in resolution, which we will quantify later. This double focusing process at the input and output is the ultrasound equivalent of optical confocal imaging.

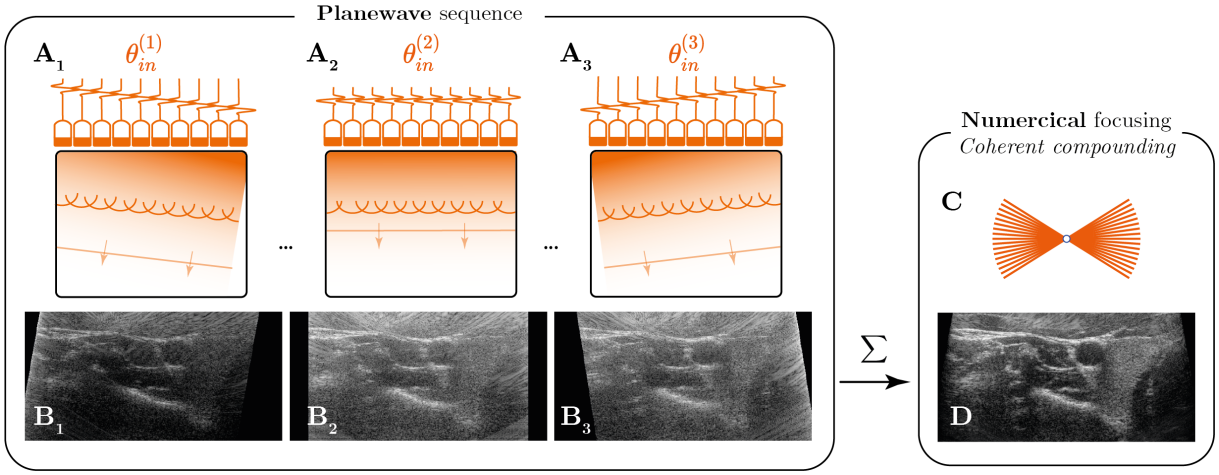

Figure 1.11: **Synthetic focusing or coherent compounding.** Carotid imaging of a healthy volunteer (**A**) A plane wave can be generated by appropriately delaying the individual transducers and assuming a constant speed-of-sound in the medium. (**B**) A single plane wave can be used to reconstruct an ultrasound image of the medium. (**C**) The coherent summation of the individual images can be viewed as a numerical focusing process at the input, resulting in a (**D**) contrast-enhanced image. *Adapted from* [Montaldo, 2009].

Main steps in ultrasound imaging

In general, ultrasound imaging can be summarized in the following three steps:

- (i) insonification of the medium with a successive number of ultrasound waves, referred to as $\mathbf{i}_{\text{in}}$. In the next chapter, various insonification bases will be presented;
- (ii) recording of the backscattered wavefronts at each transducer $\mathbf{u}_{\text{out}}$ of the probe;
- (iii) an image is then generated by applying appropriate time-delays to numerically focus on the same point both at emission and reception. Such an operation can be performed with a Delay-And-Sum (DAS) algorithm, which can be expressed mathematically as follows:

$$\mathcal{I}(\mathbf{r}) = \sum_{\mathbf{i}_{\text{in}}} \sum_{\mathbf{u}_{\text{out}}} A(\mathbf{i}_{\text{in}}, \mathbf{u}_{\text{out}}, \mathbf{r}) s(\mathbf{i}_{\text{in}}, \mathbf{u}_{\text{out}}, \tau(\mathbf{i}_{\text{in}}, \mathbf{r}) + \tau(\mathbf{u}_{\text{out}}, \mathbf{r})), \tag{1.17}$$

where A is an apodization factor that takes into account the directivity of the transducers.

In a single scattering regime, this quantity is an estimation of the complex reflectivity at any point of the medium convoluted with an imaging Point Spread Function:

$$\mathcal{I}(\mathbf{r}) = \gamma(\mathbf{r}) \overset{\mathbf{r}}{\circledast} \underbrace{[H_{\text{in}}(\mathbf{r}).H_{\text{out}}(\mathbf{r})]}_{\text{PSF}_{\text{conf}}(\mathbf{r})}, \tag{1.18}$$

where PSF_{conf} denotes the confocal imaging PSF, which is the product of the input and output

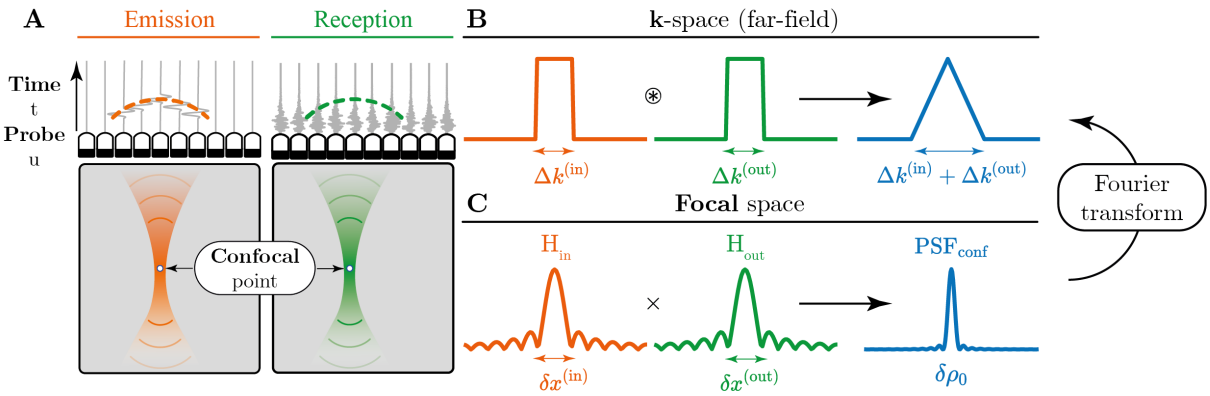

Figure 1.12: **Confocal imaging.** Conventional ultrasound imaging is equivalent to confocal imaging when all available spatial degrees of freedom available (*i.e.* the square number of transducers) are used. (**A**) Schematically, it refers to focusing on the same point during transmission and reception. (**B**) In the **k**-space, the aperture function of such a system is the convolution of the input and output imaging systems, resulting in a triangular function. (**C**) In the focal space, it corresponds to the product of the input and output PSF.

PSFs $H_{\text{in/out}}(\mathbf{r})$. In the **k**-space, the previous equation can be reformulated as follows:

$$\mathcal{I}(\mathbf{k}) = \gamma(\mathbf{k}).\left[H_{\text{in}}(\mathbf{k}) \overset{\mathbf{k}}{\circledast} H_{\text{out}}(\mathbf{k})\right]. \tag{1.19}$$

Hence, the angular support of the resulting confocal image has a triangular shape of width $4k_0\sin(\theta)$ in the **k**-space. It means that the minimum details that can be discerned on the ultrasound image scale as $\delta x_0/2$.

Methods such as *structured illumination* aim to make the angular aperture function rectangular to access high spatial frequency with a higher signal-to-noise ratio, thus increasing the resolution by a factor of 2 [Gustafsson, 2000; Ilovitsh, 2018]. However, these techniques rely on the demodulation of a specific pattern that is sent to the medium and must be well known, which is not the case when the medium is heterogeneous. For this reason, such techniques are not explored in this work, and the fundamental resolution limit we target is the confocal resolution.

4.4 Various set of imaging modality

Ultrasound imaging includes various imaging techniques based on the complex reflectivity map $\mathcal{I}$, which contains information about both the amplitude and phase of the wave-field.

4.4.1 Image of reflectivity

The most common imaging modality corresponds to the intensity of the complex field that provides an image of anatomical structures, such as the kidney in [Fig. 1.13A]. It is usually represented in a logarithmic scale as follows:

$$\mathcal{I}_{\text{dB}}(\mathbf{r}) = 10\log_{10}\left(|\mathcal{I}(\mathbf{r})|^2\right). \tag{1.20}$$

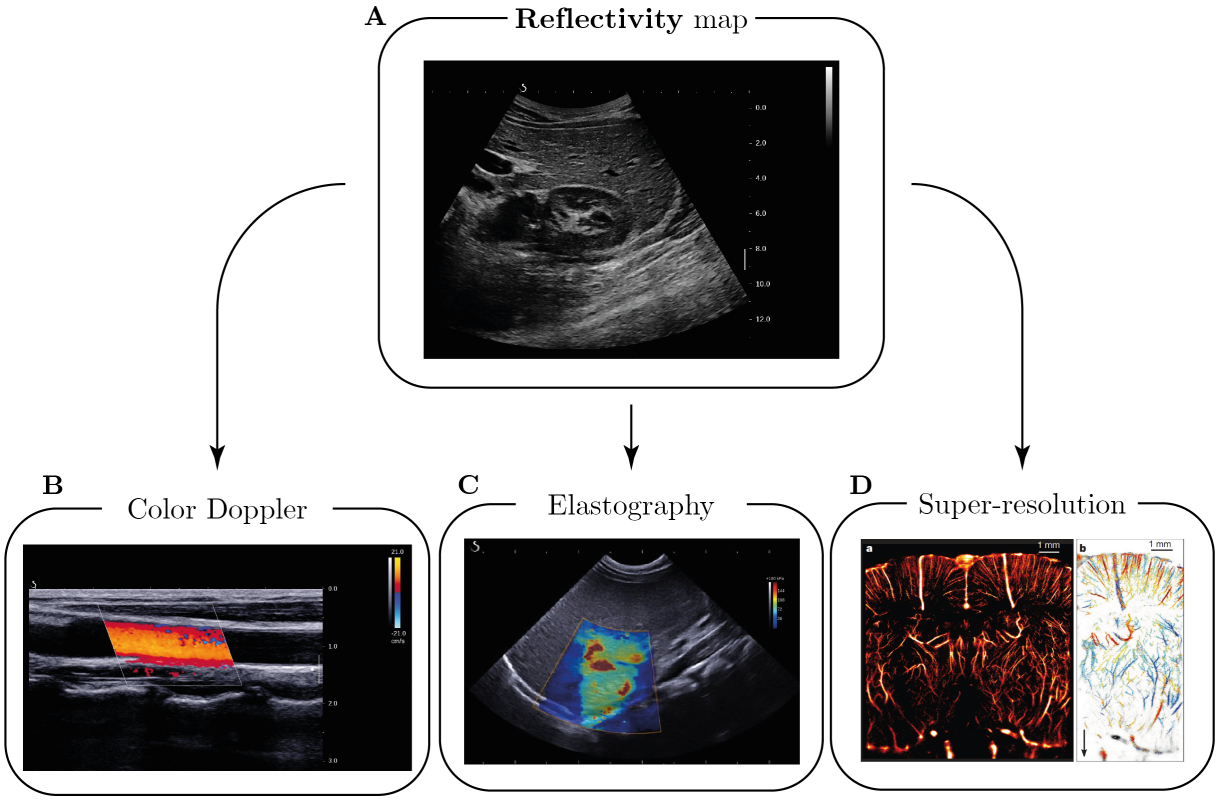

Figure 1.13: **Different modalities of ultrasound imaging.** Each imaging modality in ultrasound imaging is based on the ability to reconstruct a map of the reflectivity of an unknown medium. (**A**) Example of ultrasound reflectivity image of the kidney. (**B**) Example of *color Doppler* imaging in the carotid artery. (**C**) Example of an elastography map in a 2-month-old child to visualize a liver nodule. Extracted on *Supersonic Imagine website*. (**D**) Example of super-resolved images of blood vessels in rat brain using Ultrasound Localization Microscopy (ULM). *Extracted from* [Errico, 2015].

4.4.2 Doppler imaging

Other imaging modalities can be built from the complex image to study the dynamics of biological tissue with ultrafast imaging. For this purpose, multiple images $\mathcal{I}(\mathbf{r}, t_\mathrm{p})$ are created at different times t_p. The complex images are then filtered to extract only the signals that correspond to what is moving in the field of view. The filtered images are noted $\mathcal{I}^{(\mathrm{filt})}$.

In the past, high-pass filters along the time dimension have been used to extract blood motion based on the different characteristics of tissue and blood motion [Bjaerum, 2002; Yoo, 2003]. However, such filters are not optimal because they assume that the spectral features of blood and tissue motion do not overlap. However, this assumption does not hold for vessels with low flow velocities, which affects accuracy when reconstructing small vessels or when tissue motion is strong, such as in cardiac applications. One solution to overcome this problem is to exploit not only the temporal but also the spatial features of tissue and blood motion using singular value decomposition (SVD) [Ledoux, 1997; Kruse, 2002; Lovstakken, 2006; Yu, 2010], the full potential of which can be unlocked thanks to ultrafast plane wave acquisition [Demene, 2015;

Baranger, 2018]. Such a mathematical operator is described in more detail in Chapter 2 (see Section 3.3.1).

Whatever the type of filter used to enhance the signal coming from a moving target in the field-of-view, the image of vessels can be obtained by simply summing the intensity of all images as follows:

$$PW(\mathbf{r}) = \sum_{t_\mathrm{p}} \left| \mathcal{I}^{(\mathrm{filt})}(\mathbf{r}, t_\mathrm{p}) \right|^2 . \tag{1.21}$$

This is what is known as the Power Doppler image. One can go even further by tracking the Doppler shift caused by moving blood cells to create a velocity map known as Color Flow Imaging, the expression of which writes [Demené, 2014]:

$$CD(\mathbf{r}, t'_\mathrm{p}, \omega_\mathrm{p}) = \left| \sum_{t_\mathrm{p}} \mathcal{I}^{(\mathrm{filt})}(\mathbf{r}, t_\mathrm{p}) \mathcal{W}_t(t_\mathrm{p} - t'_\mathrm{p}) \exp(i\omega_\mathrm{p} t_\mathrm{p}) \right|^2 \tag{1.22}$$

where $\mathcal{W}_t$ is a Hann window function centered around zero. An example of such an imaging modality in the carotid artery is shown in [Fig. 1.13B].

4.4.3 Shear wave imaging

In the particular case of shear wave elastography [Fig. 1.13C], a movie of the shear wave can be made by looking at the phase-shift between two successive images:

$$SWE(\mathbf{r}, t_\mathrm{p}) = \arg\left[\mathcal{I}(\mathbf{r}, t_\mathrm{p}) \mathcal{I}^*(\mathbf{r}, t_\mathrm{p} + \delta t_\mathrm{p}) \right] . \tag{1.23}$$

4.4.4 Ultrasound Localization Microscopy

A more recent approach, namely *Ultrasound Localization Microscopy* (ULM), based on the detection and tracking of isolated microbubbles, even allows imaging of vessels at a resolution ten times below the diffraction limit [Fig. 1.13D]. This mode will be described in more detail in Chapter 4 when it is used to generate super-resolved and aberration-free images of sheep brain subjects.

5 *In vivo* imaging and its limitations

Each ultrasound imaging modality depends on the ability to reconstruct a map of the medium's reflectivity. In this section, we present the main limitations that affect the quality of the image and the strategies to overcome them.

The construction of an ultrasound image is essentially based on two hypotheses: (i) A global constant speed of sound c_0 in the medium and (ii) a single scattering assumption [green path in Fig. 1.14]. For *in vivo* imaging, however, these hypotheses are far from true and the quality of the reconstruction in terms of contrast and resolution is therefore greatly impacted by the following factors:

– (i) the **spatial variations in the speed-of-sound** lead to wavefront distortion during propagation [White, 1968; White, 1978; Marcus, 1975; Banjavic, 1978; Halliwell, 1978; Foster, 1979; Mast, 1997; Mast, 1998] and thus time delay errors during beamforming. These adverse effects are the so-called **aberrations**, which reduce both the resolution and contrast of the image. Note that aberrations also account for refraction phenomena occurring at tissue interfaces. However, such detrimental effects can be compensated if one is able to estimate them;

– (ii) the **absorption** impacts the amplitude of the wave through propagation and can thus drastically reduce the signal-to-noise ratio (SNR) at deep depth. **Attenuation** which defines the loss of energy of the wave of a medium is the combination of scattering, absorption and specular reflection. The two first phenomena are characterized by an extinction length l_e, which is defined as follows:

$$\frac{1}{l_\mathrm{e}} = \frac{1}{l_\mathrm{s}} + \frac{1}{l_\mathrm{a}}, \tag{1.24}$$

where l_s is the scattering mean free path, *i.e.* the mean distance between two scattering events, and l_a is the absorption mean free path. In a single scattering regime, the scattering mean free path can be considered much larger than l_a, and the attenuation can be attributed entirely to the absorption. Attenuation is often expressed in dB/cm/MHz because it depends strongly on frequency [Duck, 1990; Bamber, 2005]. Thus, when designing the spectral characteristics of an ultrasound probe, a compromise must be made between penetration depth and resolution. In any case, the attenuation is compensated for using a time gain compensation function (TGC), so that a homogeneous background intensity is seen over the entire field-of-view;

– (iii) the **reverberation** of the transmitted wave in a particular layer can lead to ghost image replicas of a given object in the reconstructed image, and is thought to be responsible for the ultrasound *clutter* that affects image quality in *e.g.* echocardiography [Fatemi, 2019]. Reverberation is associated with multiple reflections and is thus a special case of multiple scattering;

– (iv) the **multiple scattering**, which occurs upstream the focal plane, is usually considered a major problem for imaging because the deterministic relationship between the echo travel time and the position of the scatterer is no longer valid. In practice, it is the result of a random walk process [red path in Fig. 1.14] and therefore appears as a coherent noise that reduces image contrast. The use of the Born expansion [Born, 1926], which decomposes each scattering event, can well describe a strongly scattering medium, but it is mainly limited to numerical simulations because it requires a perfect knowledge of the medium with the position and diffraction pattern of each scatterer. Long neglected in ultrasound imaging, multiple scattering is, for instance, the main cause of imaging failure in the lung, where the strong concentration of air droplets causes strong scattering. In this particular case, recent work suggests that the diffusion constant may be an interesting bioindicator for the diagnosis of specific pathologies [Mohanty, 2017; Aubry, 2008b]. In addition, recent

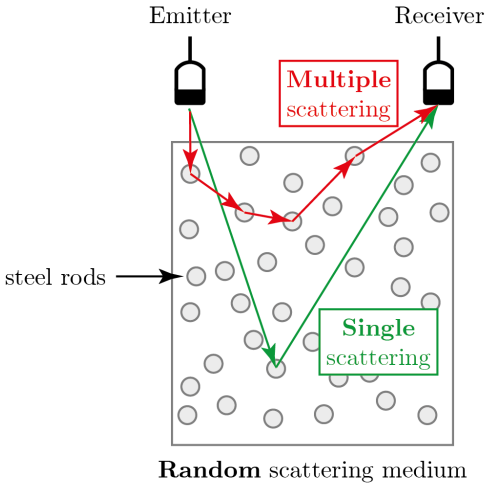

Figure 1.14: **Single and multiple scattering.** Single scattering refers to a scattering path in which the originally emitted wave is diffracted only once before reaching the receiver. Multiple scattering refers to all scattering paths that involve multiple scattering events before returning to the receiver. Multiple scattering is usually considered a detrimental effect in imaging because it appears as coherent noise in the ultrasound RF signal. Thus, it is not trivial to decompose all scattering events, unless the medium is already fully characterized.

studies have quantified the multiple scattering rate locally [Lambert, 2022b] and show that it is far from negligible, even in cases such as the liver. A preliminary work performed by Antton Goïcoechea during his post-doc at the Institut Langevin show that the scattering mean free path in this case is of the order of about 20 mm [Goïcoechea, 2023];

– (v) the **motion** during a long acquisition will affect resolution if no effort is made to compensate for it. Motion may refer to probe motion, tissue motion (also called *clutter*), and out-of-plane motion. This may account for the lower resolution range of images based on plane wave compounding compared to conventional focused beams. In addition, this may also affect the method described in the following chapter, where the reflection matrix of the medium, *i.e.* the inter-element responses of the probe, requires a relatively long acquisition with N insonifications.

Transcranial imaging, which today is mainly limited to Color Doppler, can be considered the most difficult case of ultrasound imaging because it combines all the adverse effects mentioned above and described in [Fig. 1.15]. A plane wave passing through the cranial layer is distorted [Fig. 1.15A], which severely affects the PSF and thus resolution at any point in the brain [Fig. 1.15B]. In addition, reverberations can occur in the cranial layer, resulting in ghost artifacts in the image and severely affecting reconstruction at shallow depths, as demonstrated in a head phantom experiment using a phased array probe [Fig. 1.15C]. Furthermore, multiple scattering may occur due to the porosity of the cranial layer, which consists of an irregular arrangement of cortical and trabecular bone (diploë), varying greatly from person to person and position to position. Last but not least, the cranial layer leads to a strong attenuation of the transmitted wave [Pinton, 2012] and thus to a very low signal-to-noise ratio, which has limited

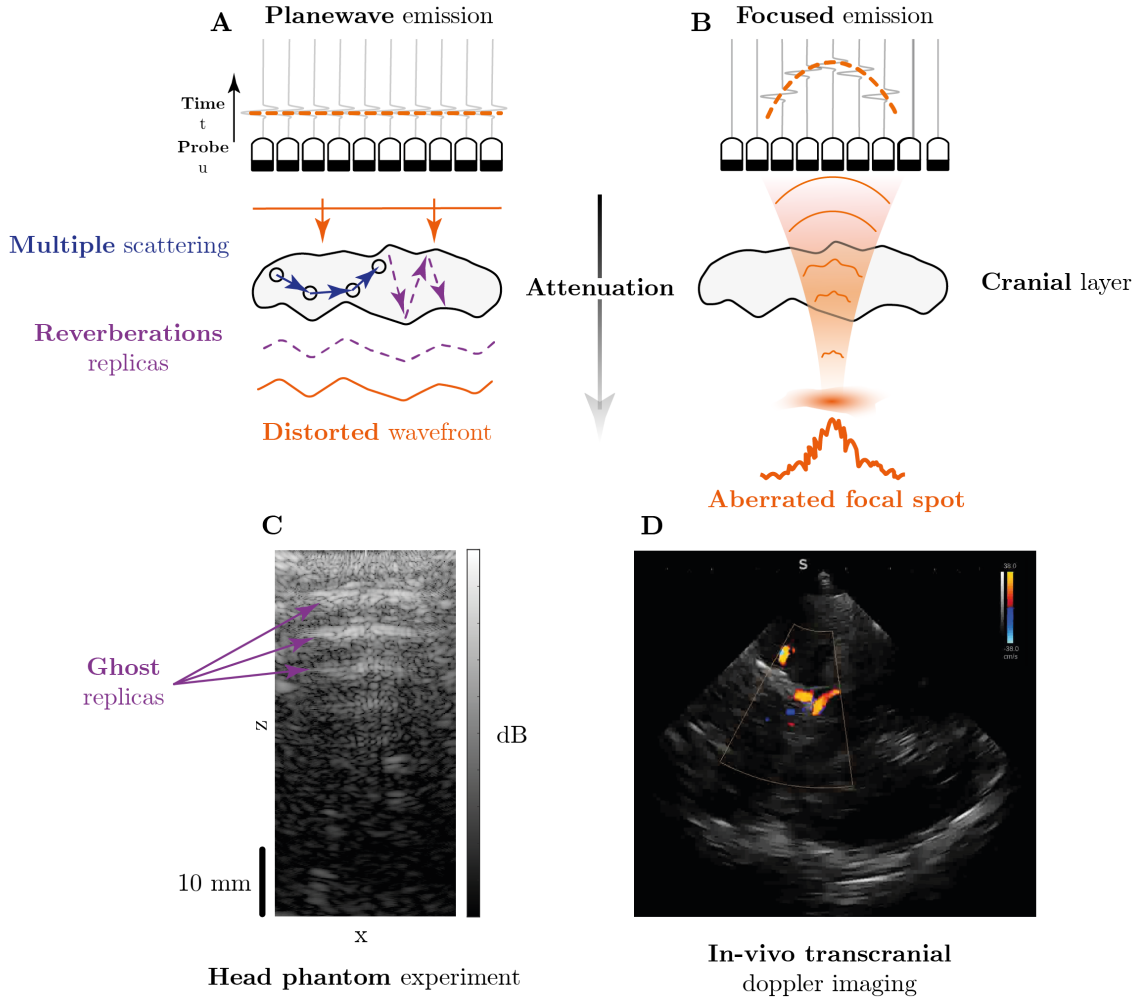

Figure 1.15: **Challenge in transcranial ultrasound imaging.** (**A**) Adverse effects of a plane wave transmitted through the cranial layer. First, the strong index fluctuations in the cranial layer distort the wavefront at the output. Second, the highly varying porosity from one individual to another and from one position to another can lead to multiple scattering. Reverberations artifacts can also occur in the cranial layer, resulting in ghost echoes of the initial wavefront. Last but not least, the attenuation by the cranial layer drastically reduces the energy passing through the cranial layer and thus drastically affects the signal-to-noise ratio of the transcranial image. (**B**) The focusing process is severely compromised. Distortion of the wavefront results in an aberrated focal spot, leading to a sharp decrease in resolution. (**C**) Head phantom imaging experiment with a phased-array probe. Reverberations in the skull layer give rise to ghost replicas at shallow depths. (**D**) Poorly resolved and low contrasted *in vivo* transcranial image of a healthy volunteer, superimposed on the Doppler image.

brain ultrasound imaging to low-frequency ultrasound probes ($\sim$ 1 MHz).

Since this is the most important topic of this work, an overview of the adverse effects of spatial variations in the speed of sound and the current strategies for resolving them will now be presented.

5.1 Manifestations of the aberrations

In medical ultrasound imaging, aberrations are mainly due to a mismatch between the hypothesis of the speed of sound used for beamforming and the actual speed-of-sound in the medium [Anderson, 1998]. This is the case, for example, in transcranial imaging, where the porosity of the cranial layer leads to strong lateral variations of the speed of sound, which in turn can lead to higher transverse aberrations. The effects of such an incorrect hypothesis during beamforming are examined in the simple case of using a linear array to image a tissue mimicking phantom [Fig. 1.16B], with a constant speed-of-sound ($c_\mathrm{p} = 1540$ m/s). First, the reconstructed image shows lower overall contrast compared to the ideal image [Fig. 1.16A], which is evident at large depths where the bright spots are no longer visible. Also, the image of each target (nylon rod) is characterized by a larger transverse size. Last but not least, the overall image is shifted upward. The reason for this effect becomes clear when considering the calculated time-of-flight for a given point in both cases [Fig. 1.16C]. A change in the speed-of-sound results in a shift of the time-of-flight, which shifts the image upward compared to the ideal image. This is the case, for example, when imaging the liver, as the ultrasound wave passes through layers of fat and muscle before reaching the organ. The difference between these two time-of-flights directly provides the time-error for that point, which can be expressed as a phase shift (at the central frequency) between the individual transducers.

In the following, we will discriminate between transverse and axial effects of aberrations. Transverse aberrations account for a transverse spreading and distortion of the focal spot. Axial aberrations result in an incorrect axial positioning of scatterers in the ultrasound image. Transverse aberrations will be tackled in Chapter 3 and 4 while axial ones will be investigated in Chapter 5 and 6.

To quantify the strength of the aberrations and thus their effect on the image, one can examine the root-mean-square of the time delay error. Various studies have examined numerous anatomical parts, and found values between 23 and 60 ns RMS, for example, in the human breast [Trahey, 1991; Freiburger, 1992; Gauss, 2001; Gauss, 1997]. Time errors can also be expressed as phase delays, since the effects of aberrations directly depends on the frequency range of the experiment [Davros, 1985; Nock, 1989].

5.2 Focusing quality

Another approach to evaluate the strength of aberrations is to examine the focusing quality across the image. To this end, the ratio between the coherent intensity and the total incoherent intensity of an input focused beam can be studied, which defines the coherence factor C [Mallart,

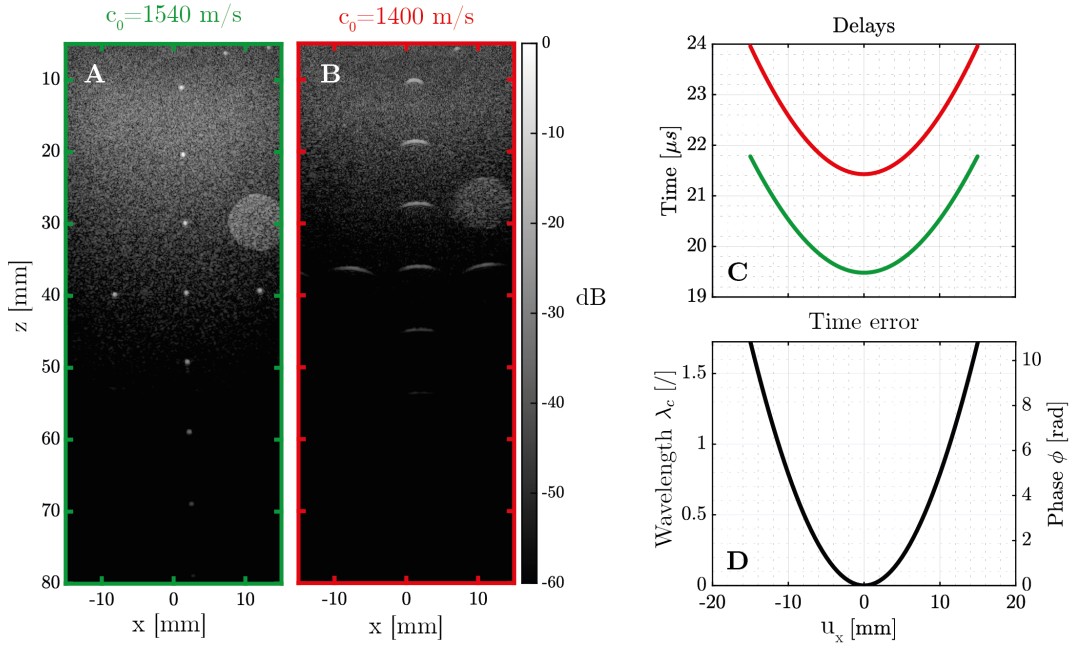

Figure 1.16: **Effect of an incorrect speed-of-sound hypothesis.** (**A, B**) Example of reconstructed confocal image assuming a correct ($c_0 = 1540$ m/s) and an incorrect ($c_0 = 1400$ m/s) speed-of-sound, respectively. (**C**) Delays calculated in each case to focus at a given point, $(x, z) = (0, 30)$ mm. (**D**) Time difference between the two delays expressed either as a phase-shift ($\phi = 2\pi f_c \Delta t$) or a number of wavelength ($N\lambda_c = \frac{\phi}{2\pi}$), with $f_c = 7.5$ MHz the central frequency. The speed-of-sound hypothesis has a great impact on both the resolution and the contrast of the image. In addition, an incorrect speed-of-sound induce a shift of the image since the depth-axis depends on the speed-of-sound hypothesis. This can be seen directly on the time-delay that are shifted with respect to each other.

1994; Hollman, 1999] that can be expressed as follows:

$$C(\mathbf{r}) = \frac{1}{N_{\mathbf{u}_{\text{out}}}} \frac{\overbrace{\left| \sum_{\mathbf{u}_{\text{out}}} s'(\mathbf{u}_{\text{out}}, \mathbf{r}) \right|^2}^{\text{Coherent}}}{\underbrace{\sum_{\mathbf{u}_{\text{out}}} \left| s'(\mathbf{u}_{\text{out}}, \mathbf{r}) \right|^2}_{\text{Incoherent}}}, \tag{1.25}$$

where $s'(\mathbf{u}_{\text{out}}, \mathbf{r}) = s(\mathbf{r}, \mathbf{u}_{\text{out}}, \tau(\mathbf{u}_{\text{out}}, \mathbf{r}, c_0))$ are the realigned signal associated with the focusing point $\mathbf{r}$. In the speckle, any realization of disorder, *i.e.* any speckle grain, is the result of a random process. Speckle fluctuations should thus be smoothed out by a spatial average over the coordinate $\mathbf{r}$, *i.e.* over different realizations of speckle grain.

Based on the Matrix Imaging formalism described in Chapter 2, Lambert et al. [Lambert, 2020b; Lambert, 2022b] introduced another focusing criterion that appears to be a more sensitive parameter for studying local focusing quality. First, the confocal character of the focusing criterion measurement enables a better transverse resolution of the focusing quality. Second, the focusing criterion allows us to distinguish between single scattering, multiple scattering, and

noise, so that the measurement of focusing quality can be based only on the contribution of single scattering, whereas the coherence factor cumulates the three effects [Lambert, 2022b].

5.3 Adaptive focusing

To solve these problems and improve the focusing quality, several methods have been developed over the years, known as **adaptive focusing**. It was introduced many years ago in astronomy to correct for the aberrations of starlight as it passes through the atmosphere [Babcock, 1953; Labeyrie, 1970; Muller, 1974; Roddier, 1999]. The distortion of the wavefront was measured, and a feedback loop with deformable mirrors was set up to compensate for its effects, which is better known as adaptive optics. This idea was later transposed to ultrasound imaging, where adaptive focusing can be applied by changing the time-delays of the transducer to compensate for the time-delay error caused by an aberrating layer.

This concept is shown schematically in [Fig. 1.17]. Assuming a medium with a constant and known speed of sound, the time-delay law for focusing on a given point is known [Fig. 1.17A] resulting in a PSF, whose size is predicted by diffraction theory. However, if spatial variations in the speed of sound occur due to an aberrating layer, the wavefront will be distorted after passing through the aberrating layer, resulting in a degraded focal point [Fig. 1.17B] and thus affecting the resolution of the image. Adaptive focusing can be seen in the light of time reversal when considering a point source, namely a *guide star*, from which the distorted wavefronts can be measured on the ultrasound probe [Fig. 1.17C]. The latter can also be used as a time reversal mirror [Fink, 1992] to refocus the wave in the medium, as if the wave was playing the movie of its propagation in the reverse direction. In other words, time reversal, allows focusing at the exact same position of the source, with a diffraction-limited resolution [Fig. 1.17D].

5.3.1 Extraction of the aberration law

Although the principle of adaptive focusing appears simple, its complexity lies in the estimation of the aberration law, since ultrasound imaging does not necessarily contain a guide star, such as a source or a strong reflector, but rather random scatterers that produce a speckle pattern.

A first set of adaptive focusing techniques in ultrasound is based on the **optimization of a particular image parameter** [Hirama, 1982; Nock, 1989]. An example is the iterative addition of small time-delays at each transducer to maximize the speckle brightness of the image. The main drawback of this method is that it is time-consuming, and convergence problems can appear.

A second type of adaptive focusing technique examines the **spatial correlations** of the re-aligned received signals [Flax, 1988; Mallart, 1994; Montaldo, 2011; Måsøy, 2005]. Interestingly, the authors even show that it was possible to extract such distorted wavefronts in the speckle, which can be considered a real breakthrough, since from a physical point of view it means that they were able to artificially create a virtual guide star or a coherent virtual reflector in a random medium.

One strategy for using time reversal, regardless of the medium under study, may be to **use**

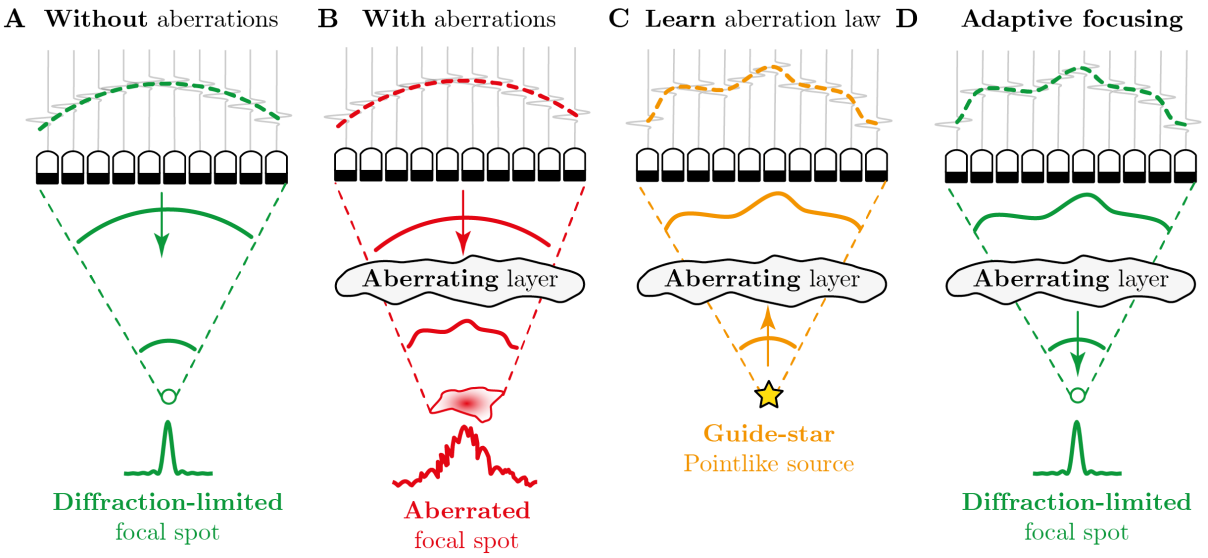

Figure 1.17: **Adaptive focusing in ultrasound imaging.** (**A**) Cylindrical delays are applied to each transducer to generate a converging wave, resulting in a focal spot limited by the diffraction. (**B**) Applying the same cylindrical law to an aberrated medium results in a distorted wavefront and thus an aberrated focal spot whose resolution is greatly reduced compared to the ideal case. (**C**) Assuming a point source at the focus, a distorted wavefront can be measured directly on the probe. (**D**) Time-reversal or phase conjugation of such a wavefront leads to a perfect cylindrical law at the output, resulting in a diffraction limited focal spot. *Inspired from* [Lambert, 2020c].

a priori information about the medium, such as other imaging techniques like *Computed Tomography*, which provides a map of the density and speed of sound that can be used to simulate the wave-field generated by a virtual source within the medium [Aubry, 2003]. However, this is mainly limited to ultrasound brain therapy and requires precise positioning of the probe. When moving from therapy to imaging, one can take advantage of iterative time reversal and the singular value decomposition of its operator. Those approaches are described in more detail in Chapter 2 [Montaldo, 2004; Aubry, 2001; Robert, 2005].

5.3.2 Isoplanicity

Let us now assume that we are able to extract the aberration law at a given point. We now describe its range of validity, especially with respect to spatial stability [Fig. 1.18A]. Such a focusing law can be decomposed into the sum of two terms:

- (i) a geometric component related to the specific position of a given point;
- (ii) a distorted component associated with the aberration.

One can assume that focused waves propagating towards neighboring points see the same medium heterogeneities. They are only shifted or tilted due to geometric consideration [Fig. 1.18B]. This is the near-field phase screen model [ODonnell, 1988], where aberrations are assumed

to occur only in the plane of the transducer and generate spatially-invariant distorted focal spots in the medium.

However, this assumption is far from true in *in vivo* imaging and generally applies only to a limited area called the *isoplanatic patch* [Babcock, 1953; Labeyrie, 1970; Muller, 1974; Roddier, 1999]. In other words, aberrations can be **spatially distributed** and require an iterative process to correct their effects in each isoplanatic patch supported by the field-of-view.

Thus, the size of the isoplanatic patch is a crucial parameter that must be considered if distributed aberrations are to be fully corrected. It thus determines the computational time required to correct the entire field-of-view. Mertz et al. [Mertz, 2015] have shown that the size of the isoplanatic patch l_p can be derived from the correlation length l_k of the far-field aberrating phase screen:

$$l_\mathrm{p} = \frac{2l_\mathrm{k}}{\sqrt{1+2\sigma_k^2}}, \tag{1.26}$$

where σ_k is the standard deviation of the normal distribution. The physical meaning of (Eq. 1.26) is that the more complex the aberration, the higher the spatial frequencies it contains and the smaller the isoplanatic patch (*i.e.* the smaller its correlation length).

It is also important to note that the decomposition of the aberrations in terms of spatial frequencies depends on the choice of basis, as their effects may vary from one basis to another. Although aberrations in ultrasound imaging were originally studied in the transducer basis, other bases may be more appropriate for correction. For example, aberrations generated by multilayered media are better described using the plane wave (far-field) basis, since they are invariant by translation in this basis [Lambert, 2022a]. More generally, the optimal basis would naively be the plane of the aberrating layer [Fink, 1997; Kwon, 2023]. However, the usual picture of aberration as a near- or mid-field phase screen, associated with a well-defined aberrating layer, is too simple to describe the reality of *in vivo* imaging, when the entire medium contributes to the distortion of the wavefronts.

Only few studies have reported experimental values in ultrasound imaging, with results that vary widely from one study to another. They range from a few lambdas to a few centimeters. Liu et al. [Liu, 1998] used a point-like target placed in ex vivo abdominal tissue and achieved measurement of isoplanatic patch of size of about 16.7 mm transversely and 39 mm axially. Dahl et al. measured spatial stability in the breast, liver, and thyroid [Dahl, 2005] and found values ranging from 0.4 to 1.1 mm in the transverse direction with double values in the axial direction. Several studies for the skull also show that the spatial stability of aberration is larger in the axial direction than in the transverse direction [Vignon, 2008; Robin, 2023].

Thus, the numerous adaptive focusing techniques described previously should ideally be repeated for each point in the field-of-view and therefore require an iterative and time-consuming physical process to correct spatially distributed aberrations [Måsøy, 2005; Montaldo, 2011]. Recently, thanks to a drastic increase in terms of computational power and memory capacity, spatially distributed aberrations can now be addressed by adaptive focusing techniques in post-processing. Indeed, synthetic focusing allows the extraction of the aberration law in post-processing without iteration of a physical and time-consuming experiment. The “LAPAC”

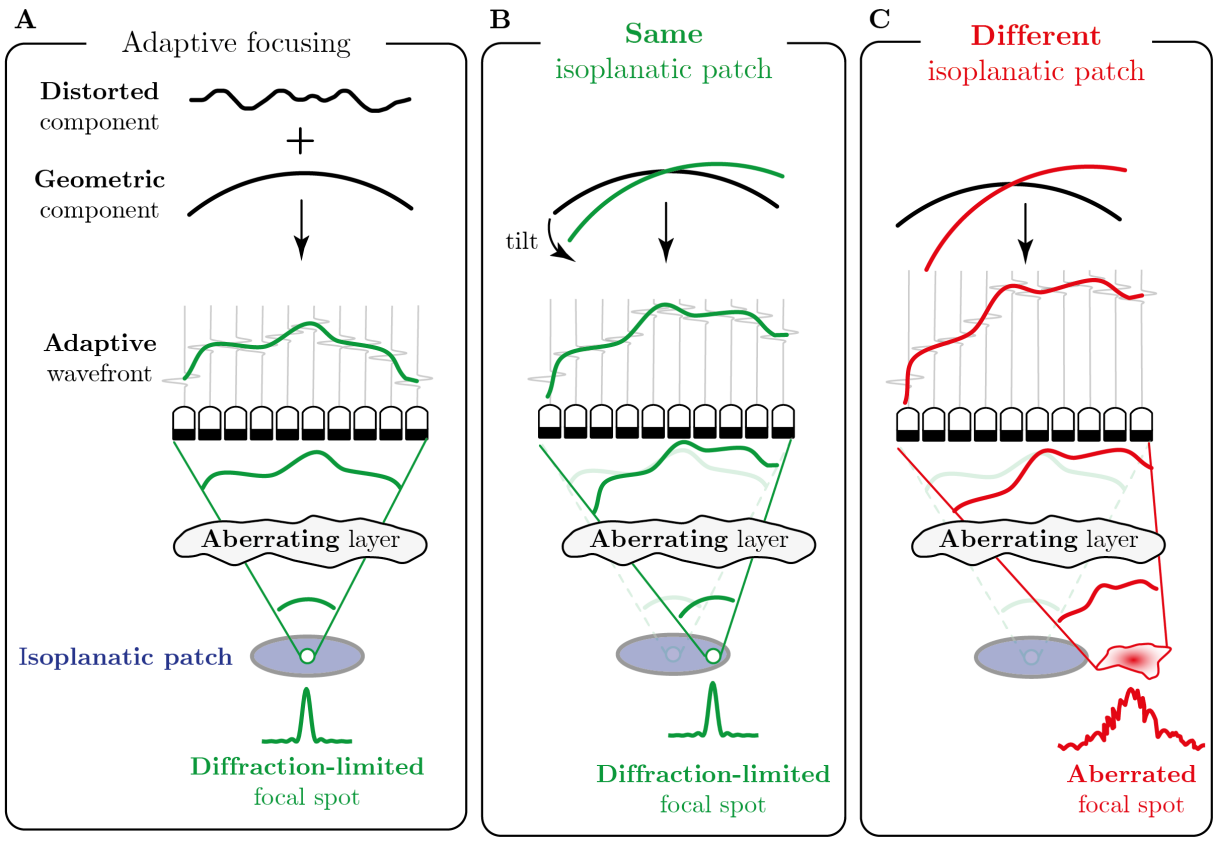

Figure 1.18: **Isoplanicity.** (**A**) An adaptive wavefront that focuses perfectly at a targeted point can be decomposed as the sum of a distorted and a geometrical component. If the geometrical part is associated to the position of the focal point, the distorted component describes the aberration seen from a spatial area called the isoplanatic patch. In other words, the same distorted wavefront is associated to several neighboring focal points such that (**B**) a simple tilt of the geometrical component allow to focus perfectly on a neighboring focal point. (**C**) However, when tilt is too high, or equivalently when considering a too far focal point, the adaptive wavefront will not be adapted, resulting in an aberrated focal spot. *Inspired from* [Lambert, 2020c].

method [Chau, 2019], which refers to "locally-adaptive phase aberration correction", combines previous state-of-the-art methods [Gauss, 2001; Silverstein, 2003] and enables correction of aberrations both in transmit and receive, resulting in a 10% contrast improvement *in vivo*. At the Langevin institute, inspired by the seminal work of Robert et al. [Robert, 2005] on the time reversal operator, a "distortion matrix approach" has been developed by Lambert et al. [Lambert, 2020c; Lambert, 2022a; Lambert, 2020a]. It will be described in details in Chapters 2, 3 and 4.

The transfer of adaptive focusing techniques for real-time imaging has already shown its advantages [Rigby, 2000; Måsøy, 2022], and the implementation of such computationally intensive methods therefore depends on computational power.

5.4 Speed-of-sound: the holy grail

At last, another range of adaptive focusing techniques are based on speed of sound estimates that appear particularly relevant in situation like transcranial imaging where the skull layer induces a large difference of speed of sound as compared to the brain. In such a case, segmentation of the cranial layer with a global estimation of the speed of sound may help to correct for refraction events using ray tracing that solves the **eikonal equation** [Smith, 1986; Yasuda, 2019; Lindsey, 2014]. The difficulty in this case lies in the estimation of a local speed of sound map that is an active research topic.

Today, there are mainly two types of methods for extracting local speed-of-sound estimates. The first set of techniques is founded on the improvement of a quality criterion with regard to the beamforming speed-of-sound. Then, the local speed of sound is determined by solving an inverse problem [Jakovljevic, 2018]. A second set of techniques examines the local phase-shifts between various insonification directions on the grounds that each insonification direction is affected differently by the medium's heterogeneities [Jaeger, 2015a]. This topic will be better described in Chapter 6 where a method to recover an integrated speed-of-sound map will be presented.

Since it enables the extraction of the perfect time-of-flight connecting each transducer to each focusing point to provide a close-to-ideal image of the medium [Vyas, 2012; Augustin, 2021; Ali, 2022], the extraction of spatial variations in wave velocity could indeed be considered the holy grail of imaging. Both older and recent studies also demonstrate that its quantification could be utilized as a bioindicator to identify abnormal soft tissue characteristics [Bamber, 1979; Sehgal, 1986], such as malignant tumors or hepatic steatosis [Imbault, 2017; Imbault, 2018; Dioguardi Burgio, 2019].

6 Conclusion

Ultrasound imaging is widely used by radiologists to investigate and diagnose pathologies because it is non-invasive and can be performed in real-time. It is based on the backscattered echoes of ultrasound waves propagating through an unknown medium. An ultrasound image is generated by a double focusing process both at emission and reception.

However, the reconstruction is not always optimal because it is based on strong hypotheses about the medium (homogeneous speed-of-sound and single scattering). Every ultrasound imaging modality is thus affected by speed-of-sound heterogeneities that induce aberrations and multiples scattering that generate an incoherent background on the ultrasound image. In recent years, numerous strategies have been developed to correct aberrations by adaptive focusing.

In the next chapter, we present a general matrix framework adapted to ultrasound imaging that has already shown promising results not only in ultrasound but also in other fields of wave physics such as optics, seismic imaging, and radar. It is based on recording the reflection matrix of the medium, which holds all the information available on the medium. This reflection matrix yields much more information than a conventional ultrasound image, and its projection onto suitable bases can be used not only to compensate for aberrations, but also to quantify multiple

scattering or even to map the speed-of-sound.

In Chapter 3, matrix imaging is extended to 3D imaging using ultrasound matrix arrays, which can drastically increase the available number of spatial degrees of freedom, and its advantages over 2D imaging are discussed in a transcranial imaging experiment on a head phantom.

In Chapter 4, contrast imaging with microbubbles is examined. First, it is shown how matrix imaging can be combined with other ultrasound modalities. In the specific case of Ultrasound Localization Microscopy, transcranial preclinical experiments were performed in sheep subjects in which both super-resolved and aberration-corrected images of cerebral vessels were obtained. Second, preliminary results on the measurement of the resonance frequency of monodisperse bubbles are presented, which could have potential application in blood pressure measurement.

In Chapters 5 and 6, a paradigm shift will be made, as we will now investigate the axial dimension to extract and map local defocus due to spatial variations in the speed of sound *in vivo*. This approach seems to be relevant not only for the particular case of multilayered media, but also allows local mapping of the integrated speed of sound and thus promising results for the extraction *in vivo* of the local sound velocity.

Chapter 2

Matrix imaging

Objectives

Matrix imaging is introduced here to go beyond conventional imaging. By recording the reflection matrix of an unknown medium, aberrations, multiple scattering, and spatial variations in the speed-of-sound can be studied. Such quantitative parameters of the medium can indeed be determined by projecting such a matrix onto suitable bases. The strength of this approach lies in its general formalism, which can be applied to **any field of wave physics** where an unknown, static and linear medium is studied using a multi-element technology. In this section, ultrasound imaging is used as a playground to demonstrate all possible applications of matrix imaging.

Contents

1 Introduction

In wave physics, a matrix formalism is particularly appropriate when the wave-field can be controlled by transmission or reception arrays of N independent elements. Since an inhomogeneous medium can be treated as one realization of a random process, some aspects of random matrix theory may be fruitfully applied to wave control and transport through complex media [Beenakker, 1997; Rotter, 2017]. Beyond a fundamental study of wave propagation in complex media, a matrix formalism can be fruitful for many applications. Indeed, the transmission or reflection matrix contains all the information accessible on the medium. A set of post-processing operations can then be applied to extract the relevant information as a function of the problem considered, without the need for any iterative physical procedure.

The strength of such a matrix formalism lies in its generality, which extends beyond the realm of ultrasound imaging and can be applied to any multi-element technology that records backscattered reflected wavefronts of an unknown medium. The main differences between each field lie in the experimental acquisition of the reflected wave-field: array of transducers in acoustics [Langevin, 1920], spatial light modulators and camera in optics, geophones network in seismic imaging, [Dennison, 1953] or phased array antennas in radar.

Historically, it was mainly studied in transmission because it was originally used to describe wave propagation through heterogeneous media for the purpose of communication and focusing through scattering media [Moustakas, 2000; Foschini, 1998; Tanter, 2001; Derode, 2003b; Popoff, 2010a; Kim, 2012; Papadopoulos, 2012; Čižmár, 2012; Popoff, 2010b]. It was later extended to detection experiments in a reflection configuration [Prada, 1996; Aubry, 2009b; Popoff, 2011; Badon, 2016; Blondel, 2018] before turning lately to imaging [Kang, 2017; Badon, 2020; Lambert, 2020c; Velichko, 2020; Touma, 2021], where aspects such as aberrations and multiple scattering are addressed in an epi-detection configuration. Today, matrix imaging has reached a point where it can be used for quantitative imaging, not only to image the reflectivity of a medium, but also to extract bio-indicators such as the multiple scattering rate or the speed of sound. Over the past five years, the group of A. Aubry is developing a universal and non-invasive reflection matrix approach for wave imaging and characterization in scattering media.

In this chapter, we will first introduce the matrix formalism in a transmission configuration and then extend this formalism to a reflection configuration, since in most ultrasound imaging applications we only have access to one side of the medium.

The starting point of ultrasound matrix imaging (UMI) is the recording of the reflection matrix of the medium. Historically, such a matrix was originally recorded in the canonical basis, *i.e.* by recording the impulse responses between each transducer of an ultrasound probe [Prada, 1996; Aubry, 2009b]. Later, it was shown that the reflection matrix even allows synthesizing virtual sources and detectors at any point in the medium by applying appropriate delay laws at the input or output of the matrix to perform numerical focusing of the ultrasound data in post-processing [Robert, 2008a].

The reflection matrix can thus be studied in several bases, of which we will focus on the following three: (i) the transducer basis, in which the reflection matrix is recorded on reception

and which is particularly suitable for compensating for aberrations caused by lateral variations in the speed of sound at the surface of the medium; (ii) the plane wave basis, which is often used as the transmission basis for recording the reflection matrix and which is most suitable for correcting for aberrations caused by axial variations in the speed of sound; (iii) the focused basis in which the ultrasound image is generated and which allows local quantification of the focusing quality and multiple scattering. The focused reflection matrix plays a central role in matrix imaging, as it is the most important component of the UMI framework.

In recent work, the projection of such a matrix onto a dual basis, *i.e.* the distortion matrix [Lambert, 2020c; Lambert, 2022a], has been considered as a key quantity in the UMI framework for compensating aberrations. In short, it allows revealing hidden spatial correlations that can be used to extract the transmission matrix that connects each sensor to any point of the field of view and whose estimation is the main objective of matrix imaging. Once this is known, an ideal focusing process can be performed in post-processing to produce an image of the medium that is free of aberration problems and even multiple scattering.

2 The transmission matrix (T)

Before dealing with the transmission matrix inside the medium, we will describe the transmission matrix that can be measured on both sides of the medium. In the past, this matrix has been studied thanks to the development of antenna arrays in electromagnetism and transducer arrays in acoustics. After defining the concept, we will see how it can be acquired before enumerating its main properties and describing the advances it has enabled in terms of applications.

Among the most important properties of the transmission matrix are the bimodal distribution [Dorokhov, 1984; Beenakker, 1997; Gérardin, 2014] and its correlations [Goetschy, 2013; Hsu, 2017], which allow one to describe wave transport through diffusive media and to quantify the performances of "multiple input multiple output" (MIMO) communications [Foschini, 1998; Derode, 2003b]. However, here, we only investigate the extent to which it can be used for focusing in disordered media.

2.1 Definition

We consider here a heterogeneous medium with a plane at the entrance of the medium characterized by the coordinate ($\mathbf{u}_i$) and a plane at the exit of the medium characterized by the coordinate ($\mathbf{u}_j$). Assuming that propagation through a complex scattering medium is **linear** and invariant by translation (*i.e.* static medium), any output beam $\mathcal{E}_{\text{out}}^{(\text{T})}(\mathbf{u}_j,t)$ of the sample can be related to the entrance field $\mathcal{E}_{\text{in}}(\mathbf{u}_i,t)$ by the transmission operator $\mathcal{T}$ such that:

$$\mathcal{E}_{\text{out}}^{(\text{T})}(\mathbf{u}_j,t)=\int_{-\infty}^{+\infty}\text{d}\mathbf{u}_i\left[\mathcal{E}_{\text{in}}(\mathbf{u}_i,t)\overset{t}{\circledast}\mathcal{T}(\mathbf{u}_i,\mathbf{u}_j,t)\right], \tag{2.1}$$

where $\overset{t}{\circledast}$ denotes a convolution product over time and the superscript $^{(T)}$ refers to "transmission".

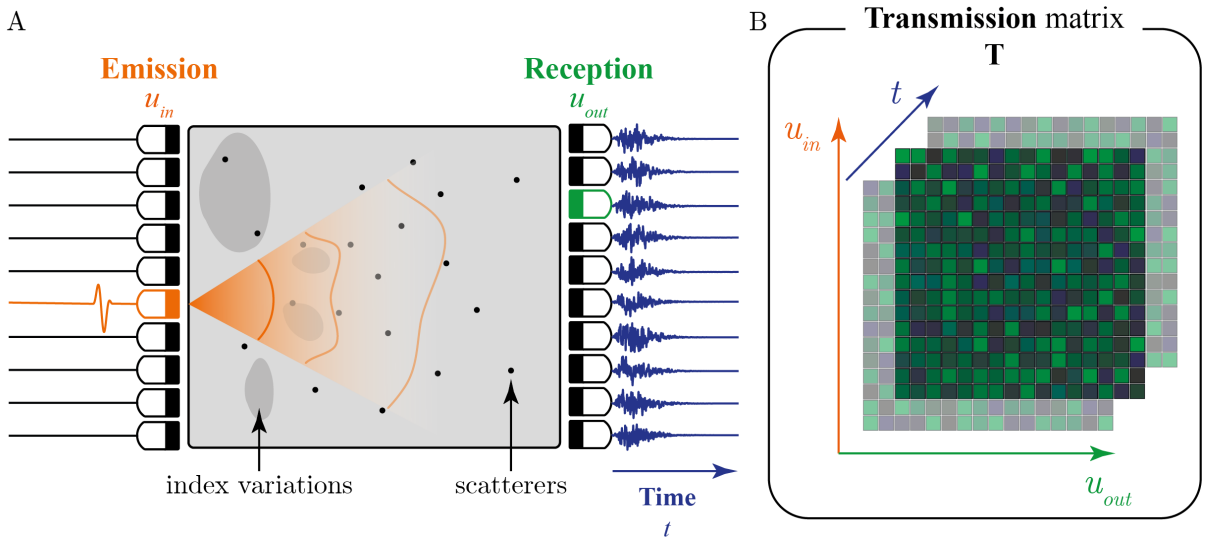

Figure 2.1: **The multi-spectral transmission matrix acquired in ultrasound imaging.** The impulse responses are recorded between each emitter at the input and each receiver at the output. This wealth of information is stored in the so-called transmission matrix, denoted **T**.

2.2 Acquisition

In practice, as any multi-element technology only provides a discrete control and measure of the wave-front on a finite number of emitters ($\mathbf{u}_{\text{in}}$) and receiver ($\mathbf{u}_{\text{out}}$), the definition of the transmission matrix **T** can be derived from (Eq. 2.1) such that:

$$E_{\text{out}}^{(\text{T})}(\mathbf{u}_{\text{out}},t) = \sum_{\mathbf{u}_{\text{in}}} \left[E_{\text{in}}(\mathbf{u}_{\text{in}},t) \overset{t}{\circledast} \text{T}(\mathbf{u}_{\text{in}},\mathbf{u}_{\text{out}},t) \right]. \tag{2.2}$$

In ultrasound imaging, the transmission matrix can be acquired using two arrays of piezoelectric transducers placed on each side of the medium. A transducer $\mathbf{u}_{\text{in}}$ emits a short pulse such that the emitted wave-field can be written:

$$E_{\text{in}}(\mathbf{u}_{\text{in}},t) \equiv \mathcal{E}_{\text{in}}(\mathbf{u}_i = \mathbf{u}_{\text{in}},t) = \delta(t)\delta(\mathbf{u}_i - \mathbf{u}_{\text{in}}), \tag{2.3}$$

where δ is the Dirac distribution, and the transmitted wave-field $E_{\text{out}}^{(\text{T})}(\mathbf{u}_{\text{out}},t)$ is recorded for a given receiver $\mathbf{u}_{\text{out}}$ [Fig. 2.1A]. Repeating this process for each pair $(\mathbf{u}_{\text{in}},\mathbf{u}_{\text{out}})$, we obtain the full transmission matrix of the medium [Fig. 2.1B].

In the time Fourier domain, (Eq. 2.2) becomes a simple matrix product:

$$\mathbf{E}_{\text{out}}^{(\text{T})}(\mathbf{u}_{\text{out}},\omega) = \mathbf{E}_{\text{in}}^{\top}(\mathbf{u}_{\text{in}},\omega) \times \mathbf{T}(\omega), \tag{2.4}$$

where $\top$ stands for matrix transpose and $\omega = 2\pi f$ is the pulsation, with f the frequency.

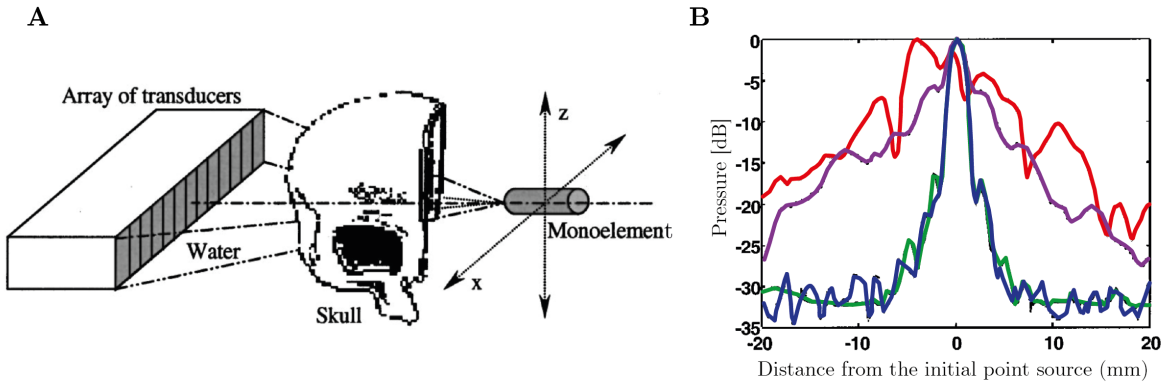

Figure 2.2: **Time-reversal & spatio-temporal inverse filter.** (**A**) One half-skull is located between the image plane and the array of 127 transducers. (**B**) Directivity patterns obtained by time reversal through pure water (green line), time-reversal (purple line), inverse filter (blue line) and cylindrical law (red line). *Extracted from* [Aubry, 2001].

2.3 Matrix operations for wave control

The transmission matrix is a powerful tool for predicting the wave-field at a given output surface when the incident wave-field at a given input surface is known. Interestingly, the inversion of the transmission matrix directly provides the input wave-field to be applied to obtain a desired output field (*e.g.* to perform focusing) so that:

$$\mathbf{E}_{\text{in}}^{\top}(\mathbf{u}_{\text{in}},\omega) = \mathbf{E}_{\text{out}}^{(\text{T})}(\mathbf{u}_{\text{out}},\omega) \times \mathbf{T}^{-1}(\omega). \tag{2.5}$$

However, matrix inversion is far from trivial unless the $\mathbf{T}-$matrix is unitary such that $\mathbf{T}^{-1} = \mathbf{T}^{\dagger}$ ($\dagger$ stands for transpose conjugate), which is not verified if information is lost through propagation (*e.g.* in the presence of absorption) or if the transmitted wave-field is incompletely recorded. A comparison between phase-conjugation (using $\mathbf{T}^{\dagger}$) and inverse filter (using $\mathbf{T}^{-1}$) was performed in early transcranial imaging experiments [Tanter, 2000; Tanter, 2001; Aubry, 2001; Montaldo, 2004]. In particular, the authors have shown that time-reversal (equivalent to phase conjugation in the time domain) can compensate for the aberration caused by the cranial layer, but not for attenuation. Only when a spatio-temporal inverse filter is used can a similar contrast be obtained as without the aberrating layer [blue curve in Fig. 2.2B].

Beyond ultrasound imaging, the transmission matrix has also been investigated with microwaves between arrays of antennas or with light using wave front shaping devices and cameras. In optics, the experimental setups are far more complex because they involve interferometric measurements that require fine alignment of the optical components to detect both the amplitude and the phase of the electromagnetic wave-field, quantities that an ultrasound probe provides directly thanks to its lower frequency range.

In optics, such a matrix was experimentally measured for the first time in 2010 [Popoff, 2010a] and was used to focus anywhere at the output of the medium, while an iterative approach requires a lengthy optimization process [Vellekoop, 2007] that must be repeated for each target point. The matrix approach can be used not only to turn any scattering medium into a lens,

but also to simulate the response of the medium to any incident wave in post-processing. This property comes into play especially in reflection, when we try to focus in the scattering medium rather than through it.

3 The reflection matrix (R)

Although some imaging techniques rely on the transmission of a wave through a complex medium (*e.g.* ultrasound tomography for breast imaging [Glover, 1977b; Greenleaf, 1987; Glover, 1977a]), non-invasive imaging is usually performed in a configuration in which only one side of the medium is accessible. In this case, a reflection matrix can be recorded, and a similar mathematical formalism can be applied.

3.1 Definition & acquisition

The reflection matrix

Assuming linear propagation through a static medium, the reflection matrix, noted $\mathbf{R}$, is defined by an equation similar to the previous one (Eq. 2.2), but with the emitter and receiver located on the same side of the medium [Fig. 2.3], so that:

$$E_{\text{out}}^{(\text{R})}(\mathbf{u}_{\text{out}},t)=\sum_{\mathbf{u}_{\text{in}}}\left[E_{\text{in}}(\mathbf{u}_{\text{in}},t)\overset{t}{\circledast}\text{R}(\mathbf{u}_{\text{in}},\mathbf{u}_{\text{out}},t)\right], \tag{2.6}$$

where the superscript $^{(\text{R})}$ now refers to "reflection".

This equation re-writes in the Fourier domain as follows:

$$E_{\text{out}}^{(\text{R})}(\mathbf{u}_{\text{out}},\omega)=E_{\text{in}}^{\top}(\mathbf{u}_{\text{in}},\omega)\times\mathbf{R}(\omega). \tag{2.7}$$

As before, the $\mathbf{R}-$matrix can be captured by recording the impulse responses between each emitter and receiver. The individual elements of the reflection matrix can be expressed in this way as $\mathbf{R_{uu}}(t)\equiv[R(\mathbf{u}_{\text{in}},\mathbf{u}_{\text{out}},t)]$, where the subscript "$_{\mathbf{uu}}$" denotes the transducer basis for both emission and reception. Such an acquisition refers to the canonical basis. Interestingly, the $\mathbf{R}-$matrix can even be passively recorded using coda-wave cross-correlations. This approach has revolutionized the field of seismology for the last twenty years [Weaver, 2002; Campillo, 2003; Derode, 2003a; Chaput, 2012; Colombi, 2014].

3.2 Physical interpretation

The main difference between the reflection and transmission matrices is that only back-scattered wave-fronts are detected in an epi-detection configuration. In other words, the ballistic wave cannot be recorded, and only the secondary back-scattered waves are captured by the reflection matrix.

In an epi-detection configuration and under a single scattering assumption, a wave insonifies the medium and interacts with the short-scale heterogeneities of the medium and generate

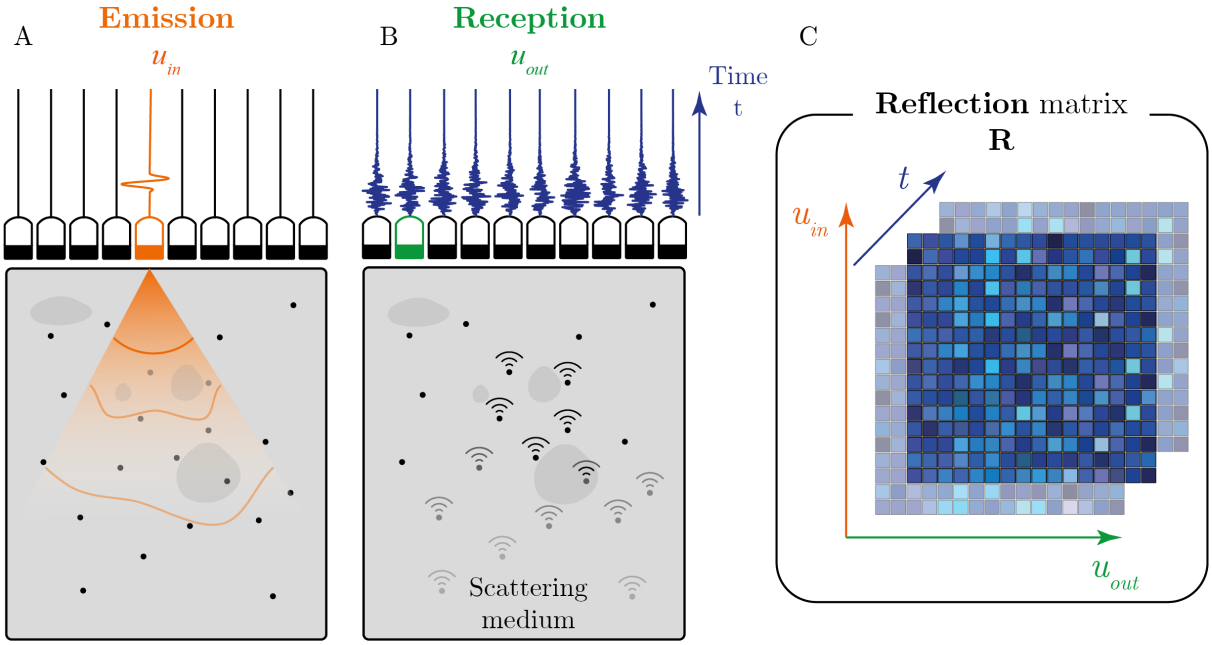

Figure 2.3: **The multi-spectral reflection matrix acquired in ultrasound imaging.** The impulse responses are recorded between each emitter at the input and each receiver at the output, both located on the same side of the medium. All this wealth of information is stored in the so-called reflection matrix, denoted **R**.

secondary waves propagating in the opposite direction of propagation. Mathematically, this process can be written as follows:

$$\mathbf{R_{uu}}(\omega) = \mathbf{G}_{\text{in}}^{\top}(\omega) \times \mathbf{\Gamma}(\omega) \times \mathbf{G}_{\text{out}}(\omega), \tag{2.8}$$

where $\mathbf{\Gamma} = [\gamma(\mathbf{r}, \omega)]$ is a diagonal matrix that accounts for the medium reflectivity and $\mathbf{G}_{\text{in/out}}(\omega) = [G(\mathbf{r}, \mathbf{u}_{\text{in/out}}, \omega)]$ are the Green matrices describing the propagation of the incident and reflected waves, respectively, inside the medium. In terms of matrix coefficients, the previous equation writes:

$$R(\mathbf{u}_{\text{in}}, \mathbf{u}_{\text{out}}, \omega) = \int \mathrm{d}\mathbf{r}' \mathrm{G}_{\text{in}}(\mathbf{u}_{\text{in}}, \mathbf{r}', \omega) \gamma(\mathbf{r}', \omega) \mathrm{G}_{\text{out}}(\mathbf{u}_{\text{out}}, \mathbf{r}', \omega). \tag{2.9}$$

In the presence of a stronger scattering regime, a Born development [Born, 1926] of the reflection matrix can be performed to grasp the multiple scattering events undergone by the wave during its propagation inside the medium [Brütt, 2022]. However, its application is usually limited to numerical simulations, since it requires an exact knowledge of the medium, which is by definition impossible in the case of an unknown medium.

3.3 Pioneering works

In this section, we present some pioneering work based on the reflection matrix acquired in the canonical basis, $\mathbf{R_{uu}}(t) \equiv [R(\mathbf{u}_{\text{in}}, \mathbf{u}_{\text{out}}, t)]$. Its applications initially concerned the detection of hidden objects in complex scattering media, before being transposed to imaging experiments.

3.3.1 The DORT method

Historically and as part of the Ph.D. thesis of Claire Prada, one of the first applications of the reflection matrix approach was to gain mathematical insight into the iterative time reversal process.

An **iterative time-reversal (ITR) experiment** consists in insonifying an unknown medium with an arbitrary wave-front $\mathbf{E}_{\text{in}}^{(0)} = [E_{\text{in}}^{(0)}(\mathbf{u}_{\text{in}}, \omega)]$, typically a plane wave [Fig. 2.4A], and recording the reflected wave-field $\mathbf{E}_{\text{out}}^{(0)}$, as depicted in [Fig. 2.4B$_1$], such that:

$$\mathbf{E}_{\text{out}}^{(0)}(\omega) = \left[\mathbf{E}_{\text{in}}^{(0)}(\omega)\right]^{\top} \times \mathbf{R}_{\mathbf{uu}}(\omega). \tag{2.10}$$

This wave-field is time-reversed and back-emitted into the medium as shown in [Fig. 2.4B$_2$] such that $\mathbf{E}_{\text{in}}^{(1)} = \left[\mathbf{E}_{\text{out}}^{(0)}\right]^{*}$. The reflected wave-field is recorded once again such that:

$$\mathbf{E}_{\text{out}}^{(1)}(\omega) = \left[\left[\mathbf{E}_{\text{in}}^{(0)}(\omega)\right]^{\dagger} \times \mathbf{R}_{\mathbf{uu}}^{*}(\omega)\right] \times \mathbf{R}_{\mathbf{uu}}(\omega), \tag{2.11}$$

and the process can be iterated, resulting in the following equation at the n^{th}-step:

$$\mathbf{E}_{\text{out}}^{(n)}(\omega) = \left[\mathbf{E}_{\text{in}}^{(0)}(\omega)\right]^{\dagger} \times \left[\mathbf{R}_{\mathbf{uu}}^{*}(\omega) \times \mathbf{R}_{\mathbf{uu}}(\omega)\right]^{n}. \tag{2.12}$$

The operator $[\mathbf{R}_{\mathbf{uu}}^{*}(\omega) \times \mathbf{R}_{\mathbf{uu}}(\omega)]$ is the so-called time-reversal operator. As the reflection matrix is symmetric thanks to spatial reciprocity (*i.e.* $\mathbf{R}^{\top} = \mathbf{R}$), the former equation can be re-written as:

$$\mathbf{E}_{\text{out}}^{(n)}(\omega) = \left[\mathbf{E}_{\text{in}}^{(0)}(\omega)\right]^{\dagger} \times \left[\underbrace{\mathbf{R}_{\mathbf{uu}}^{\dagger}(\omega) \times \mathbf{R}_{\mathbf{uu}}(\omega)}_{\mathbf{C}(\omega)}\right]^{n}, \tag{2.13}$$

where $\mathbf{C}$ is the covariance matrix of the reflection matrix, that can be diagonalized as follows:

$$\mathbf{C}(\omega) = \mathbf{U}^{\dagger}(\omega) \times \mathbf{\Sigma}(\omega) \times \mathbf{U}(\omega) \tag{2.14}$$

$$C(\mathbf{u}, \mathbf{u}', \omega) = \sum_i U_i^{*}(\mathbf{u}, \omega)\sigma_i(\omega)U_i(\mathbf{u}', \omega), \tag{2.15}$$

where $\mathbf{\Sigma}$ is a diagonal matrix containing the eigenvalues σ_i in descending order: $\sigma_1 > \sigma_2 > .. > \sigma_N$. $\mathbf{U}$ is a unitary matrix that contain the orthonormal set of eigenvectors, $\mathbf{U}_i(\omega) = [U_i(\mathbf{u}, \omega)]$. Interestingly, for $n \to \infty$, the ITR process converges towards a time-reversal invariant that is nothing other than the first eigenvector [Fig. 2.4C]:

$$\lim_{n\to\infty}\left[\mathrm{E}_{\text{out}}^{(n)}(\mathbf{u}, \omega)\right] = \underbrace{\left[\sum_{\mathbf{u}'} \sigma_1^n(\omega) E_{\text{in}}^{(0)*}(\mathbf{u}', \omega) U_1^{*}(\mathbf{u}', \omega)\right]}_{\text{scalar}} \mathrm{U}_1(\mathbf{u}, \omega) \tag{2.16}$$

$$\propto \mathrm{U}_1(\mathbf{u}, \omega). \tag{2.17}$$

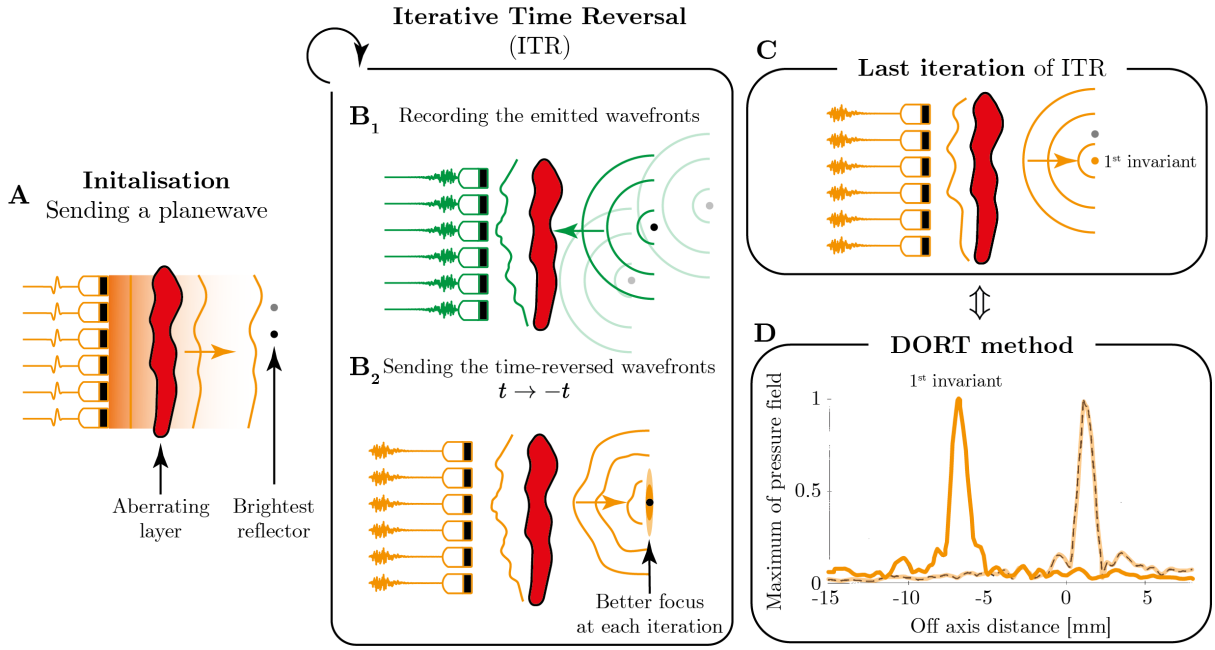

Figure 2.4: **Iterative Time Reversal & DORT method.** (**A**) A plane wave insonifies the medium. (**B**) Backscattered wavefronts are recorded, time-reversed and sent back to the medium. This process is iterated and (**C**) converges towards the wavefront that focuses perfectly on the brightest reflector, which is nothing more than the first invariant of the time reversal operator $\mathbf{R}^* \times \mathbf{R}$. (**D**) DORT method applied to focus on two wires through an aberration layer. Experimental transmission of the two first eigenvectors of the time reversal operator. *Adapted from* [Prada, 1996].

The iterative time reversal is thus the physical counterpart to the power method used in mathematics to determine an eigenvector of a matrix. This pioneering work demonstrates the strength of the matrix formalism to simulate in post-processing a complex set of wave propagation experiments through the medium, in order to learn how to focus inside it. Here, a tedious focusing process (iterative time reversal) is simply done by performing an SVD of the reflection matrix. This SVD can even do better than iterative time reversal, since higher order eigenvectors provide the time reversal invariants that enable us to focus on each target of the medium [Fig. 2.4D]. This is the principle of the DORT method (French acronym for "decomposition of the time reversal operator") [Prada, 1994; Prada, 1996; Prada, 2003].

However, the DORT method applies only to a single scattering regime. To tackle a stronger scattering regime, Aubry and Derode used characteristic field correlations of the reflection matrix, showing a new interest in a matrix approach of wave propagation.

3.3.2 Random matrix theory to overcome multiple scattering

These input-output correlations in the reflection matrix were studied to distinguish between singly- and multiply-scattered echoes [Aubry, 2009b]. The experimental set-up under study, immersed in water, was a scattering medium made of randomly distributed steel rods between an ultrasound probe and a target. The canonical reflection matrix **R** is acquired [as shown in

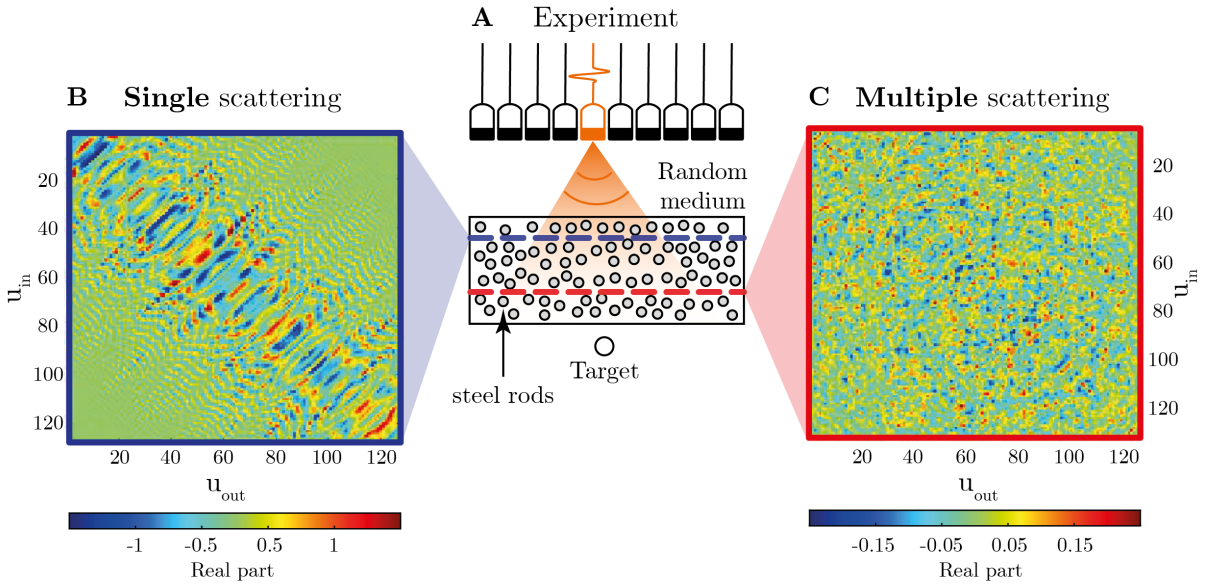

Figure 2.5: **Far-field analysis of the reflection matrix in a random scattering medium.** (**A**) Recording of the canonical reflection matrix in a scattering medium made of randomly distributed cylinders. (**B**) At short times, the contribution of single scattering dominates, so that long-range correlations, typical of the memory effect, are observed along its diagonals. (**C**) At long times, when the contribution of multiple scattering dominates, the matrix exhibits a random feature. In both cases, spatial reciprocity ensures the symmetry of the matrices. *Extracted and adapted from* [Aubry, 2008a].

Fig. 2.5A], time-gated and then projected in the frequency domain as follows:

$$R(\mathbf{u}_{\text{in}},\mathbf{u}_{\text{out}},z,\omega)=\int \mathrm{d}t R(\mathbf{u}_{\text{in}},\mathbf{u}_{\text{out}},t)\underbrace{\mathcal{W}_t(t-\frac{2z}{c_0})}_{\text{Time gating}}\exp(j\omega t), \tag{2.18}$$

where $\mathcal{W}_t(t-\frac{2z}{c_0})$ is a Hann time window centered around the ballistic time corresponding to the depth z assuming a global speed-of-sound c_0 in the medium.

At a given frequency, this matrix exhibits strong differences at short and long times that can be directly attributed to different scattering regimes. Even though symmetry is ensured in both cases due to spatial reciprocity of wave propagation, the first matrix extracted at short times exhibits much larger range correlations [Fig. 2.5B], that can be understood when looking at its theoretical expression in a paraxial approximation [Aubry, 2009a]:

$$R(\mathbf{u}_{\text{in}},\mathbf{u}_{\text{out}},z,\omega)\propto\mathbf{\Gamma}_{\text{rand}}\underbrace{\frac{\exp(i2\omega z/c_0)}{z}\exp\left(i\omega\frac{(\mathbf{u}_{\text{in}}-\mathbf{u}_{\text{out}})^2}{4zc_0}\right)}_{\text{deterministic term}}, \tag{2.19}$$

where $\mathbf{\Gamma}_{\text{rand}}$ is a random term and z is the depth.

Interestingly, the deterministic term depends only on the difference between the position of the input and output transducers, which explains the long-range correlations along the anti-diagonals of the matrix. This observation is typical of the **memory effect**, which was first

experimentally demonstrated in a transmission configuration [Freund, 1988; Feng, 1988] by tilting the angle of incidence of an expanded laser beam and observing the spatial shift of the speckle pattern at the output of a scattering medium. This effect can be generalized in reflection [Katz, 2014; Stern, 2019] and its correlation length, *i.e.* the area over which it remains valid, is nothing but the isoplanatic angle. The isoplanatic angle is inversely proportional to the average distance between the first and the last scattering event experienced by the wave in the medium: it is therefore long-range for single/recurrent scattering and short-range for conventional multiple scattering [Aubry, 2014; Brütt, 2022]. Unfortunately, this correlation length decreases with depth as multiple scattering becomes more important, resulting in only short-range correlations whose size is roughly equivalent to a single speckle grain. Hence, the reflection matrix becomes fully random at long time, as described in [Fig. 2.5C].

Based on this observation, the authors have developed a filter that removes the contribution of multiple scattering in the reflection matrix. Interestingly, they even show how the DORT method, which originally failed in the multiple scattering regime, could benefit from this filter to detect objects embedded inside or hidden behind strongly scattering media [Aubry, 2009a; Aubry, 2009b].

Moreover, this observation is at the heart of a computational adaptive focusing technique developed in optics to correct aberrations in optical microscopy [Yoon, 2020; Kang, 2017; Kwon, 2023]. In a nutshell, the authors developed an iterative algorithm to restore the long-range correlations along the anti-diagonals of **R** to achieve imaging of biological tissues at depths larger than 100 µm, a regime where optical imaging usually fails due to aberrations and multiple scattering.

3.3.3 From detection to imaging

The DORT method described in (Section 3.3.1) is not adapted for clinical ultrasound imaging, as it only enables selective focusing on targets of a sparse scattering medium (*i.e.* containing only a few reflectors).

However, it has been shown that the aberration law can be extracted in a completely random medium generating ultrasound speckle by performing spatial cross-correlations on adjacent transducers [ODonnell, 1988], as shown in [Fig. 2.6A]. From a physical point of view, this demonstration is particularly noteworthy because it shows that an artificial guide-star can be built even in a random medium (*i.e.* without the presence of a strong reflector).

Inspired by this work, the DORT method was then extended to input focused beams [Robert, 2005], namely the fDORT method, and to the case of random media for clinical imaging applications [Fig. 2.6B]. A set of focused beams is used to generate different virtual sources [Robert, 2008b] at different points $\mathbf{r}_{\text{in}} = (x_{\text{in}}, z_{\text{in}})$ such that a partial reflection matrix is stored as $R_{\text{p}}(\mathbf{r}_{\text{in}}, \mathbf{u}_{\text{out}}, t)$.

To coherently sum each input beam, the associated received signals must first be delayed so that each input focal point is virtually *de-scanned*, *i.e.* brought to the same reference position, using the following time delay law $\Delta\tau_{\text{fDORT}}(\mathbf{r}_{\text{in}}, \mathbf{u}_{\text{out}}, c_0) = |u_{\text{out}} - x_{\text{in}}|^2/(c_0 z_{\text{in}})$ [Robert, 2007]. Subsequently, time-gating to select echoes from different depths and a Fourier transform are

performed similarly as in (Eq. 2.18):

$$R_{\text{fDORT}}(\underbrace{[x_{\text{in}}, z]}_{\mathbf{r}_{\text{f}}}, \mathbf{u}_{\text{out}}, \omega) = \int \mathrm{d}t \underbrace{R_{\text{p}}(\mathbf{r}_{\text{in}}, \mathbf{u}_{\text{out}}, t + \Delta\tau_{\text{fDORT}}(\mathbf{r}_{\text{in}}, \mathbf{u}_{\text{out}}, c_0))}_{\text{Realigned signals}} \underbrace{\mathcal{W}_t(t - \frac{2z}{c_0})}_{\text{Time gating}} \exp(j\omega t). \tag{2.20}$$

Each point $\mathbf{r}_{\text{f}} = (x_{\text{in}}, z)$ provides a different realization of disorder and their spatial correlations can be studied through the correlation matrix of $\mathbf{R}_{\text{fDORT}}$ as follows:

$$C_{\text{fDORT}}(\mathbf{u}_{\text{out}}, \mathbf{u}_{\text{out}}{}', \omega) = \langle R_{\text{fDORT}}(\mathbf{r}_{\text{f}}, \mathbf{u}_{\text{out}}, \omega) R_{\text{fDORT}}(\mathbf{r}_{\text{f}}, \mathbf{u}'_{\text{out}}, \omega) \mathcal{W}(\mathbf{r}_{\text{f}} - \mathbf{r}_{\text{p}}) \rangle_{\mathbf{r}_{\text{f}}}, \tag{2.21}$$

where $\mathcal{W}$ is a spatial average window that consider only neighboring points around a central point $\mathbf{r}_{\text{p}}$.

If each input focal point $\mathbf{r}_{\text{f}}$ belongs to the same isoplanatic patch and the correlation matrix converges towards its ensemble average (*i.e.* a sufficient number of realization of disorder are considered), $\mathbf{C}_{\text{fDORT}}$ is of rank 1 and the corresponding singular vector $\mathbf{V}_1 = [V_1(\mathbf{u}_{\text{out}})]$ directly yields the aberration law $T(\mathbf{u}_{\text{out}})$ [Varslot, 2004; Måsøy, 2005]. In other words, an artificial guide-star, located in the barycenter of the considered $\mathbf{r}_{\text{in}}$ points, can be extracted thanks to a singular value decomposition $\mathbf{R}_{\text{fDORT}}$ that enables us to perform a coherent average of input focal spots to synthesize a virtual guide star. Subsequently, the process must be repeated by applying the phase conjugates of the aberration laws to achieve better focusing, reduce the size of the guide star, and thus improve the estimation of the aberration laws

This iterative feature is the major drawback of this method, as it requires physical focusing inside the medium to create a virtual guide star for each isoplanatic area of the medium, which is a time-consuming process. Inspired by a previous work that used decoupled Gaussian beams at emission and reception to probe the diffuse halo in a random medium [Aubry, 2008a], we introduce, in the next section, a general formalism for projecting the $\mathbf{R}-$matrix onto a focused basis. In particular, we will go beyond a simple time-gating to better select the echoes coming from a given focal point. In addition, the aberration correction process is fully achieved numerically, so that more robust results can be obtained compared to an iterative physical focusing process!

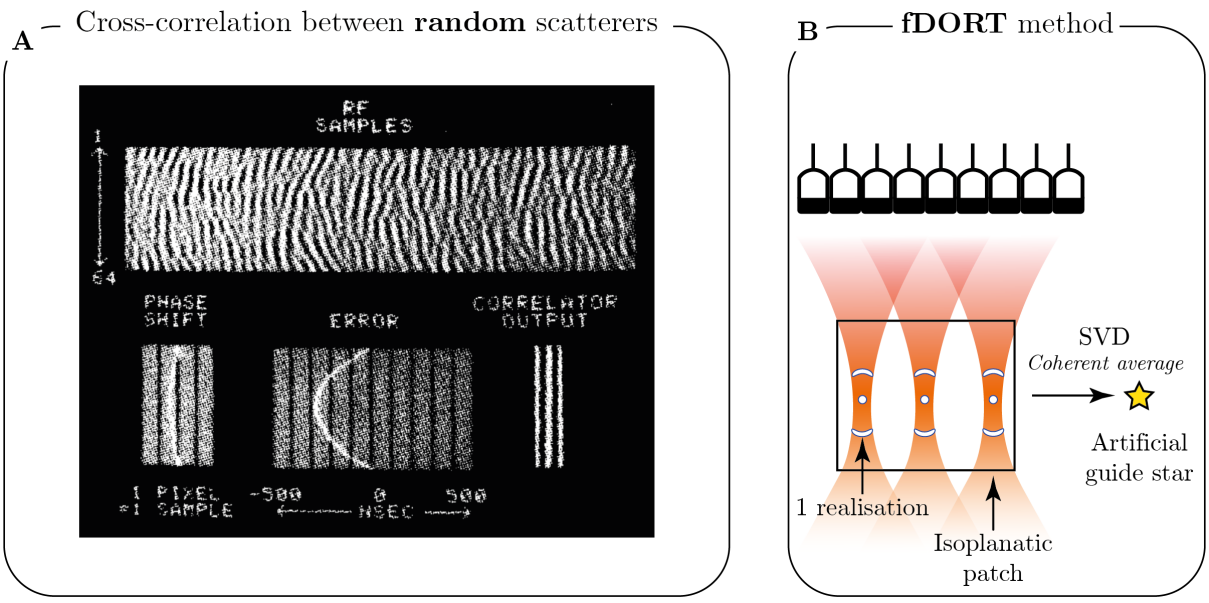

Figure 2.6: **Using spatial correlations to build an artificial guide-star from random scatterers.** (**A**) Absolute value of cross-correlation measure of delays for case of collection of random scatterers insonified with unfocused transmitter. *Extracted from* [ODonnell, 1988]. (**B**) Extension of the DORT method to focused beams, denoted fDORT. Each input focal spot can be seen as a virtual source within the medium. A singular value decomposition of R_{fDORT} is performed to provide a coherent combination of each virtual source, thereby creating an artificial guide star that can be leveraged to measure an aberration phase law. *Inspired from* [Robert, 2008b].

4 Ultrasound Matrix Imaging

In the following, the fundamentals of Ultrasound Matrix Imaging (UMI), currently under development in the group of Alexandre Aubry at the Institut Langevin, are presented. First, the different insonification modes (besides the canonical basis) for recording the reflection matrix are presented, which are of particular interest to achieve a higher SNR and frame rate, and are therefore more suitable for *in vivo* imaging. Next, we introduce the **focused basis**, which is the cornerstone of current matrix imaging methods. Its projection onto a number of different bases allows not only quantification of focusing quality, multiple scattering and noise rates [Lambert, 2020b; Lambert, 2022b], or spatial variations in the speed-of-sound [Lambert, 2020b], but also extraction of local aberration phase laws [Lambert, 2020c; Lambert, 2022a], leading to an estimate of the transmission matrix that connects each transducer of the probe to any point of the medium. The individual steps of the matrix imaging process are presented and validated using a controlled phantom experiment. As a proof-of-concept, the entire procedure is then applied to an *in vivo* imaging experiment.

4.1 R−matrix acquisition

UMI starts with the acquisition of a three-dimensional reflection matrix, using a set of insonifications identified by the vector $\mathbf{i}_{\text{in}}$:

$$\mathbf{R_{iu}}(t) = \left[R(\mathbf{i}_{\text{in}}, \mathbf{u}_{\text{out}}, t)\right], \tag{2.22}$$

where $\mathbf{R_{iu}}(t)$ refers to the $\mathbf{R}$-matrix expressed in the $\mathbf{i}$-basis at the input and the $\mathbf{u}$-basis at the output for a given time t. $R(\mathbf{i}_{\text{in}}, \mathbf{u}_{\text{out}}, t)$ refers to one of its coefficients.

For a probe made of N_u transducers, the complete reflection matrix consists of N_i insonifications and thus forms a matrix of size $N_u^2 N_t$, where N_t is the number of time samples. Furthermore, the medium is considered as static throughout the N_i insonifications. Assuming a sampling frequency f_{s} and a frequency bandwidth Δf, the number of temporal degrees of freedom contained in $\mathbf{R}$ is of about $N_t \Delta f / f_{\text{s}}$ and the number of spatial degrees of freedom is $N_i N_u \leq N_u^2$.

4.1.1 Insonification bases

Different bases can be used to insonify an unknown medium, which are most appropriate with regard to the imaging configuration and/or conditions:

- converging waves ($\mathbf{r}_{\text{in}}$) were first used in clinical ultrasound imaging using several focused beams [Fig. 2.7A]. Their advantage lie in the higher energy deposition at the focal point than with other types of insonification, which is particularly suitable for transcranial therapy, for example [Aubry, 2003]. However, for imaging, they provide a relatively low frame-rate;

- diverging waves ($\mathbf{u}_{\text{in}}$) through a single transducer emission [Fig. 2.7B], which refers to the canonical basis and was originally developed to introduce the matrix imaging formalism [Prada, 1994]. Although it does not require assumptions about the speed-of-sound in the medium, such insonification provides very low SNR as only a single transducer is used for each emission. Virtual sources [Provost, 2014] placed above the probe ($\mathbf{v}_{\text{in}}$) [Fig. 2.7D] can be a solution to use multiple transducers and seem to be particularly relevant for ultrafast imaging with small apertures probes, such as phased array ones, used in particular for cardiac or transcranial imaging, or even matrix arrays of transducers to perform 3D imaging over a large field-of-view.

- plane waves ($\boldsymbol{\theta}_{\text{in}}$) [Fig. 2.7C], which originally led to ultra-fast [Sandrin, 1999; Tanter, 2014] and shear-wave imaging [Bercoff, 2004; Sandrin, 1999; Sandrin, 2002; Bercoff, 2003] because they allow imaging of a much larger field-of-view with a reduced number of insonifications compared with focused beams.

It should be emphasized that the transducer basis corresponds to a collection of vectors which are not linearly independent, and therefore is not a basis in the strict sense. In the following, the terms bases will nevertheless be used to refer to these different categories of wave fronts.

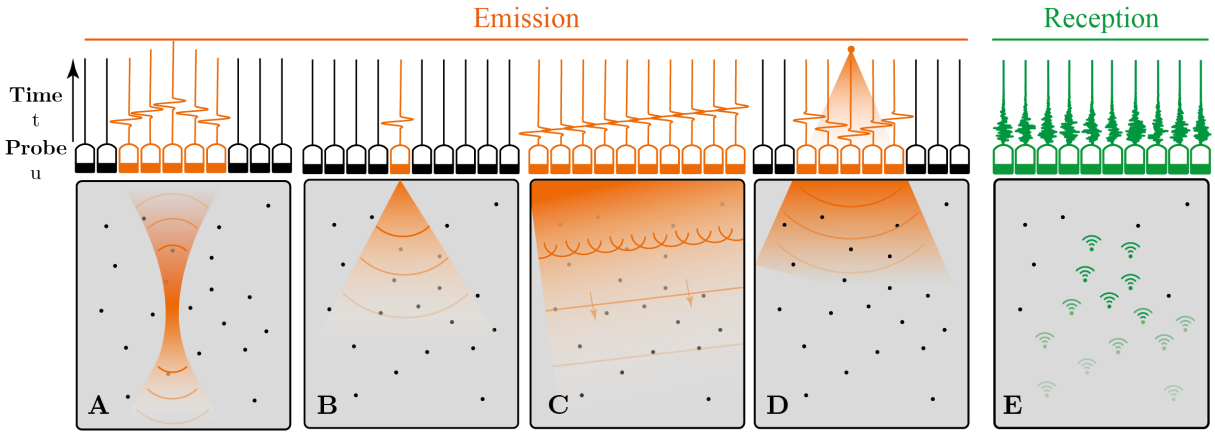

Figure 2.7: **Insonification bases in ultrasound imaging.** (**A**) Focused emission were historically used in early B-mode images to provide sufficient SNR. (**B**) Single-transducer emission was introduced to provide a mathematical framework to the iterative-time reversal experiment. However, it provides a very poor signal-to-noise ratio as it only uses one transducer. (**C**) Plane wave emission was introduced to increase the field of view with a smaller number of emissions, resulting in ultrafast imaging. (**D**) Virtual sources were introduced as a compromise between single transducer emission and plane waves, as they allow firing with multiple transducers and are less directive than a plane wave (*i.e.* provide a larger field of view). (**E**) Regardless of the emission base, the backscattered wavefronts are recorded at each transducer of the ultrasonic probe (*i.e.* in the transducer base).

In ultrafast imaging, the $\mathbf{R}-$matrix is only partially recorded at the input, since we only use a few plane waves or virtual sources to achieve a sufficient frame-rate for the intended applications. On the contrary, in the following, all the results presented are obtained using a full sequence of plane waves, which does not meet the requirements for ultrafast acquisition. Nevertheless, we will see how ultrafast acquisition can still take advantage of matrix imaging in Chapter 4.

4.1.2 Description of experiments

To introduce the UMI framework, a controlled 2D imaging experiment on a tissue mimicking phantom (CIRS, Model 050GSE) experiment is investigated. A linear probe is placed directly in contact with an ultrasound phantom [Fig. 2.8A]. This phantom (speed of sound: $c_p \sim 1540$ m/s) is composed of a random distribution of unresolved scatterers which generate ultrasonic speckle characteristic of human soft tissues. The system also contains regularly spaced nylon filaments, and, at a depth of 30 mm, a 10 mm-diameter hyperechoic cylinder, containing a higher density of unresolved scatterers.

The reflection matrix is recorded in the plane wave basis: $\mathbf{R}_{\boldsymbol{\theta}\mathbf{u}}(t) \equiv [R(\boldsymbol{\theta}_{\text{in}}, \mathbf{u}_{\text{out}}, t)]$ [Fig. 2.8B]. The characteristics of the probe and sequence parameters are described in [Table. 2.1]. In particular, a set of 81 plane waves is generated by applying steered time-delays to each transducer u_x of the probe:

$$\Delta\tau(\theta_{\text{in}}, u_x) = u_x \sin(\theta_{\text{in}})/c_0. \tag{2.23}$$

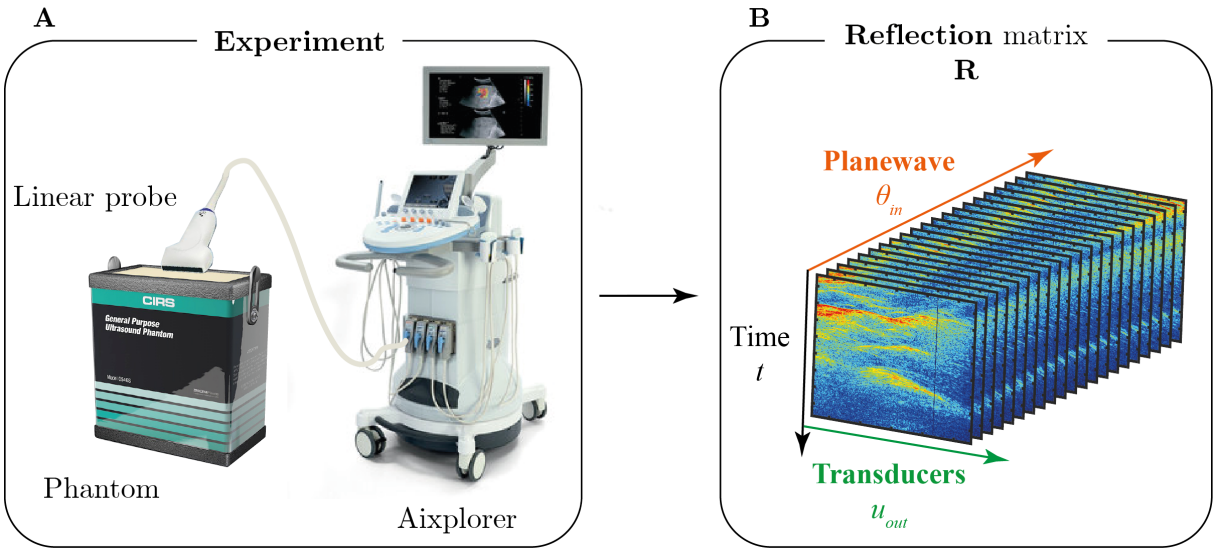

Figure 2.8: **Tissue-mimicking phantom experiment.** (**A**) A linear ultrasound probe is placed directly in contact with a tissue-mimicking phantom and raw data are recorded using an ultrafast ultrasound scanner (Aixplorer®, Supersonic Imagine / Hologic), thus forming the (**B**) reflection matrix of the medium.

Parameters			**Value**
Probe	Type		Linear
	Number of transducers	Transmit	$N_u^{(\mathrm{Tx})} = 256$
		Receive	$N_u^{(\mathrm{Rx})} = N_{u_{\mathrm{out}}} = 128$
	Transducer pitch		$\delta u = 0.2$ mm ($\approx \lambda$ at $c_0 = 1540$ m/s)
	Aperture	Transmit	$\Delta u_x^{(\mathrm{Tx})} = 51.2$ mm
		Receive	$\Delta u_x^{(\mathrm{Rx})} = 25.6$ mm
	Central frequency		$f_{\mathrm{c}} = 7.5$ MHz
	Bandwidth		$\Delta f = [2 - 10]$ MHz
Acquisition	Electronic hardware		Aixplorer®, Supersonic Imagine
	Speed-of-sound hypothesis		$c_0 = 1540$ m/s
	Plane wave angles	Maximum	$\theta_{\mathrm{in}}^{(\mathrm{max})} = 40°$ (calculated at c_0)
		Pitch	$\delta\theta_{\mathrm{in}} = 1°$ (calculated at c_0)
		Number	$N_{\theta_{\mathrm{in}}} = 81$
	Emitted signal		Burst of two half periods of f_{c}
	Sampling frequency		$f_{\mathrm{s}} = 30$ MHz
	Recording time		$\Delta t = 137$ μs

Table 2.1: **Acquisition of the reflection matrix, $\mathbf{R}_{\boldsymbol{\theta}\mathbf{u}}(t) \equiv [R(\boldsymbol{\theta}_{\mathbf{in}}, \mathbf{u}_{\mathbf{out}}, t)]$, in a phantom imaging experiment.** *Acquisition was performed by Laura Cobus.*

2D UMI is then applied to the *in vivo* imaging experiment of a human calf performed by William Lambert [Lambert, 2022b]. Similar to the phantom experiment, the reflection matrix is recorded based on plane wave insonifications. The characteristics of the probe and acquisition sequence parameters are described in [Table. 2.2].

Note that in both experiments, the reflection matrix is only partially recorded, since the

number of insonification $N_{\theta_{\text{in}}}$ is somewhat smaller than the number of transducers $N_{u_{\text{out}}}$. In other words, the input basis is incomplete, but that does not change the results presented in this chapter. The consequences of an incomplete input basis are examined in Chapter 3 (see Section 3.3).

Parameters			Value
Probe	Type		Linear
	Number of transducers		$N_u = N_{\mathbf{u}_{\text{out}}} = 192$
	Transducer pitch		$\delta u = 0.2$ mm ($\approx \lambda$ at $c_0 = 1580$ m/s)
	Aperture		$\Delta u_x = 38.4$ mm
	Central frequency		$f_{\text{c}} = 7.5$ MHz
	Bandwidth		$\Delta f = [2 - 10]$ MHz
Acquisition	Electronic hardware		Supersonic™ Mach-30, Supersonic Imagine
	Speed-of-sound hypothesis		$c_0 = 1580$ m/s
	Plane wave angles	Maximum	$\theta_{\text{in}} = 25°$ (calculated at c_0)
		Pitch	$\delta\theta_{\text{in}} = 0.5°$ (calculated at c_0)
		Number	$N_{\boldsymbol{\theta}_{\text{in}}} = 101$
	Emitted signal		Burst of three half periods of f_{c}
	Pulse Repetition Frequency		1 kHz
	Sampling frequency		$f_{\text{s}} = 40$ MHz
	Recording time		$\Delta t = 80$ μs

Table 2.2: **Acquisition of the reflection matrix, $\mathbf{R}_{\boldsymbol{\theta}\mathbf{u}}(t) \equiv [R(\boldsymbol{\theta}_{\mathbf{in}}, \mathbf{u}_{\mathbf{out}}, t)]$, for an *in vivo* human calf imaging experiment [Lambert, 2020a].** *Acquisition was performed by William Lambert.*

4.2 Projection in the focused basis

In conventional imaging, the usual method to build an ultrasound image is to numerically focus the ultrasound data at the same location in emission and reception for any point in the field-of-view, using a Delay-And-Sum algorithm (DAS). Interestingly, the projection of the $\mathbf{R}-$matrix onto a focused basis can be viewed as an extended and more general *beamforming* process in which the input and output focal points are decoupled. A focused reflection matrix can be built, which is the cornerstone of matrix imaging. This matrix has been studied in detail in previous works that are not limited to ultrasound imaging [Lambert, 2020c; Lambert, 2020b; Lambert, 2022b; Lambert, 2022a; Brütt, 2022], but also finds applications in other fields of wave physics, such as optics [Badon, 2020; Najar, 2023; Balondrade, 2023] or seismic imaging [Blondel, 2018; Touma, 2021], again showing the numerous applications of such a general approach to wave propagation.

4.2.1 Numerical focusing or *beamforming*

In previous works [Lambert, 2020b; Lambert, 2020c], the projection of the $\mathbf{R}-$matrix into the focused basis was performed in the frequency domain, using monochromatic and homogeneous Green's functions (constant speed-of-sound c_0) in order to focus numerically at different points

at the input $\mathbf{r}_{\text{in}} = (x_{\text{in}}, z)$ and the output $\mathbf{r}_{\text{out}} = (x_{\text{out}}, z)$. Under a matrix formalism, it writes:

$$\mathbf{R_{rr}}(\omega) = [\mathbf{R_{xx}}(z,\omega)] = \mathbf{G}_0^{(\text{in})*}(\omega) \times \mathbf{R_{iu}}(\omega) \times \mathbf{G}_0^{(\text{out})\dagger}(\omega), \tag{2.24}$$

where $\mathbf{G}_0^{(\text{in/out})}$ are the homogeneous propagation matrices defined as follows:

$$G_0^{(\text{in})} = A_{\text{in}}(i_{\text{in}}, \mathbf{r}_{\text{in}}) \exp(i\omega\tau(i_{\text{in}}, \mathbf{r}_{\text{in}}, c_0)), \tag{2.25}$$

$$G_0^{(\text{out})} = A_{\text{out}}(u_{\text{out}}, \mathbf{r}_{\text{out}}) \exp(i\omega\tau(u_{\text{out}}, \mathbf{r}_{\text{out}}, c_0)), \tag{2.26}$$

where A_{in} and A_{out} are apodization factors that limit the extension of the synthetic aperture at the input and output. This synthetic aperture is dictated by the transducers' directivity [Perrot, 2021]. If no synthetic aperture is used (*i.e.* $\forall(i_{\text{in}}, \mathbf{r}_{\text{in}}, u_{\text{out}}, \mathbf{r}_{\text{out}})$, $A_{\text{in/out}} = 1$), the propagation matrices should check $\mathbf{G}_0 \times \mathbf{G}_0^\dagger = \mathbf{G}_0^\dagger \times \mathbf{G}_0 = \mathbf{I}$ in the far-field, where $\mathbf{I}$ is the identity matrix.

To recover the axial resolution corresponding to the frequency bandwidth for each depth of the field-of-view, a sum over the frequencies, which can be seen as an inverse Fourier transform or a time-gating process at the ballistic time ($t = 0$ in the focused basis), is performed:

$$\mathbf{R_{xx}}(z) = \sum_{\omega>0} \mathbf{R_{xx}}(z,\omega), \tag{2.27}$$

where only the positive frequencies are considered in the sum to recover the analytic signal (amplitude and phase), as would be the case with a Hilbert transform.

However, building the focused reflection matrix in the frequency domain based on (Eq. 2.24 & 2.27) is particularly time-consuming because it involves a huge amount of RAM (either on CPU or GPU) to store each monochromatic Green matrices that can reach high dimensions. Since it is not trivial to parallelize this process, we prefer to perform such processing in the time domain.

Projection of the R-matrix in the focused basis

In terms of matrix coefficients, the injection of (Eqs. 2.25 & 2.26) into (Eqs. 2.24 & 2.27) leads to the projection of the reflection matrix in the focused basis [Lambert, 2020b]:

$$R_{\mathcal{F}}(\mathbf{r}_{\text{in}}, \mathbf{r}_{\text{out}}) = \sum_{\mathbf{i}_{\text{in}}} \sum_{\mathbf{u}_{\text{out}}} \underbrace{A(\mathbf{i}_{\text{in}}, \mathbf{r}_{\text{in}}, \mathbf{u}_{\text{out}}, \mathbf{r}_{\text{out}})}_{\text{synthetic aperture}} R\left(\mathbf{i}_{\text{in}}, \mathbf{u}_{\text{out}}, \tau(\mathbf{i}_{\text{in}}, \mathbf{r}_{\text{in}}) + \tau(\mathbf{u}_{\text{out}}, \mathbf{r}_{\text{out}})\right), \tag{2.28}$$

where A is the product of the input and output apodization factors that limit the synthetic aperture and R is the analytical signal of the reflection matrix.

Note: *To simplify notations in the following, we will omit the index $\mathcal{F}$ and refer to the focused reflection matrix as* $\mathbf{R}$ *instead of* $\mathbf{R}_{\mathcal{F}}$*. More generally, the reflection matrix will be referred to as* $\mathbf{R}$*, regardless of the base in which it is expressed.*

It is important to note that the IQ signal is considered in (Eq. 2.28), *i.e.* the complex value of the $\mathbf{R}$-matrix, to access both the amplitude and phase of the wave-field. Hence, the focused

$\mathbf{R}-$matrix can be built in the time domain via a conventional delay-and-sum beamforming scheme that consists in applying appropriate time-delays in order to focus at different points at input $\mathbf{r}_{\text{in}} = (x_{\text{in}}, z)$ and output $\mathbf{r}_{\text{out}} = (x_{\text{out}}, z)$. In the different bases, those time delays write:

$$\text{Transducer basis: } \tau(\mathbf{u}, \mathbf{r}) = \frac{|\mathbf{u} - \mathbf{r}|}{c_0} = \frac{\sqrt{(x - u_x)^2 + z^2}}{c_0}, \tag{2.29}$$

$$\text{Plane wave basis: } \tau(\boldsymbol{\theta}, \mathbf{r}) = [x \sin\theta_x + z \cos\theta_x] / c_0, \tag{2.30}$$

$$\text{Virtual source basis : } \tau(\mathbf{v}, \mathbf{r}) = \frac{|\mathbf{v} - \mathbf{r}|}{c_0} = \frac{\sqrt{(x - v_x)^2 + (z - v_z)^2}}{c_0}, \tag{2.31}$$

Technical note: Practically, an additional time delay $\tau_{\text{origin}}(\mathbf{i}_{\text{in}})$ must be considered in (Eq. 2.28) when plane waves or virtual sources are involved, in order to set the same time origin for each insonification, so that a coherent compounding can be achieved.

4.2.2 Mathematical expression and physical interpretation

Mathematically, the focused reflection matrix can be expressed by injecting (Eq. 2.8) in (Eq. 2.24), resulting in:

$$\mathbf{R}_{\mathbf{xx}}(\omega) = \mathbf{H}_{\text{in}}^{\top}(\omega) \times \boldsymbol{\Gamma} \times \mathbf{H}_{\text{out}}(\omega), \tag{2.32}$$

with $\mathbf{H}_{\text{in/out}} = \mathbf{G}_{\text{in/out}} \times \mathbf{G}_0^{\dagger}$ the focusing matrices whose coefficients $H_{\text{in/out}}(\mathbf{r}, \mathbf{r}_{\text{in/out}}, \omega)$ correspond to the transmit and receive point spread functions (PSF), that is to say the spatial amplitude distribution of the wave-field in the focal plane when trying to focus at $\mathbf{r}_{\text{in/out}}$. In terms of matrix coefficients, (Eq. 2.27) re-writes:

$$R(\mathbf{r}_{\text{in}}, \mathbf{r}_{\text{out}}, c_0) = \int\int \mathrm{d}\omega \mathrm{d}\mathbf{r}' H_{\text{in}}(\mathbf{r}_{\text{in}}, \mathbf{r}', \omega, c_0) \gamma(\mathbf{r}') H_{\text{out}}(\mathbf{r}_{\text{out}}, \mathbf{r}', \omega, c_0). \tag{2.33}$$

The physical meaning of the focused $\mathbf{R}$-matrix can be understood in light of the concept of virtual sources (or transducers in the specific case of acoustics) introduced in previous work [Robert, 2008b]. The transmitted energy is focused on the input focal point, $\mathbf{r}_{\text{in}}$, which can be considered as a virtual source. Similarly, the output focal point, $\mathbf{r}_{\text{out}}$, can be seen as a virtual receiver embedded in the medium, synthesized by selecting the time-echoes emanating from its vicinity. However, the concept of virtual transducers is purely didactic, as they do not act as active energy sources. Moreover, such virtual transducers are strongly directional, either downward for $\mathbf{r}_{\text{in}}$ and upward for $\mathbf{r}_{\text{out}}$ [Lambert, 2022b].

We now make an isoplanatic assumption. This means that the input and/or output PSFs can be considered to be spatially invariant: $H_{\text{in/out}}(\mathbf{r}, \mathbf{r}_{\text{in/out}}) = H_{\text{in/out}}(\mathbf{r} - \mathbf{r}_{\text{in/out}})$. We will come back to the range of validity of this approximation later. Under this assumption and in the single scattering regime, the focused $\mathbf{R}-$matrix coefficients can be expressed as follows [Lambert, 2020b]:

$$R(x_{\text{in}}, x_{\text{out}}, z) = \int \mathrm{d}x \gamma(x, z) \underbrace{H_{\text{in}}(x - x_{\text{in}}, x_{\text{in}}, z) H_{\text{out}}(x - x_{\text{out}}, x_{\text{out}}, z)}_{\text{Imaging PSF}}. \tag{2.34}$$

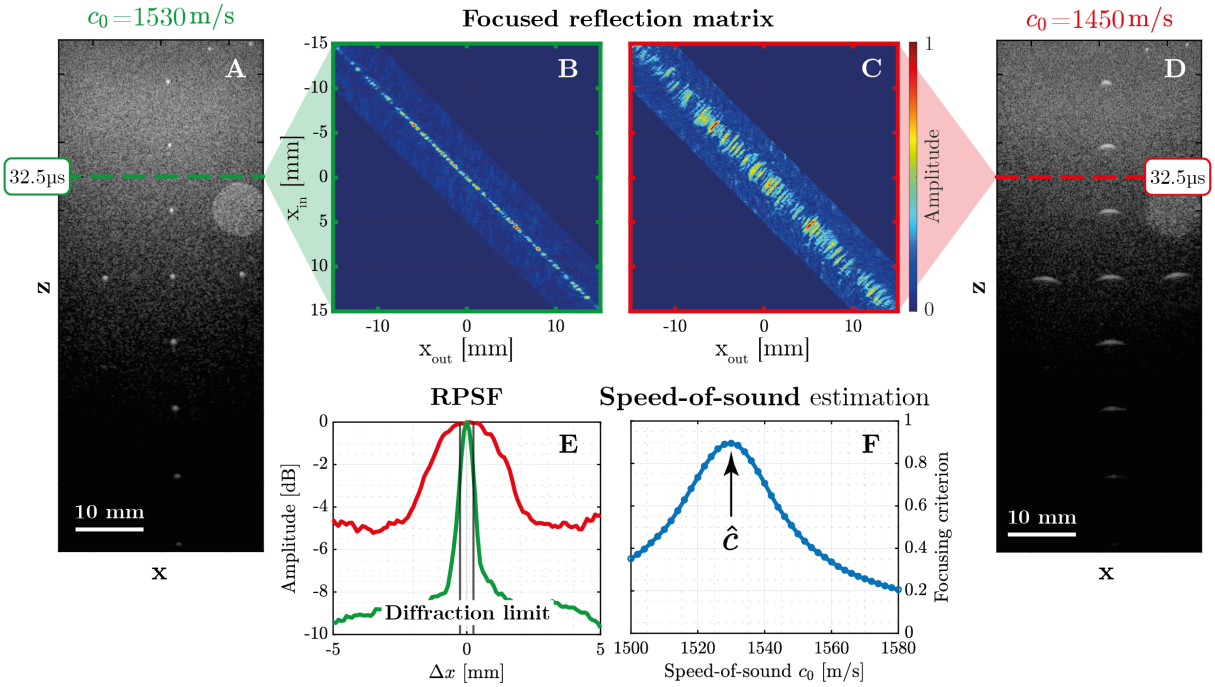

Figure 2.9: **Focused R−matrix, RPSF & focusing criterion.** Results corresponds to the tissue mimicking phantom experiment [Table. 2.1]. (**A, D**) Confocal image and (**B, C**) amplitude of the focused reflection matrix at time $t = 32.5\mu s$ for a correct and an incorrect speed-of-sound hypothesis ($c_0 = 1530$ m/s and $c_0 = 1450$ m/s), respectively. (**E**) RPSF extracted in both cases (red: incorrect speed-of-sound, green: correct speed-of-sound) and compared to the theoretical diffraction limit whose support is delimited by black vertical lines. (**F**) Focusing criterion as a function of the speed-of-sound hypothesis. *Inspired from* [Lambert, 2020b].

4.2.3 Confocal imaging

In a single scattering regime, the energy is expected to be near the diagonal of the focused reflection matrix (*i.e.* $x_{\text{in}} = x_{\text{out}}$).

Confocal imaging

Hence, each pixel of the main diagonal of $\mathbf{R_{xx}}(z)$ provides the transverse cross-section of the confocal ultrasound image $\mathcal{I}$ at depth z, as described in [Fig. 2.9A-B]:

$$\mathcal{I}(\mathbf{r}) = |R(\mathbf{r}_{\text{in}} = \mathbf{r}_{\text{out}})|^2 = |R(x_{\text{in}}, x_{\text{out}} = x_{\text{in}}, z)|^2 \,, \tag{2.35}$$

where $\mathbf{r} = \mathbf{r}_{\text{in}} = \mathbf{r}_{\text{out}}$ is the confocal point.

The combination of (Eq. 2.28) and (Eq. 2.35) leads to a classical DAS algorithm where numerical focusing is performed at the same point at emission and reception:

$$\mathcal{I}(\mathbf{r}) = \left| \sum_{\mathbf{i}_{\text{in}}} \sum_{\mathbf{u}_{\text{out}}} A(\mathbf{i}_{\text{in}}, \mathbf{u}_{\text{out}}, \mathbf{r}) R(\mathbf{i}_{\text{in}}, \mathbf{u}_{\text{out}}, \tau(\mathbf{i}_{\text{in}}, \mathbf{r}) + \tau(\mathbf{u}_{\text{out}}, \mathbf{r})) \right|^2 . \tag{2.36}$$

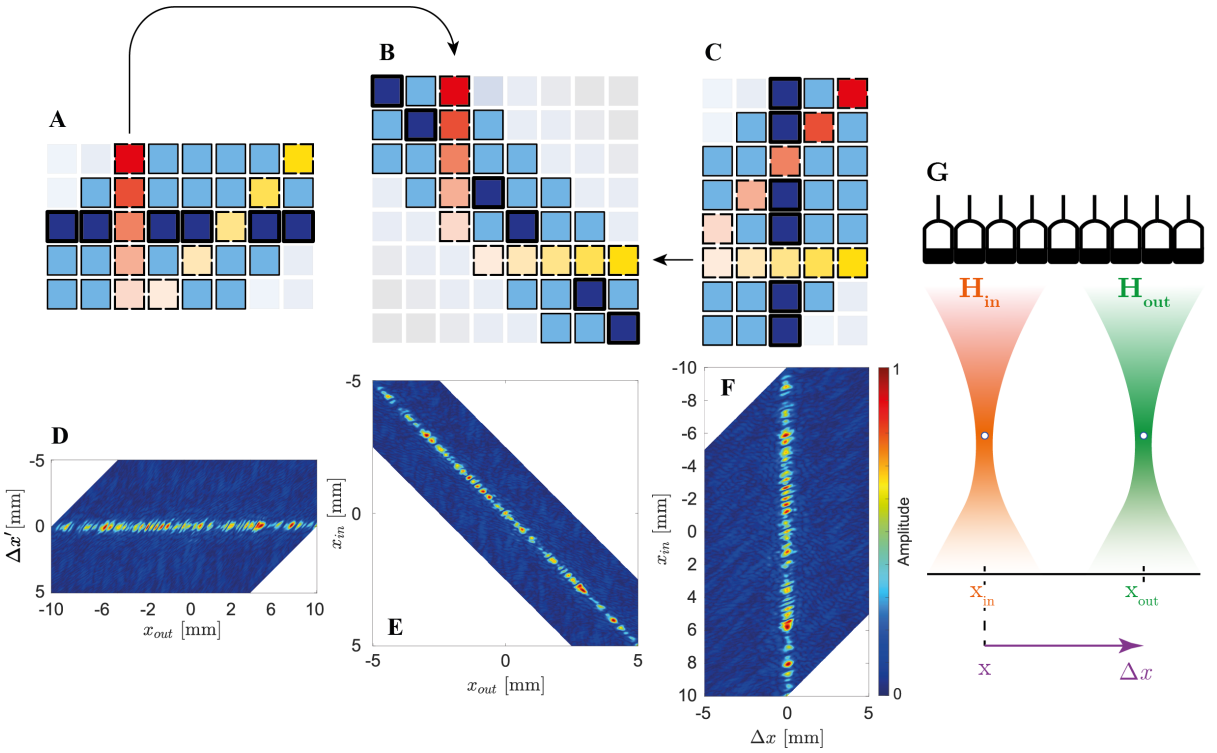

Figure 2.10: **The de-scan focused basis.** (**A**) The de-scan focused basis with respect to the output focusing points: $R_{\mathcal{D}}(\Delta x', x_{\text{out}})$, with $\Delta x' = x_{\text{in}} - x_{\text{out}}$. (**B**) The focused basis $R(x_{\text{in}}, x_{\text{out}})$. (**C**) The de-scan focused basis with respect to the input focusing points: $R_{\mathcal{D}}(x_{\text{in}}, \Delta x)$, with $\Delta x = x_{\text{out}} - x_{\text{in}}$. (**D-F**) Experimental data in the speckle regime acquired in a tissue mimicking phantom [Table 2.1]. (**G**) Schematic view of the input and output focal spots.

From another point-of-view, the diagonal feature of the focused $\mathbf{R}-$matrix is the near-field equivalent in the real space of the far-field memory effect described earlier [Fig. 2.5B], the real and **k**-space being linked by a two-dimensional spatial Fourier transform.

From this general point of view, different change of bases can be performed either to reduce the amount of data or to probe with better accuracy the quality of focusing at each point.

4.3 The de-scan focused basis

The sparsity of such matrices suggests that only the responses between adjacent focal points appear relevant. Thus, instead of storing the responses between all pairs $(x_{\text{in}}, x_{\text{out}})$, it is less data-intensive to store them in a de-scan basis $[R_{\mathcal{D}}(\Delta x, x, z)] \equiv [R(x_{\text{in}}, x_{\text{out}}, z)]$, as described in [Fig. 2.10A, D, C and F]. Mathematically, it consists of the following change of variables [Fig. 2.10G]:

$$\underbrace{\begin{bmatrix} x_{\text{in}} \\ x_{\text{out}} \end{bmatrix}}_{\text{Focused basis}} \rightarrow \underbrace{\begin{bmatrix} x \\ \Delta x \end{bmatrix} = \begin{bmatrix} x_{\text{in}} \\ x_{\text{out}} - x_{\text{in}} \end{bmatrix}}_{\text{De-scan basis}}, \tag{2.37}$$

where $x = x_{\text{in}}$ and $\Delta x = x_{\text{out}} - x_{\text{in}}$.

We use the term "de-scan" because the output (x_{out}) is scanned with respect to the input (x_{in}). Thus, it is a change of representation in which the reflection matrix is rearranged so that

all input focal points are brought to the same location.

These considerations also apply to the recording of the $\mathbf{R}-$matrix and can drastically reduce the amount of stored data, since at a given time and for a given transducer $\mathbf{u}_{\text{in}}$ only the neighboring transducers $\mathbf{u}_{\text{out}}$ are relevant (according to their directivity).

4.4 Focusing quality

The wealth of the focused reflection matrix lies in its off-diagonal elements (*i.e.* $x_{\text{in}} \neq x_{\text{out}}$), which provide much more information than just the confocal image. In other words, the focused reflection matrix uses all the spatial degrees of freedom available in the previously acquired reflection matrix, while conventional imaging only uses a small portion of the available information. We now show how to quantify aberrations in ultrasound speckle (without any guide star) by investigating the off-diagonal elements of $\mathbf{R_{xx}}(z)$.

4.4.1 RPSF & common midpoint basis

Although the de-scan basis allows a reduction in the amount of data stored, it is not the optimal basis to probe the focusing quality locally because it does not center the input and output around the same point. To this end, a change of variables is applied to go from the focused basis to a common midpoint basis:

$$\underbrace{\begin{bmatrix} x_{\text{in}} \\ x_{\text{out}} \end{bmatrix}}_{\text{Focused basis}} \rightarrow \underbrace{\begin{bmatrix} x_{\text{m}} \\ \Delta x \end{bmatrix} = \begin{bmatrix} \frac{x_{\text{in}}+x_{\text{out}}}{2} \\ x_{\text{out}} - x_{\text{in}} \end{bmatrix}}_{\text{Common midpoint basis}}. \tag{2.38}$$

This change of variables has been studied in previous works to obtain super-resolved images, namely *pixel reassignment* [Müller, 2010; Sheppard, 2013; Sommer, 2021]. It is described schematically in [Fig. 2.11] and in our case simply consists in extracting each anti-diagonal of the focused reflection matrix $\mathbf{R_{xx}}(z)$, as follows:

$$R_{\mathcal{M}}(\underbrace{\{x_{\text{m}}, z\}}_{\mathbf{r}_{\text{m}}}, \Delta x) = R\left(x_{\text{m}} - \frac{\Delta x}{2}, x_{\text{m}} + \frac{\Delta x}{2}, z\right), \tag{2.39}$$

where $\mathbf{R}_{\mathcal{M}}$ refers to the reflection matrix in a common midpoint basis and $\mathbf{r}_{\text{m}} = (x_{\text{m}}, z)$ is the common midpoint of the input and output focal spots spaced by a distance $\Delta x = x_{\text{out}} - x_{\text{in}}$.

Its averaged intensity profile provides what we call the "reflection point spread function",

$$RPSF(\mathbf{r}_{\text{m}}, \Delta x) = \left\langle \left| R_{\mathcal{M}}(\mathbf{r}'_{\text{m}}, \Delta x) \right|^2 \mathcal{W}(\mathbf{r}'_{\text{m}} - \mathbf{r}_{\text{m}}) \right\rangle_{\mathbf{r}'_{\text{m}}}, \tag{2.40}$$

where $\langle . \rangle$ denotes a spatial average.

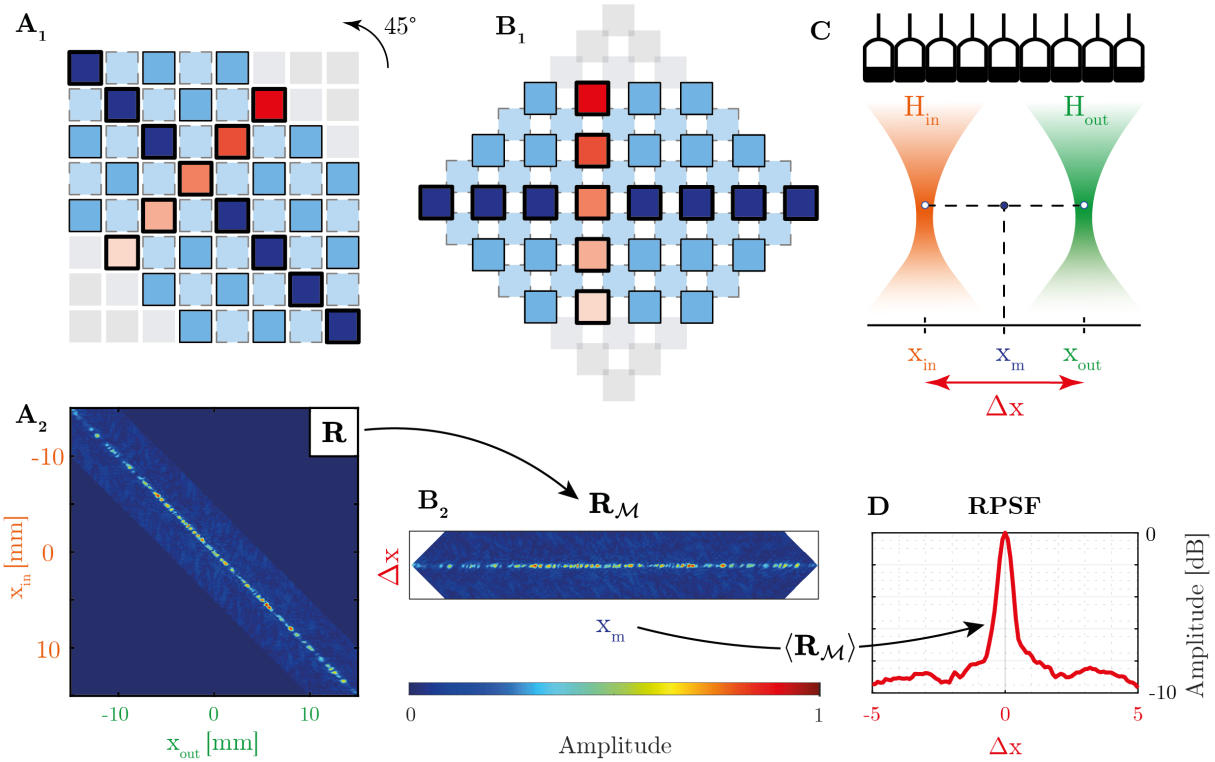

Figure 2.11: **Common midpoint representation.** Switching from the (**A**) focused basis to the (**B**) common midpoint representation corresponds to a 45° rotation of the focused reflection matrix. Index "1" shows a schematic representation of such a transformation, while index "2" shows experimental ultrasound data in speckle of an ultrasound phantom with a linear probe. Note that the change from the focused to the common midpoint representation implies two new sampling grids, represented by solid and dashed lines. (**C**) Schematic representation of the position of the input x_{in} and the output x_{out} focal spots, spaced by Δx and their common midpoint x_{p}. (**C**) Extracted RPSF by spatial averaging over all midpoints x_{m} at depth $z = 30$ mm.

Reflection Point Spread Function (RPSF)

In the **speckle regime** (random reflectivity), this quantity directly probes the local focusing quality [Fig. 2.9E] as its ensemble average scales as an incoherent convolution between the input and output PSFs [Lambert, 2020b] (see. Appendix 4.3):

$$RPSF(\mathbf{r}_{\mathrm{m}}, \Delta x) \propto \left(|\mathbf{H}_{\mathrm{in}}|^2 \overset{\Delta x}{\circledast} |\mathbf{H}_{\mathrm{out}}|^2 \right) (\mathbf{r}_{\mathrm{m}}, \Delta x). \tag{2.41}$$

In the **specular regime** (scatterer larger than the wavelength), reflectivity can be assumed constant and (Eq. 2.41) is slightly modified as follows (see. Appendix 4.3):

$$RPSF(\mathbf{r}_{\mathrm{m}}, \Delta x) \propto \left| \mathbf{H}_{\mathrm{in}} \overset{\Delta x}{\circledast} \mathbf{H}_{\mathrm{out}} \right|^2 (\mathbf{r}_{\mathrm{m}}, \Delta x). \tag{2.42}$$

The effects of aberrations in the focused reflection matrix are presented experimentally in a

speckle area of the tissue mimicking phantom [Fig. 2.9C]. Assuming an incorrect speed-of-sound during the beamforming process leads to a spread of the energy off the diagonal elements. An example of RPSF assuming a correct or an incorrect speed-of-sound hypothesis is presented in [Fig. 2.9E]. Interestingly, the width of the RPSF can directly be an indicator of the focusing quality at any point of the medium.

The theoretical expression of the RPSF (Eqs. 2.41 and 2.42) shows the advantages of moving to a common midpoint basis, since it depends equally on the input and output aberrations, which is relevant to construct a focusing criterion that scales equally according to the input and output aberrations.

4.4.2 The focusing criterion

A **focusing criterion** [Lambert, 2020b] has thus been introduced to compare the experimental transverse resolution measured on the RPSF to the ideal one predicted by the diffraction theory at each point of the medium:

$$F(\mathbf{r}) = \frac{\delta x_0(\mathbf{r})}{\delta x(\mathbf{r})}, \tag{2.43}$$

where δx is the experimental resolution of the RPSF (extracted on its full width at half maximum amplitude) and δx_0 the theoretical diffraction limit defined as follows:

$$\delta x_0(z) \sim \frac{\lambda_c}{2\sin\left\{\arctan\left[\Delta u_x/(2z)\right]\right\}}, \tag{2.44}$$

with Δu_x the lateral extension of the probe, λ_c the central wavelength and z the depth. The ideal resolution can be evaluated more precisely and locally at any point by numerically modeling (equation 2.41) but at a cost of a longer computation time.

The authors showed that the focusing criterion was a more sensitive criterion to probe the focusing quality than the coherence factor [Mallart, 1994] as depicted in [Fig. 2.13D-E]. Here, the focusing criterion shows that aberrations are more important on the left-hand side of the image, whereas the coherence factor only show a global value through the image. This increase in contrast can be explained by the fact that the focusing criterion, unlike the coherence factor, discriminates the effect of aberrations from multiple scattering and noise contributions. Moreover, while the coherence factor is computed from a single sided focusing process, the gain in transverse resolution is achieved by the decoupling of the input and output in the case of UMI. Thus, the focusing criterion appears to be a relevant observable to scan the local variations of the focusing quality.

Besides, the focusing criterion can also be used as an optimization parameter to retrieve the speed-of-sound of the medium [Lambert, 2020b] as presented in [Fig. 2.9F]. Repeating this process for all the point in the medium could thus lead to a speed-of-sound map of an unknown medium $c(\mathbf{r})$. This aspect will constitute the main topic of Chapter 6.

The slight difference between the optimal value of the speed-of-sound ($\hat{c} = 1530$ m/s) and the manufacturer's value ($c_\mathrm{p} = 1540$ m/s) is attributed to the acoustic lens of the probe, which is not taken into account here, leading to an underestimation of the speed of sound at shallow

depths. To avoid such a bias, one strategy could be to determine both the thickness and the speed of sound of the acoustic lens and to model a two-layer medium in the beamforming process. Assuming a paraxial approximation, another simpler strategy might be to shift the focal plane by the same value for each point in the medium, as we will show in Chapter 5.

4.5 Multiple scattering quantification

Experimental measurement of the RPSF can also be used to investigate the relative part of the multiple scattering. To do so, the normalized RPSF intensity profile can be decomposed as the sum of three contributions [Lambert, 2022b]:

$$\langle \mathrm{RPSF} \rangle(\mathbf{r}, \Delta x) = \underbrace{\alpha_{\mathrm{S}}(\mathbf{r}) \mathrm{RPSF}_0(\mathbf{r}, F(\mathbf{r})\Delta x)}_{\text{Single scattering}} + \underbrace{\alpha_{\mathrm{M}}(\mathbf{r}) \hat{I}_M(\mathbf{r}, \Delta x)}_{\text{Multiple scattering}} + \underbrace{\alpha_{\mathrm{N}}(\mathbf{r})}_{\text{Electronic noise}} \quad , \tag{2.45}$$

where $\alpha_{\mathrm{S}}(\mathbf{r})$, $\alpha_{\mathrm{M}}(\mathbf{r})$, and $\alpha_{\mathrm{N}}(\mathbf{r})$, are the respective rates of local single scattering, multiple scattering, and noise.

The first term accounts for the single scattering contribution and assumes that, on average, aberrations reduce the effective numerical aperture. The spatial dependence of F is thus a re-scaled version of the diffraction-limited profile $\mathrm{RPSF}_0(\mathbf{r}, \Delta x)$ that would be obtained in absence of aberrations. The second term accounts for the diffusive halo of multiple scattering, modeled here as a Gaussian profile [Aubry, 2007], such that $\hat{I}_M(\mathbf{r}, \Delta x) = \exp\left[-\Delta x^2/(2\sigma_M(\mathbf{r})^2)\right]$, with σ_M its spatial extent. At last, the third term accounts for electronic noise, modeled here as a constant background. As presented in [Fig. 2.12], the free parameters $\{F, \alpha_{\mathrm{S}}, \alpha_{\mathrm{M}}, \sigma_M\}$ are then estimated through a fitting procedure of the RPSF.

The authors applied this approach to extract locally the relative part of the multiple scattering and the electronic noise in the *in vivo* case of the human calf, as shown in [Fig. 2.13B-C]. This experimental result suggests that multiple scattering that is usually discarded in ultrasound imaging is far from being negligible in *in vivo* imaging. Even more, recent studies suggest that the extraction of scattering parameters such as the diffusion constant [Aubry, 2007] can constitute a new biomarker that could be used to detect pathologies such as the lung parenchyma [Mohanty, 2017].

However, at large depths, multiple scattering and noise are difficult to discriminate since they both give rise to a flat plateau in the RPSF. In the next chapter, a new estimator based on spatial reciprocity of wave propagation, that can be observed directly on the symmetry of the $\mathbf{R}-$matrix, will be introduced to estimate the rate of multiple scattering even at large depths and applied in transcranial imaging.

4.6 Adaptive focusing

Going beyond focusing quality or multiple scattering quantification, matrix imaging even allows the extraction of local aberration laws, thus giving access to the transmission matrix $\mathbf{T}$ that connects each transducer of the probe to any focal point of the medium. From the focused reflection matrix, another matrix can be extracted numerically that emphasizes the isoplanatic

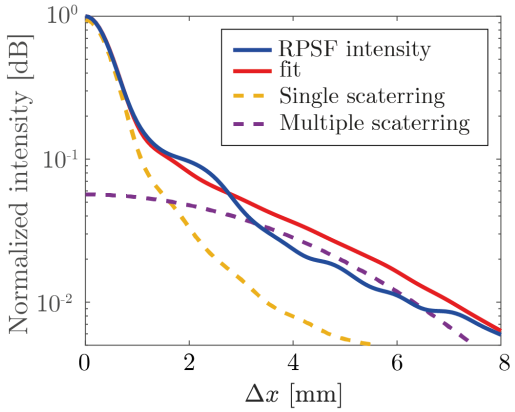

Figure 2.12: **Validation of the fitting process (Eq. 2.45) on the RPSF intensity profile.** Result of the fit at $z = 33$ mm in the low speckle regime: the fit parameters are $F = 0.96$, $\alpha_M = 5.5\%$ and $\sigma_M = 3.4$ mm. *Extracted from* [Lambert, 2022b].

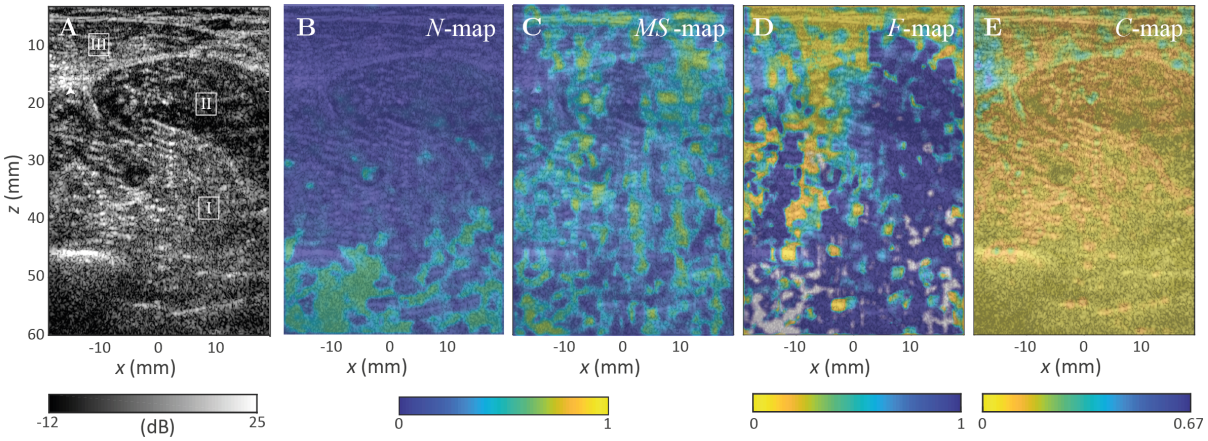

Figure 2.13: **Focusing quality and multiple scattering for *in vivo* imaging of a human calf.** Mapping of local focusing quality and multiple scattering in the calf imaging experiment. (**A**) Ultrasound image of the calf. (**B**) Noise rate $\alpha_N(\mathbf{r})$. (**C**) Multiple scattering rate $\alpha_M(\mathbf{r})$. (**D**) F-factor. (**E**) $C-$factor. In (**B**, **C**) yellow areas correspond to a weak SNR and high multiple scattering rate, respectively. In (**D**, **E**) blue and yellow areas correspond to a high and low quality of focus, respectively. In (**D**), gray areas highlights location where the estimation of the focusing criterion is not reliable because the incoherent background is too high ($\alpha_N+\alpha_M > 0.75$). *Extracted from* [Lambert, 2022b].

correlations of the focused reflection matrix, namely the **distortion matrix**. Such a matrix, which was experimentally introduced in optics during Amaury Badon's PhD [Badon, 2020], contains the aberrations of the reflected wavefront for each point in the medium and can be used to numerically correct the reflection matrix from aberrations. This procedure was successfully applied to optics [Badon, 2020; Barolle, 2021; Najar, 2023], acoustics [Lambert, 2022a], seismic imaging [Touma, 2021] and is currently investigated for radar imaging. In this section, the basics framework of the aberration correction process are presented and further applied to the human calf experiment.

4.6.1 The phase-screen model

Aberration has been modelled in the past as a phase screen in the transducers plane, $\mathrm{T}(\mathbf{u})$. However, this simple model is not sufficient to describe a medium with spatially distributed aberrations. In this section, the aberrations are modelled as a phase-screen that depends on the position and is expressed in terms of a basis $\mathbf{c}$, which is not necessarily the transducer plane, since it is nontrivial in which basis the isoplanicity is maximized [Mertz, 2015]. In other words, assuming such aberration, the Green's function of the medium can be expressed as a correction to the homogeneous model such that:

$$\mathrm{G}(\mathbf{r},\mathbf{c}) = \underbrace{\mathrm{G}_0(\mathbf{r},\mathbf{c})}_{\text{Homogeneous}} \circ \underbrace{\mathrm{T}(\mathbf{r},\mathbf{c})}_{\text{Aberrations}} , \tag{2.46}$$

where $\circ$ denotes a Hadamard product (*i.e.* an element-wise matrix product). Thus, the $\mathbf{T}-$matrix contains the spatial variations of the wavefront distortions, *i.e.* the transmission matrix of the medium that connects each transducer (when $\mathbf{c} = \mathbf{u}$) to each point in the field-of-view. The next section shows how this matrix can be estimated using the "distortion matrix framework" [Badon, 2020; Lambert, 2020c; Touma, 2021], and used to compensate the $\mathbf{R}-$matrix of aberrations.

First, we will introduce the general transmission matrix formalism, which is the holy grail of imaging as it connects each input wave-field to any point in the field-of-view.

4.6.2 The distortion matrix

Aberration compensation in the UMI framework, using the distortion matrix concept [Lambert, 2020c; Lambert, 2022a], consists in the following steps:

- projecting the focused $\mathbf{R}-$matrix either at input ($\mathbf{R_{cr}}$) or output ($\mathbf{R_{rc}}$) in a correction basis [Fig. 2.14B];
- extracting wave distortions exhibited by $\mathbf{R}$ when compared to a reference matrix that would have been obtained in an ideal homogeneous medium of wave velocity c_0 [Fig. 2.14C]. The resulting distortion matrix $\mathbf{D}$ contains the aberrations induced when focusing on any point $\mathbf{r}$, expressed in the correction basis;
- An estimation of the transmission matrix $\hat{\mathbf{T}}_{\mathrm{in/out}}$ can be made [Fig. 2.14D-E] through a time reversal analysis very similar to the one described in the fDORT method [Robert, 2005], that consists in a singular value decomposition of $\mathbf{D}$. The great difference is that every step is now performed numerically and iterated at input and output;
- A better estimation of the Green function $\hat{\mathbf{G}}_{\mathrm{in/out}}$ can be performed and be further used to correct the $\mathbf{R}-$matrix.

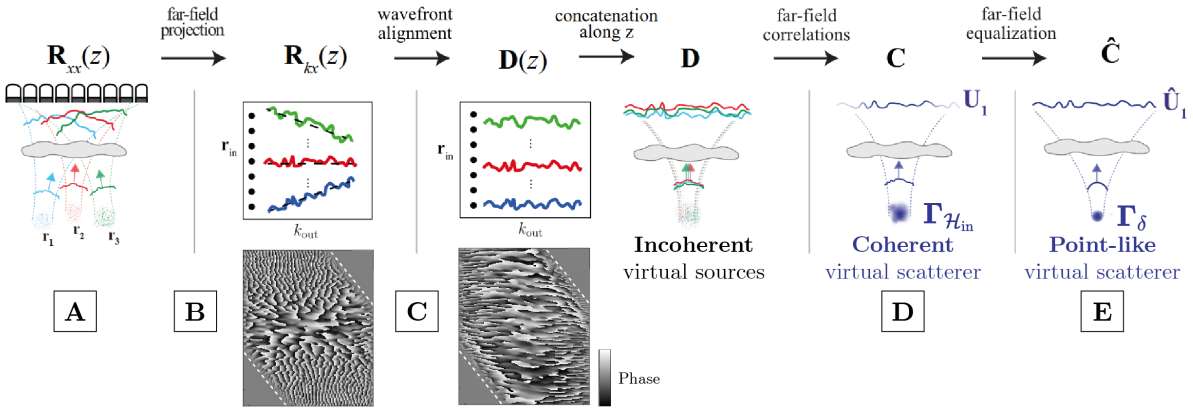

Figure 2.14: **Time-reversal analysis of the distortion matrix.** (**A**) Each input focused insonification gives rise to a tilted reflected wave front. (**B**) After far-field projection, each wave field is stored along a line of $\mathbf{R_{xk}}(z)$. (**C**) By removing the geometrical tilt (dashed black line in B) of each reflected wave front, a set of distortion matrices $\mathbf{D_{xk}}(z)$ is obtained at each depth z. These matrices are concatenated to yield a full-field distortion matrix $\mathbf{D}$ that is equivalent to a reflection matrix but with input focal spots $H_{\rm in}(x - x_{\rm in})$ virtually shifted at the same location (**D**) Its correlation matrix $\mathbf{C}$ mimics the time-reversal operator associated with a virtual specular reflector of scattering distribution $|H_{\rm in}(x)|^2$ (**E**) The normalized correlation matrix $\mathbf{C}$ makes the virtual reflector point like. Its SVD then yields the transmission matrix over each isoplanatic patch contained in the field-of-view. Ultrasound data in panel B & C show the phase of the reflection matrix and the distortion matrix at depth $z = 30$ mm. *Extracted from* [Lambert, 2020c].

4.6.3 Physical interpretation

This process of subtracting the geometric component to build the $\mathbf{D}-$matrix is equivalent to the one described in [Montaldo, 2011], which consists of de-scanning each focal spot as if it came from the same location, thus increasing the spatial correlations between each reflected wavefront. In this context, we can note that the de-scan focused reflection matrix $\mathbf{R}_{\mathcal{D}}$ defined in (Section 4.3) is not only an interesting matrix for memory optimization, but also the Fourier transform of the $\mathbf{D}$-matrix (see Appendix 5.2).

The SVD applied to the $\mathbf{D}$-matrix enables a realignment in phase (coherent combination) of each input focal spot to synthesize a virtual guide star (or coherent reflector) [Fig. 2.14D]. Mathematically, this assertion can be proved by considering the correlation matrix $\mathbf{C} = \mathbf{D} \times \mathbf{D}^\dagger$ of $\mathbf{D}$. The correlation matrix can be expressed as follows (see. Appendix 5.1):

$$\mathbf{C} \propto \mathbf{G}_{\rm out}^\dagger \times \mathbf{\Gamma}_{\mathbf{H}_{\rm in}} \times \mathbf{G}_{\rm out}, \tag{2.47}$$

where $\mathbf{\Gamma}_{\mathbf{H}_{\rm in}}$ is diagonal, and its coefficients are directly proportional to the input focal spot $|H_{\rm in}(x)|^2$. $\mathbf{\Gamma}_{\mathbf{H}_{\rm in}}$ is equivalent to a scattering matrix associated with a virtual coherent reflector whose scattering distribution corresponds to the input focal spot intensity $|H_{\rm in}(x)|^2$ and $\mathbf{C}$ is analogous to a reflection matrix associated with a single scatterer of reflectivity $|H_{\rm in}(x)|^2$ as shown in [Fig. 2.14D].

In the asymptotic case where we suppose a perfect input focal spot so that $\mathbf{H}_{\rm in}(x) = \delta(x)$,

(Eq. 2.47) becomes:

$$\mathbf{C} \propto \hat{\mathbf{T}}_{\text{out}}^{\dagger} \times \mathbf{\Gamma}_{\delta} \times \hat{\mathbf{T}}_{\text{out}}. \tag{2.48}$$

In contrast to the operator $\mathbf{\Gamma}_{\mathbf{H}_{\text{in}}}$ of (Eq. 2.47), $\mathbf{\Gamma}_{\delta}$ is a scattering matrix associated with a point-like (diffraction-limited) reflector at the origin [Fig. 2.14E]. A reflection matrix associated with such a point-like reflector is of rank 1. The phase of the first eigenvalue of the correlation matrix directly holds the aberration transmittance $\mathrm{T}_{\text{out}}(\mathbf{o}) \equiv \exp\left(j\arg\left[\mathrm{U}_{\text{out}}^{(1)}(\mathbf{o})\right]\right)$ and the propagation matrix can be updated according to (Eq. 2.46).

The correction process is thus a simple phase conjugation of the time-gated reflection matrix. It is equivalent to an application of time delays on the ultrasound data, such that $\Delta t_i = \arg(U)/(2\pi f_{\text{c}})$, with f_{c} the central frequency. Weighting the aberration compensation with the absolute value [Bendjador, 2020] of the singular vector would be hazardous as it would act as a low-pass filter on the data and thus would alter the resolution of the ultrasound image.

4.6.4 Input and Output iteration

The process described above is not restrained to the output, and can be applied similarly at the input. Iterative correction can thus be performed on both sides as described in [Fig. 2.15]. The simple case of an incorrect speed-of-sound hypothesis during beamforming is investigated in the tissue mimicking phantom. Aberrations are clearly visible on the focused reflection matrix, where the energy spreads well beyond the confocal signal $x_{\text{in}} = x_{\text{out}}$ (or $\Delta x = 0$ in a de-scan basis). A first correction is applied at the input that allows to bring back energy in the vicinity of the confocal signal. However, the diffraction-limit is not reached and the symmetry of the matrices is lost [Fig. 2.15B_2]. It is only when correcting in a second step at the output that the diffraction limit is reached and that symmetry of the matrices is ensured.

4.6.5 Bias on the transmission matrix estimator $\hat{\mathbf{T}}$

Besides, the fact that the first eigenspace of the correlation matrix directly holds the aberration transmittance relies on several strong hypotheses (see Appendix 5.1):

Assumptions for extracting the aberration law

- **Isoplanetism** is ensured such that each output focal points $\mathbf{r}$ considered for building the correlation matrix is associated to the same distorted wavefronts;
- **A sufficient number of resolution cells is considered** so that the correlation matrix of $\mathbf{D}$ converges towards its ensemble average $\mathbf{C} \to \langle \mathbf{C} \rangle$ [Varslot, 2004; Måsøy, 2005];
- A perfect **diffraction-limited focal spot** ($H_{\text{in}} = \delta$), or equivalently, a point-like virtual guide star, is considered.

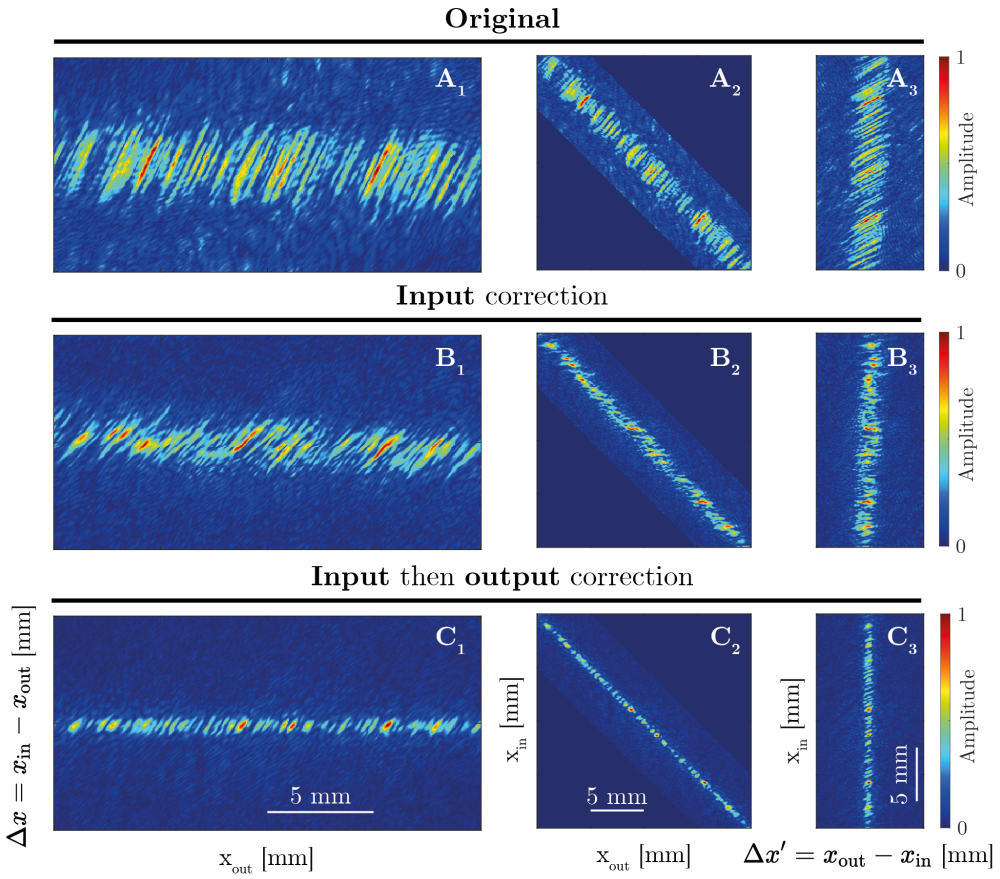

Figure 2.15: **Iteration of the correction process at the input and the output.** Results presented here are in the tissue mimicking phantom and assuming an incorrect speed-of-sound hypothesis during numerical focusing. The correction process is investigated through the distortion matrix approach. (**A**) Original reflection matrix present aberrations as energy spreads well beyond the confocal signal. (**B**) A first correction is applied only at the input. (**C**) A second correction is applied at the output. Resolution is close to the diffraction limit after the correction process.

The first two hypotheses constitute the following dilemma: On the one hand, the local spatial average window $\mathcal{W}$ should be as small as possible to grasp the rapid variations of the RPSFs across the field of view. On the other hand, the convergence of the correlation matrix is only guaranteed if the spatial window $\mathcal{W}$ is much larger than the size of the focal spot [Lambert, 2020c; Lambert, 2022a]. This condition indicates that a gradual compensation of aberrations shall be favored rather than a direct partition of the field-of-view into small boxes [Yoon, 2020]. An optimal UMI process should proceed as follows: first, compensate for input and output wave distortions at a large scale to reduce the size of the guide star; then, decrease the size of the spatial window $\mathcal{W}$ and improve the resolution of the $\mathbf{T}-$matrix estimator. In other words, an iterative correction on gradually reduced patches allows us to address higher spatial frequencies of aberrations associated with smaller isoplanatic areas. The whole process can be iterated, leading to a **multi-scale compensation of wave distortions**. A new criterion based on spatial reciprocity will be introduced in the next chapter to monitor the convergence of the

correlation matrix. In other words, spatial reciprocity will provide an objective criterion to know at what point the reduction of the patch $\mathcal{W}$ and more generally the correction process should be stopped.

The third hypothesis of a point-like virtual guide star is a strong hypothesis which is anything but true, and thus introduces a strong bias due to the blurring of the guide star because aberrations and multiple scattering also affect its quality. In practice, the finite size of the guide star limits the estimation of the aberration law to a reduced angular support when performing a singular value decomposition. In previous work, $\mathbf{\Gamma}_{\mathbf{H}_{\text{in}}}$ was made pointlike by normalizing the correlation matrix (*i.e.* taking only the phase). However, this method inherently increases the noise, especially for large wavevectors. To circumvent this issue, a new algorithm, *designed by Arthur Le Ber* and inspired both by the iterative time-reversal experiment and the CLASS algorithm [Yoon, 2020], will be presented in the next chapter.

The aberration correction process based on the distortion matrix is very similar to the method described in [Bendjador, 2020] where the main difference lies in the application of the SVD on the beamformed data for different insonifications. Although performing the SVD just before a coherent compound of beamformed images is attractive for real-time imaging, the process remains very partial as: (i) alternating aberration correction in transmit and receive modes is required in order to gradually reduce the blurring of the virtual guide star and reduce the bias made on the estimation of the aberration transmittance; (ii) performing aberration correction in different bases (plane wave, transducer, intermediate plane [Mertz, 2015]) is needed to address all kind of aberrations in the medium; (iii) preforming a multi-scale analysis is necessary to ensure at best the isoplanicity condition at each step of the process.

4.6.6 *In vivo* results

The **D**-matrix framework was successfully applied to several *in vivo* experiments using linear ultrasound probes with plane wave insonifications [Lambert, 2022a]. Here, the results are presented in the particular case of a human calf imaging experiment. The local aberration laws are shown for several spatial regions of the field-of-view. This set of aberration phase laws forms the transmission matrix of the medium [Fig. 2.16]. This wealth of information is further used to produce images with a far better contrast, as shown in [Fig. 2.17B-C]. In addition, resolution is greatly enhanced when comparing the focusing criterion before and after the correction process [Fig. 2.17A, D].

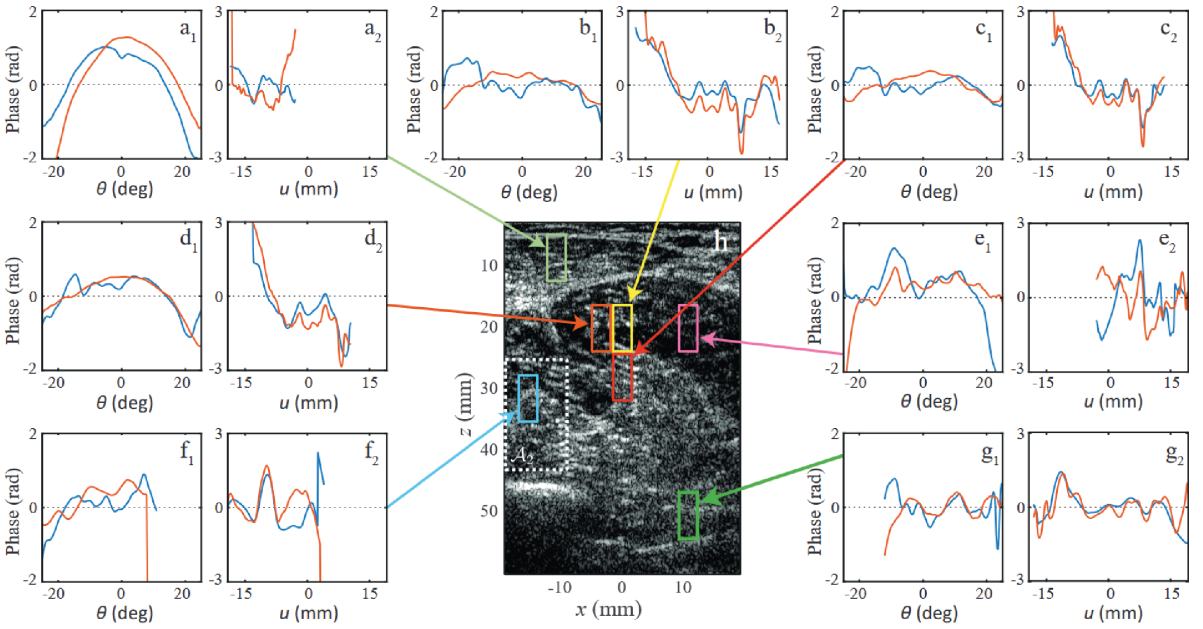

Figure 2.16: **Estimation of $\hat{\mathbf{T}}$ in the *in vivo* case of a human calf.** (**A-G**) Aberrations phase laws associated to several areas displayed in the (**H**) confocal image. Subscript "1" and "2" stands for plane-wave and transducer basis, respectively. The blue and red curve stands for input and output, respectively. *Extracted from* [Lambert, 2020a].

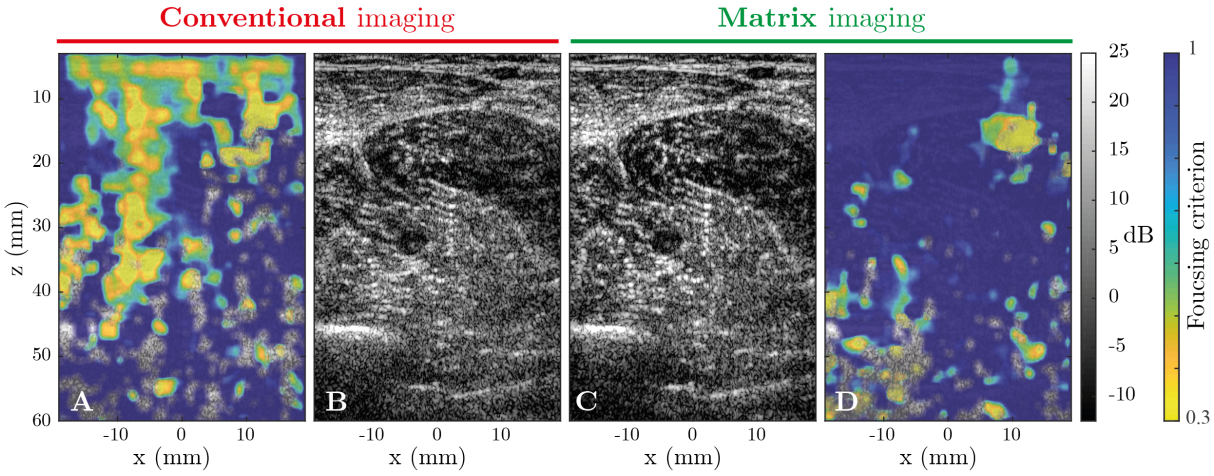

Figure 2.17: **Results of the aberration correction process applied to the *in vivo* case of the human calf.** (**A**) Focusing criterion superimposed to the corresponding conventional ultrasound image. (**B**) Conventional multi-focus image. (**C**) Corrected multi-focus image after the matrix imaging process. (**D**) Focusing criterion superimposed to the corrected image. The ultrasound images have been normalized by their mean intensity. *Extracted from* [Lambert, 2020a].

5 Summary

Key concepts in Matrix Imaging

Non-invasive Ultrasound Matrix Imaging (UMI) could be sum up [Fig. 2.18] to these two following key concepts:

- Information about a static, linear medium is acquired in a reflection matrix that records the impulse responses between each emitter and each receiver of a given multi-element technology:

$$\mathbf{R_{io}}(t) \Leftrightarrow \mathbf{R_{io}}(\omega), \tag{2.49}$$

  where **i** and **o** account for emission and reception bases.

- While decoupling input and output, the **R**−matrix is then projected onto various suitable bases to extract local quantitative parameters that characterize the medium, as described in [Table 2.3].

In particular, projecting the **R**−matrix in a focused basis allow to locally probe the focusing quality, the multiple scattering rate or even allow performing speed-of-sound measurements. The projection of the **R**−matrix in a dual basis can be investigated to extract local distortions of the reflected wavefronts and thus estimate the transmission matrix **T** linking any element of the probe to any point of the medium. Numerical adaptive focusing can thus be performed to reach contrast-enhanced images with close to diffraction limit resolution.

	Symbol	**Adapted for**
Acquisition	$\mathbf{R_{io}}(t) = [R(\mathbf{i}_{\text{in}}, \mathbf{o}_{\text{out}}, t)]$	Data recording
Focused basis	$\mathbf{R_{xx}}(z)$	Focusing quality and multiple scattering quantification [Lambert, 2022b]
Far-field basis	$\mathbf{R_{kk}}(z)$	Specular/speckle discrimination [Lambert, 2020c] and global aberration correction [Yoon, 2020]
Dual basis	$\mathbf{R_{cr}}/\mathbf{D_{cr}}$ and $\mathbf{R_{rc}}/\mathbf{D_{rc}}$	$\hat{\mathbf{T}}$−matrix and local adaptive correction [Lambert, 2022a]

Table 2.3: **Different bases for the R−matrix.**

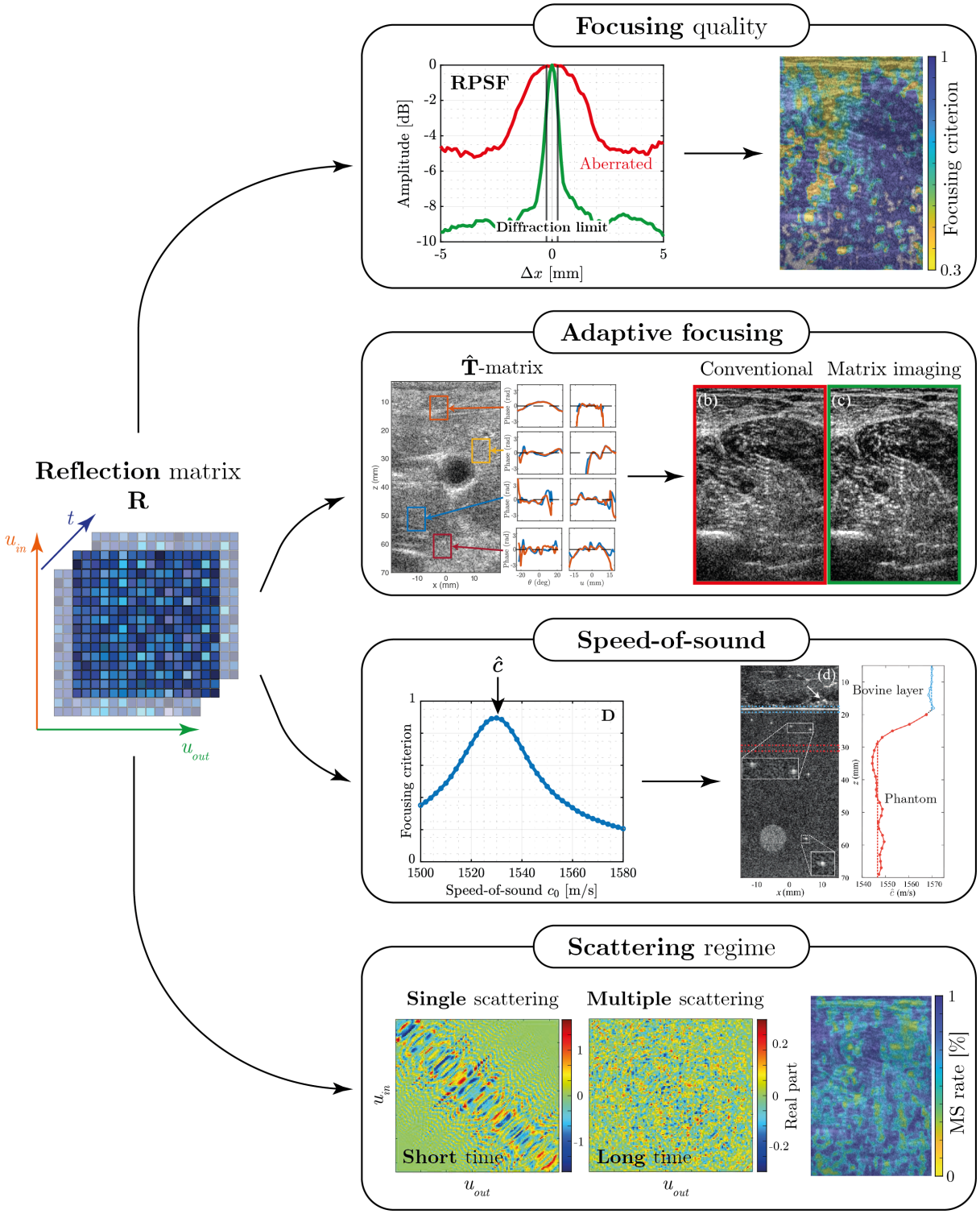

Figure 2.18: **A summary of Ultrasound Matrix Imaging framework & its applications.** *Adapted from* [Lambert, 2022b; Lambert, 2020c; Lambert, 2020b; Lambert, 2022a; Aubry, 2008a].

6 Conclusion

The general formalism of matrix imaging has been successfully applied to 2D ultrasound imaging. Pioneering work led to its establishment with academic experiments that incorporated mathematical insights into physical experiments. More recently, it has been successfully applied to local characterization of an unknown medium, allowing extraction of the transmission matrix connecting any transducer to any point in the medium, even in the ultrasound speckle, resulting in contrast-enhanced and near diffraction-limited ultrasound images.

With this in mind, the main objective of the following work is to explore all degrees of freedom of ultrasound wave propagation by recording the reflection matrix.

To this end, UMI is extended to 3D imaging in Chapter 3, using a matrix array of transducers that provide a much larger number of spatial degrees of freedom than conventional probes. In parallel, new elements are introduced to make the correction process more robust. An iterative algorithm that outperforms SVD and a spatial reciprocity-based criterion for monitoring the spatial convergence of this new method are presented. In addition, the difficult case of trans-cranial imaging, where not only a high level of aberration but also a large attenuation due to absorption, multiple scattering and reverberation in the cranial layer occurs, is addressed. Finally, we demonstrate how UMI can be easily combined with ultra-fast imaging, and show its relevance in the specific case of Ultrasound Localization Microscopy using an *in vivo* experiment on trans-cranial imaging in sheep subjects.

Another way to increase the number of degrees of freedom lies in the way the focused reflection matrix is constructed. So far, only the responses between emitted and received focal spots located at the same depth, *i.e.* only transverse responses, have been studied. In Chapter 4, we propose to scan the responses axially in both depth and time to build a generalized spatio-temporal focused reflection matrix. This matrix will be leveraged for specific target characterization such as bubbles by probing their spectral ultrasonic response.

Although the concept of the distortion matrix allows a full compensation of transverse aberrations, it does not provide an ideal image of the medium reflectivity. Indeed, the position of each scatterer remains uncertain, since it depends on the speed-of-sound hypothesis made during beamforming. In Chapter 5, we will show how the focused $\mathbf{R}$-matrix allows us to estimate the local axial defocus for each point, resulting from the error between the true and the assumed speed-of-sound. In addition, spatial variations in the speed-of-sound can be studied for any point in the medium, resulting in images with a much higher accuracy of distances (see Chapter 6).

Chapter 3

From 2D to 3D matrix imaging

Objectives

Switching from 2D to 3D imaging drastically increases the number of available **spatial degrees of freedom**. This not only leads to a strong enhancement of contrast and resolution in the elevation plane, but also allows a better control of wavefronts and thus a finer correction of aberrations. We will first extend our matrix approach to 3D imaging in a controlled phantom experiment before turning to the difficult case of **transcranial imaging**.

Contents

1 Introduction

Thanks to the increasing capacity of data storage devices and computers, 3D imaging has become an active research topic as it allows scanning a volume instead of a plane and therefore holds much more information than conventional *B-mode* imaging with a 1D array of transducers, that restricts the control of the ultrasonic wave-field over two-dimensions (one-dimensional space and time). First, 3D imaging enables a volumetric visualization of tissues, which is particularly suitable for ultrasound imaging modes such as Doppler or elastography. Blood flow can be tracked with a much higher accuracy and propagation of shear-waves can be detected not only in the transverse direction, but in all spatial directions. This feature is important to study the shear anisotropy of the medium. In addition, 3D imaging is less operator-dependent because it does not depend on the angular position of the probe.

Besides, although it gave rise to striking results in optical microscopy [Kang, 2017; Badon, 2020; Yoon, 2020; Kwon, 2023; Najar, 2023] or seismic imaging [Blondel, 2018; Touma, 2021], the experimental demonstration of matrix imaging has been, so far, limited with ultrasonic waves [Lambert, 2020c; Bendjador, 2020; Sommer, 2021; Lambert, 2022a]. Indeed, the first proof-of-concept experiments employed a linear array of transducers. Yet, aberrations in the human body are 3D-distributed and a 1D control of the wave-field is not sufficient for a fine compensation of wave-distortions.

In this chapter, we first **extend Ultrasound Matrix Imaging (UMI) to 3D imaging** using a fully populated matrix array of transducers [Ratsimandresey, 2002; Provost, 2014; Provost, 2015]. The overall method is validated by means of a well-controlled experiment of a tissue-mimicking phantom, first without aberrations and then by combining *ex vivo* porcine tissues as an aberrating layer on top. Thanks to its great **number of spatial degrees of freedom**, 3D imaging provides a higher density of independent speckle grains, which controls the spatial resolution of the transmission matrix estimator $\hat{\mathbf{T}}$ [Lambert, 2022a] that connects each transducer to each voxel of the field-of-view. A **more local correction** can thus be reached, compared to 2D imaging

In these experiments, we will also introduce new elements that make our correction framework more robust. Inspired by the CLASS method developed in optical microscopy [Kang, 2017; Yoon, 2020], aberrations will be compensated by a novel **iterative phase reversal (IPR)** algorithm that is more efficient than a singular value decomposition (SVD) [Robert, 2008a; Lambert, 2020c; Bendjador, 2020]. Unlike previous work, the convergence of this algorithm is ensured by examining the **spatial reciprocity between input and output**. This new criterion acts as a guide star to ensure that the spatial averaging is sufficient to converge properly towards the transmission matrix $\mathbf{T}$, and thus indicates at what point we should stop the correction process.

Then, we will address the difficult case of **transcranial imaging** on a controlled head phantom whose skull induces a strong attenuation, aberration, and multiple scattering of the ultrasonic wave-field, phenomena that UMI can quantify independently of each other [Lambert, 2020b; Lambert, 2022b].

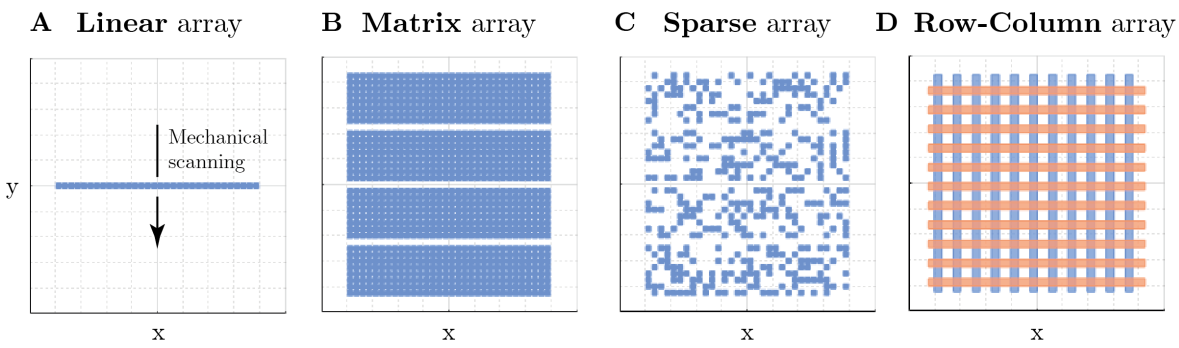

Figure 3.1: **Schematic views of various methods for 3D ultrasound imaging.** (**A**) Linear array, (**B**) matrix array, (**C**) sparse array and (**D**) Row-Column Array (RCA).

2 3D ultrasound imaging

Volumetric images were first obtained by **mechanically scanning** the elevation plane (y-plane) of 1D arrays (linear, phase or curve) [Huang, 2017] either by translation [Dabrowski, 2001; Guo, 1996] as described in [Fig. 3.1A], rotation [Tong, 1996; Downey, 1996] or a tilt [Gilja, 1995; Delabays, 1995]. However, wave propagation is still recorded in a plane (*i.e.* projected along the y-axis) and therefore does not provide as much information as a 3D control of the wave-field, whether it be physically or in post-processing. Hence, great efforts were made to improve the flexibility of aperture and focusing in the elevation dimension by 1.25, 1.5 and 1.75D arrays [Wildes, 1997; Fernandez, 2003] before 2D matrix arrays could be fabricated.

Using a **fully populated matrix array** of transducers [Fig. 3.1B] [Ratsimandresey, 2002; Savord, 2003] is theoretically the easiest way to take advantage of wave propagation in all directions of space. When combined with Matrix Imaging, their huge amount of data is a real gold-rush for wavefront shaping. However, real-time imaging and post-processing still remain major challenges and are highly dependent on current advances in central and graphics processors (CPU & GPU). In addition, this means difficult manufacture of the many electronic wires that must be connected independently to each transducer, as well as complex hardware design to drive the transducers of the probe simultaneously.

The use of sparse arrays [Fig. 3.1C] [Roux, 2018; Roux, 2016; Davidsen, 1993; Diarra, 2013; Austeng, 2002] can be a solution for less cumbersome electronics, but comes at the price of a reduced active surface area (*i.e.* lower sensitivity) and also induces side-lobes. Another approach to reduce the number of channels is to use *micro-beamforming* [Blaak, 2009; Lok, 2018] to partially *beamform* the ultrasound data before recording. However, this solution intrinsically degrades the accuracy of the focusing process. Recently, much focus has been placed on Row-Column-Array probes (RCA) [Flesch, 2017] to drastically reduce the number of channels by using complete rows of transducers in emission and columns in reception, and inversely [Fig. 3.1D]. This reduces the number of channels from N^2 to $2N$ but at the cost of a degraded PSF compared to a matrix array of transducers.

In this chapter, we intend to take full advantage of the benefits of 3D imaging, which lie in its high spatial degrees of freedom (*i.e.* the number of input and output channels). Hence, we

will use a fully populated matrix array of transducers [Ratsimandresey, 2002], referred to as $\mathcal{P}_1$, manufactured by Vermon and whose characteristics are described in [Table 3.1] and [Fig. 3.2]. It is important to note that the probe is divided into 4 blocks of 256 elements, with 3 deadlines between each block [Fig. 3.2C]. This provides a slightly larger aperture, but also side-lobes in that direction.

The electronic hardware used to drive the probe was developed by Supersonic Imagine (member of Hologic group) in the context of collaboration agreement with the Institut Langevin. It allows it to emit with all elements (1024 transducers) and record with half of the probe (512 transducers). Two insonifications are then required to record a complete acquisition over all received channels of the probe. Commercial electronic hardware for controlling matrix array probes such as Vantage Research Ultrasound Systems (Verasonics) is based on multiplexed electronics [Hara, 2005] that use only a maximum of 256 transducers simultaneously. This implies to recombine synthetic apertures to emulate an insonification that would use all the elements of the probe. This means both a lower SNR and a lower frame-rate than our system, which would correspond to a synchronized combination of 4 commercial Verasonics systems at the same time.

Number of transducers		$N_u = 32 \times 32 = 1024$ (with 6 dead elements)
Geometry (y-axis)		3 inactive rows between each block of 256 elements
Transducer	Pitch	$\delta u = 0.5$ mm ($\approx \lambda$ at $c = 1540$ m/s)
	Kerf	50 μm
	Width	0.4 mm
Aperture (active surface)		$\mathbf{\Delta u} = \begin{pmatrix} \Delta u_x \\ \Delta u_y \end{pmatrix} = \begin{pmatrix} 16.3 \text{ mm} \\ 17.8 \text{ mm} \end{pmatrix}$
Central frequency		$f_c = 3$ MHz
Bandwidth (at -6dB)		$80\% \rightarrow \Delta f = [1.8 - 4.2]$ MHz
Transducer directivity		$\theta_{max} = \pm 31°$ at $c = 1540$ m/s
Acoustic lens		None
Impedance matching layer		0.3 mm of silicone
Maximum voltage $\begin{pmatrix} + \\ - \end{pmatrix}$ [Volts]		$V_{\max} = \begin{pmatrix} 50 \\ 140 \end{pmatrix}$ Volts

Table 3.1: **Matrix array datasheet** $\mathcal{P}_1$.

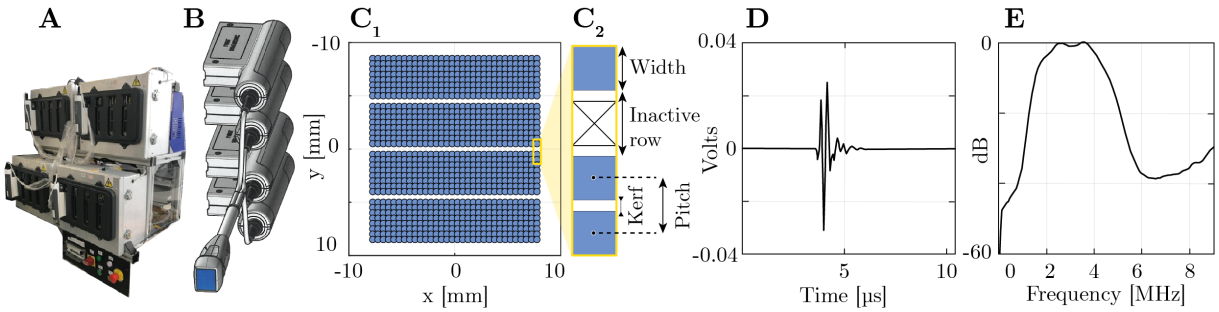

Figure 3.2: **Probe characteristics ($\mathcal{P}_1$). (A)** Electronic hardware used to drive the **(B)** 2D matrix probe. **(C)** Position of transducers separated in 4 blocks of 256 elements regularly spaced by 0.5 mm. **(D)** Average impulse response and corresponding **(E)** spectrum provided by the manufacturer (Vermon).

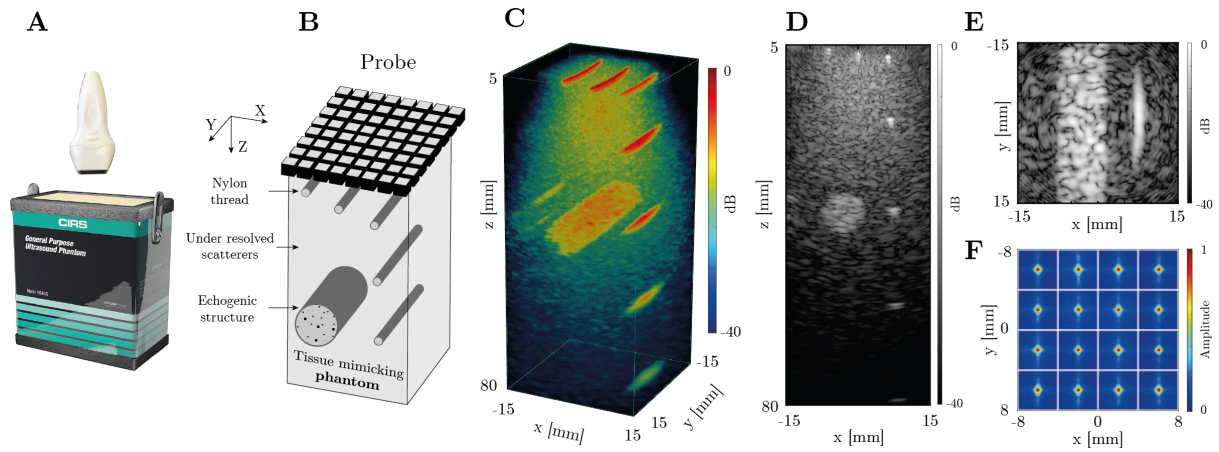

Figure 3.3: **Matrix imaging of a tissue mimicking phantom. (A, B)** Schematic of the experiment. **(C)** Maximum Intensity Projection (MIP) of the confocal volume. **(D, E)** Axial and transverse cross-section, respectively. **(F)** Local RPSFs in the speckle.

3 Phantom experiment without aberrations

Before tackling more imaging complex media, matrix imaging framework is first extended to 3D imaging of a controlled tissue mimicking phantom (CIRS, Model 054GS) presenting no aberrations. The probe ($\mathcal{P}_1$) is directly placed in contact with the phantom and impedance matching is done with water [Fig. 3.3 A, B]. The phantom (speed of sound: $c_p = 1540$ m/s) is composed of random distribution of unresolved scatterers which generate ultrasonic speckle characteristic of human tissues. The system also contains nylon filaments placed at regular intervals, with a point-like cross-section, and, at a depth of 40 mm, a 10 mm-diameter hyperechoic cylinder, containing a higher density of unresolved scatterers.

3.1 Reflection matrix acquisition

3D Ultrasound Matrix Imaging (UMI) starts with the acquisition of the reflection matrix (or $\mathbf{R}-$matrix) using the matrix array of transducers $\mathcal{P}_1$. Depending on the experiment performed, different insonification bases can be used.

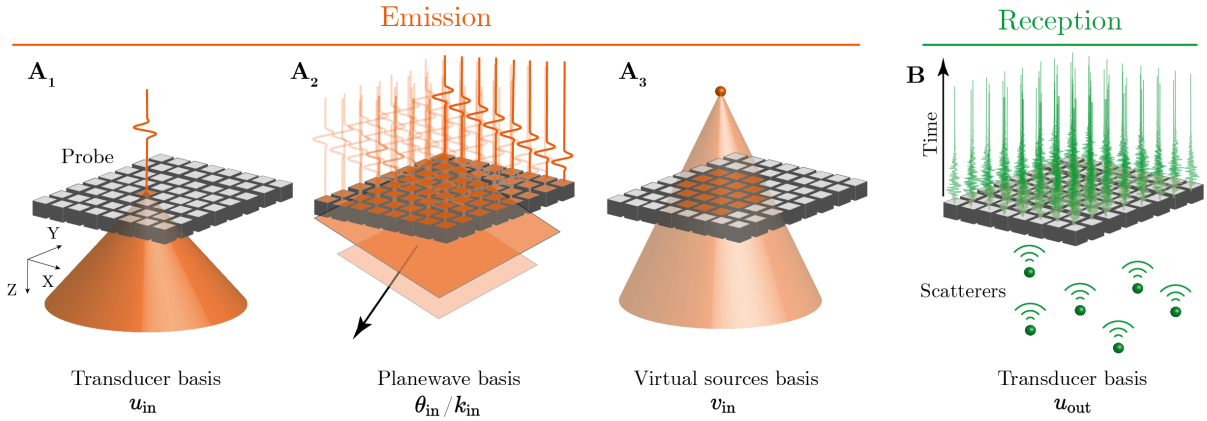

Figure 3.4: **Reflection matrix acquisition.** (**A**) The **R**-matrix can be acquired in the ($\mathbf{A}_1$) transducer, ($\mathbf{A}_2$) plane-wave or ($\mathbf{A}_3$) virtual sources basis in transmit and (**B**) recording the back-scattered wave-field on each transducer in the receive mode.

3.1.1 Canonical/Transducer basis

The **R**-matrix can be acquired in the transducer basis using successive single transducer emissions ($\mathbf{u}_{\text{in}}$) [Fig. 3.4A_1], *i.e.* by acquiring the impulse responses between each transducer of the probe ($\mathbf{u}_{\text{in}} \rightarrow \mathbf{u}_{\text{out}}$). This set of wave-fields forms a reflection matrix acquired in the canonical basis, $\mathbf{R}_{\mathbf{uu}}(t) \equiv [R(\mathbf{u}_{\text{in}}, \mathbf{u}_{\text{out}}, t)]$. Although this matrix contains all the information accessible in an epi-detection configuration (*i.e.* in reflection) without making assumptions about the static medium, it suffers from a poor Signal-to-Noise Ratio (SNR) because it involves only one transducer for each emission.

3.1.2 Plane wave basis

To improve the signal-to-noise ratio, the **R**-matrix can be acquired using a set of plane waves [Montaldo, 2009] [Fig. 3.4A_2]. For each plane wave of angles of incidence $\boldsymbol{\theta}_{\text{in}} = (\theta^{\text{in}}_{(x)}, \theta^{\text{in}}_{(y)})$, the time-dependent reflected wave field is recorded by each transducer $\mathbf{u}_{\text{out}}$. This set of wave-fields forms a reflection matrix acquired in the plane wave basis, $\mathbf{R}_{\boldsymbol{\theta}\mathbf{u}}(t) = [R(\boldsymbol{\theta}_{\text{in}}, \mathbf{u}_{\text{out}}, t)]$. Since the transducer and plane wave bases are related by a simple Fourier transform at the central frequency

$$R(\mathbf{k}_{\text{in}}, \mathbf{u}_{\text{out}}, t) = \sum_{\mathbf{u}_{\text{in}}} R(\mathbf{u}_{\text{in}}, \mathbf{u}_{\text{out}}, t) \exp(j\mathbf{u}_{\text{in}}.\mathbf{k}_{\text{in}}), \tag{3.1}$$

the array pitch δu and probe dimension $\boldsymbol{\Delta u}$ dictates the sampling of the **k**-space as follows:

$$\text{Aperture: } \Delta k = \frac{2\pi}{\delta u}, \tag{3.2}$$

$$\text{Pitch: } \delta k = \frac{2\pi}{\max([\Delta u_x; \Delta u_y]} = \frac{2\pi}{\Delta u_y}, \tag{3.3}$$

and each wavevector **k** can finally be associated with a single plane wave as follows:

$$k_{(x/y)} = \frac{2\pi}{\lambda_c} \sin(\theta_{(x/y)}), \tag{3.4}$$

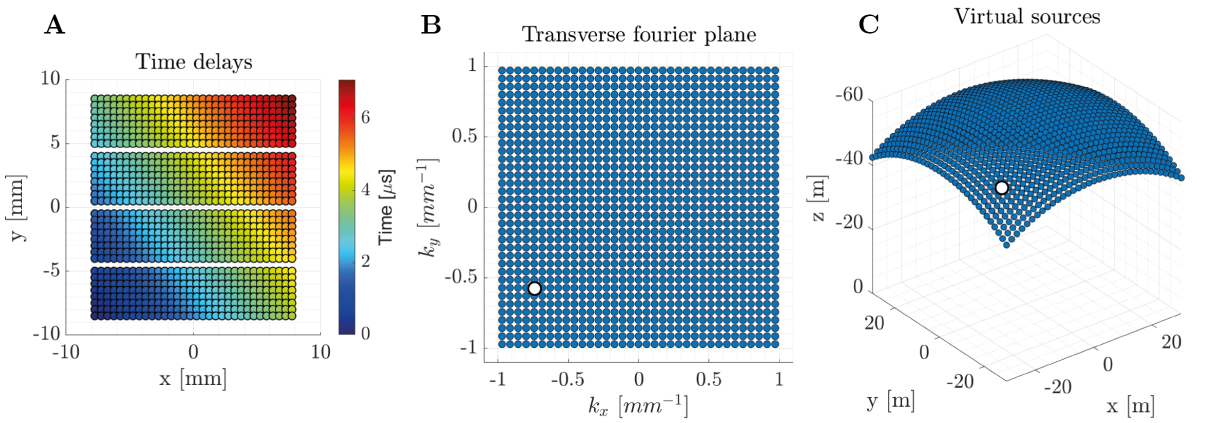

Figure 3.5: **Plane wave insonification. (A)** A plane wave is generated by applying appropriate time-delays upon each transducer of the probe. **(B)** Plane wave basis represented in the Fourier space. The white spot corresponds to the plane wave generated in pannel **(A)**. **(C)** Placing virtual sources far away from the probe (here on a radius of 60 m) is equivalent to generate plane waves.

with $\lambda_c = c_0/f_c$ the central wavelength. A set of 1225 plane waves [Fig. 3.5B] are thus generated by applying appropriate time delays $\tau(\boldsymbol{\theta}_{\text{in}}, \mathbf{u}_{\text{in}})$ to each transducer $\mathbf{u}_{\text{in}} = (u_x, u_y)$ of the probe [Fig. 3.5A]:

$$\tau(\boldsymbol{\theta}_{\text{in}}, \mathbf{u}_{\text{in}}) = [u_x \sin\theta_x + u_y \sin\theta_y]/c_0. \tag{3.5}$$

3.1.3 Virtual sources basis

Another insonification basis, that provides a higher field-of-view compared to plane waves, consists in insonifying the medium with diverging waves associated with **virtual sources** located above the probe [Provost, 2014] [Fig. 3.4A$_3$] such that:

$$\mathbf{v} = \begin{pmatrix} v_x \\ v_y \\ v_z \end{pmatrix} = -\frac{\mathcal{R}}{k_c} \begin{pmatrix} k_x \\ k_y \\ \sqrt{k_c^2 - k_x^2 - k_y^2} \end{pmatrix}, \tag{3.6}$$

with $\mathcal{R}$ the curvature radius of the virtual sources and $k_c = \frac{2\pi}{\lambda_c}$ the wave-number at the central frequency. This set of wave-fields forms a reflection matrix acquired in a virtual sources' basis, $\mathbf{R_{vu}}(t) \equiv [R(\mathbf{v}_{\text{in}}, \mathbf{u}_{\text{out}}, t)]$. A set of 1225 diverging waves are thus generated by applying appropriate time delays $\tau(\mathbf{v}_{\text{in}}, \mathbf{u}_{\text{in}})$ to each transducer $\mathbf{u}_{\text{in}} = (u_x, u_y)$ of the probe:

$$\tau(\mathbf{v}_{\text{in}}, \mathbf{u}_{\text{in}}) = \frac{|\mathbf{v}_{\text{in}} - \mathbf{u}_{\text{in}}| - \min_{\mathbf{u}_{\text{in}}}[|\mathbf{v}_{\text{in}} - \mathbf{u}_{\text{in}}|]}{c_0}. \tag{3.7}$$

A virtual source spreads over multiple couples $(k_x,\ k_y)$ in the $\mathbf{k}-$space except when $\mathcal{R}$ is large enough to be associated with a single plane wave [Fig. 3.5C].

3.2 The focused reflection matrix

Whatever the insonification sequence, the reflectivity of a medium at a given point $\mathbf{r}$ can be estimated in post-processing by a coherent compound of incident waves delayed to virtually focus on this point, and coherently summing the echoes recorded by the probe coming from that same point [Fig. 3.6A]. UMI basically consists in decoupling the input ($\mathbf{r}_{\text{in}}$) and output ($\mathbf{r}_{\text{out}}$) focusing points [Fig. 3.6B] as follows:

$$\underbrace{\left[\begin{array}{c}\mathbf{r}_{\text{in}}=\begin{pmatrix}x_{\text{in}}\\y_{\text{in}}\\z_{\text{in}}\end{pmatrix}=\begin{pmatrix}\boldsymbol{\rho}_{\text{in}}\\z_{\text{in}}\end{pmatrix}\\ \mathbf{r}_{\text{out}}=\begin{pmatrix}x_{\text{out}}\\y_{\text{out}}\\z_{\text{out}}\end{pmatrix}=\begin{pmatrix}\boldsymbol{\rho}_{\text{out}}\\z_{\text{out}}\end{pmatrix}\end{array}\right]}_{\text{Focused basis } R}\leftrightarrow\underbrace{\left[\begin{array}{c}\mathbf{r}=\begin{pmatrix}x\\y\\z\end{pmatrix}=\begin{pmatrix}\boldsymbol{\rho}\\z\end{pmatrix}\\ \mathbf{r}+\boldsymbol{\Delta\rho}=\begin{pmatrix}x+\Delta x\\y+\Delta y\\z\end{pmatrix}=\begin{pmatrix}\boldsymbol{\rho}+\boldsymbol{\Delta\rho}\\z\end{pmatrix}\end{array}\right]}_{\text{De-scan basis } R_{\mathcal{D}}} \tag{3.8}$$

with $\mathbf{r}$ a focal point designated by its Cartesian coordinates, $\boldsymbol{\rho}=(x,y)$ its transverse coordinates and $\boldsymbol{\Delta\rho}=\boldsymbol{\rho}_{\text{out}}-\boldsymbol{\rho}_{\text{in}}$ the distance between the input and output focusing points. Subscripts "in" and "out" denotes the input and output propagation, respectively.

By applying appropriate time delays to the transmission ($\mathbf{u}_{\text{in}}/\boldsymbol{\theta}_{\text{in}}/\mathbf{v}_{\text{in}}$) and reception ($\mathbf{u}_{\text{out}}$) channels, $\mathbf{R_{uu}}(t)$, $\mathbf{R_{\theta u}}(t)$ and $\mathbf{R_{vu}}(t)$ can be projected at each depth z in a focused basis, thereby forming a broadband focused reflection matrix:

$$\mathbf{R_{rr}}(z)\equiv[R(\underbrace{\{x_{\text{in}},y_{\text{in}}\}}_{\boldsymbol{\rho}_{\text{in}}},\underbrace{\{x_{\text{out}},y_{\text{out}}\}}_{\boldsymbol{\rho}_{\text{out}}},z)]. \tag{3.9}$$

The focused $\mathbf{R}-$matrix is built in the time domain via a conventional delay-and-sum beamforming scheme that consists in applying appropriate time-delays in order to focus at different points at input ($\mathbf{r}_{\text{in}}$) and output ($\mathbf{r}_{\text{out}}$):

$$R(\boldsymbol{\rho}_{\text{in}},\boldsymbol{\rho}_{\text{out}},z)=\sum_{\mathbf{i}_{\text{in}}}\sum_{\mathbf{u}_{\text{out}}}\underbrace{A(\{\mathbf{i}_{\text{in}},\mathbf{r}_{\text{in}}\},\{\mathbf{u}_{\text{out}},\mathbf{r}_{\text{out}}\})}_{\text{synthetic aperture}}R\left(\mathbf{i}_{\text{in}},\mathbf{u}_{\text{out}},\tau(\mathbf{i}_{\text{in}},\mathbf{r}_{\text{in}})+\tau(\mathbf{u}_{\text{out}},\mathbf{r}_{\text{out}})\right), \tag{3.10}$$

where $\mathbf{i}=\mathbf{u}$, $\boldsymbol{\theta}$ or $\mathbf{v}$ accounts for the insonification basis. A is an apodization factor that limits the extent of the synthetic aperture at emission and reception. This synthetic aperture is dictated by the transducers' directivity $\theta_{\max}\sim 30°$ [Perrot, 2021]. In the different insonification bases, the time delays write:

$$\text{Transducer basis: } \tau(\mathbf{u},\mathbf{r})=\frac{|\mathbf{u}-\mathbf{r}|}{c_0}=\frac{\sqrt{(x-u_x)^2+(y-u_y)^2+z^2}}{c_0}, \tag{3.11}$$

$$\text{Plane wave basis: } \tau(\boldsymbol{\theta},\mathbf{r})=\left(x\sin\theta_x+y\sin\theta_y+z\sqrt{1-\sin^2\theta_x-\sin^2\theta_y}\right)/c_0, \tag{3.12}$$

$$\text{Virtual source basis: } \tau(\mathbf{v},\mathbf{r})=\frac{|\mathbf{v}-\mathbf{r}|}{c_0}=\frac{\sqrt{(x-v_x)^2+(y-v_y)^2+(z-v_z)^2}}{c_0}, \tag{3.13}$$

with $c_0 = 1540$ m/s the speed-of-sound hypothesis corresponding to the tissue mimicking phantom. An additional time $\Delta\tau_{\text{origin}}(\mathbf{i}_{\text{in}})$ must be considered in (Eq. 3.10) when plane-waves or virtual sources are involved, in order to set the same time origin for each insonification, so that a coherent compounding can be achieved.

The novelty compared to previous work is that now, instead of just scanning focal points on a 1D line (X), 3D imaging enables to reach the responses between virtual emitters & receivers along a plane (XY). Since the focal plane is bi-dimensional, each matrix $\mathbf{R}_{\boldsymbol{\rho\rho}}(z)$ has a four-dimension structure: $R(\{x_{\text{in}}, y_{\text{in}}\}, \{x_{\text{out}}, y_{\text{out}}\}, z)$. $\mathbf{R}_{\boldsymbol{\rho\rho}}(z)$ is thus concatenated in 2D as a set of block matrices to be represented graphically [Fig. 3.6E]. In such a representation, every sub-matrix of $\mathbf{R}$ corresponds to the reflection matrix between lines of virtual transducers located at y_{in} and y_{out}, whereas every element in the given sub-matrix corresponds to a specific couple $(x_{\text{in}}, x_{\text{out}})$ [Fig. 3.6C]. Each coefficient $R(x_{\text{in}}, y_{\text{in}}, x_{\text{out}}, y_{\text{out}}, z)$ corresponds to the complex amplitude of the echoes coming from the point $\mathbf{r}_{\text{out}} = (x_{\text{out}}, y_{\text{out}}, z)$ in the focal plane when focusing at the point $\mathbf{r}_{\text{in}} = (x_{\text{in}}, y_{\text{in}}, z)$ (or conversely, since $\mathbf{R}_{\boldsymbol{\rho\rho}}(z)$ is a symmetric matrix due to spatial reciprocity).

Computational note

As 3D imaging induces a huge amount of data, dealing with the complete focused reflection matrix becomes drastically time-consuming. As a consequence, instead of storing the responses between all the couples $[R(\boldsymbol{\rho}_{\text{in}}, \boldsymbol{\rho}_{\text{out}}, z)]$, we prefer to store it in a de-scan basis $[R_{\mathcal{D}}(\boldsymbol{\Delta\rho}, \boldsymbol{\rho}, z)]$ as described in the (equation 3.8). This explains why the edges of $[\mathbf{R}_{\mathbf{xx}}(z)]$ are not examined in [Fig. 3.6C]. Since the focused reflection matrix is a sparse matrix, the useful information is close to the confocal signal. We only need to scan far enough away from the confocal signal to probe potential aberrations.

This basis was introduced during the Ph.D. of William Lambert [Lambert, 2020a] *with linear arrays (2D imaging) and becomes necessary for 3D imaging.*

3.2.1 Confocal imaging

As already shown with 2D UMI, each pixel of the main diagonal of $\mathbf{R}_{\boldsymbol{\rho\rho}}(z)$ [Fig. 3.6E] provides the transverse cross-sections of the confocal ultrasound image:

$$\mathcal{I}(\boldsymbol{\rho}, z) = |R(\boldsymbol{\rho}_{\text{in}} = \boldsymbol{\rho}_{\text{out}}, z)|^2 = |R_{\mathcal{D}}(\boldsymbol{\Delta\rho} = 0, \boldsymbol{\rho}, z)|^2, \tag{3.14}$$

with $\mathbf{r}_c = (\boldsymbol{\rho}, z)$ the confocal point. [Fig. 3.3C] shows the 3D confocal volume of the tissue mimicking phantom using Maximum Intensity Projection (MIP). Examples of B-scan (XZ) and C-scan (XY) are also displayed [Fig. 3.3D,E]. Interestingly, nylon thread is detected only under the probe, whereas ultrasound speckle can be detected over a larger field-of-view [Fig. 3.3E]. This highlights the difference between specular and under-resolved scatterers. Specular reflection is induced by objects whose shape is much larger than the wavelength (*e.g.* nylon thread). For a given incident plane wave, the reflected echo takes place in a single direction, whose orientation is dictated by the Snell-Descartes law. If the specular reflector is off-axis, only a small part of

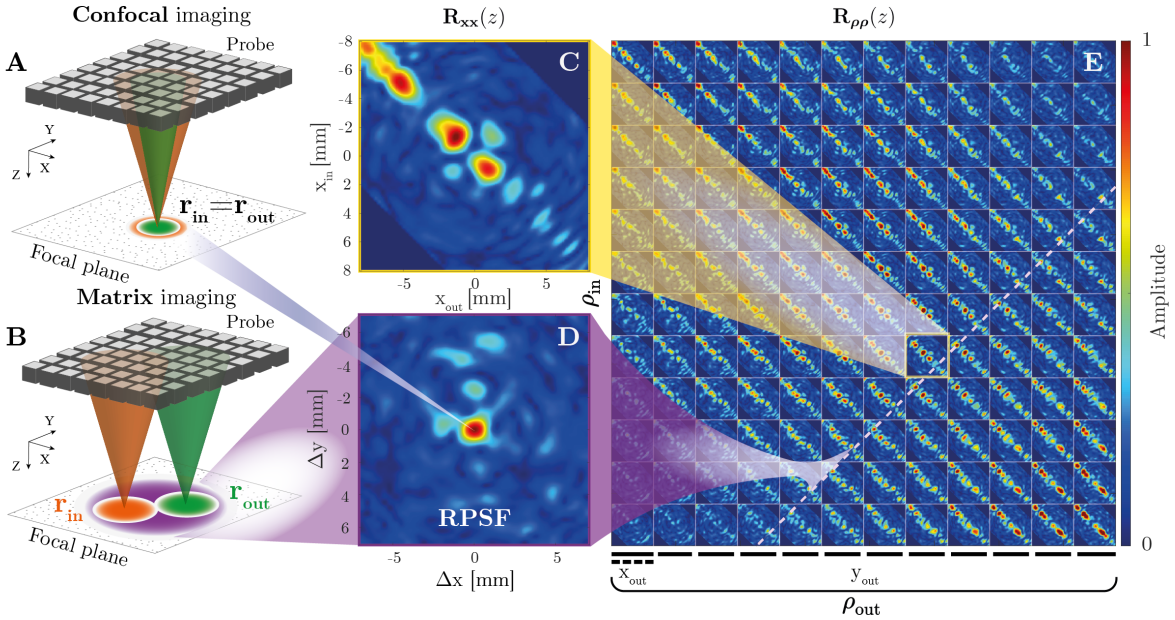

Figure 3.6: **3D Ultrasound Matrix Imaging (UMI).** (**A**) Confocal imaging consists in a simultaneous focusing of waves at input and output. (**B**) In UMI, the input ($\mathbf{r}_{\text{in}}$) and output ($\mathbf{r}_{\text{out}}$) focusing points are decoupled. (**C**, **E**) Focused $\mathbf{R}-$matrix recorded by 1D and 2D probes, respectively. (**D**) UMI enables a quantification of aberrations by extracting a local RPSF (displayed here in amplitude) from each antidiagonal of $\mathbf{R}_{\boldsymbol{\rho\rho}}(z)$.

the reflected wave-field can be captured by the probe. On the contrary, in the speckle regime, unresolved scatterers isotropically back-scatter energy in all directions of space and can therefore be detected at much greater off-axis distances than specular reflectors.

3.2.2 Focusing quality & RPSF

We now show how to quantify aberrations in ultrasound speckle (without any guide star) by investigating the antidiagonals of $\mathbf{R}_{\boldsymbol{\rho\rho}}(z)$. In particular, all the theoretical expressions shown in the previous chapter for 2D imaging can be applied to 3D imaging, so that the transverse coordinate, previously x, now becomes $\boldsymbol{\rho} = (x, y)$. In the single scattering regime, the focused $\mathbf{R}-$matrix coefficients can thus be expressed as follows [Lambert, 2020b]:

$$R(\boldsymbol{\rho}_{\text{in}}, \boldsymbol{\rho}_{\text{out}}, z) = \int \mathrm{d}\boldsymbol{\rho} H_{\text{in}}(\boldsymbol{\rho} - \boldsymbol{\rho}_{\text{in}}, \boldsymbol{\rho}_{\text{in}}, z)\gamma(\boldsymbol{\rho}, z)H_{\text{out}}(\boldsymbol{\rho} - \boldsymbol{\rho}_{\text{out}}, \boldsymbol{\rho}_{\text{out}}, z), \tag{3.15}$$

with $\mathbf{H}_{\text{in/out}}$, the input/output point spread function (PSF); and γ the medium reflectivity. This last equation shows that each pixel of the ultrasound image (diagonal elements of $\mathbf{R}_{\boldsymbol{\rho\rho}}(z)$) results from a convolution between the sample reflectivity and an imaging PSF which is itself a product of the input and output PSFs.

The off-diagonal points in $\mathbf{R}_{\boldsymbol{\rho\rho}}(z)$ can be exploited for a quantification of the focusing quality at any pixel of the ultrasound image. By extracting each antidiagonal of $\mathbf{R}_{\boldsymbol{\rho\rho}}(z)$, the focused

reflection matrix is expressed in a common midpoint representation $R_{\mathcal{M}}$ as follows:

$$R_{\mathcal{M}}(\underbrace{\{\boldsymbol{\rho}_m, z\}}_{\mathbf{r}_\mathrm{m}}, \Delta\boldsymbol{\rho}) = R(\underbrace{\boldsymbol{\rho}_m - \Delta\boldsymbol{\rho}/2}_{\boldsymbol{\rho}_\mathrm{in}}, \underbrace{\boldsymbol{\rho}_m + \Delta\boldsymbol{\rho}/2}_{\boldsymbol{\rho}_\mathrm{out}}, z). \tag{3.16}$$

In the speckle regime (random reflectivity), this quantity directly probes the local focusing quality as its ensemble average scales as an incoherent convolution between the input and output PSFs [Lambert, 2020b]:

$$RPSF(\mathbf{r}_\mathrm{m}, \boldsymbol{\Delta\rho}) \propto \left(|H_\mathrm{in}|^2 \overset{\boldsymbol{\Delta\rho}}{\circledast} |H_\mathrm{out}|^2 \right) (\mathbf{r}_\mathrm{m}, \boldsymbol{\Delta\rho}). \tag{3.17}$$

In practice, this ensemble average is performed by a local spatial average. The field-of-view is divided into spatial regions $\mathcal{W}(\mathbf{r} - \mathbf{r}_\mathrm{m})$ that are defined by their central midpoint $\mathbf{r}_\mathrm{m} = (\boldsymbol{\rho}_\mathrm{m}, z_\mathrm{m})$ and their spatial extension $\mathbf{w} = (w_{\boldsymbol{\rho}}, w_z) = (\{w_x, w_y\}, w_z)$. A local average of the back-scattered intensity can then be performed in each region:

$$RPSF(\mathbf{r}_\mathrm{m}, \boldsymbol{\Delta\rho}) = \left\langle \left| R_{\mathcal{M}}(\mathbf{r}'_\mathrm{m}, \boldsymbol{\Delta\rho}) \right|^2 \mathcal{W}(\mathbf{r}'_\mathrm{m} - \mathbf{r}_\mathrm{m}) \right\rangle_{\mathbf{r}'_\mathrm{m}}, \tag{3.18}$$

where $\mathcal{W}(\mathbf{r}'_\mathrm{m} - \mathbf{r}_\mathrm{m}) = 1$ for $|\boldsymbol{\rho}'_\mathrm{m} - \boldsymbol{\rho}_\mathrm{m}| < w_\rho/2$ and $|z'_\mathrm{m} - z_\mathrm{m}| < w_z/2$, and zero otherwise.

[Fig. 3.3F] shows local RPSFs in a transverse plane of speckle, where side-lobes are observed in the $y-$axis. This effect is due to the irregular sampling of the transducer plane, since matrix arrays consist of four blocks of 256 elements, separated here by a distance of 0.6 mm [Fig. 3.2C_1].

3.3 Sampling at the input

In addition to a higher SNR, plane waves [Montaldo, 2009] or virtual sources [Provost, 2014] insonifications are required to track the dynamics of biological tissues, whether it be for vascular imaging (ultrafast Doppler & ULM) or elastography because they provide a much higher frame-rate than the canonical basis. However, ultrafast imaging implies a partial recording of the reflection matrix as it involves the insonification of the medium by a few plane waves (which is necessary to consider the medium fixed between this set of plane waves). An incomplete insonification basis induces a bad sampling of the **k**-space, leading to *aliasing* in the focal plane when performing the coherent compound of beamformed images [Fig. 3.7]. Indeed, the combination of beamformed images obtained for each plane wave insonification can be seen as a Fourier transform ($\mathbf{k} \rightarrow \mathbf{r}$). Thus, to avoid spatial aliasing, the coefficients $\mathbf{R}_{\boldsymbol{\rho\rho}}(z)$ associated with a transverse distance $|\boldsymbol{\rho}_\mathrm{out} - \boldsymbol{\rho}_\mathrm{in}|$ larger than the superior bound $\Delta\boldsymbol{\rho}_\mathrm{max} \sim \lambda_c/(2\delta\theta)$ (Shannon criterion) should be filtered via a confocal filter.

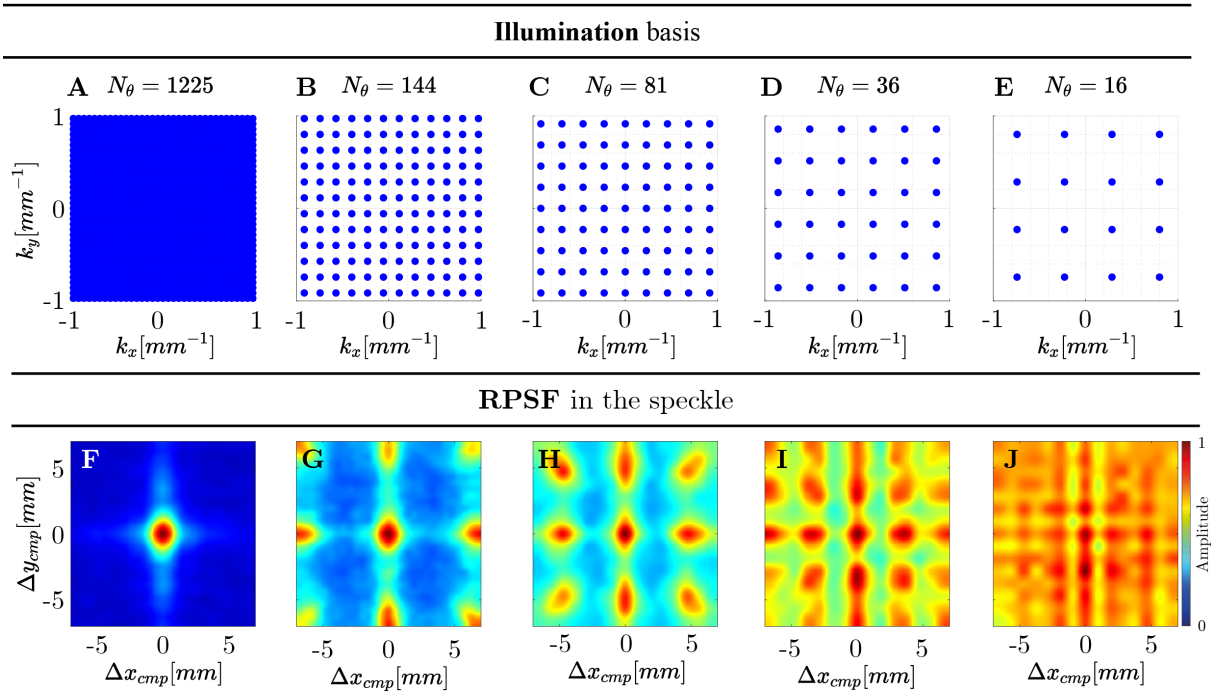

Figure 3.7: **Insonification sequence.** (**A**-**E**) Representation of different plane wave insonification sequence in the **k**−space. (**F**-**J**) Aliasing effect exhibited by the RPSFs due to incompleteness of insonification sequence displayed in panels (**A**-**E**), respectively. These RPSFs have been measured in a speckle area of a tissue-mimicking phantom.

Input sampling consideration

Hence, the number of independent incident waves N_{in} needed to correct aberrations should scale as the number of resolution cells $N_{\mathcal{W}}$ over which the RPSF spreads. In other words, the **R**−matrix can be down-sampled at the input to shorten the acquisition time, provided that *aliasing* artifacts do not overlap with the RPSF.

4 Phantom experiment with aberrations

A second experiment is performed to introduce aberrations into the tissue mimicking phantom. A 12-mm thick pork chop is placed on top of the phantom. It is immersed in water to ensure its acoustical contact with the probe and the phantom. Since the pork chop contains a part of muscle tissue ($c_\mathrm{m} \approx 1560 \pm 50$ m/s [Goss, 1978]) and a part of fat tissue ($c_\mathrm{f} \approx 1480 \pm 10$ m/s), it acts as an aberrating layer. This experiment mimics the situation of abdominal *in vivo* imaging, in which layers of fat and muscle tissues generate strong aberration and scattering at shallow depths.

4.1 Reflection matrix acquisition

The reflection matrix is acquired by recording the impulse response between each transducer of the probe ($\mathcal{P}_1$) using IQ modulation with a sampling frequency $f_\mathrm{s} = 6$ MHz. To that aim, each transducer $\mathbf{u}_\mathrm{in}$ emits successively a sinusoidal burst of three half periods at the central frequency f_c. For each excitation $\mathbf{u}_\mathrm{in}$, the back-scattered wave-field is recorded by all probe elements $\mathbf{u}_\mathrm{out}$ over a time length $\Delta t = 139$ μs. This set of impulse responses is stored in the canonical reflection matrix $\mathbf{R_{uu}}(t) = [R(\mathbf{u}_\mathrm{in}, \mathbf{u}_\mathrm{out}, t)]$.

4.2 Manifestations of the aberrations

The focused reflection matrix $\mathbf{R_{\rho\rho}}(z)$ is built numerically from the reflection matrix $\mathbf{R_{uu}}(t)$ according to equations (3.10 & 3.11) and assuming the speed-of-sound of the phantom ($c_\mathrm{p} = 1540$ m/s).

4.2.1 In the confocal image

The corresponding 3D image $\mathcal{I}(\mathbf{r})$ is displayed in [Fig. 3.8B] using Maximum Intensity Projection (MIP). Spatial variations of the speed-of-sound in fat and muscle give rise to aberrations that decrease both the contrast and resolution of the confocal image, especially under the fat layer, where the speed-of-sound error is the greatest. Longitudinal and transverse cross-sections illustrate these effects by highlighting the distortion exhibited by the image of the deepest nylon rod [Fig. 3.8C, D].

4.2.2 In the RPSFs

[Fig. 3.9A] displays the mean RPSFs with their associated focusing criterion [Lambert, 2020b], in an area of speckle at depth $z = 30$ mm. Here, an analog of the focusing criterion is extracted with a fit, where each RPSF is fitted (in amplitude) with the following Gaussian model:

$$f(a,b) = a\exp(\frac{-x^2}{2\sigma_0^2})\exp(\frac{-y^2}{2\sigma_0^2}) + b, \tag{3.19}$$

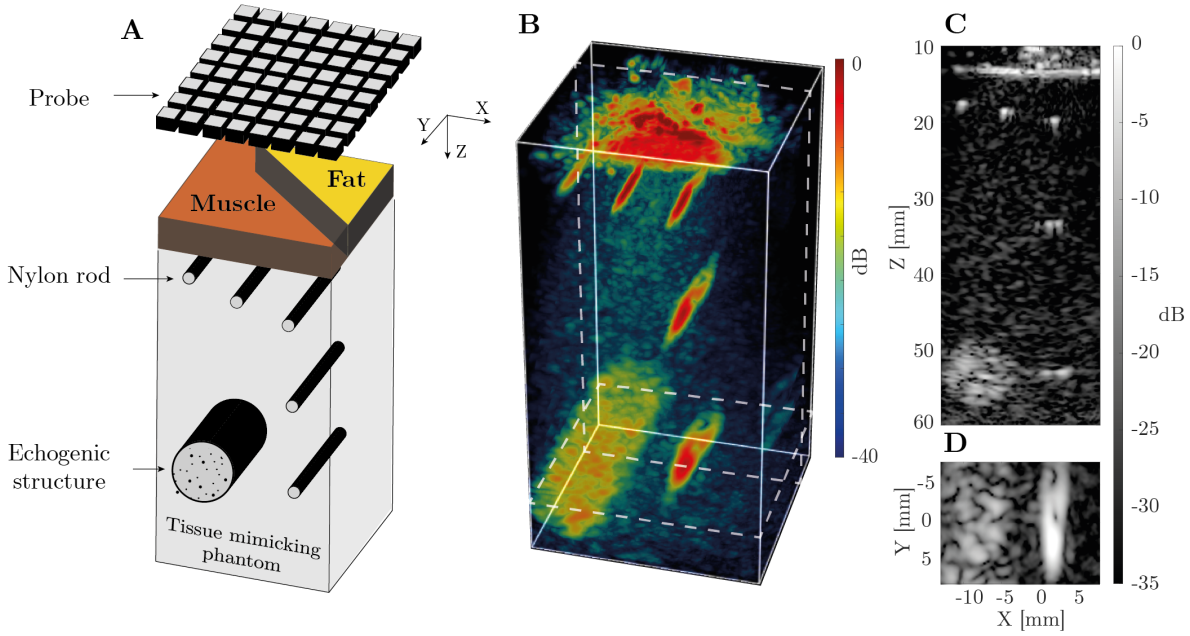

Figure 3.8: **Pork chop experiment.** (**A**) Schematic of the experiment (**B**) MIP volume, (**C**) longitudinal and (**D**) transverse cross-section of the conventional confocal volume (*i.e.* before any correction).

where (a, b) are the free parameters while $\sigma_0(z) = \frac{\delta\rho_0(z)}{\sqrt{2log(2)}}$ is constrained to the theoretical diffraction limit [black dashed line in Fig. 3.9C]:

$$\delta\rho_0(z) \sim \frac{\lambda_c}{2\sin\left\{\arctan\left[\Delta u/(2z)\right]\right\}}, \tag{3.20}$$

with Δu the lateral extension of the probe. The coefficient of determination r^2 of the fit is an indicator of good agreement between ideal and experimental resolution, and thus a direct quantitative criterion of the focusing quality. In practice, this Gaussian model provides a quick way to compare the experimental RPSF with the ideal case predicted by the diffraction theory. However, better accuracy can be obtained by fitting or comparing with the theoretical expression of (Eq. 3.17).

The focusing criterion shows that aberrations from muscle (lower left) to fat (upper right) becomes increasingly important. This indicates that the aberrations are spatially distributed in multiple isoplanatic patches and therefore require local correction. In addition, [Fig. 3.9C] clearly shows a distorted RPSF which spreads well beyond the diffraction limit. This RSPF also exhibits a strong anisotropy that could not have been grasped by 2D UMI.

4.2.3 Contrast & resolution

Contrast and resolution are evaluated by means of the RPSF. Equivalent to the full width at half maximum commonly used in 2D UMI, the transverse resolution $\delta\rho$ is assessed in 3D based

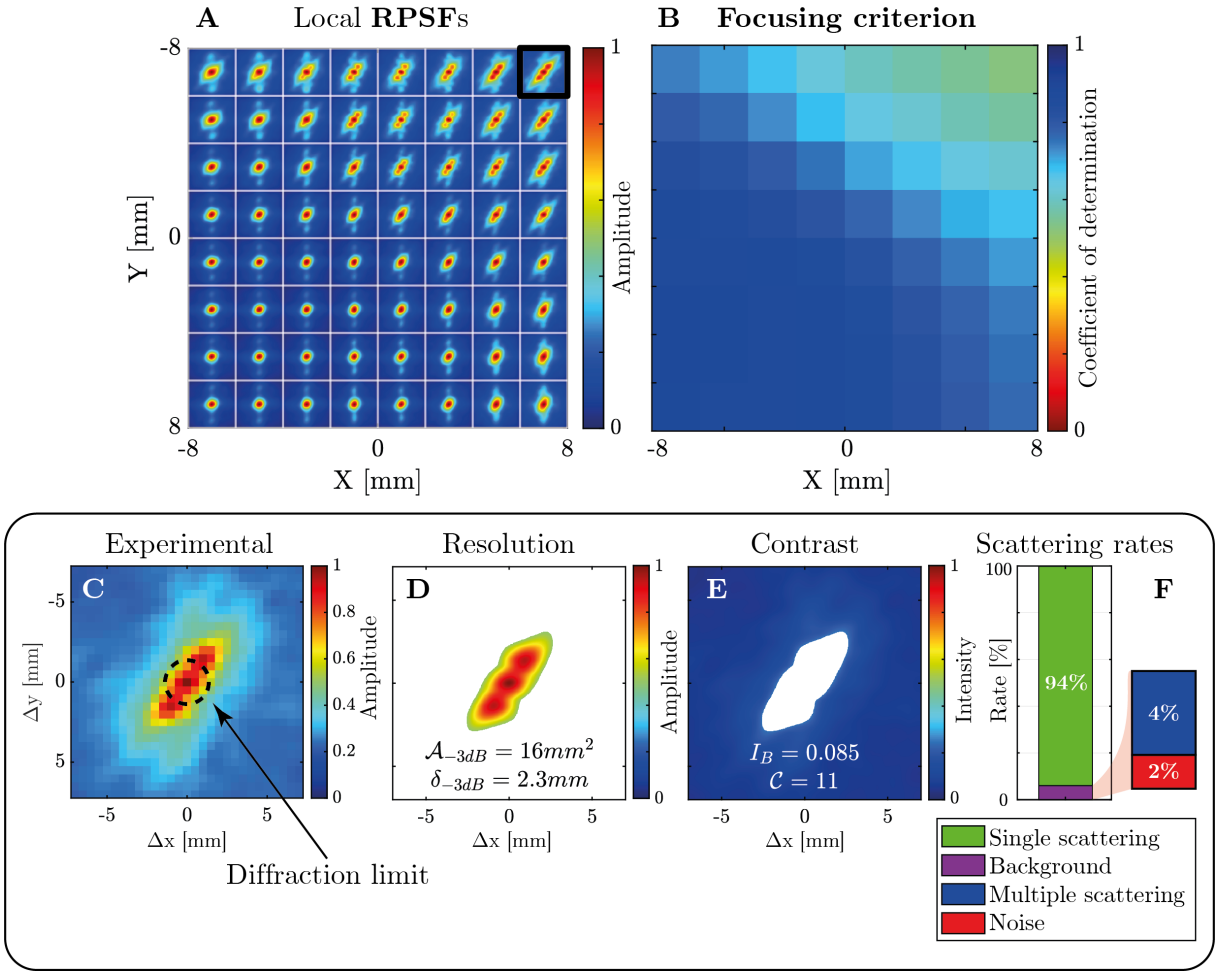

Figure 3.9: **RPSFs analysis in the pork chop experiment.** **(A)** Transverse RPSFs in the speckle and corresponding **(B)** focusing criterion associated to each RPSF expressed here as the coefficient of determination r^2 of a Gaussian fit with the expected diffraction limit. **(C)** Experimental data of the RPSF associated to the black box in panel **(A)**. **(D)** Resolution $\delta\rho_{(-3dB)}$ extracted on the amplitude of the RPSF (equation 3.21). **(E)** Contrast $\mathcal{C}$ extracted on the intensity of the RPSF (equation 3.23). **(F)** Scattering rates evaluated through the anti-symmetry rate β of the $\mathbf{R}-$matrix (equation 3.26).

on the area $\mathcal{A}_{(-3dB)}$ at half maximum of the RPSF amplitude:

$$\delta\rho_{(-3dB)} = \sqrt{\mathcal{A}_{(-3dB)}/\pi}. \tag{3.21}$$

The contrast, $\mathcal{C}$, is computed locally by decomposing the normalized RPSF, noted $\overline{RPSF}$, as the sum of three components [Lambert, 2022b]:

$$\overline{RPSF}(\mathbf{r}_\mathrm{p}, \Delta\boldsymbol{\rho}) = \frac{RPSF(\mathbf{r}_\mathrm{p}, \Delta\boldsymbol{\rho})}{RPSF(\mathbf{r}_\mathrm{p}, \Delta\boldsymbol{\rho} = \mathbf{0})} = \alpha_\mathrm{S}(\mathbf{r}_\mathrm{p}) + \underbrace{\alpha_\mathrm{M}(\mathbf{r}_\mathrm{p}) + \alpha_\mathrm{N}(\mathbf{r}_\mathrm{p})}_{\alpha_\mathcal{B}(\mathbf{r}_\mathrm{p})}. \tag{3.22}$$

α_S is the single scattering component that corresponds to a confocal peak. α_M is a multiple scattering contribution that gives rise to a diffuse halo; α_N corresponds to electronic noise, which

results in a flat plateau. A local contrast can then be deduced from the ratio between α_S and the incoherent background $\alpha_{\mathcal{B}} = \alpha_M + \alpha_N$,

$$\mathcal{C}(\mathbf{r}_p) = \frac{\alpha_S(\mathbf{r}_p)}{\alpha_{\mathcal{B}}(\mathbf{r}_p)} = \frac{1 - \alpha_{\mathcal{B}}(\mathbf{r}_p)}{\alpha_{\mathcal{B}}(\mathbf{r}_p)}. \tag{3.23}$$

4.2.4 Single & multiple scattering rates

As described in [Lambert, 2022b], the single scattering, multiple scattering and noise rates can be directly computed from the decomposition of the RPSF with a fitting procedure (Eq. 3.22). However, at large depths, multiple scattering and noise are difficult to discriminate since they both give rise to a flat plateau in the RPSF. In that case, the **spatial reciprocity** can be invoked to differentiate their contribution. The multiple scattering component actually gives rise to a fully **symmetric R**-matrix, while electronic noise is associated with a fully random matrix. The relative part of the two components can thus be leveraged by computing the degree of anti-symmetry in the **R**−matrix (see Appendix 4.4). To that aim, the **R**-matrix is first projected onto its antisymmetric subspace at each depth as follows:

$$\mathbf{R}^{(A)}_{\boldsymbol{\rho\rho}}(z) = \frac{\mathbf{R}_{\boldsymbol{\rho\rho}}(z) - \mathbf{R}^{\top}_{\boldsymbol{\rho\rho}}(z)}{2}, \tag{3.24}$$

where the superscript $^{\top}$ stands for matrix transpose. In a common midpoint basis, (Eq. 3.24) writes:

$$\mathrm{R}^{(A)}_{\mathcal{M}}(\mathbf{r}_m, \boldsymbol{\Delta\rho}) = \frac{\mathrm{R}_{\mathcal{M}}(\mathbf{r}_m, \boldsymbol{\Delta\rho}) - \mathrm{R}_{\mathcal{M}}(\mathbf{r}_m, -\boldsymbol{\Delta\rho})}{2}. \tag{3.25}$$

A local anti-symmetric rate β can be computed as follows:

$$\beta(\mathbf{r}_p) = \frac{\left\langle \left|\mathrm{R}^{(A)}_{\mathcal{M}}(\mathbf{r}_m, \boldsymbol{\Delta\rho})\right|^2 \mathcal{W}(\mathbf{r}_m - \mathbf{r}_p)\mathcal{D}(\Delta\boldsymbol{\rho}) \right\rangle_{[\mathbf{r}_m, \boldsymbol{\Delta\rho}]}}{\left\langle \left|\mathrm{R}_{\mathcal{M}}(\mathbf{r}_m, \boldsymbol{\Delta\rho})\right|^2 \mathcal{W}(\mathbf{r}_m - \mathbf{r}_p)\mathcal{D}(\Delta\boldsymbol{\rho}) \right\rangle_{[\mathbf{r}_m, \boldsymbol{\Delta\rho}]}}, \tag{3.26}$$

where $\mathcal{D}(\Delta\boldsymbol{\rho})$ is a de-scan window function that eliminates the confocal peak such that the computation of β is only made by considering the incoherent background. Typically, we chose $\mathcal{D}(\Delta\boldsymbol{\rho}) = 1$ for $\Delta\boldsymbol{\rho} > 6\delta\rho_0(z)$, and zero otherwise.

Assuming equipartition of the electronic noise between its symmetric and antisymmetric subspace, the multiple scattering rate α_M and noise ratio α_N can then be deduced:

$$\alpha_M(\mathbf{r}_p) = (1 - 2\beta(\mathbf{r}_p))\, \alpha_{\mathcal{B}}(\mathbf{r}_p), \tag{3.27}$$

$$\alpha_N(\mathbf{r}_p) = 2\beta(\mathbf{r}_p)\alpha_{\mathcal{B}}(\mathbf{r}_p). \tag{3.28}$$

In this experiment, single scattering largely dominates, as shown in [Fig. 3.9F]. In order to validate such a method for evaluating the multiple scattering rate, an experiment could be carried out in which the reflection matrix of a highly scattering medium is recorded several times and then averaged. The multiple scattering rate should remain the same with or without averaging, while the noise rate should decrease after averaging.

4.3 Aberration correction

Aberration compensation in the UMI framework is performed using the **distortion matrix** concept. Introduced for 2D UMI [Lambert, 2020c; Lambert, 2022a], it is now extended to 3D imaging and consists of the following steps:

- projecting the focused $\mathbf{R}-$matrix either at input or output in a correction basis [Fig. 3.10B, G];
- extracting wave distortions exhibited by $\mathbf{R}$ when compared to a reference matrix that would have been obtained in an ideal homogeneous medium of wave velocity c_0 [Fig. 3.10C, H].

The resulting distortion matrix $\mathbf{D} = [\mathrm{D}(\mathbf{c}, \mathbf{r})]$ contains the aberrations induced when focusing on any point ($\mathbf{r}$), expressed in the correction basis ($\mathbf{c}$). Finally, an estimation of the transmission matrix $\hat{\mathbf{T}} \equiv [\hat{T}(\mathbf{c}, \mathbf{r})]$ can be made and further used to correct the $\mathbf{R}-$matrix from aberrations

4.3.1 The distortion matrix

First, the focused reflection matrix $\mathbf{R}_{\boldsymbol{\rho\rho}}(z)$ [Fig. 3.10A, F] is projected onto a dual basis $\mathbf{c}$ at the output $\mathbf{R}_{\boldsymbol{\rho c}} \equiv [R(\boldsymbol{\rho}_{\text{in}}, \mathbf{c}_{\text{out}}, z)]$ [Fig. 3.10B, G]:

$$\mathbf{R}_{\boldsymbol{\rho c}}(z) = \mathbf{R}_{\boldsymbol{\rho\rho}}(z) \times \mathbf{G}_0(z), \tag{3.29}$$

where $\times$ stands for a matrix product and $\mathbf{G}_0$ the homogeneous Green's matrix predicted by the propagation model. In the transducer basis ($\mathbf{c} = \mathbf{u}$), its coefficients correspond to the $z-$derivative of the Green's function [Lambert, 2022a]:

$$\mathrm{G}_0^{(u)}(\boldsymbol{\rho}, \mathbf{u}) = \frac{z e^{ik_c|\mathbf{u}-\mathbf{r}|}}{4\pi|\mathbf{u}-\mathbf{r}|^2}, \tag{3.30}$$

where k_c is the wavenumber at the central frequency. In the Fourier basis ($\mathbf{c} = \mathbf{k}$), $\mathbf{G}_0$ simply corresponds to the Fourier transform operator [Lambert, 2020c]:

$$\mathrm{G}_0^{(k)}(\boldsymbol{\rho}, \mathbf{k}) = \exp(j\mathbf{k}.\boldsymbol{\rho}) = \exp(j[k_x x + k_y y]). \tag{3.31}$$

At each depth z, the reflected wave-fronts contained in $\mathbf{R}_{\boldsymbol{\rho c}}$ are then decomposed into the sum of a geometric component $\mathbf{G}_0$, that would be ideally obtained in absence of aberrations, and a distorted component that corresponds to the gap between the measured wave-fronts and their ideal counterparts [Fig. 3.10C] [Lambert, 2020c; Lambert, 2022a]:

$$\mathbf{D}_{\boldsymbol{\rho c}}(z) = \mathbf{G}_0^*(z) \circ \mathbf{R}_{\boldsymbol{\rho c}}(z), \tag{3.32}$$

where the symbol $\circ$ stands for a Hadamard product and $*$ for complex conjugate. $\mathbf{D_{rc}} = [\mathbf{D}_{\boldsymbol{\rho c}}(z)] = [D(\boldsymbol{\rho}_{\text{in}}, \mathbf{c}_{\text{out}}, z)]$ is the so-called **distortion matrix**. Note that the same operations can be performed by exchanging input and output to obtain the input distortion matrix $\mathbf{D_{cr}}$.

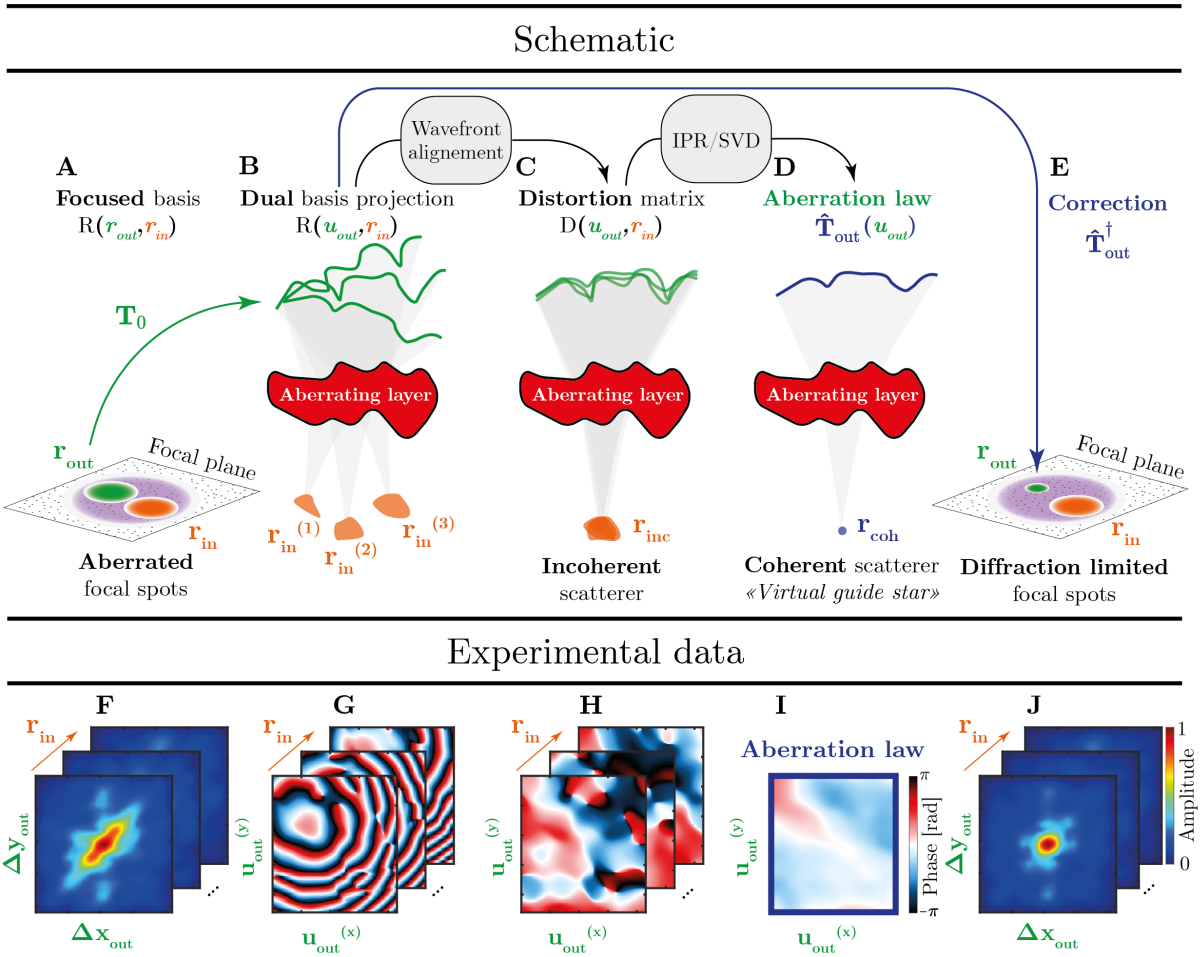

Figure 3.10: **Distortion Matrix framework** (Pork chop experiment). **(A)** The focused reflection matrix $R(\mathbf{r}_{\text{in}}, \mathbf{r}_{\text{out}})$ is projected in a **(B)** dual basis $R(\mathbf{r}_{\text{in}}, \mathbf{u}_{\text{out}})$ that contains the aberrated wavefronts (in the transducer basis $\mathbf{u}_{\text{out}}$) associated to each focal point ($\mathbf{r}_{\text{in}}$). The geometrical component is removed to assess only the **(C)** distorted part of the wavefronts $D(\mathbf{r}_{\text{in}}, \mathbf{u}_{\text{out}})$. **(D)** A time reversal analysis (SVD or IPR) is then performed to extract the aberration law associated to all the focusing point $\mathbf{r}_{\text{in}}$, assuming isoplanetism. **(G-I)** Experimental data corresponding to **(B-D)**. **(E)** Green functions are then corrected, thus providing a diffracted-limited resolution at the output. **(F, J)** RPSF before and after correction, respectively. This framework can then be applied similarly to the input.

4.3.2 Time reversal analysis of the correlation matrix

The next step is to exploit local correlations in $\mathbf{D_{rc}}$ to extract the $\mathbf{T}$-matrix. To that aim, a set of correlation matrices $\mathbf{C}_{\text{out}}(\mathbf{r}_{\text{p}})$ shall be considered between distorted wave-fronts in the vicinity of each point $\mathbf{r}_{\text{p}}$ in the field-of-view:

$$\mathbf{C}_{\text{out}}(\mathbf{r}_{\text{p}}) = [C(\mathbf{c}_{\text{out}}, \mathbf{c}'_{\text{out}}, \mathbf{r}_{\text{p}})] = \langle D(\mathbf{r}_{\text{in}}, \mathbf{c}_{\text{out}}) D^*(\mathbf{r}_{\text{in}}, \mathbf{c}'_{\text{out}}) \mathcal{W}(\mathbf{r}_{\text{in}} - \mathbf{r}_{\text{p}}) \rangle_{\mathbf{r}_{\text{in}}} . \tag{3.33}$$

An equivalent operation can be performed at input in order to extract a local correlation matrix $\mathbf{C}_{\text{in}}(\mathbf{r}_{\text{p}})$ from the input distortion matrix $\mathbf{D_{cr}}$. In terms of matrix, it writes:

$$\mathbf{C}_{\text{out}} = \mathbf{D}_{\mathbf{rc}}^{\dagger} \times \mathbf{D_{rc}}, \tag{3.34}$$

$$\mathbf{C}_{\text{in}} = \mathbf{D_{cr}} \times \mathbf{D}_{\mathbf{cr}}^{\dagger}. \tag{3.35}$$

In previous works on 2D UMI [Lambert, 2020c; Lambert, 2022a], the $\mathbf{T}$-matrix was estimated by performing a singular value decomposition of $\mathbf{D_{rc}}$:

$$\mathbf{D_{rc}} = \mathbf{V}_{\text{in}}^{\dagger} \times \mathbf{\Sigma} \times \mathbf{U}_{\text{out}}, \tag{3.36}$$

or, equivalently, the eigenvalue decomposition of $\mathbf{C}_{\text{out}}$ (see Appendix 12):

$$\mathbf{C}_{\text{out}} = \mathbf{U}_{\text{out}}^{\dagger} \times \mathbf{\Sigma}^2 \times \mathbf{U}_{\text{out}}, \tag{3.37}$$

where $\mathbf{\Sigma}$ is a diagonal matrix containing the singular values σ_i in descending order: $\sigma_1 > \sigma_2 > .. > \sigma_N$. $\mathbf{U}_{\text{out}}$ and $\mathbf{V}_{\text{in}}$ are unitary matrices that contain the orthonormal set of output and input eigenvectors, $\mathbf{U}_{\text{out}}^{(i)} = [U_{\text{out}}^{(i)}(\mathbf{c}_{\text{out}})]$ and $\mathbf{V}_{\text{in}}^{(i)} = [V_{\text{in}}^{(i)}(\mathbf{r}_{\text{in}})]$.

The reason of this eigenvalue decomposition can be intuitively understood by considering the asymptotic case of a point-like input focusing beam, $H_{\text{in}}(\boldsymbol{\rho}) \to \delta(\boldsymbol{\rho})$. Assuming the correlation matrix converges to its ensemble average $\langle \mathbf{C} \rangle$, it can be expressed as follows (see Appendix 5.1):

$$\langle \mathbf{C}_{\text{out}} \rangle \propto \mathbf{T}_{\text{out}}^{\dagger} \times \mathbf{\Gamma}_{\delta} \times \mathbf{T}_{\text{out}}, \tag{3.38}$$

where $\mathbf{\Gamma}_{\delta}$ is a scattering matrix associated with a point-like (diffraction-limited) reflector centered at the origin. (Eq. 3.37) thus becomes $C(\mathbf{c}_{\text{out}}, \mathbf{c}'_{\text{out}}) = \mathrm{T}_{\text{out}}(\mathbf{c}_{\text{out}})\mathrm{T}^{*}_{\text{out}}(\mathbf{c}'_{\text{out}})$. $\mathbf{D_{rc}}$ is then of rank 1 and the first output singular vector $\mathbf{U}_{\text{out}}^{(1)}$ yields an estimation of the aberration transmittance, $\hat{\mathbf{T}}_{\text{out}}$. The updated Green functions can be deduced:

$$\hat{\mathrm{G}}_{\text{out}}(\mathbf{c}_{\text{out}}, \mathbf{r}_{\text{p}}) = \hat{\mathrm{T}}_{\text{out}}(\mathbf{c}_{\text{out}})\mathrm{G}_0(\mathbf{c}_{\text{out}}, \mathbf{r}_{\text{p}}). \tag{3.39}$$

4.3.3 Iterative Phase Reversal (IPR)

However, in reality, the input PSF, $\mathbf{H}_{\text{in}}$, is of course far from being point-like. The spectrum of $\mathbf{D_{rc}}$ displays a continuum of singular values [Fig. 3.11D]. The effective rank of $\mathbf{C}_{\text{out}}$ is shown to scale as the number of resolution cells covered by the input PSF $\mathbf{H}_{\text{in}}$ [Lambert, 2022a]:

$$M_{\delta} \sim (\delta\rho_{\text{in}}/\delta\rho_0)^2, \tag{3.40}$$

where $\delta\rho_{\text{in}}$ is the spatial extension of the input PSF. The amplitude of the corresponding eigenvectors $\mathbf{U}_{\text{out}}^{(i)}$ depends on the exact shape of the virtual guide star, that is to say, on aberrations induced by the incident wave-front.

[Fig. 3.11E and F] show the modulus of two first eigenvectors, $\mathbf{U}_{\text{out}}^{(1)}$ and $\mathbf{U}_{\text{out}}^{(2)}$. They clearly show a complementary feature. While $\mathbf{U}_{\text{out}}^{(1)}$ is associated with the fat layer, $\mathbf{U}_{\text{out}}^{(2)}$ maps

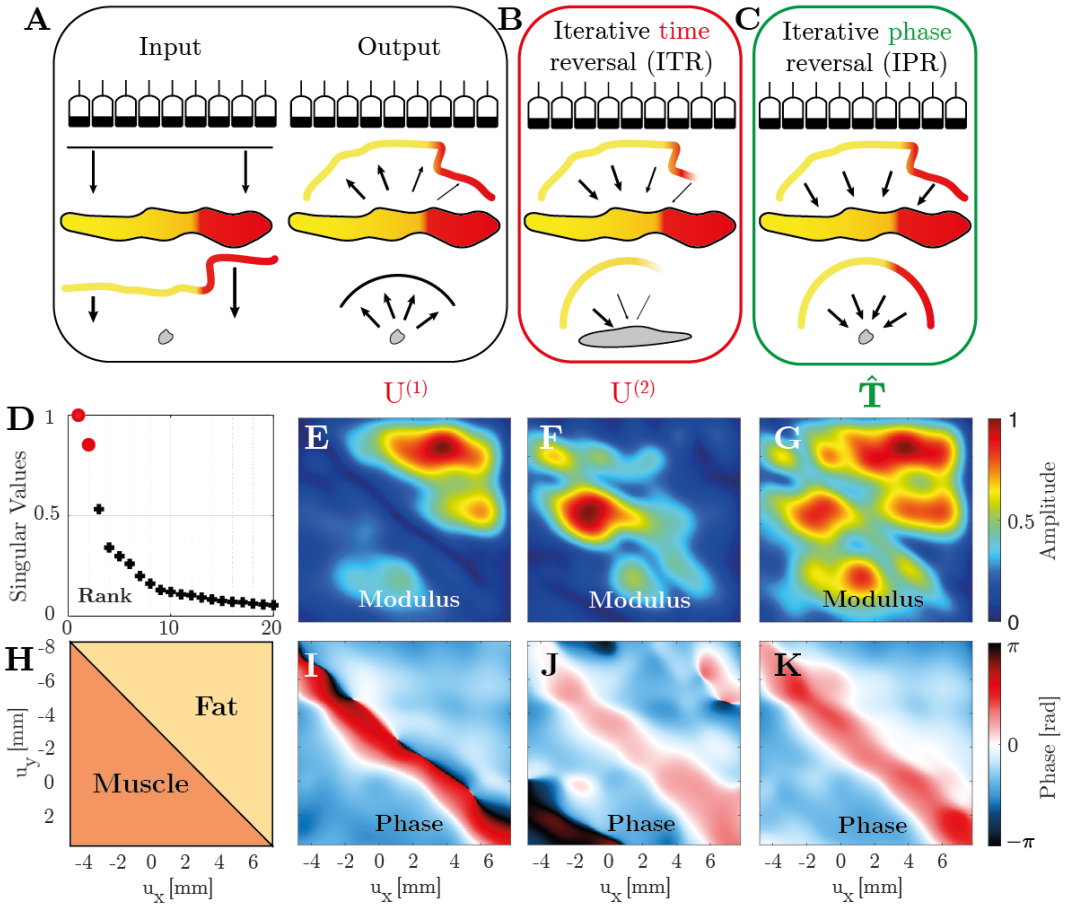

Figure 3.11: **Iterative Time Reversal *versus* Iterative Phase Reversal.** (**A**) The first step of ITR and IPR corresponds to the following fictitious experiment: Insonifying the medium by an arbitrary wave-front (here a plane wave) using an array of transducers and recording the reflected wave-front with the same probe. (**B**) The ITR process consists in time-reversing this wave-front in post-processing and sending it back into the medium, recording again the reflected wave-front, and so on. (**C**) The IPR process is similar but normalizes the amplitude of the time-reversed wavefront at every iteration. (**D**) Singular value distribution of $\mathbf{D_{rc}}$ for a box $\mathcal{W}$ of dimension $\mathbf{w} = (w_x, w_y, w_z) = (2, -5, 2)$ mm centered around point $\mathbf{r}_\mathrm{p} = (3, -5.5, 23)$ mm. (**E**, **F**) Modulus of the two first eigenvectors $\mathbf{U}_\mathrm{out}^{(i)}$. (**G**) Modulus of the vector $\mathbf{C}_\mathrm{out} \times \hat{\mathbf{T}}_\mathrm{out}$. (**H**) Delimitation of muscle and fat over the probe surface. (**I-K**) Phase of $\mathbf{U}_\mathrm{out}^{(1)}$, $\mathbf{U}_\mathrm{out}^{(2)}$ and $\hat{\mathbf{T}}_\mathrm{out}$.

onto the muscle part of the pork chop [Fig. 3.11H]. This result can be understood by the discontinuity of the speed-of-sound between the muscle and fat parts of the pork chop that breaks the spatial invariance and isoplanicity. As a consequence, the SVD process tends to converge onto eigenstates associated with the most isoplanatic components of $\mathbf{D_{rc}}$.

This property is not satisfactory in the present case, since each eigenvector only covers a part of the probe aperture. In other words, the phases of $\mathbf{U}^{(1)}$ [Fig. 3.11I] and $\mathbf{U}^{(2)}$ [Fig. 3.11J] are only satisfying estimators of $\mathbf{T}$ over some parts of the probe. Therefore, they cannot independently lead to an aberration compensation over the full numerical aperture.

To circumvent that problem, one can take advantage of the analogy with iterative time reversal (ITR). The eigenvector $\mathbf{U}_{\text{out}}^{(1)}$ can actually be seen as the result of the following fictitious experiment that consists in insonifying the virtual scatterer by an arbitrary wave-front and recording the reflected wave-field [Fig. 3.11A]. This wave-field is time-reversed and back-emitted towards the virtual scatterer [Fig. 3.11B]. This process can then be iterated many times and each step can be mathematically written as:

$$\sigma \mathbf{W}^{(n+1)} = \mathbf{C}_{\text{out}} \times \mathbf{W}^{(n)}, \tag{3.41}$$

with $\mathbf{W}^{(n)}$, the wave-front at iteration n of the ITR process and σ, the scatterer reflectivity. ITR is shown to converge towards a time-reversal invariant that is nothing other than the first eigenvector, $\mathbf{U}_{\text{out}}^{(1)} = \lim_{n\to+\infty} \mathbf{W}^{(n)}$.

To optimize the estimation of aberrations over the full probe aperture, *the idea of Arthur Le Ber* was to modify the ITR/SVD process by still re-emitting a phase-reversed wave-field but with a constant amplitude on each probe element [Fig. 3.11C]. In practice, this operation is performed using the following IPR algorithm:

$$\hat{\mathbf{W}}_{\text{out}}^{(n+1)} = \exp\left[j \arg\left\{\mathbf{C}_{\text{out}} \times \hat{\mathbf{W}}_{\text{out}}^{(n)}\right\}\right], \tag{3.42}$$

where $\hat{\mathbf{W}}_{\text{out}}^{(n)}$ is the estimator of $\mathbf{T}_{\text{out}}$ at the n^{th} iteration of IPR. $\hat{\mathbf{W}}_{\text{out}}^{(0)}$ is an arbitrary wave-front that initiates IPR (typically a plane wave). $\hat{\mathbf{T}}_{\text{out}} = \lim_{n\to\infty} \hat{\mathbf{W}}_{\text{out}}^{(n)}$ is the result of this IPR process. In practice, the IPR process converge after about $N = 200$ iterations. Unlike ITR, IPR equally addresses each angular component of the imaging process to reach a diffraction-limited resolution. [Fig. 3.11G] illustrates this fact by showing the modulus of $\mathbf{C}_{\text{out}} \times \hat{\mathbf{T}}_{\text{out}}$. Compared with $\mathbf{U}_{\text{out}}^{(1)}$ [Fig. 3.11E] and $\mathbf{U}_{\text{out}}^{(2)}$ [Fig. 3.11F], it clearly shows that the phase-reversed invariant $\hat{\mathbf{T}}_{\text{out}}$ simultaneously addresses each angular component of the aberrated wave-field. $\hat{\mathbf{T}}_{\text{out}}$ is thus a much better estimator of the $\mathbf{T}-$matrix [Fig. 3.11K] than the aberration phase laws extracted by the SVD process [Fig. 3.11I and J].

When applied to the whole field-of-view, the IPR algorithm is mathematically equivalent to the CLASS algorithm developed in optical microscopy [Kang, 2017]. However, the IPR algorithm is much more efficient for a local compensation of aberrations. For IPR, the angular resolution $\delta\theta$ of the aberration phase law is only limited by the angular pitch of the plane wave insonification basis or the pitch δu of the transducer array in the canonical basis: $\delta\theta_I \sim \delta u/\lambda$. With CLASS, the resolution $\delta\theta_C$ of the aberration law is governed by the size of the spatial window $\mathcal{W}$ on which the focused reflection matrix is truncated: $\delta\theta_C \sim z/w_\rho$. It can be particularly detrimental when high-order aberrations and small isopalanatic patches are targeted.

4.3.4 Correction

This iterative phase reversal algorithm, repeated for each point $\mathbf{r}_{\text{p}}$, yields an estimator $\hat{\mathbf{T}}_{\text{out}}$ of the $\mathbf{T}$-matrix. Its digital phase conjugation enables a local compensation of aberrations

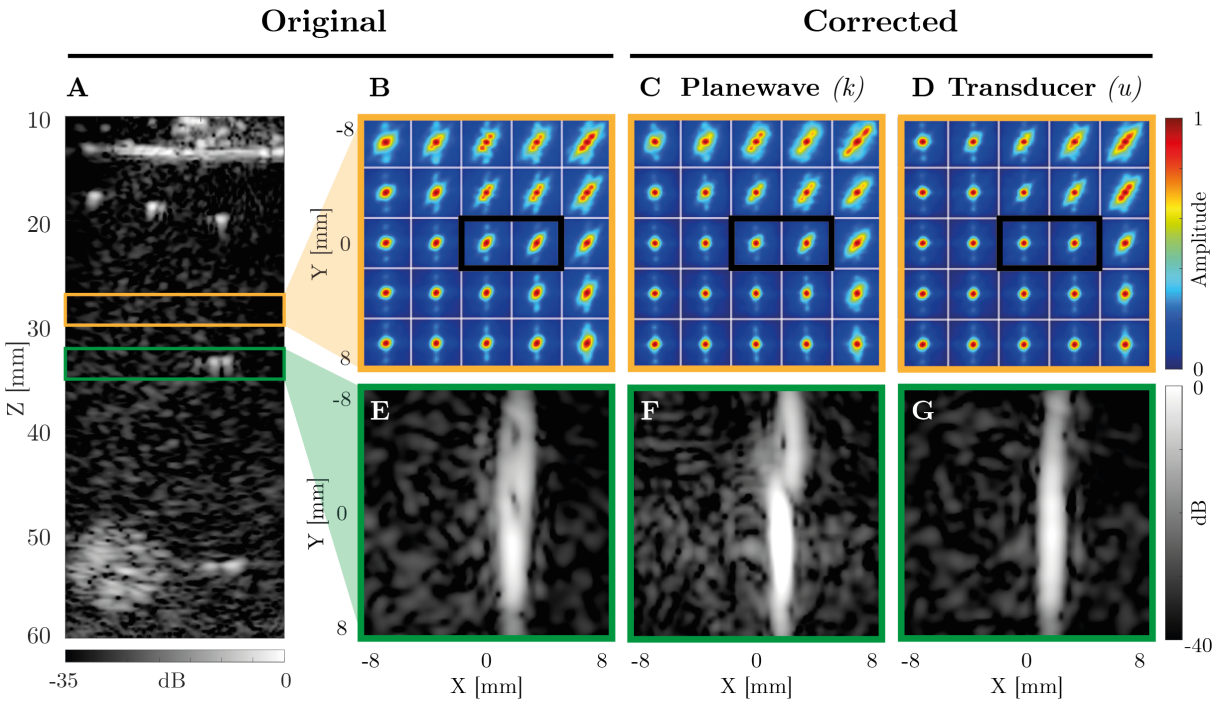

Figure 3.12: **Correction in the transducer (u) *versus* plane wave (k) basis in the pork chop experiment.** A one-step correction among all the transverse plane is investigated in two different area : speckle (orange box) and strong reflector (green box). **(A, B, E)** Original images and RPSFs. Black boxes show relevant areas of the field-of-view for comparison. **(C, F)** Correction in the plane wave basis. **(D, G)** Correction in the transducer basis.

[Fig. 3.10J]. The focused $\mathbf{R}-$matrix can be updated as follows:

$$\mathbf{R}_{\boldsymbol{\rho\rho}}^{(\mathrm{corr})}(z) = \mathbf{R}_{\boldsymbol{\rho c}}(z) \times \hat{\mathbf{G}}_{\mathrm{out}}^{\dagger}(z), \tag{3.43}$$

where the symbol † stands for transpose conjugate. The same process is then applied to the input correlation matrix $\mathbf{C}_{\mathrm{in}}$ for the estimation of the input Green functions $\mathbf{G}_{\mathrm{in}} = \mathbf{H}_{\mathrm{in}} \times \mathbf{G}_0$.

4.3.5 Choice of correction basis (k or u)

Now, the influence of the correction basis (far-field k or transducer u) is investigated in two particular areas [Fig. 3.12]: speckle (random reflectivity due to under-resolved scatterers) and strong reflector (nylon rod). The correction is applied only once at the input and then at the output, considering a patch whose transverse dimension matches the size of the probe. In the speckle region [Fig. 3.12B, C, D], the correction is only partial in both cases, since isoplanicity is not verified in the entire transverse plane as shown by the RPSFs. However, the transducer basis still provides a better correction than the plane-wave basis, as can be seen in the black boxes in panels C and D. In the strong reflector region [Fig. 3.12E, F, G], the correction in the transducer basis allows the nylon filament to return to its straight shape. In contrast, the correction in the plane wave basis does not properly correct the aberrations, making the nylon filament even less straight than before. This suggests that the transducer basis is better at correcting aberrations

in this experiment, since it ensures a higher isoplanetism. This was to be expected, since the aberrator (pork chop) is located under the probe and exhibits transverse variations in the speed of sound that are strongly anisoplanatic in the plane wave basis. Subsequently, the aberrations in this experiment will be corrected only in the transducer basis.

4.3.6 Spatial convergence of the $\hat{\mathbf{T}}-$matrix

The 3D distribution of the speed-of-sound breaks the spatial invariance of input and output PSFs. A full-field compensation of aberrations as performed by original adaptive focusing techniques does not allow a fine compensation of aberrations, as described in [Fig. 3.12D]. Access to the transmission matrix $\mathbf{T} = [\mathrm{T}(\mathbf{u},\mathbf{r})]$ linking each transducer and each medium voxel is required rather than just an estimation of a single aberration transmittance $\mathrm{T}(\mathbf{u})$. To that aim, a local correlation matrix $\mathbf{C}(\mathbf{r}_\mathrm{p})$ (Eq. 3.33) should be considered around each point $\mathbf{r}_\mathrm{p}$ over a sliding box $\mathcal{W}(\mathbf{r})$. The choice of its spatial extension $\mathbf{w}$ is subject to the following dilemma:

Spatial extension dilemma

On the one hand, the spatial window $\mathcal{W}$ should be as small as possible to grasp the rapid variations of the RPSFs across the field of view. On the other hand, these areas should be large enough to encompass a sufficient number of independent realizations of disorder [Lambert, 2022a]. More quantitatively, the bias made on our $\mathbf{T}$-matrix estimator at the output actually scales as (see Appendix 5.3):

$$||\delta\hat{\mathrm{T}}_\mathrm{out}(\mathbf{u},\mathbf{r})||^2 \sim \frac{1}{C_\mathrm{in}^2 N_\mathcal{W}}. \tag{3.44}$$

C is the so-called coherence factor, already introduced in Chapter 1, which is a direct indicator of the focusing quality [Mallart, 1994], but that also depends on the multiple scattering rate and the noise background [Lambert, 2022b]. $N_\mathcal{W}$ is the number of diffraction-limited resolution cells in each spatial window. This expression is more precise than the one presented in Chapter 2 (see Section 4.6.5) because it also takes into account the effects of noise and multiple scattering, which will also affect the estimation of $\mathbf{T}$.

To study experimentally this convergence of our estimator, the evolution of estimated input and output aberration phase laws, $\hat{\mathrm{T}}_\mathrm{in/out}(\mathbf{u},\mathbf{r}_\mathrm{p})$, is investigated at a given point $\mathbf{r}_\mathrm{p}$ for different box size $\mathbf{w}$. $\hat{\mathbf{T}}_\mathrm{in}$ is supposed to converge for a sufficiently large box size ($N_\mathcal{W} = 100$) and this asymptotic value can be considered as the reference $\mathbf{T}_\mathrm{in}$ in the following. The evolution of the normalized scalar product,

$$\langle\hat{\mathbf{T}}_\mathrm{in}|\mathbf{T}_\mathrm{in}\rangle = \frac{\left|\hat{\mathbf{T}}_\mathrm{in}^\dagger \times \mathbf{T}_\mathrm{in}\right|}{\sqrt{\|\hat{\mathbf{T}}_\mathrm{in}\|^2\|\mathbf{T}_\mathrm{in}\|^2}} = N_u^{-1}\left|\hat{\mathbf{T}}_\mathrm{in}^\dagger \times \mathbf{T}_\mathrm{in}\right|, \tag{3.45}$$

as a function of $N_\mathcal{W}$ shows the convergence of the IPR process [Fig. 3.13D]. The error made on the aberration phase law, $||\delta\hat{\mathbf{T}}||^2/2 = 1 - \langle\hat{\mathbf{T}}_\mathrm{in}|\mathbf{T}_\mathrm{in}\rangle$, can be deduced and the scaling law of

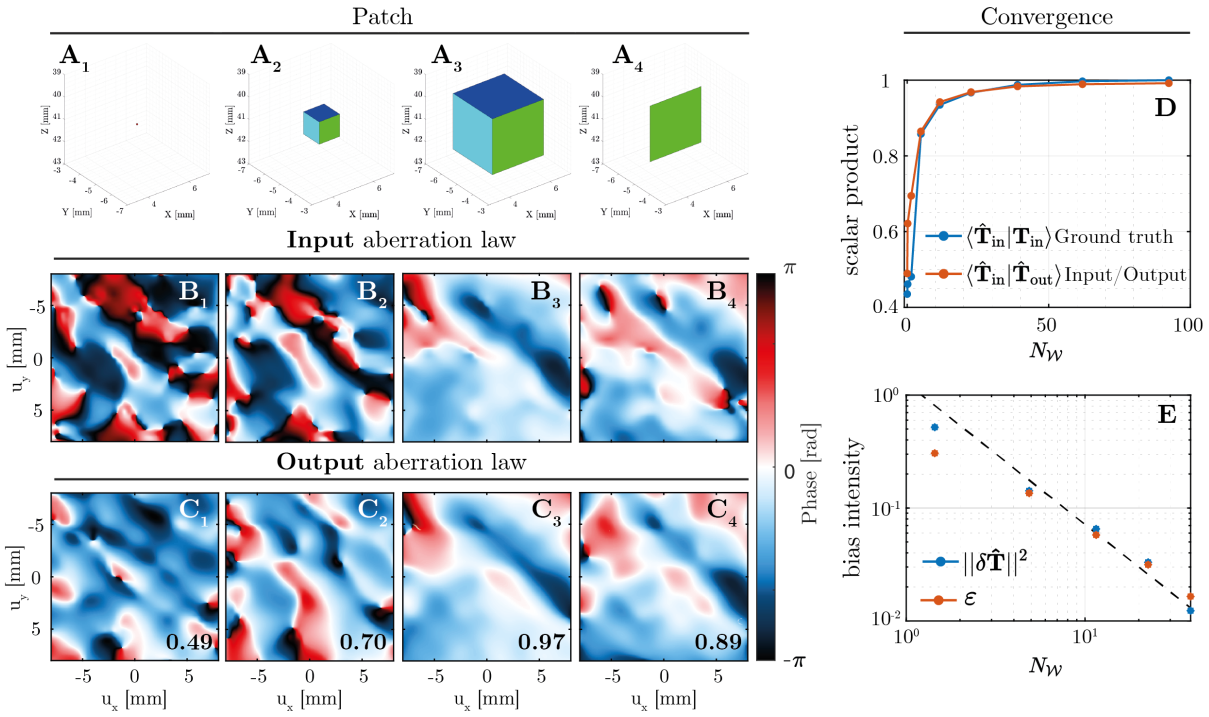

Figure 3.13: **Convergence of the UMI process towards the T-matrix.** (**A**) Spatial window $\mathcal{W}(\mathbf{r})$ used to compute $\mathbf{C}(\mathbf{r}_\mathrm{p})$ at point $\mathbf{r}_\mathrm{p} = (5, -5, 41)$ mm. (**B**,**C**) Extracted input and output aberration laws, respectively. (**D**) Scalar products, $\langle \hat{\mathbf{T}}_\mathrm{in} | \mathbf{T}_\mathrm{in} \rangle (\mathbf{r}_\mathrm{p})$ (blue curve) and $\langle \hat{\mathbf{T}}_\mathrm{in} | \hat{\mathbf{T}}_\mathrm{out} \rangle (\mathbf{r}_\mathrm{p})$ (orange curve), versus the number of resolution cells $N_\mathcal{W}$. (**E**) Corresponding bias intensity, $||\delta\hat{\mathbf{T}}||^2$ (blue curve), compared with its estimator ε (orange curve) based on spatial reciprocity, as a function of $N_\mathcal{W}$. The plot is in log-log scale and the theoretical power law (Eq. 3.44) is shown for comparison with a dashed black line.

(Eq. 3.44) with respect to $N_\mathcal{W}$ is checked [Fig. 3.13E].

The question that arises now is how we can, in practice, know if the convergence of $\hat{\mathbf{T}}$ is fulfilled without any *a priori* knowledge on $\mathbf{T}$. An answer can be found by comparing the estimated input and output aberration phase laws in [Fig. 3.13]. For a sufficiently large box ($N_\mathcal{W} > 50$), $\hat{\mathbf{T}}_\mathrm{in}$ and $\hat{\mathbf{T}}_\mathrm{out}$ are almost equal, while, for a small box ($N_\mathcal{W}$ <20), a large discrepancy can be found between them. Thus, their scalar product $\langle \hat{\mathbf{T}}_\mathrm{in} | \hat{\mathbf{T}}_\mathrm{out} \rangle$ is a relevant observable for monitoring the convergence of our estimator $\hat{\mathbf{T}}$. Its evolution actually closely follows the scalar product between $\hat{\mathbf{T}}_\mathrm{in}$ and $\mathbf{T}_\mathrm{in}$ previously investigated [Fig. 3.13D], which means that the parameter, $\varepsilon = 1 - \langle \hat{\mathbf{T}}_\mathrm{in} | \hat{\mathbf{T}}_\mathrm{out} \rangle$, is a reliable estimator of the bias intensity $||\delta\hat{\mathbf{T}}||^2/2$ [Fig. 3.13E]. In the following, spatial reciprocity will thus be used as a guide star for assessing the convergence of the UMI process.

This inverse scaling of the bias with $N_\mathcal{W}$ demonstrates the advantage of 3D UMI with respect to 2D since $N_\mathcal{W} \sim \mathbf{w}^d$, with d the imaging dimension. For a given precision, 3D UMI provides a better spatial resolution for our $\mathbf{T}-$matrix estimator. This superiority is demonstrated by [Fig. 3.13C$_3$,C$_4$] that shows a much better agreement between $\hat{\mathbf{T}}_\mathrm{in}$ and $\hat{\mathbf{T}}_\mathrm{out}$ for a 3D box [Fig. 3.13A$_3$] than for a 2D patch of equal dimension $\mathbf{w}$ [Fig. 3.13A$_4$]. [Fig. 3.14] also demonstrates this superiority. When considering a subdivision of the field-of-view in 2D-planes

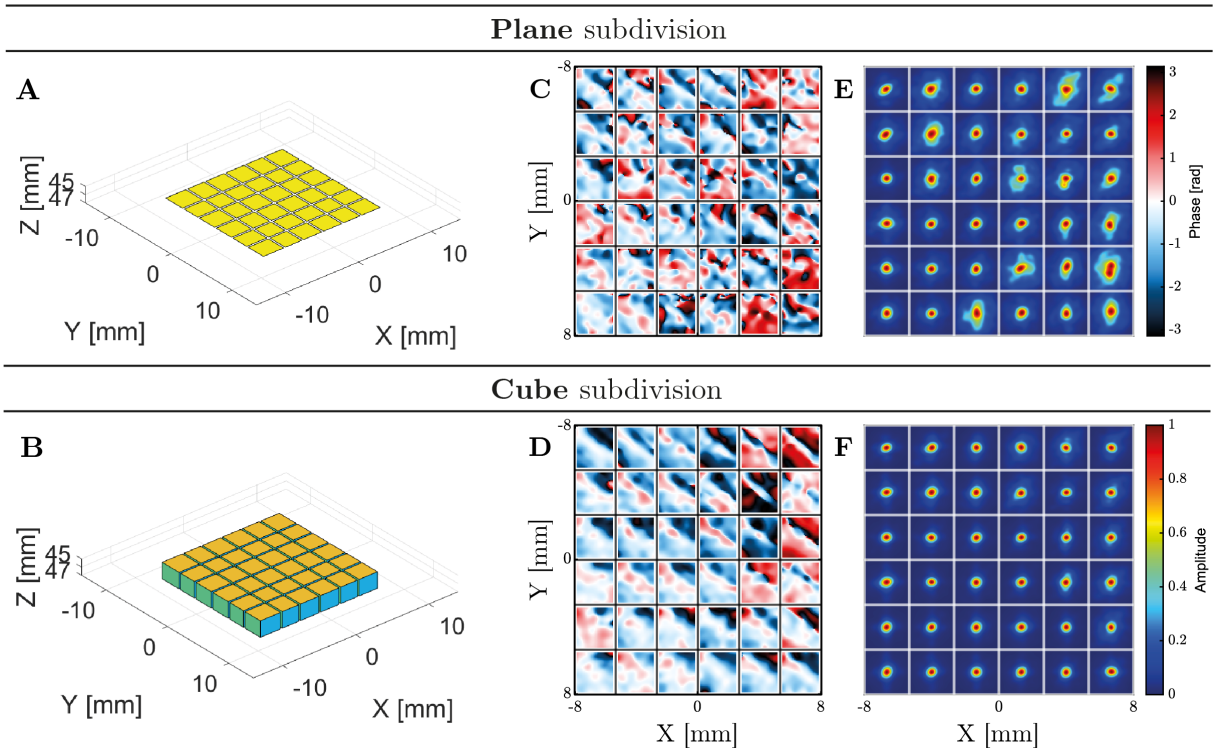

Figure 3.14: **Estimation of $\hat{\mathbf{T}}$ on 2D or 3D patches** (Pork chop experiment, $z = 46$ mm). **(A, B)** Plane or cube subdivision of the field-of-view with their corresponding **(C, D)** aberration laws and **(E, F)** corrected RPSFs, respectively. The correction is applied to a neighboring upstream region to avoid any bias between the $\hat{\mathbf{T}}-$estimation and the correction process, assuming isoplanetism between the two areas.

[Fig. 3.14A], the convergence of the $\hat{\mathbf{T}}-$matrix is not ensured [Fig. 3.14C] leading to an imperfect correction of RPSFs [Fig. 3.14E]. Subdivision in cubes [Fig. 3.14B] allows us to average over sufficient resolution cells, leading to diffraction limited resolution [Fig. 3.14F]. The correction is applied to a neighboring upstream region to avoid any bias between the estimation of $\mathbf{T}$ and the correction process, assuming isoplanetism between the two areas.

4.3.7 Multi-scale compensation of wave distortions

The dependence of the bias intensity $||\delta\hat{\mathbf{T}}||^2$ with the coherence factor C is also crucial, since it indicates that a gradual compensation of aberrations shall be favored rather than a direct partition of the field-of-view into small boxes [Yoon, 2020]. An optimal UMI process should proceed as follows: first, compensate for input and output wave distortions at a large scale to increase the coherence factor C; then, decrease the size of the spatial window $\mathcal{W}$ to improve the resolution of the $\mathbf{T}-$matrix estimator. The whole process can be iterated, leading to a multi-scale compensation of wave distortions.

[Fig. 3.15] demonstrates the benefit of a multi-scale analysis of wave distortions with a gradual decrease of spatial windows $\mathcal{W}$ at each step of the UMI process [Fig. 3.15A]. To that aim, this aberration correction scheme is compared with a direct estimation of the $\mathbf{T}-$matrix over the smallest patches $\mathcal{W}$ [Fig. 3.15D]. The estimated transmission matrices $\hat{\mathbf{T}}$ differ in both cases

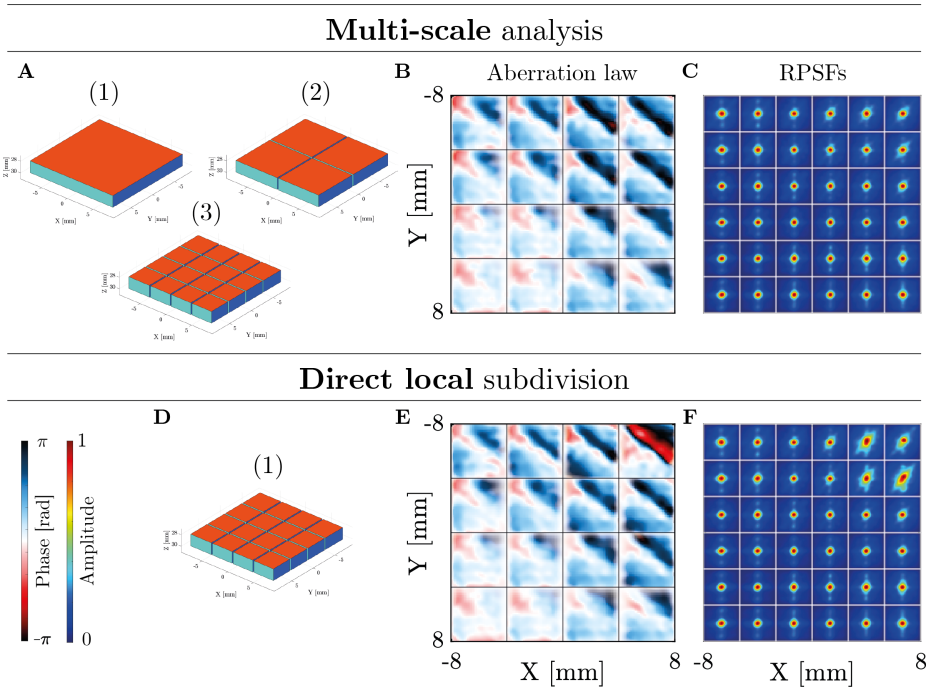

Figure 3.15: **Multi-scale *versus* direct local analysis of wave distortions** (pork chop experiment, $z = 29$ mm). (**A**) Representation of the spatial windows used at each step of UMI. (**B**) Aberration phase laws $\hat{\mathbf{T}}_{\text{multi-scale}}$ extracted by a multi-scale analysis. (**C**) RPSFs after multi-scale aberration compensation. (**D**) Representation of the spatial windows used for a direct local compensation of wave distortions. (**E**) Aberration phase laws $\hat{\mathbf{T}}_{\text{direct}}$ extracted by a local analysis of **D**. (**F**) RPSFs after local aberration compensation.

[see comparison between Fig. 3.15B and E] especially under the fat layer. The RPSFs obtained after phase conjugation of $\hat{\mathbf{T}}$ demonstrate the benefit of the multi-scale analysis [Fig. 3.15C] compared with a direct local investigation of wave distortions [Fig. 3.15F]. The fat area is actually the most aberrated in the field-of-view. The initial coherence factor C is thus much smaller in this area, which induces a strong bias on $\hat{\mathbf{T}}$ when wave distortions are investigated over a reduced isoplanatic patch. On the contrary, a multi-scale analysis enables a gradual enhancement of this coherence factor in this area and finally leads to an unbiased estimation of $\mathbf{T}$.

To ensure the convergence of the IPR algorithm, several iterations of the aberration correction process are thus performed while reducing the size of the patches $\mathcal{W}$ with an overlap of 50% between them. Three correction steps are performed, as described in [Table 3.2] and [Fig. 3.16A-C]. At each step, the correction is performed both at input and output. Each step gives access to higher spatial frequencies of the aberration phase laws that generally exhibit a smaller isoplanatic length [Fig. 3.16E-G].

Technical note: The $\hat{\mathbf{T}}-$matrix [Fig. 3.16D] denotes the cumulated aberration laws that

Correction step (i)	1°	2°	3°
Number of transverse patches	1×1	2×2	4×4
$w_{\boldsymbol{\rho}} = (w_x, w_y)$ [mm]	16	12	8
w_z [mm]	3	3	3

Table 3.2: **Size of the correction patches $\mathcal{W}$ in the pork chop expriment.**

combine the $\hat{\mathbf{W}}^{(i)}-$matrix associated to each step (i) of the correction process [Fig. 3.16E-G]:

$$\hat{\mathbf{T}}_{\text{in/out}} = \prod_i \hat{\mathbf{W}}^{(i)}_{\text{in/out}}. \tag{3.46}$$

Correction of the $\mathbf{R}-$matrix (equation 3.43) is applied only if spatial reciprocity is ensured at each step, *i.e.* if the scalar product $\langle \hat{\mathbf{W}}^{(i)}_{\text{in}} | \hat{\mathbf{W}}^{(i)}_{\text{out}} \rangle$ is larger than 0.9 (see Appendix 5.4).

The result of 3D UMI is displayed in [Fig. 3.16]. It shows the evolution of the $\hat{\mathbf{T}}-$matrix at each step [Fig. 3.16E-G] and the corresponding local RPSFs [Fig. 3.16I-K]. The comparison with the initial and full-field maps of RPSFs [Fig. 3.16H] highlights the benefit of a local compensation via the $\hat{\mathbf{T}}-$matrix, with a diffraction-limited resolution reached everywhere. The local aberration phase laws exhibited by $\hat{\mathbf{T}}$ perfectly match with the distribution of muscle and fat in the pork chop.

4.3.8 Contrast & resolution enhancement

The comparison of the final 3D image and its cross-sections [Fig. 3.17A_2, B_2, C_2] with their initial counterparts [Fig. 3.17A_1, B_1, C_1] shows the success of the UMI process, in particular for the deepest nylon rod, which has retrieved its straight shape. [Fig. 3.17D, E] shows the performance of UMI by comparing the RPSFs before and after aberration compensation. In the most aberrated area (top right of the field-of-view), **the resolution is improved by almost a factor two, while the contrast is increased by 4.2 dB**.

4.4 Computational insights

While the UMI process is close to real-time for 2D imaging (*i.e.* for linear, curve or phased array probes), 3D UMI (using a fully populated matrix array of transducers) is still far from it [see Tab. 3.3] as it involves the processing of much more ultrasound data. Even if computing a confocal 3D image only requires a few minutes, building the focused $\mathbf{R}-$matrix from the raw data takes a few hours (on GPU with CUDA language) while one step of aberration correction only lasts for a few minutes. All the post-processing was realized with Matlab (R2021a) on a working station with 2 processors @2.20GHz, 128Go of RAM, and a GPU with 48 Go of dedicated memory.

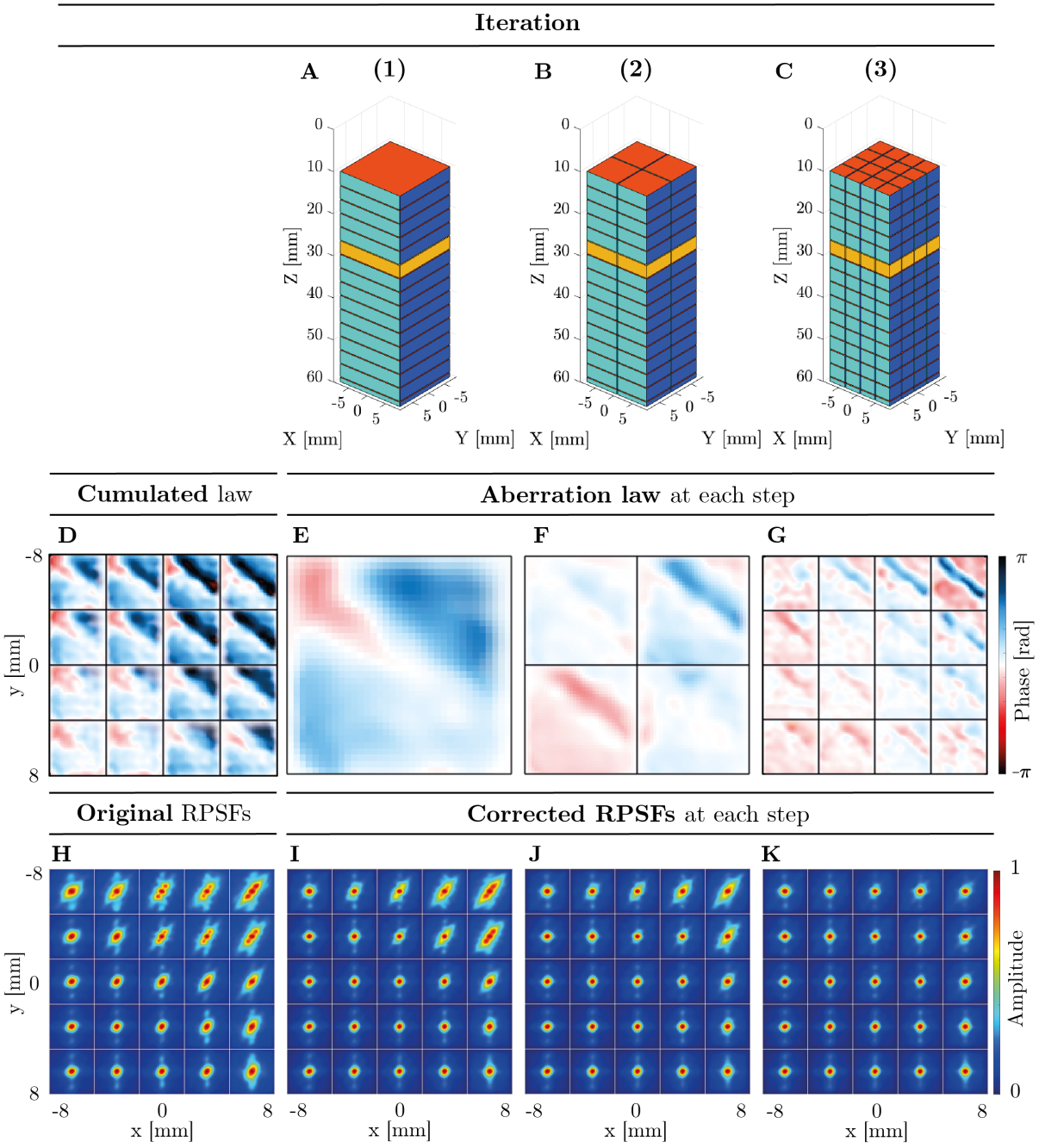

Figure 3.16: **Iteration and subdivision** (Pork chop experiment). **(E-G)** Aberration laws $\hat{\mathbf{W}}_{\text{in/out}}^{(i)}$ and **(I-K)** corrected RPSFs corresponding to each **(A-C)** step of correction (yellow box). **(D)** Cumulated aberration laws $\hat{\mathbf{T}}_{\text{in/out}}$ (Eq. 3.46). **(H)** Original RPSFs.

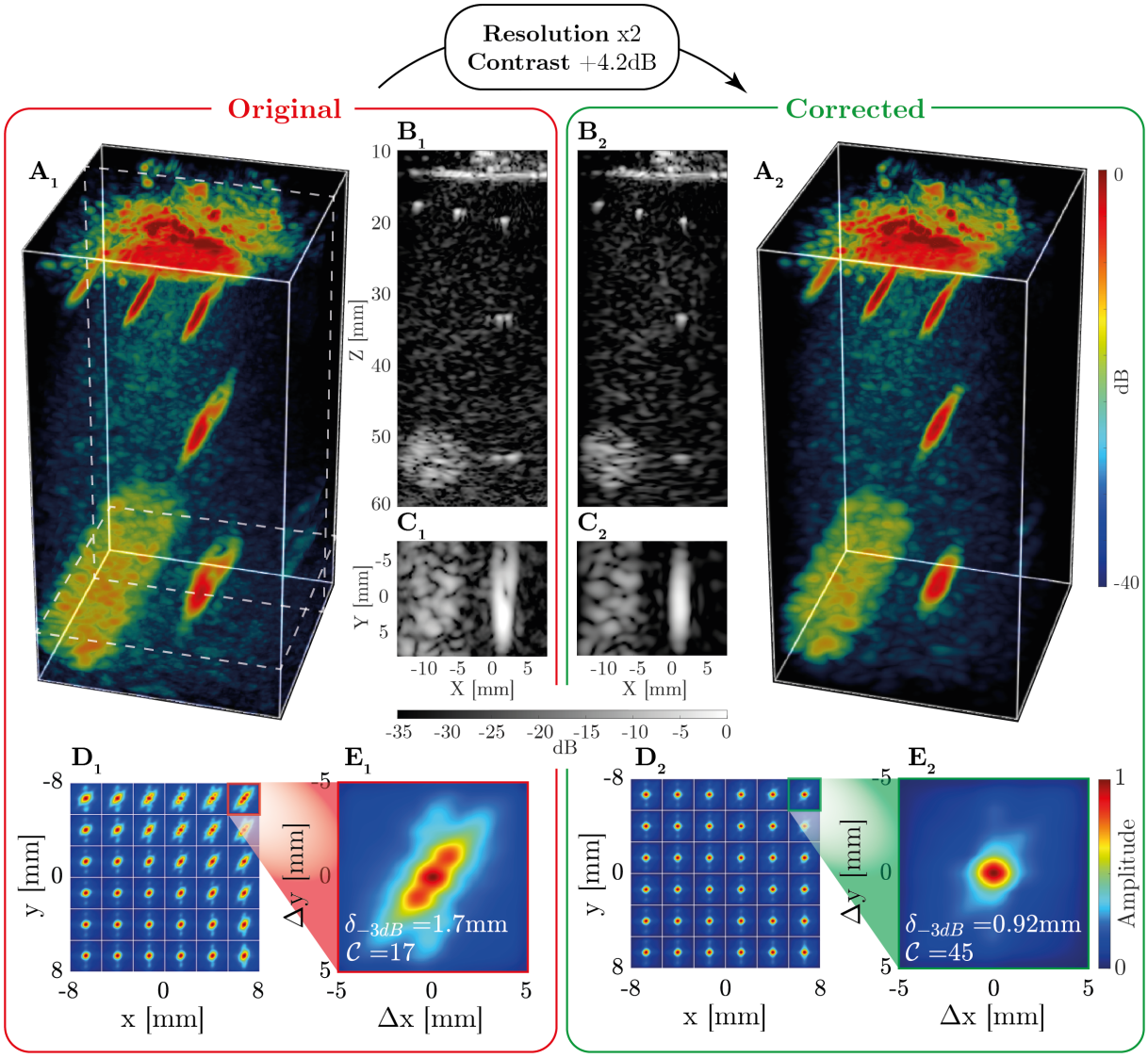

Figure 3.17: **Enhancement of the confocal volume and RPSFs after UMI process in the pork chop experiment.** (**A**) MIP volume. (**B, C**) Longitudinal and transverse cross-section, respectively. (**D**) Maps of local RPSFs ($z = 29$ mm). (**E**) A single RPSF extracted in the most aberrated area of the field-of-view. Subscript "1" and "2" corresponds to before and after the UMI process, respectively.

		2D imaging		**3D** imaging	
Number of channels [Input × Output]		$32 \times 32 \approx 10^3$		$1024 \times 1024 \approx 10^6$	
Field-of-view $(\Delta x, \Delta y, \Delta z)$		$(20, 0, 80)$ mm		$(20, 20, 80)$ mm	
		Data	**Time**	**Data**	**Time**
R-matrix acquisition $\mathbf{R_{uu}}(t)$		6 Mo	8 ms	6 Go	260 ms
Confocal image $\mathcal{I}(\mathbf{r})$		53 ko	5.1 ms	2.2 Mo	1.3 min
Matrix Imaging	Focused $\mathbf{R}-$matrix: $\mathbf{R}_{\boldsymbol{\rho\rho}}(z)$	2.2 Mo	15 ms	3.6 Go	2.3 h
	Estimation of $\hat{\mathbf{T}}$ & correction		0.15 s		4.5 min

Table 3.3: **Computational insights.** Here, we compare the typical amount of data and computational time at each post-processing step of UMI. The comparison between 2D and 3D imaging is made using a single line of transducers *versus* all the transducers of our matrix array. In both cases, the pixel/voxel resolution is fixed at 0.5 mm, which corresponds approximately to one wavelength. The maximum distance between the input and output focusing points is set to 10 mm. The estimation of **T** is here investigated without a multi-scale analysis on a single iteration at input and output.

5 Transcranial imaging

We will now address the challenging case of transcranial imaging, where the cranial layer not only induces large aberrations and reverberation artifacts, but also multiple scattering, absorption, wave mode conversion [Jing, 2021; Clement, 2004], and strong attenuation [Pinton, 2012; Hölscher, 2008], typically between $2-3$ dBcm^{-1}MHz^{-1} [White, 1978], resulting in a very low signal-to-noise ratio. As a result, transcranial ultrasound imaging is currently limited clinically to poorly resolved Doppler imaging. Yet, emerging aberration correction methods, such as the distortion matrix approach, suggest that images of the brain could be obtained with much better contrast and resolution, from which all existing ultrasound imaging modalities could benefit (B-mode, Doppler, elastography, ULM, etc.). Its success would mean a new way of imaging the brain that does not require radiation as in X-ray computed tomography (CT-scan) neither a long acquisition as in magnetic resonance imaging (MRI). Transcranial ultrasound imaging could therefore potentially be used for cancer detection or even real-time detection of cerebral-vascular accidents. In this section, we will apply the distortion matrix framework to an imaging experiment on an **adult head phantom**.

Existing methods allow focusing through the skull, but require either *a priori* information about the medium, such as skull layer segmentation [Mozaffarzadeh, 2021], density map extracted with a CT-scan [Aubry, 2003; Tiennot, 2019], or an ultrasound *guide star* in the field-of-view (*e.g.* microbubble contrast agent or the presence of a strong reflector) [Demené, 2021].

In this first experiment, we aim to demonstrate the advantages of Matrix Imaging for correcting aberrations in transcranial imaging **without *prior* information about the medium** other than a global speed-of-sound hypothesis c_0. In other words, matrix imaging allows the estimation of the transmission matrix $\hat{\mathbf{T}}$ in transcranial imaging not only for strong reflectors but also for under resolved scatterers (speckle).

5.1 Head phantom characteristics

The adult head phantom reproduces the characteristics of an adult human head [Table 3.4]. To quantify the enhancement before and after correction, the manufacturer (True Phantom Solutions) was asked to place small spherical targets made of bone-mimicking material inside the brain. They are arranged crosswise, evenly spaced in the 3 directions with a distance of 1 cm between two consecutive targets, and their diameter increases with depth: 0.2, 0.5, 1, 2, 3 mm [Fig. 3.18].

	Speed-of-sound [m/s]	**Density** [g/cm^3]	**Attenuation** @2.25 MHz [dB/cm]
Cortical bone	3000 ± 30	2.31	6.4 ± 0.3
Trabecular bone	2800 ± 50	2.03	21 ± 2
Brain tissue	1400 ± 10	0.99	1.0 ± 0.2
Skin tissue	1400 ± 10	1.01	1.7 ± 0.2

Table 3.4: **Head phantom characteristics.**

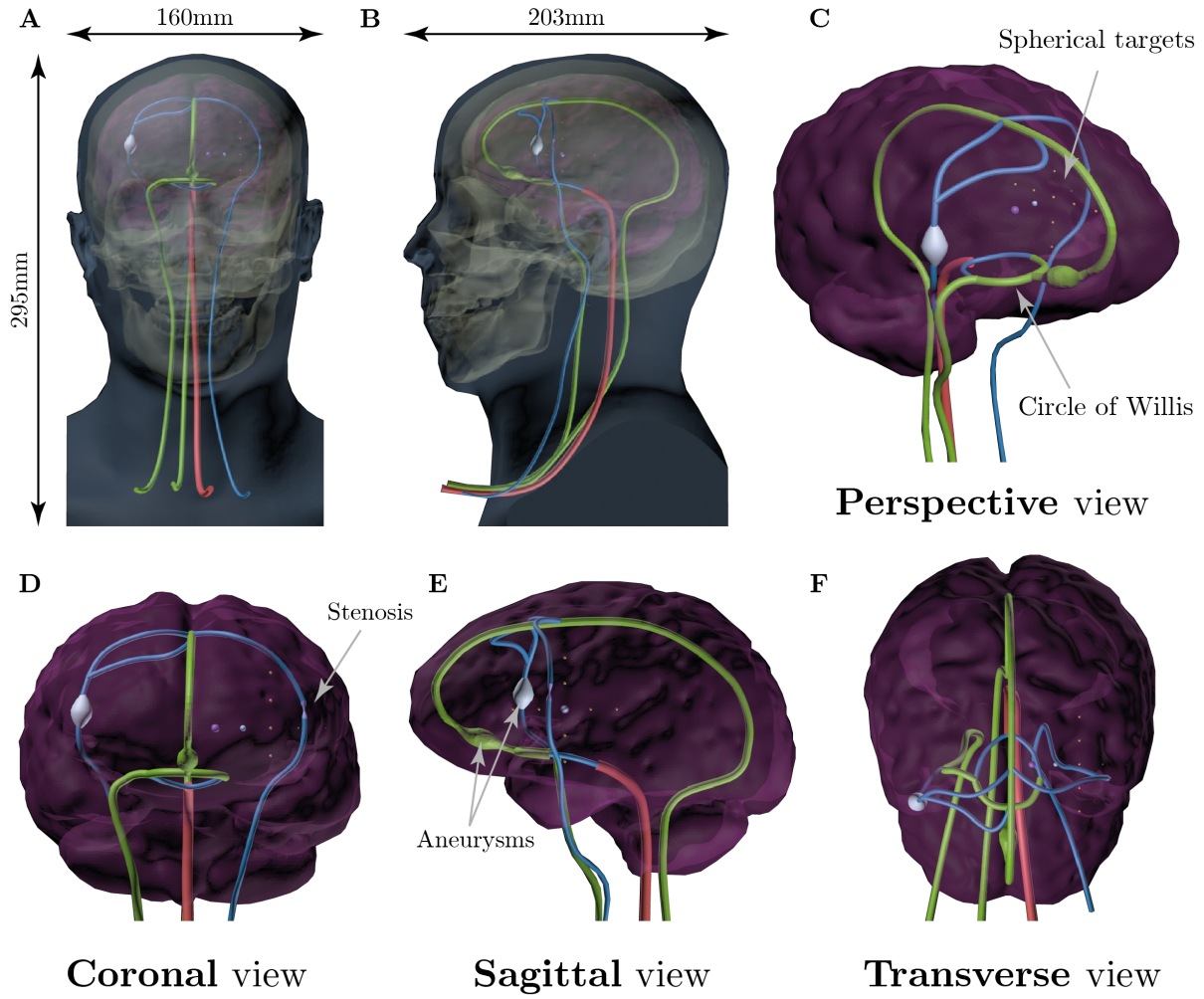

Figure 3.18: **Head phantom schematics. (A, B)** Coronal and sagittal view of the head phantom **(C-F)** Perspective, coronal, sagittal and transverse view of the brain. Small spherical targets made of bones have been placed in the brain as a 3D cross-shaped with increasing diameters : 0.2 , 0.5, 1, 2, 3mm. These schematics were provided by the manufacturer (True Phantom Solutions).

5.2 R−matrix acquisition

Ultrasound acquisition was performed jointly with Justine Robin while she was a post-doc at the Langevin Institute. The matrix array $\mathcal{P}_1$ is placed slightly above the temporal window of the head phantom [Fig. 3.23A]. Impedance matching is performed with acoustic gel. To improve the signal-to-noise ratio, the reflection matrix is recorded in the plane wave basis $\mathbf{R}_{\boldsymbol{\theta}\mathbf{u}}(t) \equiv [R(\boldsymbol{\theta}_{\text{in}}, \mathbf{u}_{\text{out}}, t)]$ [Montaldo, 2009]. A set of 1225 plane waves are thus generated according to (equation 3.2, 3.3 & 3.4, 3.5) and assuming the speed-of-sound in the brain mimicking tissue ($c_0 = 1400$ m/s). Acquisition was repeated 10 times and averaged to improve the SNR.

Skull thickness is of about 6 mm on average at the position where the probe is placed and the first spherical target is located at $z \approx 20$ mm depth, while the center of the cross is at $z \approx 40$ mm depth. The transverse size of the head is of about 14 cm.

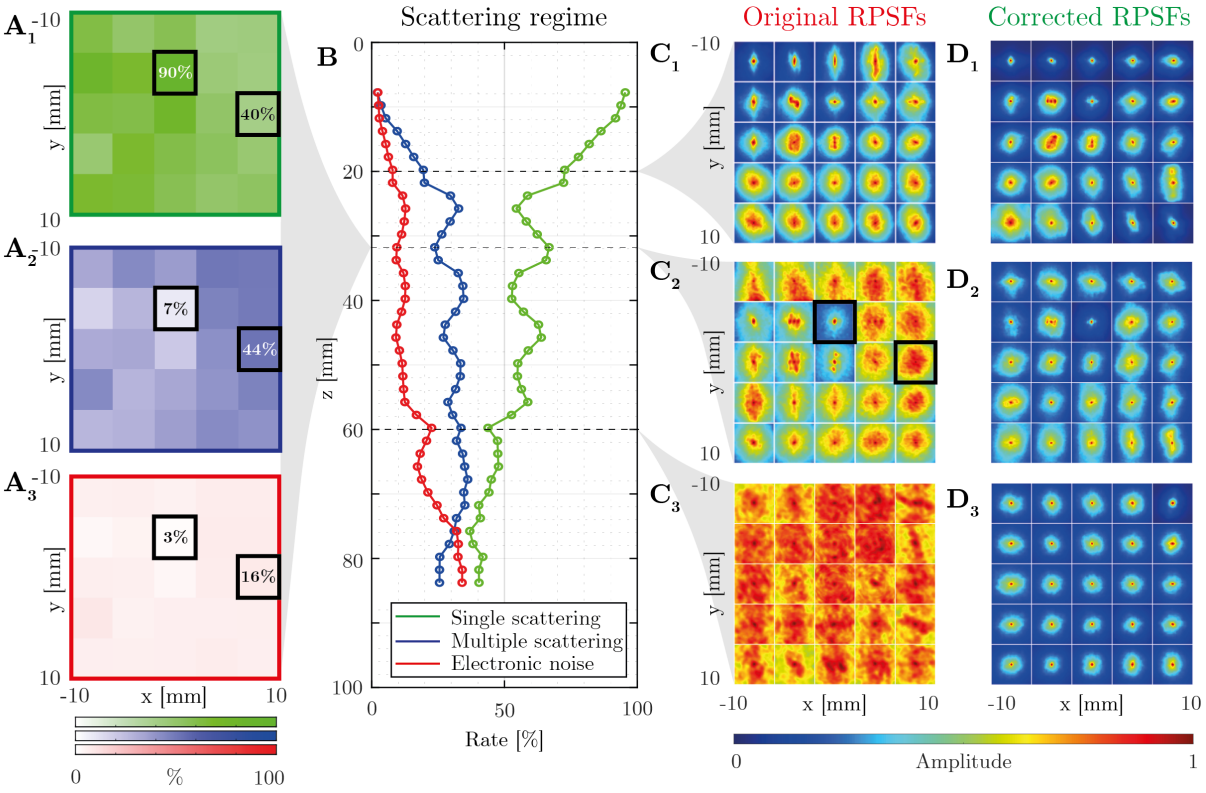

Figure 3.19: **Aberrations and multiple scattering quantification in the head phantom.** (**A**) Single scattering (green), multiple scattering (blue) and noise (red) rate at $z = 32$ mm (**B**) Single scattering, multiple scattering, and noise rates as a function of depth. (**C, D**) Maps of local RPSFs (in amplitude) before and after correction, respectively, at three different depths $z = 20$, 32 and 60 mm. Black boxes in panel (**A**) and ($\mathbf{C}_2$) corresponds to the same area.

5.3 Focusing quality

Before any correction, we quantify the problems of aberrations, multiple scattering, and noise by examining the RPSFs. To this end, the focused reflection matrix $\mathbf{R}_{\rho\rho}(z)$ is still built numerically in the time domain, according to (equation 3.10, 3.11 & 3.12) and assuming the speed-of-sound of the brain mimicking tissue ($c_0 = 1400$ m/s).

The RSPFs are characterized by a high proportion of incoherent background. This is due to multiple scattering events in the skull and electronic noise, whose relative weight can be estimated by examining the spatial reciprocity through the symmetry of the **R**-matrix (equation 3.26). [Fig. 3.19B] shows the depth evolution of the single and multiple scattering contributions, as well as electronic noise. While single scattering dominates at shallow depths ($z < 20$ mm), multiple scattering quickly reaches 35% and remains relatively constant until electronic noise increases, so that the three contributions are almost equal at depths of 75 mm. Beyond the depth evolution, 3D imaging even allows the study of multiple scattering in the transverse plane, as shown in [Fig. 3.19A]. Two areas are examined, marked with black boxes, corresponding to the RPSFs shown in [Fig. 3.19C_2] ($z = 32$ mm). In the center, the RPSFs exhibits a low background due to the presence of a spherical target, resulting in a single scattering rate of 90%. The

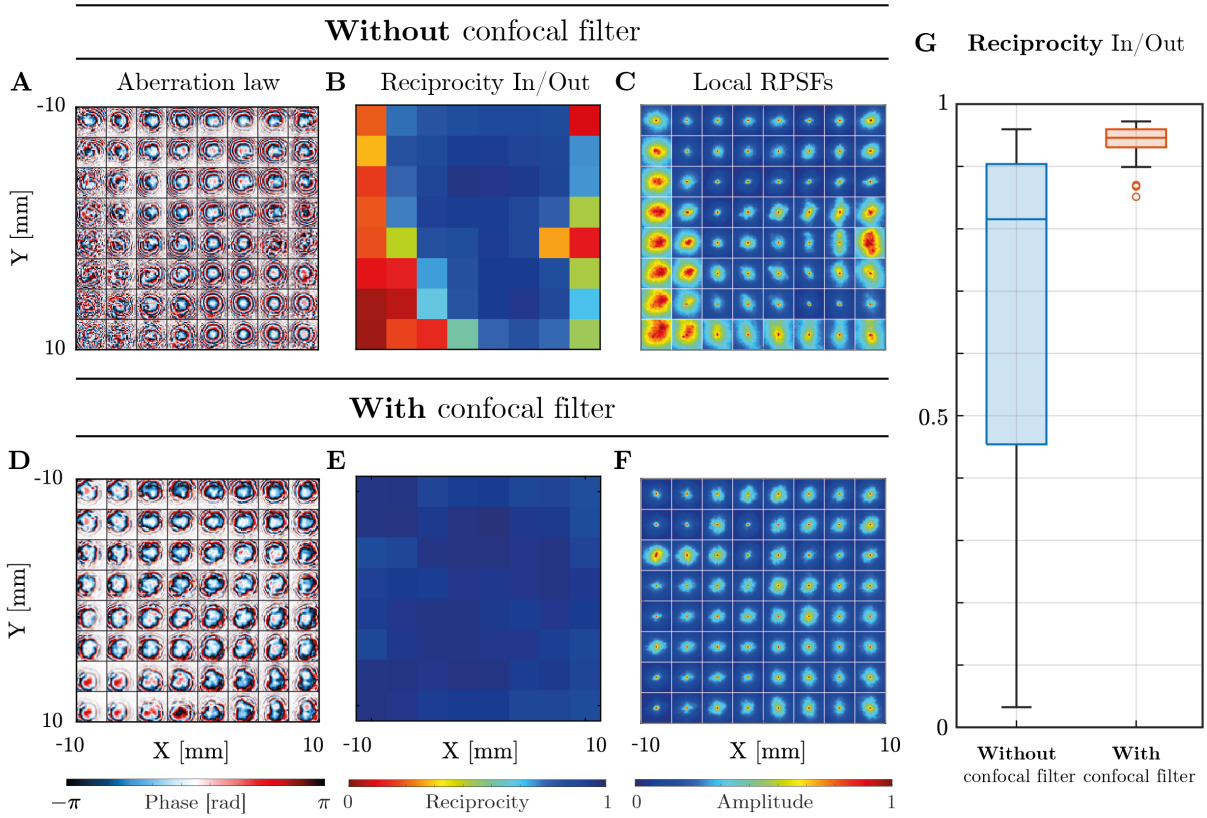

Figure 3.20: **Confocal filter in transcranial imaging.** (**A**, **D**) Output aberration phase laws $\hat{\mathbf{T}}_{\text{out}}$ extracted without and with a confocal filter. (**B**, **E**) Normalized scalar products $\langle \hat{\mathbf{T}}_{\text{in}} | \hat{\mathbf{T}}_{\text{out}} \rangle$ without and with a confocal filter, respectively. (**C**, **F**) RPSFs obtained with UMI without and with a confocal filter. (**G**) Box plot corresponding to the panels (**B**, **E**). Experimental data shown in this figure correspond to the head phantom experiment at depth $z = 50$ mm.

second box on the right, however, is characterized by a much higher background, leading to a multiple-to-single scattering ratio slightly larger than one. This high level of multiple scattering highlights the difficult task of trans-cranial imaging with ultrasonic waves.

The incoherent background exhibited by the original RPSFs [Fig. 3.19C] drastically affects the coherence factor C, which, in return, gives rise to a strong bias on the $\mathbf{T}-$matrix estimator (Eq. 3.44). Hence, our criterion based on spatial reciprocity between the input and output estimation of the transmission matrix $\langle \hat{\mathbf{T}}_{\text{in}} | \hat{\mathbf{T}}_{\text{out}} \rangle$ is therefore far from being verified over the entire field of view, as shown in [Fig. 3.20B].

5.4 Confocal filter

In order to overcome these detrimental effects, an adaptive confocal filter can be applied to the focused $\mathbf{R}-$matrix to reduce the incoherent background [Lambert, 2022a].

$$\mathbf{R}^{(\text{filt})}_{\boldsymbol{\rho}\boldsymbol{\rho}}(z) = R(\boldsymbol{\rho}_{\text{in}}, \boldsymbol{\rho}_{\text{out}}, z) \exp\left(-\frac{|\boldsymbol{\rho}_{\text{out}} - \boldsymbol{\rho}_{\text{in}}|^2}{2 l_c(z)^2} \right). \tag{3.47}$$

This filter has a Gaussian shape, with a width $l_c(z)$ that scales as $3\delta\rho_0(z)$ [Lambert, 2022a]. The application of a confocal filter drastically improves the correlation between input and output aberration phase laws [Fig. 3.20E], proof that a satisfying convergence towards the $\mathbf{T}-$matrix is obtained.

Technical note: The confocal filter is applied to a duplicate of the $\mathbf{R}-$matrix to estimate the $\hat{\mathbf{T}}-$ matrix. However, **the unfiltered $\mathbf{R}-$matrix is corrected** to preserve all useful information about the medium (*i.e.* spatial frequencies) at each step of correction.

5.5 Estimation of $\hat{\mathbf{T}}$

A similar UMI procedure is now applied to this experiment. However, given the multi-layered configuration in this experiment, the $\mathbf{D}-$matrix is examined in the plane wave basis ($\mathbf{k}$) [Lambert, 2020c]. Six correction steps are performed as described in [Table 3.5].

[Fig. 3.21] shows the evolution of the RPSF during the UMI process applied to the head phantom experiment. A gradual enhancement of the focusing process is observed at each step of UMI, which enables an estimation of the $\mathbf{T}-$matrix at a higher resolution. Correction is stopped if spatial reciprocity $\langle \hat{\mathbf{T}}_{\text{in}}^{(i)} | \hat{\mathbf{T}}_{\text{out}}^{(i)} \rangle$ does not reach 0.9 at each step of correction (i).

Correction step (i)	1°	2°	3°	4°	5°	6°
Number of transverse patches	1×1	2×2	3×3	4×4	5×5	6×6
$w_{\boldsymbol{\rho}} = (w_x, w_y)$ [mm]	20	15	13.3	10	8	6.6
w_z [mm]	5.5	5.5	5.5	5.5	5.5	5.5

Table 3.5: **Parameters of UMI in the head phantom experiment.**

[Fig. 3.22A] shows the $\hat{\mathbf{T}}-$matrix obtained at different depths in the brain phantom. Its spatial correlation function displayed in [Fig. 3.22B] provides an estimation of the isoplanatic patch size: 5 mm in the transverse direction and 2 mm in depth. This rapid variation of the aberration phase law across the field of view confirms *a posteriori* the necessity of a local compensation of aberrations induced by the skull. It also confirms the importance of 3D UMI with a fully sampled 2D array, as previous work recommended that the array pitch should be no more than 50% of the aberrator correlation length to properly sample the corresponding adapted focusing law [Lacefield, 2002]. If the size of the isoplanatic patch is consistent with values obtained in previous work for breast, liver, and thyroid [Dahl, 2005], the values in transcranial imaging appear higher here. In contrast to previous studies [Dahl, 2005; Robin, 2023], the correlation length in the axial dimension appears to be much smaller.

5.6 Resolution enhancement

The phase conjugate of the $\hat{\mathbf{T}}-$matrix at input and output enables a fine compensation of aberrations. A set of corrected RPSFs are shown in [Fig. 3.19D]. The comparison with their initial values demonstrates the success of 3D UMI: a diffraction-limited resolution is obtained almost everywhere [Fig. 3.21C], whether it be in ultrasound speckle or in the neighborhood of bright targets, at shallow or high depths, which proves the versatility of UMI. The correction

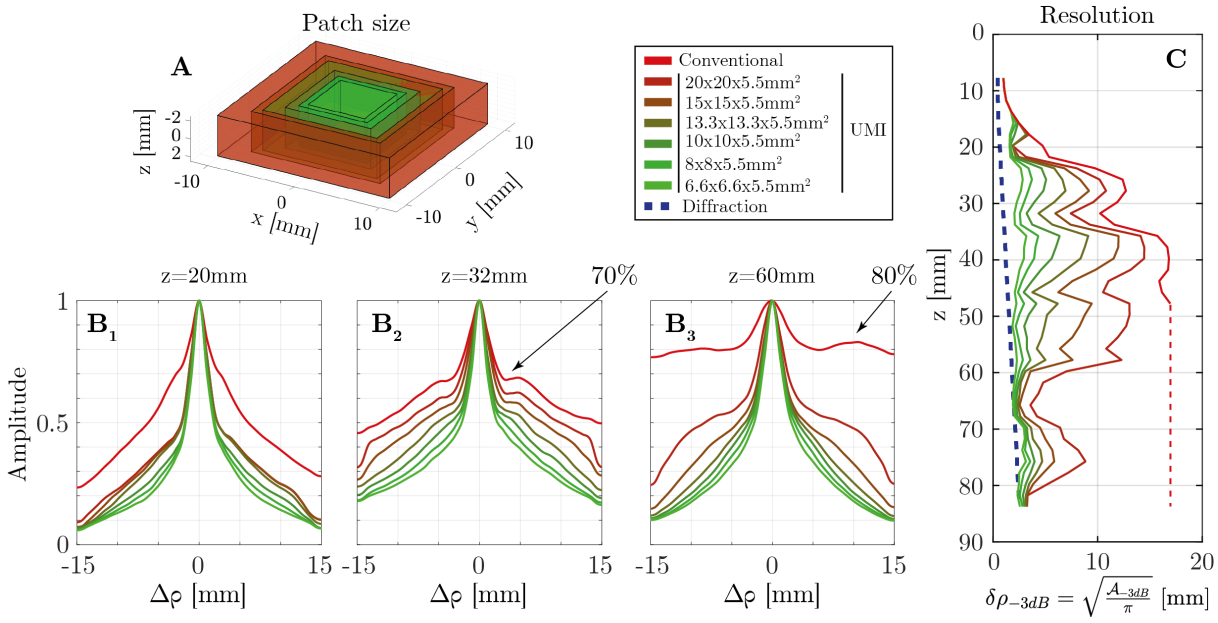

Figure 3.21: **Multi-scale compensation of wave distortions in the head phantom.** (**A**) Successive patches used to perform a multi-scale analysis of wave distortions. (**B**) Radial profile of the RPSF amplitude at each step for three different depths ($z = 20$, $z = 32$ and $z = 60$ mm). (**C**) Resolution $\delta_{(-3dB)}$ as a function of depth. Initial resolution (red line) and its value after UMI (green line) are compared with the ideal (diffraction-limited) resolution (Eq. 3.20). At large depth (red dashed line), initial resolution can not be extracted as the incoherent background is larger than 1/2 as shown in panel ($\mathbf{B}_3$).

process leads to a drastic increase of the transverse resolution of more than a factor 8 for $z > 40$ mm [Fig. 3.21C].

The performance of 3D UMI is also striking when comparing the three-dimensional image of the head phantom before and after UMI. [Fig. 3.23B and C, respectively]. The different targets were initially strongly distorted by the skull, and are now resolved with UMI. In particular, the first target, located at $z = 19$ mm and originally duplicated, has recovered its true shape. In addition, two targets laterally spaced by 10 mm are observed at 42 mm depth, as expected [Fig. 3.23A]. The image of the target observed at 54 mm depth is also drastically improved in terms of contrast and resolution but is not found at the expected transverse position. One potential explanation is the size of this target (2 mm diameter) larger than the resolution cell. The guide star is thus far from being point-like, which can induce an uncertainty on the absolute transverse position of the target in the corrected image.

5.7 2D *versus* 3D imaging

Finally, an isolated target can be leveraged to highlight the gain in contrast provided by 3D UMI with respect to its 2D counterpart. To that aim, a linear 1D array is emulated from similar raw data by collimating the incident beam in the y-direction [Fig. 3.24]. To that aim, cylindrical

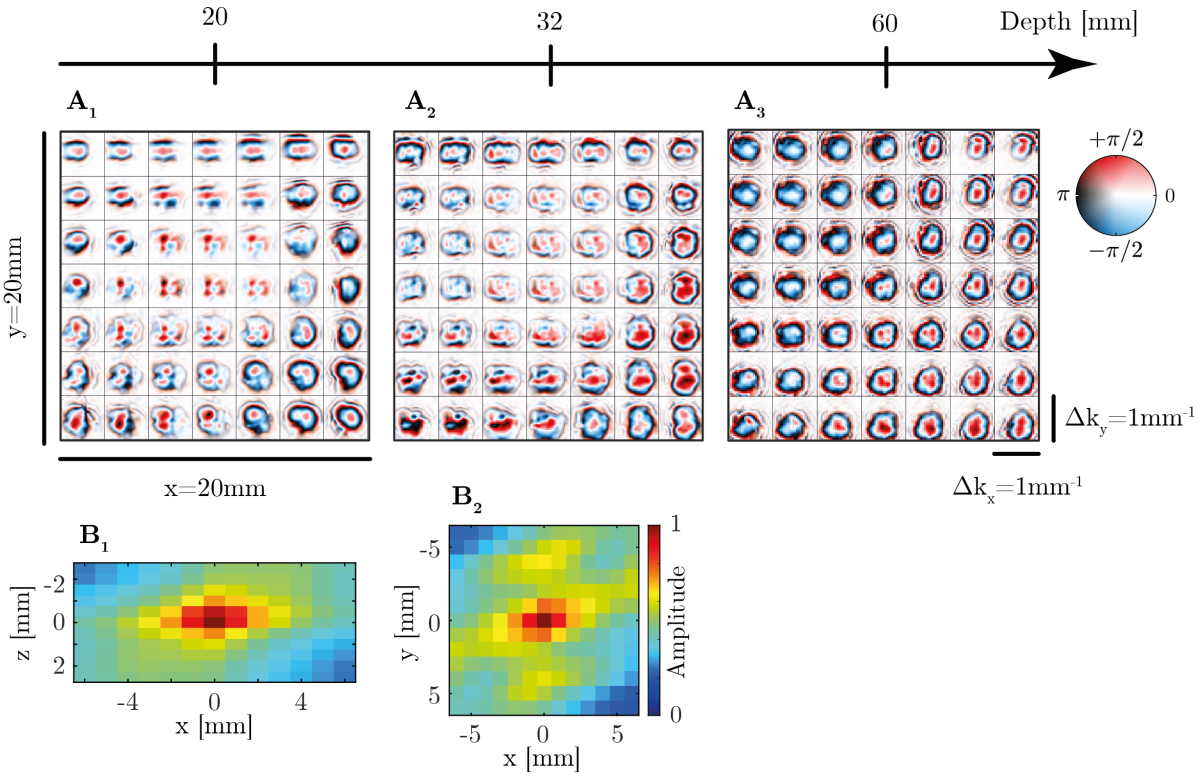

Figure 3.22: **Estimation of the transmission matrix in the head phantom.** (**A**) Aberration laws $\hat{\mathbf{T}}(\boldsymbol{\rho})$ at 3 different depths : ($\mathbf{A}_1$) $z = 20$ mm, ($\mathbf{A}_2$) $z = 32$ mm, ($\mathbf{A}_3$) $z = 60$ mm. (**B**) Correlation function of the $\hat{\mathbf{T}}$-matrix in the (xz) and (xy) plane, respectively. We attribute the side-lobes along the y-axis ($\mathbf{B}_2$) to the inactive rows separating each block of 256 elements of the matrix array.

time delays are applied at input and output:

$$\tau'(\theta^{(s)}, s, z) = \frac{s \sin\theta^{(s)} + z\cos\theta^{(s)}}{c_0}, \tag{3.48}$$

$$\tau'(u^{(s)}, s, z) = \frac{\sqrt{(s-u^{(s)})^2 + z^2}}{c_0}, \tag{3.49}$$

with $s = x$ or y, depending on our focus plane choice.

The focused $\mathbf{R}-$matrix is still built in the time domain but using this time the following delay-and-sum beamforming:

$$R^{(2D)}(y_{\text{in}}, y_{\text{out}}, z) = \sum_{\boldsymbol{\theta}_{\text{in}}}\sum_{\mathbf{u}_{\text{out}}} R\left(\boldsymbol{\theta}_{\text{in}}, \mathbf{u}_{\text{out}}, \underbrace{\tau'(\theta_{\text{in}}^{(y)}, y_{\text{in}}, z) + \tau'(u_{\text{out}}^{(y)}, y_{\text{out}}, z)}_{\text{2D beamforming along } (y\text{-}z)\text{-plane}} + \underbrace{\tau'(\theta_{\text{in}}^{(x)}, x_{\text{f}}, z_{\text{f}}) + \tau'(u_{\text{out}}^{(x)}, x_{\text{f}}, z_{\text{f}}) - 2z_{\text{f}}/c_0}_{\text{Cylindrical law to focus at } (x_{\text{f}}, z_{\text{f}})}\right). \tag{3.50}$$

The images displayed in [Fig. 3.24B_1,C_1] are obtained by synthesizing input and output beams collimated in the $(y,z)-$plane by focusing on a line located at ($x_{\text{f}} = 0$ mm, $z_{\text{f}} = 37.25$ mm), thereby mimicking the beamforming process by a conventional linear array of transducers.

The ultrasound image is displayed before and after 2D UMI in [Fig. 3.24B_1 and C_1], re-

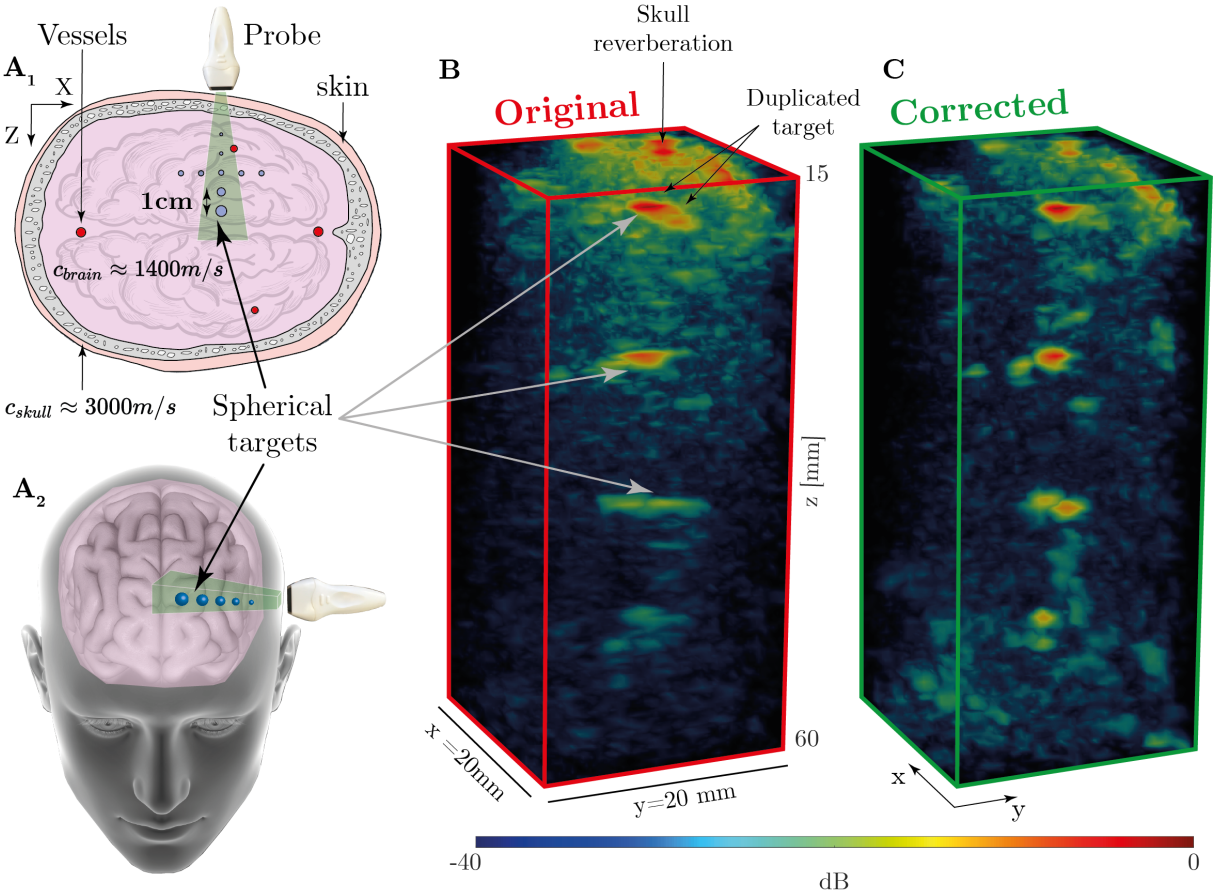

Figure 3.23: **Ultrasound Matrix Imaging (UMI) of the head phantom.** (**A**) Top and oblique views of the experimental configuration. *Image credits: Harryarts and kjpargeter on Freepik.* (**B, C**) Original and UMI images, respectively.

spectively. The radial average of the corresponding focal spots is displayed in [dashed lines in Fig. 3.24D]. Even if 2D UMI enables a diffraction limited resolution, the contrast gain G is quite moderate ($G_{2D} \sim$ 8dB). As it scales as the number of degrees of freedom, 3D UMI provides a much stronger enhancement of the target echo of about $G_{3D} \sim 18$ dB [Fig. 3.24B_2,C_2 and solid lines in D].

Hence, [Fig. 3.24] demonstrates the necessity of a 2D ultrasonic probe for trans-cranial imaging. Indeed, the complexity of wave propagation in the skull can only be harnessed with a 3D control (x, y, t) of the incident and reflected wave fields.

5.8 Perspectives

Although these results are striking, they were obtained in a phantom experiment, and some additional studies need to be performed to improve the robustness of our method.

First, the size of the confocal filter (Eq. 3.47) was set here to a fixed and arbitrary value at each step of the correction process. However, an optimal value for each correction step (*i.e.* each spatial window $\mathcal{W}$) could be investigated using spatial reciprocity as a guide star.

A complementary approach to multi-scale analysis is to perform the correction in different

correction planes between the probe and the focusing plane [Kwon, 2023], but it is only efficient if those correction planes belong to different depth-of-fields.

Then, as the major challenge in transcranial imaging lies in its severe attenuation, one perspective of this work is to use the $\hat{\mathbf{T}}-$matrix in a second acquisition to better focus physically in the medium to increase the signal-to-noise ratio. Eventually, the distortion matrix framework could even be applied once again to correct remaining aberrations.

Besides, since a large error is made in the skull layer assuming a constant speed-of-sound, Matrix Imaging could greatly benefit from skull segmentation methods [Mozaffarzadeh, 2021] and more generally speed-of-sound mapping [Jaeger, 2022; Ali, 2021] when building the focused reflection matrix (Eq. 3.10) in order to get better estimates of distances. However, segmentation of the skull is anything but trivial, as one must account for numerous reverberations that make estimating skull thickness difficult.

These reverberations have been omitted in this work, but drastically pollute the image at shallow depths ($z < 20$ mm). To cope with this issue, a poly-chromatic approach to matrix imaging is required. Indeed, the aberration compensation scheme proposed through this chapter is equivalent to a simple application of time delays on each transmit and receive channel. On the contrary, reverberation compensation requires the tailoring of a complex spatio-temporal adaptive (or even inverse) filter. To that aim, 3D UMI provides an adequate framework to exploit, at best, all the spatio-temporal degrees of freedom provided by a high-dimension array of broadband transducers.

Finally, some challenges remain for *in vivo* brain imaging. To date, UMI has only been applied to a static medium, whereas biological tissue is usually in motion, especially in vascular imaging where reflectivity changes rapidly over time due to blood flow. Indeed, many 3D imaging modes are designed to image blood flow, such as transcranial Doppler imaging [Ivancevich, 2008] or ULM [Bertolo, 2021; Chavignon, 2022]. These methods are strongly sensitive to aberrations [Demené, 2021; Soulioti, 2020], and their coupling with matrix imaging would be rewarding to increase the signal-to-noise ratio and improve the image resolution, not only in the vicinity of bright reflectors [Robin, 2023], but also in ultrasound speckle.

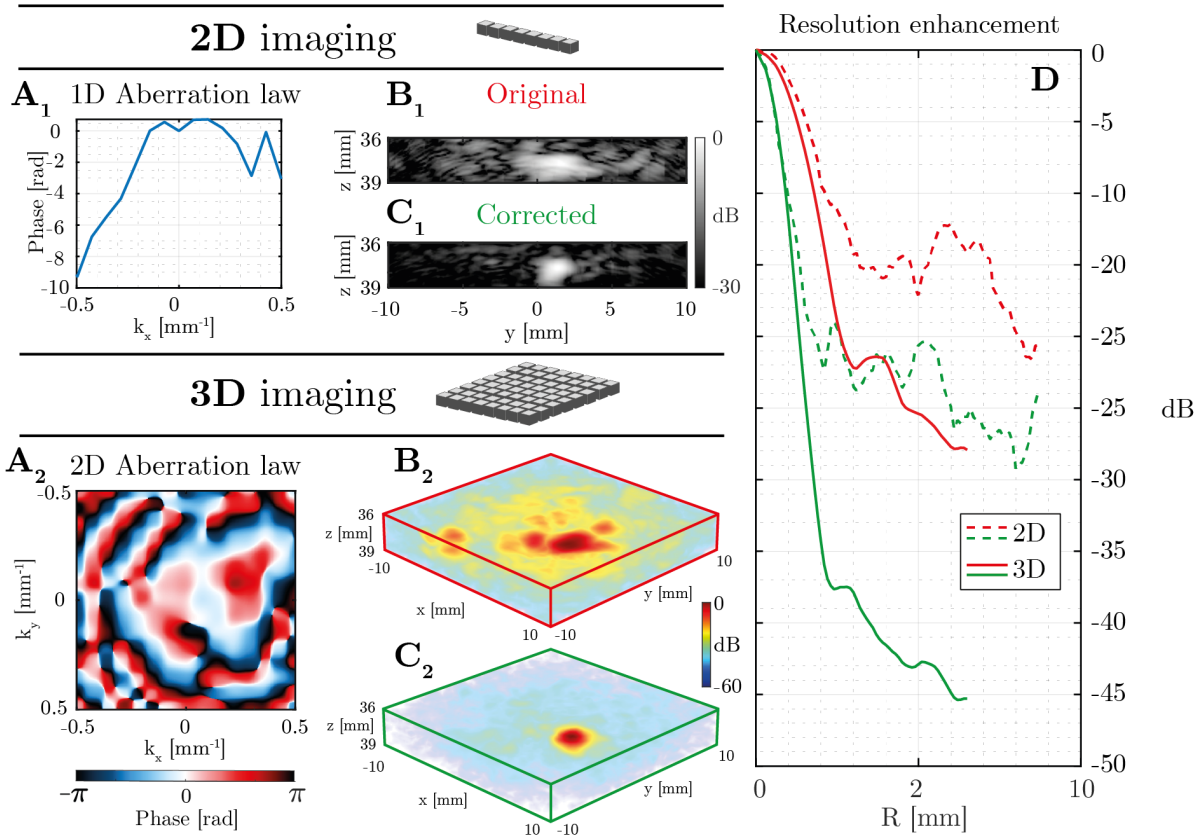

Figure 3.24: **2D *versus* 3D matrix imaging of a head phantom.** (**A**) Aberration law extracted with ($\mathbf{A}_1$) 2D or ($\mathbf{A}_2$) 3D UMI for a target located at $z = 38$ mm. (**B**, **C**) Original and corrected images of the same target. Subscript "1" and "2" stands for 2D and 3D UMI, respectively. (**D**) Imaging PSF before (red) and after (green) 2D (dotted line) and 3D (solid line) UMI.

6 Conclusion

In this chapter, Matrix Imaging was successfully extended to 3D ultrasound imaging. Aberrations were compensated both in an academic experiment and in the difficult case of transcranial imaging, which presents high attenuation and a high degree of multiple scattering. In addition, several features were introduced to make our correction procedure more robust. First, the extraction of aberration laws is now performed with a new algorithm (IPR) that allows us to reduce the size of the virtual reflector on which the aberration law is extracted without increasing the noise. In addition, a new criterion based on spatial reciprocity was introduced to monitor the convergence of our estimate of $\hat{\mathbf{T}}$. Finally, a comparison between 2D and 3D imaging was performed, showing that a large contrast gain can be obtained with 3D imaging.

Interestingly, ultrasound imaging of tissues is generally discarded for the brain because of the strong aberrations and reverberations. Interestingly, UMI can open a new route towards quantitative imaging of the brain, as a matrix framework can also enable the mapping of physical parameters such as the speed-of-sound [Jaeger, 2015a; Imbault, 2017; Jakovljevic, 2018; Lambert, 2020b], attenuation and scattering coefficients [Aubry, 2011; Brütt, 2022], or fiber

anisotropy [Papadacci, 2014; Rodriguez-Molares, 2017]. Those various observables can be extremely enlightening for brain tissue characterization.

In the next chapter, the localization and characterization of microbubbles will be examined in light of matrix imaging. First, it will be shown how matrix imaging can be combined with other ultrasound modalities. In the specific case of ultrasound localization microscopy, transcranial imaging experiments are performed *in vivo* to produce super-resolved images of sheep brain vessels. Matrix imaging is exploited to remove artifacts due to aberrations and increase the contrast of the ULM image. We will then use the temporal degrees of freedom of the reflection matrix to track the resonance frequency of monodisperse microbubbles. These two experiments are the result of a collaboration with two other academic laboratories.

Chapter 4

Matrix imaging for microbubbles localization and characterization

Objectives

The use of microbubbles in ultrasound imaging is not only an excellent tool for contrast-enhanced imaging, but can also be leveraged to produce super-resolved images. This is the principle of the dynamic imaging method called Ultrasound Localization Microscopy (ULM). Using *in vivo* transcranial imaging experiments on sheep brains, we demonstrate how such a technique can benefit from matrix imaging. In a first part, a local compensation of aberrations induced by the skull is shown to drastically eliminate artifacts that generally pollute the ULM image. In a second part, a preliminary study shows how matrix imaging paves the way towards quantitative ULM. Using monodisperse microbubbles in a phantom experiment, the temporal degrees of freedom of the reflection matrix are exploited to track the resonance frequency of such oscillating objects. Their observation is of utmost importance as it could potentially lead to intra-arterial blood pressure measurements and be of great use in monitoring strokes or heart attacks.

Contents

1 Introduction

The use of microbubbles in ultrasound imaging is widespread [Versluis, 2020; Tarighatnia, 2022; Liu, 2014]. Due to their high impedance mismatch compared to soft tissues, they were initially used as contrast agents. Clinically, they are injected intravenously, and their detection on the ultrasound image allows the visualization of vessels with a contrast enhancement of 20 to 30 dB. Another key property of microbubbles is their oscillatory nature, which makes them resonant objects and thus act as acoustic sources as they make the pressure vary over time. Fortunately, their resonance frequency, which depends directly on their diameter, matches the frequency range of most commercially available ultrasound probes. Finally, the real-time capability of ultrasound imaging allows these contrast agents to be distinguished directly and more accurately from the static part of the tissues.

For example, microbubbles can be used to monitor the development of a malignant tumor by quantifying blood flow throughout the angiogenesis process. In addition, new classes of microbubbles have shown promising results in ultrasound therapy to improve the specificity of drug delivery with encapsulated molecules or conjugated nanoparticles. They could also be used to improve the opening of the blood-brain barrier to enhance delivery of therapeutics to brain tumors.

More recently, microbubbles have even been used to produce super-resolved images of vessels, using a similar idea developed several years earlier in fluorescence microscopy [Betzig, 2006; Rust, 2006]. The principle of Ultrasound Localization Microscopy [Errico, 2015] is that isolated microbubbles, if they can be tracked over an extended period of time, can be localized with an accuracy no longer dictated by diffraction limit, resulting in a significant improvement of the resolution by a factor of about ten compared with standard ultrasound images. In recent years, it has found numerous applications in functional imaging, and also in clinical imaging, whether to produce transcranial images with much higher resolution and more contrast than current Doppler modalities [Demené, 2021] or to monitor coronary flow in the heart [Demeulenaere, 2022]. However, microbubble tracking relies on examining the focal spot associated with each bubble in the ultrasound image. It can therefore be severely affected by wave distortions caused by the cranial layer, for example. Such a method could benefit greatly from adaptive focusing to increase the bubble detection rate and localize them with higher accuracy. ULM would be able to distinguish smaller, micrometer-sized vessels with fewer reconstruction artifacts.

In addition, clinically approved contrast agents such as Sonovue refer to shell-coated membranes with large polydispersity, meaning that their size is not controlled and typically ranges from 1 to 10 μm [Stride, 2020]. This property is advantageous in that it can be adapted to any ultrasound probe, but it can also be considered as a disadvantage if one wishes to optimize the benefits of such a contrast agent on the image. In fact, since the resonance frequency of such objects directly depends on their size and on the local pressure [Minnaert, 1933], the use of polydisperse bubbles leads to a broad spectrum [Tremblay-Darveau, 2014a]. Monodisperse microbubbles [Segers, 2018] could thus be used not only to produce a higher contrasted image [Stride, 2020], but also to monitor the evolution of pressure over time [Fairbank, 1977;

Tremblay-Darveau, 2014b; Segers, 2018].

In this chapter, microbubbles are first used to map cerebral vessels in sheep using Ultrasound Localization Microscopy. In particular, we show how matrix imaging can be coupled with ULM by recording the reflection matrix prior to the ultrafast sequence used for super-resolution. In this experiment, we show that aberrations due to the cranial layer are at least partially corrected, resulting in an image with a significantly improved contrast and fewer reconstruction artifacts. We then present preliminary results of an academic experiment in which we measured the resonance frequency of monodisperse bubbles. These results may suggest that such frequency-matched contrast agents could be used to measure blood pressure and thus provide a quantitative tool for detecting or monitoring cerebrovascular accidents. Both works are the result of academic collaboration with the group of Olivier Couture for the ULM project and the group of Patrick Tabeling for the monodisperse bubble project.

2 Combining Ultrasound Localization Microscopy with Matrix Imaging

In this first section, we will show how other ultrasound imaging modalities based on ultrafast acquisitions can take advantage of Matrix Imaging. We will demonstrate this statement by considering the specific case of *Ultrasound Localization Microscopy* (ULM) in the framework of transcranial imaging experiments performed on anesthetized sheep. This work is the result of collaboration with the team of Olivier Couture (Laboratoire d'Imagerie Biomédicale, Paris, France). In particular, all experiments described in this section were performed by Antoine Coudert, who was, at that time, a PhD student in that group [Coudert, 2023]. The post-processing of ultrasound data and the analysis of the results were performed jointly.

2.1 Principle of Ultrasound Localization Microscopy

Recently, a new ultrasound imaging modality known as *Ultrasound Localization Microscopy* (ULM) [Errico, 2015] has paved the way to produce ultrasound images with a sub-diffraction resolution [Fig. 1.13D]. Inspired by research in the field of optics [Betzig, 2006; Rust, 2006] which was awarded the Nobel Prize in Chemistry in 2014, ULM represents its acoustic counterpart. Isolated microbubbles previously injected intravenously into the bloodstream are localized and tracked over time, so that resolution is no longer limited by the diffraction limit [gray ellipses in Fig. 4.1A], but by the ability to localize the center of their associated PSFs [red crosses in Fig. 4.1A] [Desailly, 2015]. The vessels can then be reconstructed from an ultrafast sequence that captures the fluid motion of the bubbles over time. In particular, this technique improves the resolution of the images by a factor of about ten, resulting in resolution down to the micrometer scale. Not only does it allow for more detailed imaging of many organs, it is seen as a real breakthrough in the field of functional imaging [Fig. 4.1B], since it allows the mapping of the complex vascular networks in the brain of small animals such as rat or mice [Demené, 2017; Deffieux, 2018; Bertolo, 2021].

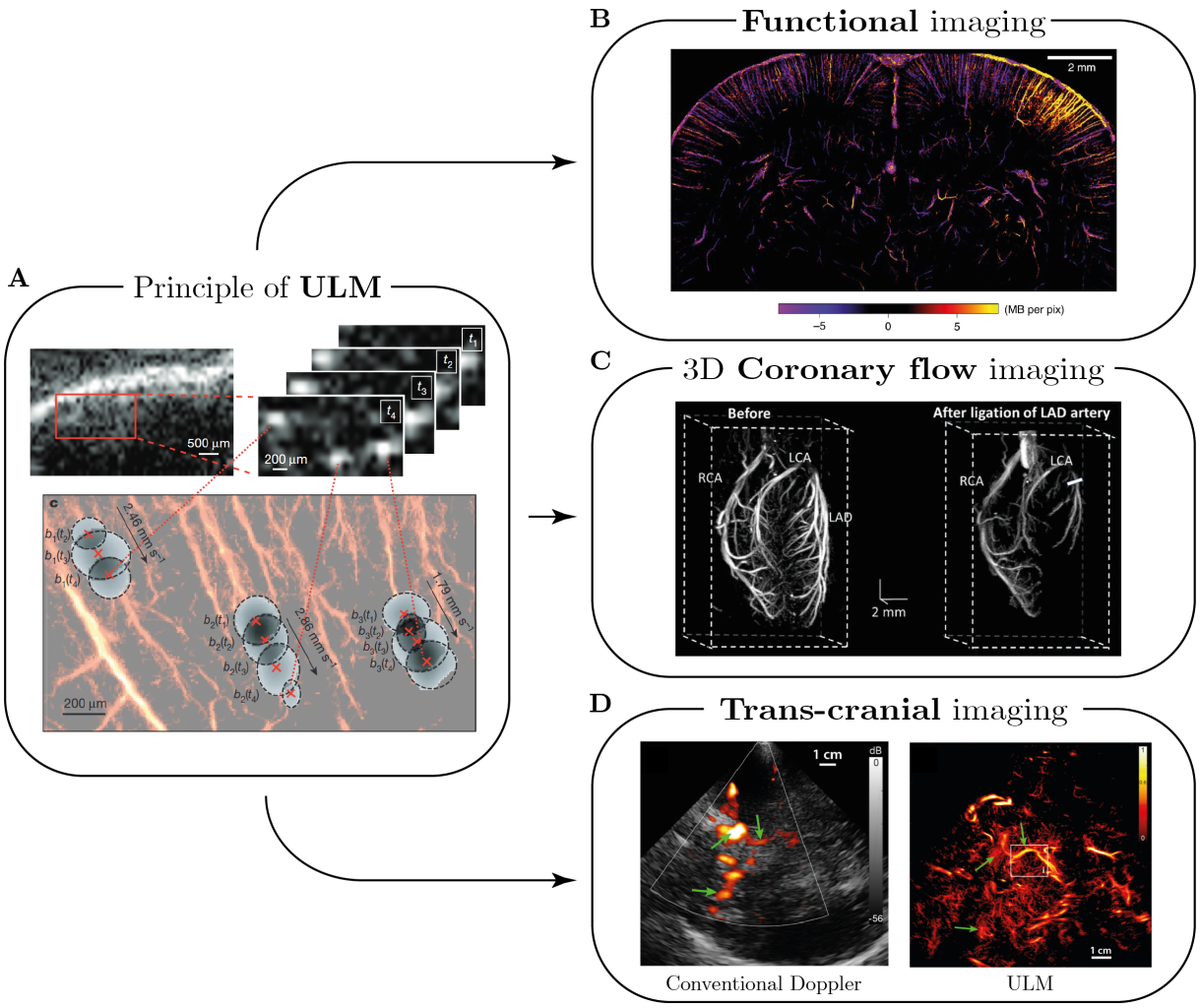

Figure 4.1: **Principle & applications of Ultrasound Localization Microscopy (ULM).** (**A**) Isolated microbubbles are localized and tracked over time to produce an image of vessels down to the micrometer scale (*extracted from* [Errico, 2015]). (**B**) Functional imaging in the rat brain after whiskers stimulation (*extracted from* [Renaudin, 2022]) (**C**) Coronary flow of an *ex vivo* rat heart before and after ligation of LAD artery (*extracted from* [Demeulenaere, 2022]) (**D**) 2D *in vivo* transcranial Doppler *versus* ULM in the human brain (*extracted from* [Demené, 2021]).

Historically, ULM imaging has long been limited to 2D imaging, which poses several issues such as [Couture, 2018]:

- Projection of vessels (3D structures) onto a plane (2D), resulting in blurred vessels;
- Non-optimal tracking of microbubbles entering and leaving the filed-of-view;
- In the presence of aberrations, not only is the sensitivity to detect bubbles lower, which affects the contrast of the super-resolved image, but also the accuracy in localizing bubbles, where high side-lobes of a degraded PSF can cause artifacts such as duplication of vessels [Xing, 2023; Robin, 2023].

Recent advances in 3D imaging with matrix arrays have made it possible to overcome these problems. For example, coronary flow can be tracked in the *ex vivo* rat heart [Fig. 4.1C] [Demeulenaere, 2022] or even brain flow in transcranial 3D imaging of the rat brain [Chavignon, 2022]. ULM imaging has even been successfully used in transcranial clinical imaging of the adult human brain [Fig. 4.1D] [Demené, 2021], where aberration correction is critical [Soulioti, 2020; Robin, 2023]. However, this previous work was limited to conventional 2D imaging with a phased array (1D probe), and the correction process was based on the presence of guide stars (*e.g.* microbubbles) in the field of view [Robin, 2023]. Corresponding RF data from these specific guide stars directly provide the aberration law. However, if the isoplanatic assumption is not verified, the low concentration of guide stars prevents from a fine compensation of aberrations. In addition, extracting the aberration law directly from the microbubble signal may not be optimal because the corresponding PSF may have large sidelobes in a highly aberrating medium, leading to a large uncertainty regarding the localization of its center. Moreover, the estimate of the output aberration law in such an ultrafast acquisition is biased by the poor focusing at the input. In other words, such an estimation of aberration does not benefit from the iterative improvement of the focusing process made possible by matrix imaging at both input and output (see Chapter 2, Section 4.6.4).

Here we will show that ULM imaging can take advantage of 3D UMI to extract local adaptive focusing laws not only in the presence of a strong reflector, but also in the presence of random speckle. A preclinical experiment is performed on an anesthetized sheep to obtain a transcranial super-resolved volume, free from aberrations.

2.2 Transcranial sheep experiment

The study was performed on a pool of 6 sheep, where the goal was first to demonstrate the ability of ULM to image cerebral vessels in large animals. Correct positioning of the probe in front of the brain was a real key point, and only in the last three sheep was ULM successfully performed as part of Antoine's PhD thesis [Coudert, 2023]. In this section, we present the coupling of these experiments with matrix imaging, using a similar formalism as described in the previous chapter to compensate for aberrations.

2.2.1 Ultrasound probe characteristics

Antoine Coudert performed the experiments using a different matrix array ($\mathcal{P}_2$) with the properties described in [Table 4.1]. In particular, a lower frequency is used to better penetrate the cranial layer, but at the expense of a lower resolution. In addition, a single multiplexed electronic system from Verasonics [Hara, 2005] is now used to drive the probe. This allows the use of less complex electronics than before, but has the disadvantage that only synthetic apertures (*i.e.* one block of 256 elements at a time) can be used, which reduces both frame rate and SNR.

Number of transducers	$32 \times 32 = 1024$ (with 5 dead elements)
Geometry (y-axis)	3 inactive rows between each block of 256 elements
Pitch	$\delta u = 0.55$ mm ($\approx \lambda/2$ at $c = 1540$ m/s)
Aperture	$\Delta u = \begin{pmatrix} \Delta u_x \\ \Delta u_y \end{pmatrix} = \begin{pmatrix} 17.6 \text{ mm} \\ 19.3 \text{ mm} \end{pmatrix}$
Central frequency	$f_c = 1.56$ MHz
Bandwidth	$60\% \rightarrow [1-2]$ MHz
Transducer directivity	$\theta_{max} = 64°$ at $c = 1540$ m/s

Table 4.1: **Matrix array datasheet $\mathcal{P}_2$.**

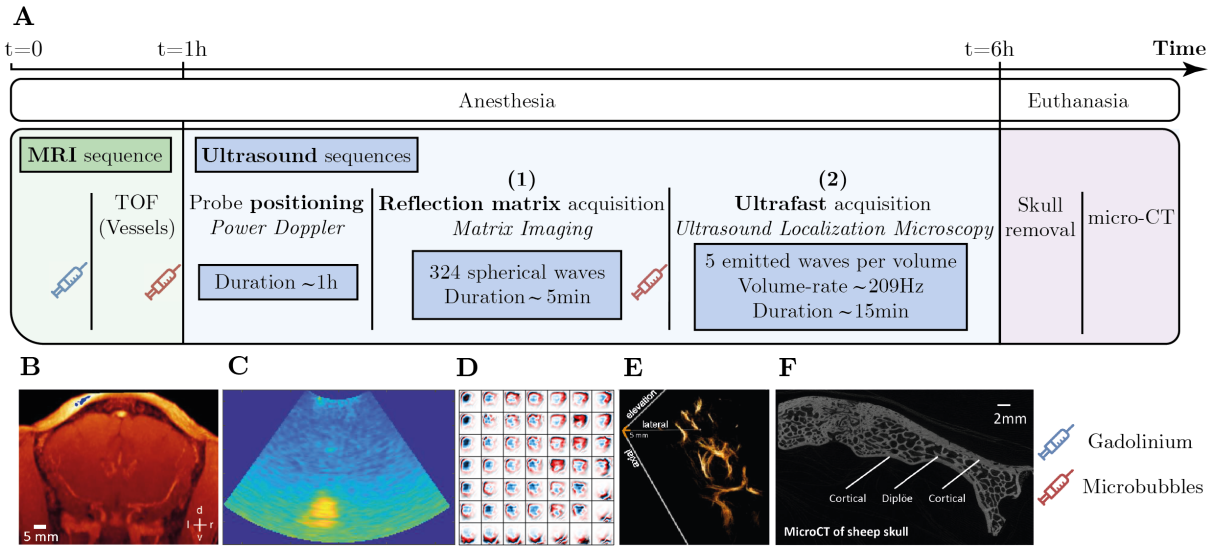

Figure 4.2: **Multi-sequences acquisition** (Sheep experiment). **(A)** Successive imaging sequences. **(B)** MRI TOF to image vessels. **(C)** Transcranial Power Doppler. **(D)** Estimation of the $\mathbf{T}-$matrix thanks to 3D UMI. **(E)** Super-resolved ULM-image. **(F)** Micro CT scan of the sheep skull. The duration of the acquisition of the $\mathbf{R}$-matrix was not optimized in this experiment and can be in principle drastically shortened.

2.2.2 From static to dynamic matrix imaging

As described in Chapter 3 (Section 3.3), the number of insonifications required for UMI scales as the number of resolution cells covered by the RPSF [Fig. 3.7]. As the aberration level through the skull is important, the uncorrected RPSFs are much larger than the diffraction limit. This means that the insonification basis should be fully sampled, limiting 3D UMI to a compounded frame-rate of only a few hertz, which is much too slow for ultrafast imaging [Tanter, 2014].

One solution to directly implement 3D UMI for dynamic imaging is to design an acquisition sequence in which the fully sampled $\mathbf{R}-$matrix is acquired prior to the following ultrafast acquisition, where the insonification basis can be drastically down-sampled. The $\hat{\mathbf{T}}-$matrix obtained from the $\mathbf{R}-$matrix can then be used to correct the ultrafast acquisition in post-processing.

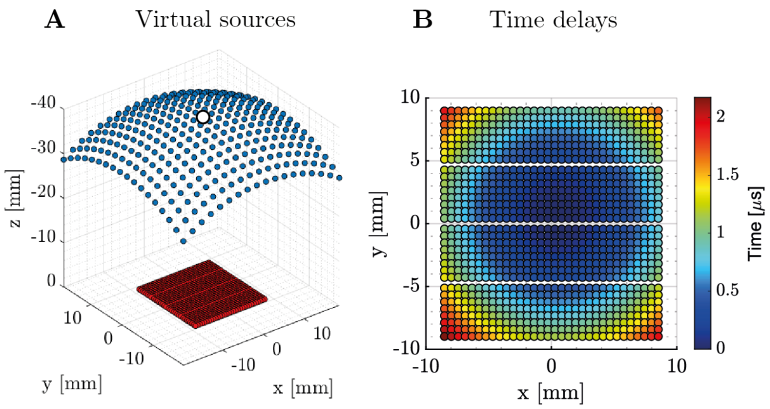

Figure 4.3: **Virtual sources insonification.** **R**−matrix acquired in a set of spherical diverging wave associated with **(A)** virtual sources above the probe (blue spot). **(B)** Time delays associated to a single diverging wave (white spot in panel **A**).

2.2.3 Multi-sequence acquisition

Prior to ultrasound acquisitions, other imaging modality are performed while the sheep is anesthetized [Fig. 4.2A]. First, MRI sequences provide *ground-truth* images of the entire brain anatomy, in particular the vessels [Fig. 4.2B]. Then, microbubbles (Sonovue, Bracco, Italy [Schneider, 1999]) are injected to provide enhanced contrasted Doppler ultrasound images, which are used to properly position the probe in front of the main brain vessels [Fig. 4.2C].

Then, the reflection matrix is captured using a set of synthetic spherical waves: $\mathbf{R_{vu}}(t) \equiv [R(\mathbf{v}_{\text{in}}, \mathbf{u}_{\text{out}}, t)]$, where the vector $\mathbf{v}_{\text{in}}$ indicates the position of the corresponding virtual sources [Fig. 4.3]. However, due to a technical problem, the complete acquisition of the reflection matrix took an unusually long time. To shorten the acquisition time, the reflection matrix was acquired only partially with 324 virtual sources (instead of 1225 as in previous experiments), which are located on a radius of 39.5 mm (Eq. 3.6). However, since we want to compensate for aberrations located below the probe and at great depths, large transverse wave-vectors, such as $\|\mathbf{k}\| > k_c/2$, are not required because they do not reach the target field-of-view. It is important to point out that in future experiments the acquisition of the fully sampled reflection matrix should not take much longer than one second, rather than 5 minutes as here [Fig. 4.2A].

Then, microbubbles are injected again to perform ultrafast acquisition for ULM imaging [Fig. 4.2E]. Acquisition is performed by a hybrid sequence of 3 cylindrical waves emitted simultaneously by the entire probe and 2 spherical waves decomposed by panels to achieve a volume rate of 209 Hz. Each pulse consists of 2 cycles with a voltage of 60 V. After 40 seconds of acquisition, a bolus of 1.75 ml (*i.e.* a single rapid injection) of Sonovue microbubbles was injected every minute for the next seven following minutes. As only few insonifications are used, the partial reflection matrix is acquired $R_{\text{p}}(\mathbf{i}_{\text{in}}, \mathbf{u}_{\text{out}}, t, t_{\text{p}})$, where t_{p} denotes each frame of the ultrafast sequence.

Finally, the sheep is euthanized, and the skull is removed to perform a micro-CT scan [Fig. 4.2F]. Interestingly, it shows the great complexity of transcranial imaging, with an inhomogeneous distribution of cortical and trabecular bone of different thickness in the transverse

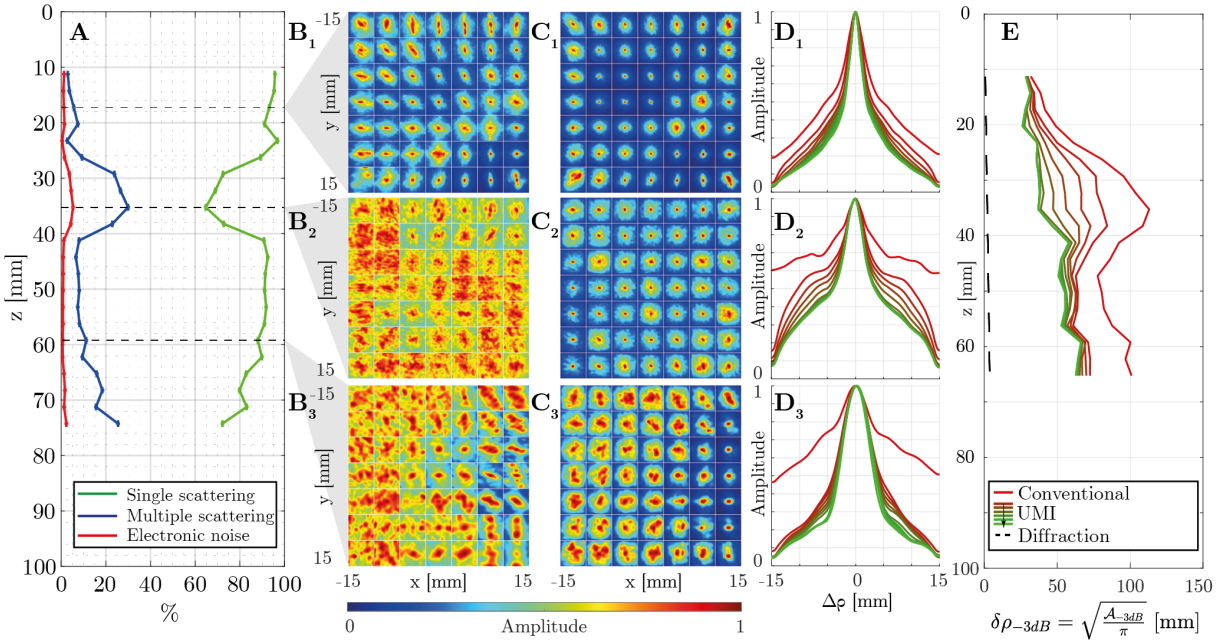

Figure 4.4: **Multi-scale analysis of wave distortions in a sheep brain experiment. (A)** Single scattering, multiple scattering and noise rate as a function of depth. **(B, C)** RPSFs before and after the UMI process at three different depths. Each RPSF is displayed in a de-scan range that varies from -15 to $+15$ mm in both x and y direction **(D)** Evolution of the radial profile of the RPSF at each step of UMI for three different depths. **(E)** Evolution of resolution enhancement as a function of depths at each step of UMI process.

direction.

2.2.4 Extracting the $\hat{\mathbf{T}}-$matrix

The focused reflection matrix $\mathbf{R}_{\rho\rho}(z)$ is still built numerically in the time domain, according to equations (3.10, 3.11 & 3.13) and assuming a speed-of-sound of $c_0 = 1540$ m/s in the brain. The same UMI procedure as the one described in the previous section is now applied to this experiment. Similar to the previous head phantom experiment, the RPSFs exhibit large transverse aberrations and high background [Fig. 4.4B], which is due to strong attenuation and multiple scattering. It appears that multiple scattering is more important in the $z = 35$ mm region [Fig. 4.4A], which is associated with a region of the field of view with less echogenic signals, as shown by looking at the confocal image in [Fig. 4.6A].

Unlike the previous chapter, however, the $\hat{\mathbf{T}}-$matrix is extracted here in the transducer basis, since it will be used to correct aberrations directly on the raw ultrafast data that are already expressed in this basis. The gradual reduction of the field-of-view partition as described in [Table 4.2] in conjunction with the use of a confocal filter with parameters similar to those described in the previous chapter ensures the convergence of the IPR process. The spatial reciprocity $\langle \hat{\mathbf{T}}_{\text{in}}^{(i)} | \hat{\mathbf{T}}_{\text{out}}^{(i)} \rangle$ is checked to be larger than 0.95 at each correction step. As in the previous section, the transmission matrix $\hat{\mathrm{T}}(\mathbf{u}, \mathbf{r})$ linking each transducer to each voxel of the field-of-view can be extracted [Fig. 4.5]. At a depth of $z = 17$ mm, the support of the aberration laws varies from

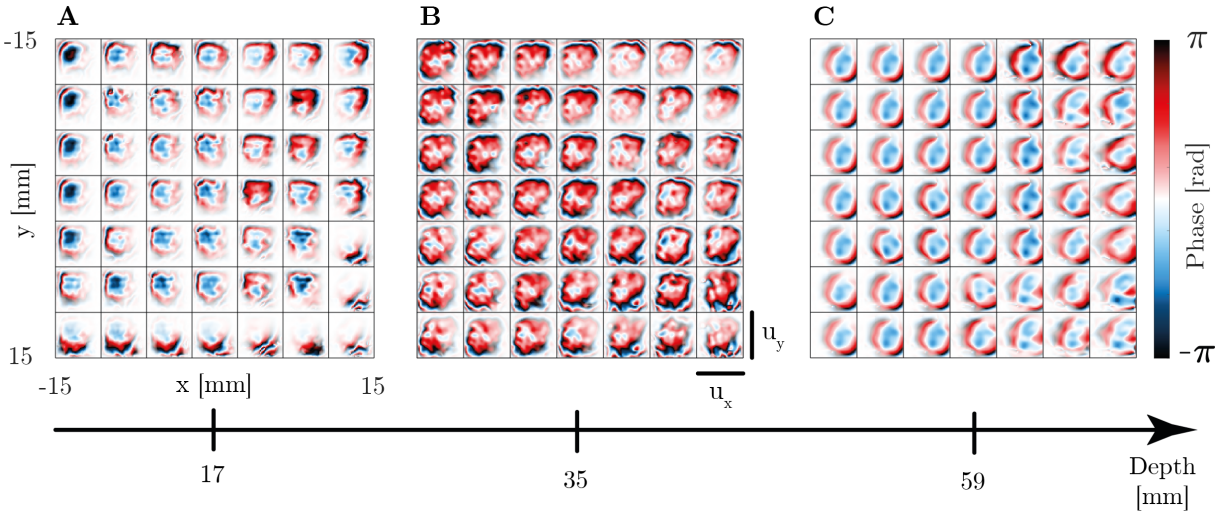

Figure 4.5: **$\hat{\mathbf{T}}$−matrix estimation in the sheep brain experiment.** Aberration laws at three different depths: **(A)** $z = 17$ mm, **(B)** $z = 35$ mm and **(C)** $z = 59$ mm.

one area to the other, because the directivity of the transducers has a greater effect at shallow depths.

Correction step (i)	1°	2°	3°	4°	5°	6°
Number of transverse patches	1×1	2×2	3×3	4×4	5×5	6×6
$w_{\boldsymbol{\rho}} = (w_x, w_y)$ [mm]	30	22.5	20	15	12	10
w_z [mm]	2.5	2.5	2.5	2.5	2.5	2.5

Table 4.2: **Parameters of UMI in the sheep experiment.**

Phase conjugation of $\hat{\mathbf{T}}$ leads to focusing laws that give rise to a drastic enhancement of RPSFs in [Fig. 4.4C], leading to a resolution enhancement by about a factor 2 [Fig. 4.4E]. UMI image associated with this first static acquisition without any bubbles shows a great enhancement of resolution and contrast [Fig. 4.6B] compared with the conventional 3D volume extracted before the correction process [Fig. 4.6A].

Nevertheless, the diffraction limit is not reached, as shown in [Fig. 4.4E]. It is very likely that this is due to the anisoplanatic nature of the experimental data, as shown by the drastic spatial variations of the RPSF in [Fig. 4.4B3]. Hence, highest order aberrations, which are associated with a smaller correlation length, cannot be extracted [Lambert, 2022a]. Such aberrations cannot be captured in this case due to the high value of the spatial criterion we have set.

In fact, not only is the **R**-matrix not fully captured, but it is not acquired in the same bases at the input and output, which affects our spatial reciprocity criterion. Here we have chosen a higher criterion than in the previous chapter to extract only low-order aberration laws that are more robust over time and can then be applied to ULM imaging. Since the high-frequency components of the aberrations change significantly over time, we limited our analysis to the lowest-order aberrations by setting a more restrictive spatial reciprocity criterion. Nevertheless, a more detailed study is needed to investigate the influence of the spatial reciprocity criterion on the extracted aberration laws and find its optimal value.

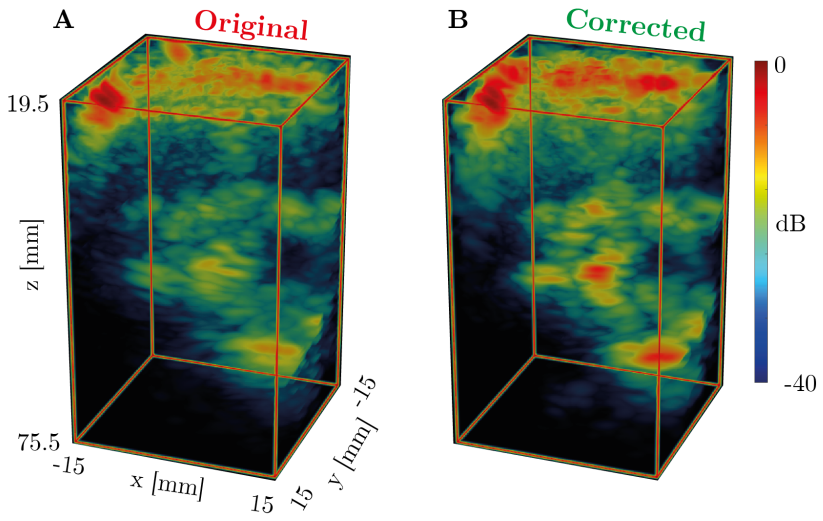

Figure 4.6: **Effect of correction on the R−matrix acquisition.** Confocal image **(A)** before and **(B)** after correction.

2.2.5 Time stability of the $\hat{\mathbf{T}}$−matrix

To investigate the overall time stability of the aberration, the **R**−matrix was recorded twice at three-hour intervals while the experiment was fixed. The first acquisition was made at $t_1 =$ 10h32min [Fig. 4.7A] and the second at $t_2 =$ 13h32min [Fig. 4.7B]. The spatial aberration maps are shown for three different depths. The differences between the aberration phase laws acquired at t_1 and t_2 are quite obvious and show that this long ULM experiment, even if it was faster than three hours, can be quite sensitive to temporal variations in the aberrations. These results can be quantified by considering the scalar product $\langle \hat{\mathbf{T}}(t_1) | \hat{\mathbf{T}}(t_2) \rangle$ of the aberrations laws between these two times [Fig. 4.7C]. The stability of the aberration phase laws exhibits large variations in both the transverse and axial directions. However, a general trend is that this stability is higher at greater depths. This stability is affected by either probe motion, tissue motion, or out-of-plane motion. In any case, we are much more sensitive to motion at shallow depths than at great depths, which is due to the geometrical spreading of the wave, or in other words, because the size of the resolution cell scales with depth.

Although the ultrafast sequence necessarily requires at least few seconds or few minutes to capture the flow of microbubbles, the duration of the **R**−matrix acquisition can be drastically reduced, as it is limited only by the number of insonifications required ($N_{\boldsymbol{\theta}_{\text{in}}} = 324$) and the multiplexed electronics that require multiple insonifications to synthesize a diverging wave, resulting in a theoretical duration of 136 ms (for a field of view of 80 mm depth and a speed of sound $c_0 = 1540$ m/s), instead of 5 min as described in [Fig. 4.2].

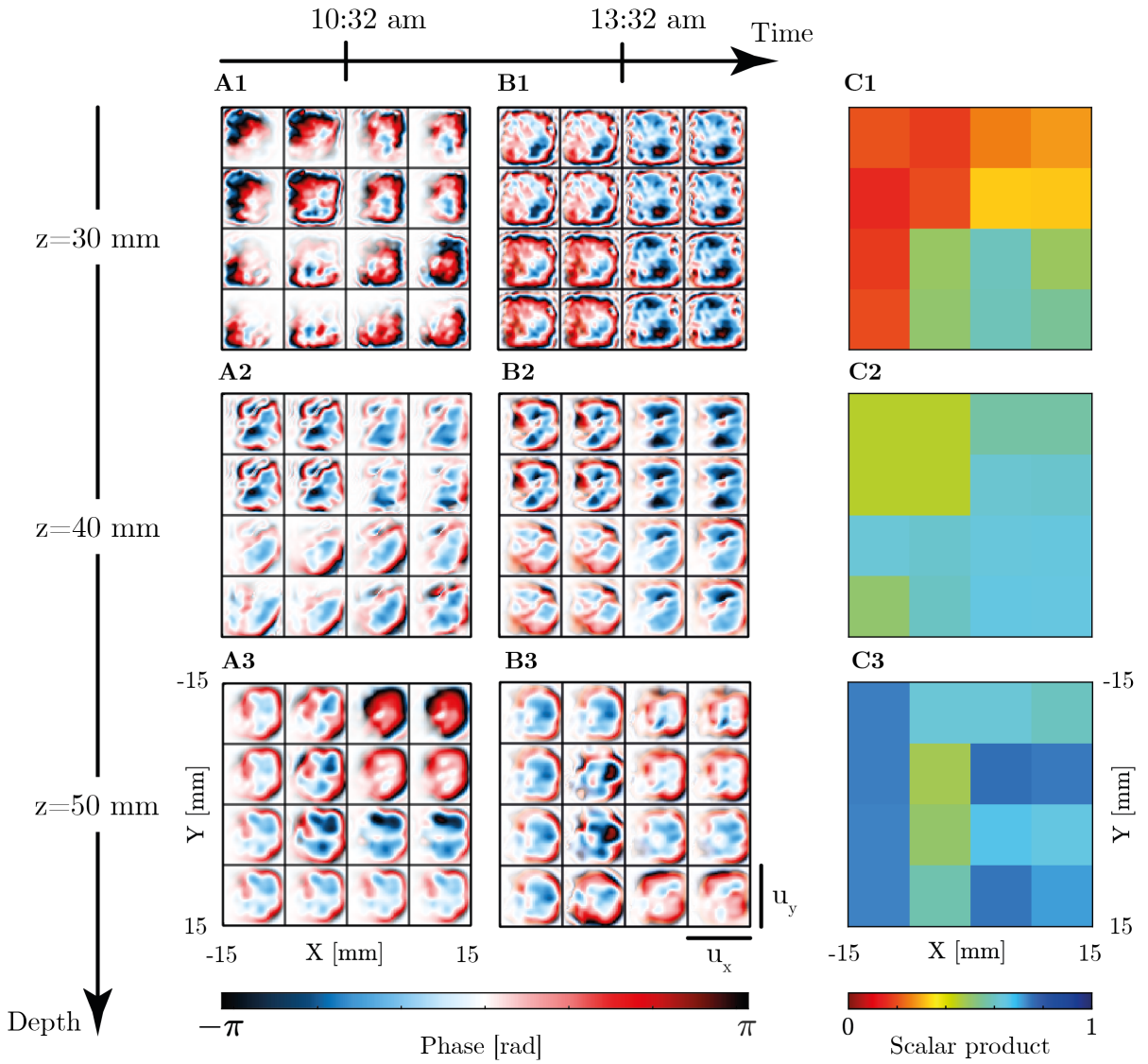

Figure 4.7: **Time stability of the transmission matrix.** The reflection matrix was acquired at two different time t_1 = 10h32min and t_2 = 13h32min while the position of the probe was kept at the same position. (**A, B**) Aberration law extracted at time t_1 and t_2, respectively. (**C**) Scalar product between the two. Each row refers to a different depth $z = 30, 40$ and 50 mm.

2.2.6 Reconstruction of super-resolved ULM image

The image associated with each frame is then constructed using a conventional delay-and-sum algorithm with appropriate time delays at the input and output:

$$\mathcal{I}(\mathbf{r}, t_\mathrm{p}) = \sum_{\mathbf{i}_\mathrm{in}} \sum_{\mathbf{u}_\mathrm{out}} R_\mathrm{p}(\mathbf{i}_\mathrm{in}, \mathbf{u}_\mathrm{out}, \tau(\mathbf{i}_\mathrm{in}, \mathbf{r}) + \tau(\mathbf{r}, \mathbf{u}_\mathrm{out}), \mathbf{r}, t_\mathrm{p}). \tag{4.1}$$

Low-pass filtering with a sliding average window along the t_p-dimension allows extraction of only the moving part of the film, *i.e.* the blood stream containing the microbubbles. The microbubbles are first detected in each frame by their corresponding PSF on the image $\mathcal{I}$. Then

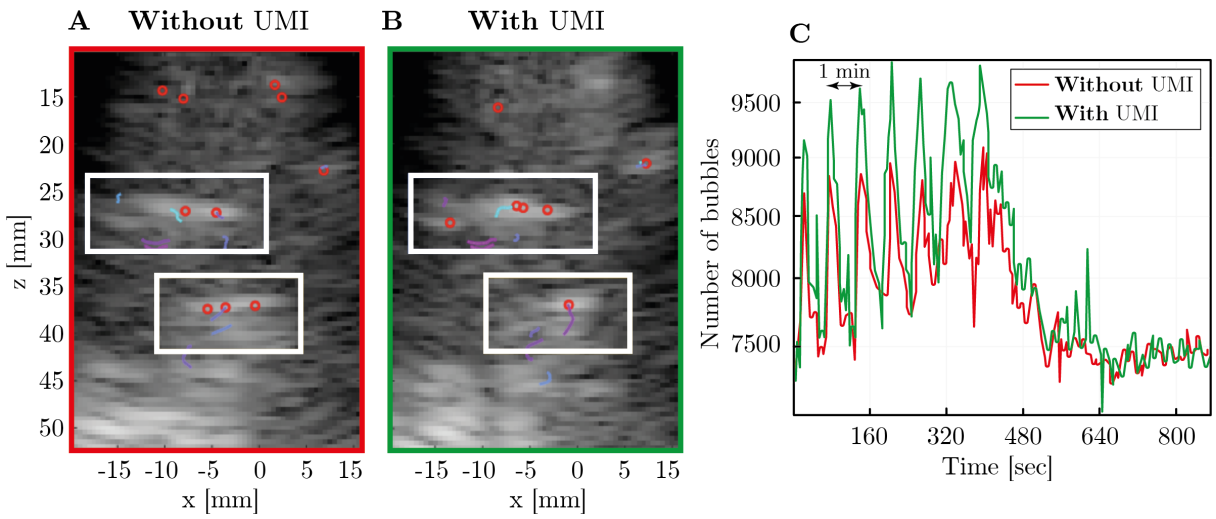

Figure 4.8: **Enhancement of bubbles detection and tracking with UMI.** (**A, B**) Detection and tracking of bubbles before and after correction, respectively. (**C**) Number of bubbles detected as a function of time.

the center of each PSF is localized, as shown by the red circles in [Fig. 4.8A]. Here, localization is based on radial centers of symmetry [Heiles, 2019; Parthasarathy, 2012], where the center of PSF is found using a gradient algorithm, thus assuming a Gaussian shape of PSF. Aberrations thus directly affect the localization of microbubbles and can lead to artifacts in the reconstruction. For example, a single microbubble affected by aberrations may have high side lobes that could be detected as two different microbubbles during reconstruction. By tracking each detected bubbles over time, it is then possible to reconstruct their trajectories over all the entire duration of the sequence, as displayed in color lines of [Fig. 4.8A]. The number of bubbles detected over time is shown in [red line in Fig. 4.8C] where the different peak corresponds to each injection of microbubbles. Finally, a super-resolved image $\mathcal{I}_{\text{ULM}}(\mathbf{r})$ is obtained by counting the number of microbubbles crossing each voxel of the field-of-view.

Such an image is displayed from different angles in [Fig. 4.9A, C, E, G]. A typical structure of the cerebral vessels can be seen even before adaptive focusing. This structure is known as the circle of Willis [Kalsoum, 2014] which is represented schematically in [Fig. 4.10A] and can be seen as the main intersection of vessels in the brain. However, part of it seems to be duplicated [Fig. 4.9C], probably due to aberrations. These kinds of artifacts have already been observed in transcranial imaging both in mouse [Xing, 2023] and human [Robin, 2023] brain.

2.2.7 Super-resolved image free from aberrations

The transmission matrix $\hat{\mathrm{T}}(\mathbf{u}, \mathbf{r})$ previously extracted with UMI can now be used to correct aberrations in the data obtained during the ultrafast sequence. Due to time constraints related to the end of the PhD, we only corrected the output basis. However, since only a few waves are used to insonify the brain, the output correction ($\mathbf{u}_{\text{out}}$) has a much larger impact. The correction is applied directly as a phase-shift on the raw data of the ultrafast sequence for each

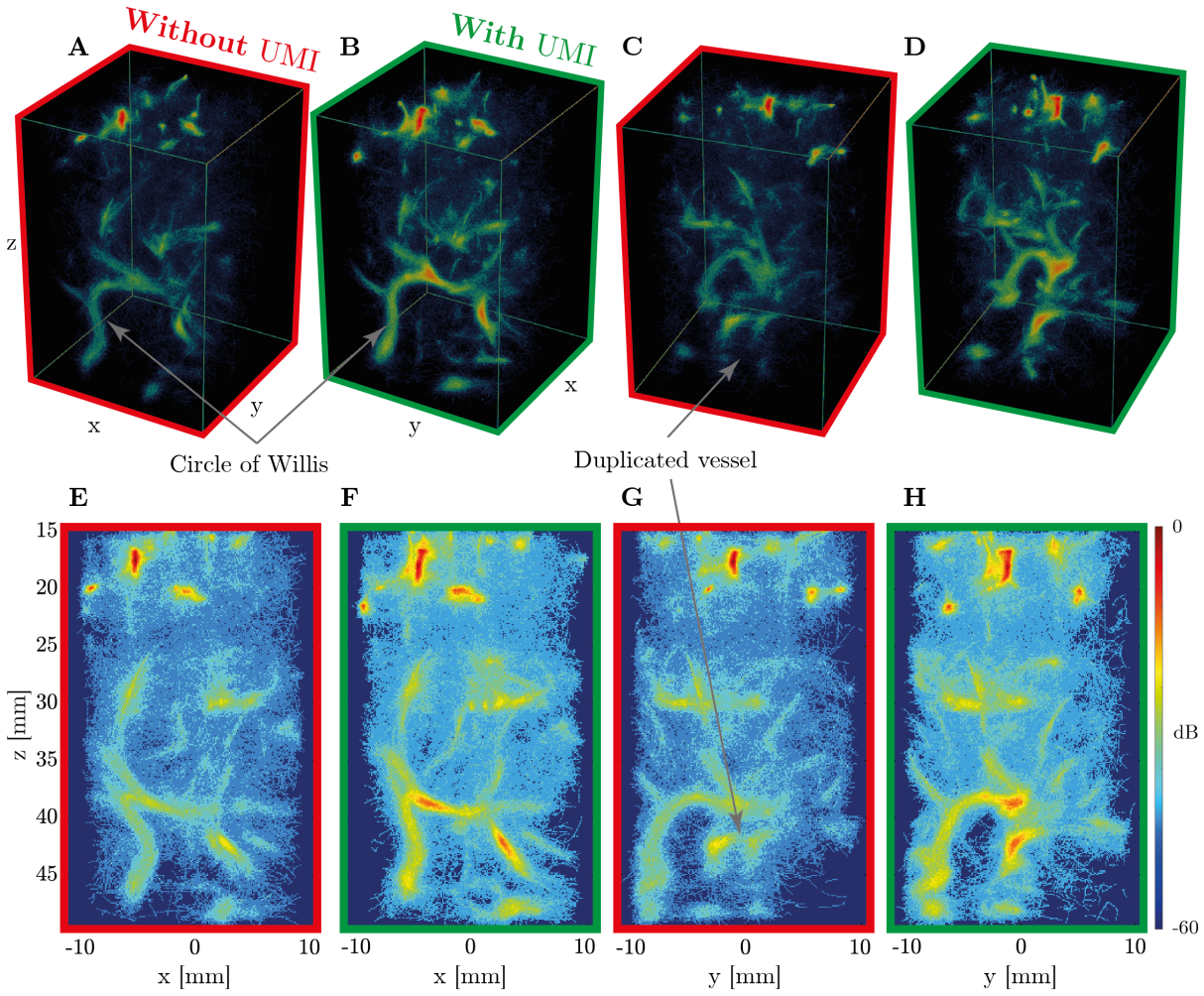

Figure 4.9: **Impact of Matrix Imaging on ULM images.** 3D images displayed as maximum intensity projections **(A, C, E, G)** before and **(B, D, F, H)** after compensation of aberrations. The circle of Willis is located around $z = 40 - 45$ mm. The same dynamic is displayed for all images.

part of the field of view:

$$R_{\mathrm{p}}^{(\mathrm{corr})}(\mathbf{i}_{\mathrm{in}}, \mathbf{u}_{\mathrm{out}}, t, \mathbf{r}, t_{\mathrm{p}}) = R_{\mathrm{p}}(\mathbf{i}_{\mathrm{in}}, \mathbf{u}_{\mathrm{out}}, t, \mathbf{r}, t_{\mathrm{p}}) \circ \hat{\mathrm{T}}^{*}(\mathbf{u}_{\mathrm{out}}, \mathbf{r}), \tag{4.2}$$

where $\circ$ stand for a Hadamard product. The ULM image is then created by a post-processing process similar to that described earlier.

First, about 10% additional microbubbles are detected at a given time throughout the acquisition, as shown in [green curve in Fig. 4.8C]. Then the comparison of the ULM images with and without UMI is shown in [Fig. 4.9]. The corrected images have a higher contrast, the structures appear brighter and smaller vessels are visible. In addition, the original duplication of the vessel is now corrected [Fig. 4.9D]. This feature can be understood when comparing the detection of the lower white box in [Fig. 4.8A & B], where originally three bubbles were detected, while after correction only one can be seen, confirming that detection and tracking was not optimal

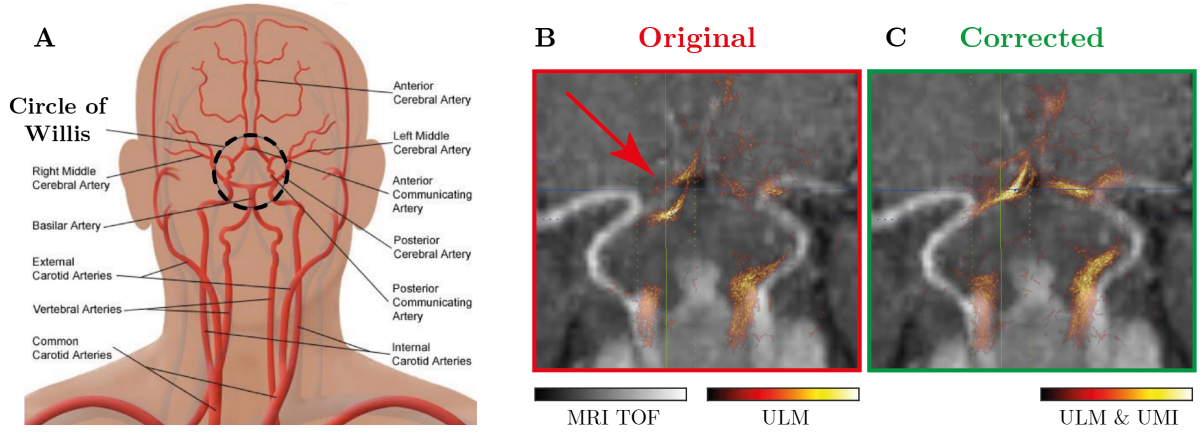

Figure 4.10: **Comparison of MRI and ULM images.** (**A**) Organization of the human cerebral circulation *This panel is extracted from* [Mamo, 2015]. (**B, C**) MRI *TOF* (gray scale) superimposed to the ULM image (red/yellow scale) before and after matrix correction of aberrations, respectively.

without adaptive focusing. Furthermore, the super-resolved images better match the anatomical structures of the sheep vascular networks extracted by MRI, as shown by [Fig. 4.10B and C].

2.3 Perspectives

Here we presented a solution for combining ULM with matrix imaging using multi-sequence acquisition. However, this may not be the only solution. If ultrafast 3D UMI acquisition is possible (in cases with lower aberrations or at shallow depths), rapid decorrelation of speckle observed in blood flow may be an opportunity because it provides numerous speckle realizations in a given voxel. Therefore, a high-resolution $\mathbf{T}-$matrix could be in principle extracted without spatial averaging and without any isoplanicity assumption [Zhao, 1992; Osmanski, 2012a]. In other words, time averaging (t_p) would replace spatial averaging ($\mathbf{r}$), and the $\hat{\mathbf{T}}-$matrix could be extracted directly from the ultrafast sequence rather than from a previous static sequence as described in this section.

Recent studies suggest that combining a large matrix array with a multi-lens diffracting layer [Favre, 2022; Favre, 2023] may help to increase the sensitivity and thus the signal-to-noise ratio in transcranial ULM imaging. However, this method involves poor sampling of the input and output basis ($\delta u \sim 4\lambda$) and therefore introduces significant grating lobes in the PSF of the system. As shown by the preliminary work of Elsa Giraudat in seismic imaging [Giraudat, 2023], who used a poorly sampled network of geophones to create a corrected image of La Soufrière volcano, matrix imaging can help compensate for the sparsity of such arrays.

Recent work suggests that ULM imaging could help in the detection and classification of cerebrovascular accidents. For example, it would be possible to distinguish between ischemic and hemorrhagic strokes in the early phase [Chavignon, 2022]. Therefore, another perspective of this work within the doctoral thesis of Louise Denis in Olivier Couture's group is to conduct a pilot study on individuals who have recently suffered a cerebrovascular accident.

3 Towards intra-arterial pressure measurement

In the previous experiment, commercially approved Sonovue bubbles [Schneider, 1999] were used to perform ultrasound localization microscopy experiments in the brain. However, such contrast agents have a wide range of diameters, leading to a broad frequency spectrum. Therefore, such contrast agents are not optimized for a particular probe because a number of microbubbles do not oscillate at a frequency within the spectral bandwidth of the probe. The use and fabrication of monodisperse microbubbles could lead to a better signal-to-noise ratio and thus better contrast. According to Minnaert's law [Minnaert, 1933], their resonance frequency is directly proportional to their size. Moreover, older and recent work shows that tracking this resonance frequency could potentially lead to *in vivo* pressure measurement [Fairbank, 1977; Tremblay-Darveau, 2014a; Segers, 2018]. This could be a real advantage when combined with ULM, for example, to obtain not only super-resolved images of the blood vessel velocity field but also quantitative measurements of blood pressure that could be leveraged to better detect or monitor cerebrovascular accidents.

In this side project, the resonance frequency of monodisperse microbubbles is investigated using ultrasound matrix imaging. Monodisperse microbubbles were prepared in the group of Patrick Tabeling (Institut Pierre Gilles de Gennes, ESPCI Paris, PSL) by Ugur Soysal and Pedro Nieckele Azevedo as described in [Soysal, 2022] in the framework of a collaboration with Arnaud Tourin and Mathias Fink. An academic experiment was performed jointly with Ugur Soysal, Pedro Nieckele Azevedo and Justine Robin on a Doppler flow tissue mimicking phantom (CIRS, Model ATS 524). The resonance frequency of monodisperse microbubbles was extracted with UMI and then compared with clinically approved polydisperse bubbles (Sonovue).

3.1 Microfluidic to produce monodipserse microbubbles

The Rayleigh-Plesset equation is usually the starting point for physical modeling of symmetrically coated microbubbles. It leads to the famous equation of a driven harmonic oscillator with a resonance frequency f_0 [Minnaert, 1933], which scales as follows:

$$f_0 \propto \frac{\sqrt{p_A}}{\mathcal{R}_0}, \tag{4.3}$$

where $\mathcal{R}_0$ is the bubble radius and p_A is the ambient pressure.

Nowadays, microfluidics can produce very monodisperse bubbles. However, to transport and preserve them, they need to be freeze-dried without compromising their quality, which is currently difficult. In this case, the uncontrolled dynamics of the freeze-drying process leads to ripening, coalescence and rearrangement processes that reduce monodispersity. The main obstacle to the use of monodisperse microfluidic bubbles in clinical studies is freeze-drying without deterioration. Recent research by Soysal et al. [Soysal, 2022] has succeeded in producing freeze-dried monodisperse microbubbles generated by microfluidics for a variety of applications, including ultrasound contrast agents protected with a nanometric PVA shell without compromising monodispersity. In this work, they propose an entirely new class of contrast agent in the

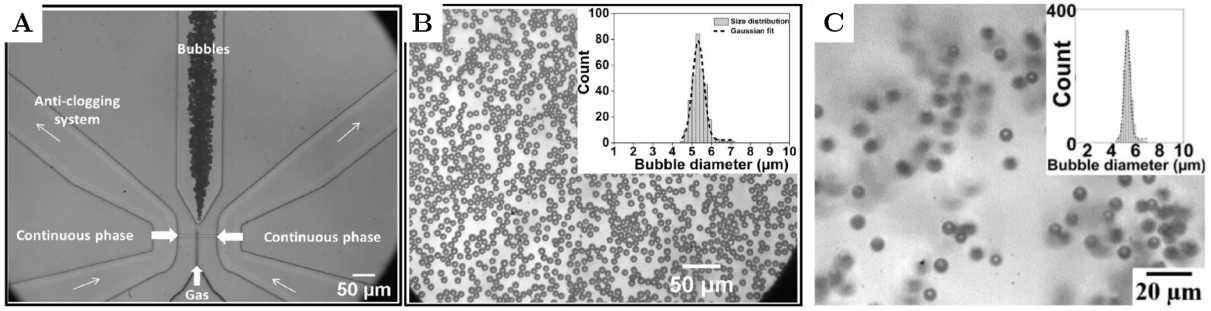

Figure 4.11: **Microfluidic generation of monodisperse 5 µm in diameter PVA microbubbles.** (**A**) Monodisperse bubbles were generated in the central channel located between river channels and after the gas channel. Bubbles exited the device without any coalescence. (**B**) Freshly generated bubbles were collected in a monolayer manner on a glass slide. The inset shows the size distribution of the collected bubbles showing average sizes, standard deviation, and CV are 5.4 µm, 0.3 µm, and 5.%, respectively. (**C**) Re-suspended and floating bubbles in DI water and their size distributions (insets) show the average diameters of the bubbles as 5.4 µm (standard deviation of 0.3 and CV of 5.5 %). *Extracted and adapted from* [Soysal, 2022].

form of a stable lyophylisate that can be transported anywhere for months, resuspended and used immediately in clinical settings. Such results are presented in [Fig. 4.11]. Microbubbles are produced using microfluidic channels [Fig. 4.11A] and further analyse to control their monodispersity [Fig. 4.11B]. Then, an example of resuspended monodisperse microbubbles show that monodispersity is ensured through the freeze-dried process [Fig. 4.11C].

In this section, we aim to study the resonance frequency of such monodisperse microbubbles using ultrasound matrix imaging. Monodisperse microbubbles with a diameter of 5.4 μm were prepared in Patrick Tabeling's team (Institut Pierre Gilles de Gennes, ESPCI Paris, PSL) by Ugur Soysal and Pedro Nieckele Azevedo as described in [Soysal, 2022].

3.2 Description of the experiment

The experiment consists of injecting such bubbles into a Doppler tissue mimicking phantom consisting of tubes surrounded by a gel that mimics the properties of human soft tissues. The bubbles are manually injected into flowing deionized water in a tube with a 8 mm diameter. Here, we aim to take advantage of the motion to filter out the static part of the field to enhance the signal backscattered by the microbubbles. To this end, we design an ultrafast acquisition in which the partial reflection matrix $R_{\mathrm{p}}(\boldsymbol{\theta}_{\mathrm{in}}, \mathbf{u}_{\mathrm{out}}, t, t_{\mathrm{p}})$ is recorded with the parameters described in [Table 4.3] as the microbubbles flow through the tube. Each frame t_{p} is formed by means of a 25 plane waves compounding. The flow rate is set manually and therefore cannot be properly controlled. Thus, the acoustic pressure is unknown.

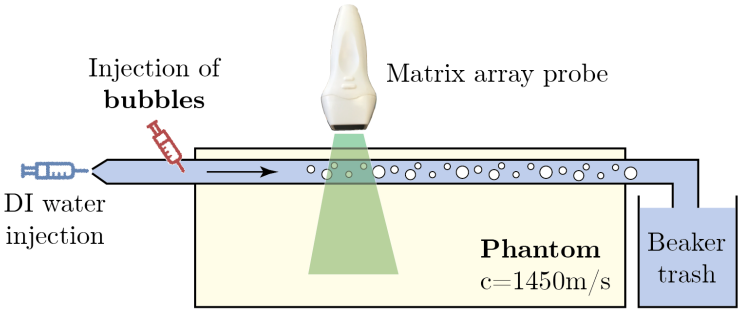

Figure 4.12: **Microbubbles characterization experiment.** DI water is injected manually (uncontrolled flow) in a tube of 8-mm diameter of a tissue mimicking phantom. Re-suspended mono-disperse bubbles [Soysal, 2022] are injected manually in the tube and an ultrasound movie of 20 seconds is recorded using the matrix array $\mathcal{P}_1$ with parameters described in [Table 4.3].

Parameters	**Value**
Plane wave angles at λ_c $\begin{pmatrix}\theta_x\\ \theta_y\end{pmatrix}$ [°]	$\begin{pmatrix}-10\ 5\ 0\ 5\ 10\\ -10\ 5\ 0\ 5\ 10\end{pmatrix}$
Number of plane waves	25
Frame-rate [Hz]	2
Number of frames	40
Duration [sec]	20
Voltage [Volts]	10

Table 4.3: **Ultrasound sequence parameters for the dynamic phantom experiment.**

3.2.1 Extracting microbubbles signal

To enhance the signal associated with the microbubbles, we first subtract the mean average of the complex IQ-signals as follows:

$$\mathbf{R}_{\mathrm{p}}^{(\mathrm{flow})} = \mathbf{R}_{\mathrm{p}} - \langle \mathbf{R}_{\mathrm{p}} \rangle_{t_{\mathrm{p}}}, \tag{4.4}$$

where $\mathbf{R}_{\mathrm{p}}^{(\mathrm{flow})}$ is the filtered matrix containing the signal from the flowing microbubbles.

Such effects are visible when viewing the confocal volume associated with a given frame t_{p} [Fig. 4.13]. The confocal image associated with the raw data only allows visualization of the two echoes coming from the edges of the tube, but not the observation of bubbles [Fig. 4.13A]. Creating the confocal image after removing the static component allows a drastic enhancement of dynamic scatterers in the field of view during the acquisition. In this case, this dynamic signal mainly corresponds to the microbubbles [Fig. 4.13B]. It can be seen that the signal outside the tube describes an ellipse [Fig. 4.13B3], which is nothing but the isochronous volume whose time of flight matches with the scatterers inside the tube. Although a spatial average seems to be sufficient in this case, this is not always sufficient *in vivo*, and more accurate filtering can be achieved using singular value decomposition to decompose the time-dependence of the $\mathbf{R}$-matrix into three subspaces: (i) static, (ii) moving, and (iii) noise part of the field of view [Demene, 2015; Baranger, 2018].

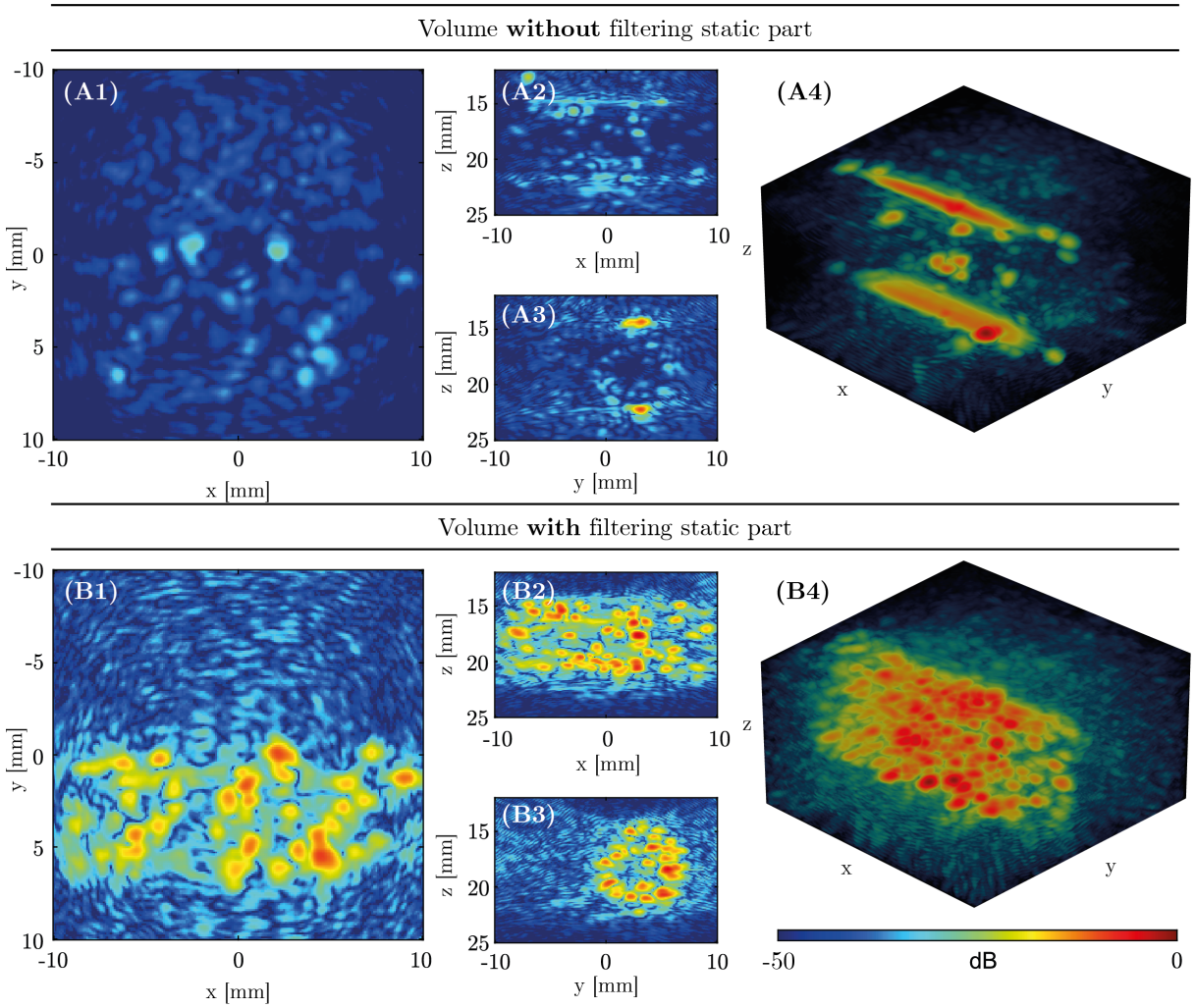

Figure 4.13: **Confocal volume with and without filtering the static part.** (**A**) Confocal volume without filtering static part. The signal corresponds to the edges of the tube. (**B**) Confocal volume obtained after filtering the static part of the signal. The remaining signal corresponds to moving microbubbles in the tube. Interestingly, what remains outside the tube corresponds to the isochronous volume, which correspond to the bubble echo times. Subscripts "1", "2" and "3" correspond to cross-sections in all directions of space, while subscript "4" corresponds to a MIP volume.

3.2.2 Velocity field in the tube

Looking at the successive frames [Fig. 4.14A-C], we can see that the bubbles appear to move faster in the center (solid line) than near the tube wall (dashed line). By cross-correlating adjacent frames, the experimental velocity field in the tube can be extracted, using a common particle image velocimetry (PIV) algorithm. The velocity distribution in the tube appears typical of a *Poiseuille flow* [Fig. 4.14D].

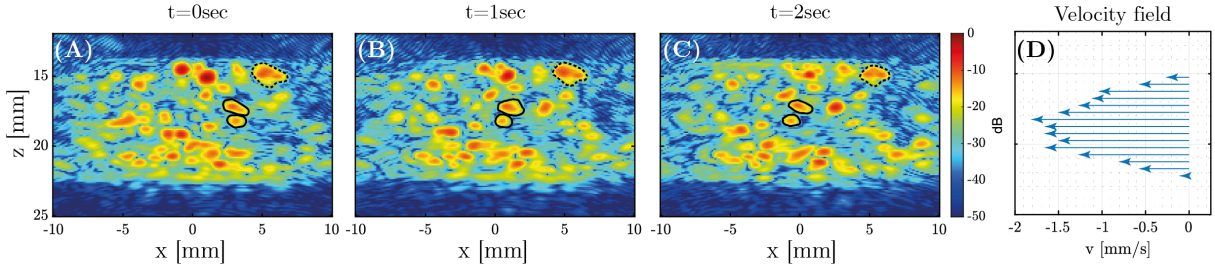

Figure 4.14: **Velocity field in the tube. (A-C)** B-scan images at each seconds in the tube with its associated **(D)** velocity field extracted through a particle image velocimetry (PIV) algorithm.

3.3 Exploiting the temporal degrees of freedom

Our goal now is to study the spectral responses of these microbubbles. Matrix imaging seems to be a suitable tool for this purpose. However, the focused **R**-matrix described in the previous chapter was limited to scanning input and output focal spots located at the same depth ($z_{\text{in}} = z_{\text{out}}$). In other words, only the transverse dependence of the **R**-matrix was investigated. Since the frequency or time dependence of the microbubbles occurs in the axial dimension, we need to go a step further and perform an axial study of the focused R matrix.

To this end, the focused reflection matrix is extended here to study its time dependence by adding a time shift δt with respect to ballistic time [Lambert, 2020a]. The beamforming process can thus be updated as follows:

$$R(\boldsymbol{\rho}_{\text{in}}, \boldsymbol{\rho}_{\text{out}}, z, \delta t) = \sum_{\mathbf{i}_{\text{in}}} \sum_{\mathbf{u}_{\text{out}}} R\left(\mathbf{i}_{\text{in}}, \mathbf{u}_{\text{out}}, \tau(\mathbf{i}_{\text{in}}, \mathbf{r}_{\text{in}}, c_0) + \tau(\mathbf{u}_{\text{out}}, \mathbf{r}_{\text{out}}, c_0) + \delta t\right), \tag{4.5}$$

where the assumed sound velocity here corresponds to the phantom $c_0 = 1450$ m/s. As the reflection matrix was acquired only partially, aliasing may appear in the transverse direction and only the confocal signal will now be studied ($\boldsymbol{\rho}_{\text{in}} = \boldsymbol{\rho}_{\text{out}} = \boldsymbol{\rho}$), such that the focused reflection matrix is reduced to the spatio-temporal confocal matrix:

$$\mathbf{R}_{\text{c}} = [R_{\text{c}}(\mathbf{r}, \delta t)] = [R(\underbrace{\boldsymbol{\rho}_{\text{in}} = \boldsymbol{\rho}_{\text{out}}, z}_{\mathbf{r}}, \delta t)], \tag{4.6}$$

with $\mathbf{r} = (\boldsymbol{\rho}, z)$ is the focal point under study. Mathematically, it can be expressed as follows (see Appendix 4.1):

$$R_{\text{c}}(\mathbf{r}, \delta t) = \int \mathrm{d}\mathbf{r}' \left(\gamma(\mathbf{r}', \delta t) \overset{\delta t}{\circledast} H_{\text{in}}(\mathbf{r}, \mathbf{r}', \delta t) \overset{\delta t}{\circledast} H_{\text{out}}(\mathbf{r}, \mathbf{r}', \delta t)\right). \tag{4.7}$$

First, we will give some physical intuitions about the information contained into this new matrix. On the one hand, for a random scattering medium, each time shift corresponds to a different isochronous volume in the medium. This aspect will be described in the next chapter. On the other hand, reflectivity of a sparse scattering medium made of isolated scatterers can be

expressed as follows:

$$\gamma(\mathbf{r},t) = \sum_i \delta(\mathbf{r}-\mathbf{r}_i)\mathcal{B}(\mathbf{r}_i,t), \tag{4.8}$$

with $\mathcal{B}(\mathbf{r}_i,t)$ the time response of each point-like reflector. Injecting (Eq. 4.8) in (Eq. 4.7) leads to:

$$R_c(\mathbf{r},\delta t) = \sum_i \mathcal{B}(\mathbf{r}_i,\delta t) \overset{\delta t}{\circledast} \left(H_{\text{in}}(\mathbf{r}_i,\mathbf{r},\delta t) \overset{\delta t}{\circledast} H_{\text{out}}(\mathbf{r}_i,\mathbf{r},\delta t) \right), \tag{4.9}$$

or, in the frequency domain,

$$R_c(\mathbf{r},\omega) = \sum_i \mathcal{B}(\mathbf{r}_i,\omega) \left(H_{\text{in}}(\mathbf{r}_i,\mathbf{r},\omega) H_{\text{out}}(\mathbf{r}_i,\mathbf{r},\omega) \right). \tag{4.10}$$

Hence, provided that one can estimate the spectral response of the system $H_{\text{in}}(\mathbf{r}_i,\mathbf{r},\omega)H_{\text{out}}(\mathbf{r}_i,\mathbf{r},\omega)$, the confocal matrix can grasp the spectral response of each acoustic reflector $\mathcal{B}(\mathbf{r}_i,\omega)$.

3.3.1 Spectral analysis of the most echogenic bubble

First, the frequency response of the most echogenic microbubbles in the field of view is studied by computed its time Fourier transform $R(\mathbf{r}_b,\omega)$ [blue curve in Fig. 4.15B], where $\mathbf{r}_b$ is the position of these microbubbles. Their spectrum has a large spectral bandwidth, which is nothing but the spectral bandwidth of the transducer. Since we assume that the oscillations of the microbubbles occur after the ballistic time, *i.e.* after the direct echo (first echo on the surface of the bubble), one strategy to highlight the bubble resonant effects is to filter the direct echo with a time filter constructed as follows:

$$R_{\text{filt}}(\mathbf{r}_{\text{b}},\delta t) = R(\mathbf{r}_{\text{b}},\delta t)\mathcal{W}_{\text{t}}(\delta t), \tag{4.11}$$

with $\mathcal{W}_t(\delta t)$ a time window defined as follows:

$$\mathcal{W}_t(\delta t) = \begin{cases} 0 \text{ for } \delta t < 0\mu s; \\ \frac{1}{2}\left(1-\cos(\frac{1}{2}\pi\delta t)\right) \text{ for } \delta t \in [0;2]\mu s; \\ 1 \text{ for } \delta t > 2\mu s. \end{cases} \tag{4.12}$$

The effect of such a filter is shown in [orange curve in Fig. 4.15]. The spectral response is shifted toward the lower frequencies, indicating that we have succeeded in at least partially removing the influence of the transducer response on our frequency analysis.

3.3.2 Statistical approach

We will now perform the same procedure described previously, but globally for all points located in the tube. An average spectrum $\mathcal{S}_{\text{tube}}$ associated to the tube can thus be extracted as follows:

$$\mathcal{S}_{\text{tube}}(\omega) = \left\langle \left| \int_{-\infty}^{+\infty} \mathrm{d}\delta t R_{\text{p}}^{(\text{flow})}(\mathbf{r},\omega)\mathcal{W}_t(\delta t)\exp(i\omega\delta t) \right|^2 \mathcal{W}_{\text{tube}}(\mathbf{r}) \right\rangle_{\mathbf{r}}, \tag{4.13}$$

with $\mathcal{W}_{\text{tube}}$ a logical window that select only focal point in the tube. The spectral shape of $\mathcal{S}_{\text{tube}}$ shows a similar slight shift to the lower frequencies [blue curve in Fig. 4.16E]. However, in order

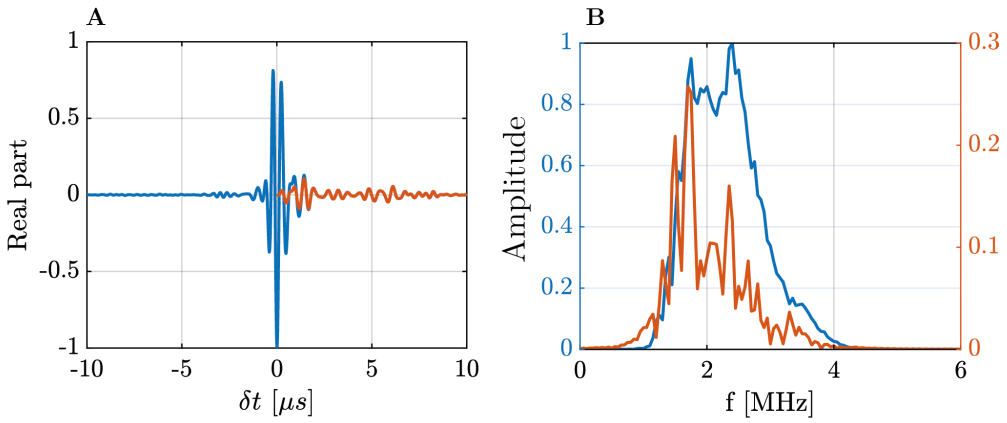

Figure 4.15: **Frequency analysis of the most echogenic bubbles.** (**A**) Time response of the most echogenic bubble in the field-of-view. A filter (Eq. 4.12) can be applied to remove the direct echo of the microbubble (orange curve). (**B**) Frequency spectrum of the original (blue curve) and filtered (orange curve) bubble response.

to better filter the spectral responses of the transducer, similar treatment can be applied to the unfiltered R_{p} matrix and locally averaging the spectral responses in the speckle located at the same depth of the tube as described in [red circle 4.16B] as follows:

$$\mathcal{S}_{\mathrm{speckle}}(\omega) = \left\langle \left| \int_{-\infty}^{+\infty} \mathrm{d}\delta t R_{\mathrm{p}}(\mathbf{r},\omega)\mathcal{W}_t(\delta t)\exp(i\omega\delta t) \right|^2 \mathcal{W}_{\mathrm{speckle}}(\mathbf{r}) \right\rangle_{\mathbf{r}}. \tag{4.14}$$

A better estimation of the microbubbles frequency response can be obtained by dividing the two obtained spectrum as follows:

$$\hat{\mathcal{S}}_{\mathrm{Monodisperse}}(\omega) = \frac{\mathcal{S}_{\mathrm{tube}}(\omega)}{\mathcal{S}_{\mathrm{speckle}}(\omega)}. \tag{4.15}$$

A peak appears at the exact resonance frequency of the monodisperse microbubble, $f_0 \approx 1.2$ MHz, as shown in [green curve 4.16E].

The same experiment with the same post-processing was then performed with polydisperse Sonovue bubbles and resulted in a broader frequency response as shown in [blue curve in Fig. 4.17]. This suggests that the use of monodisperse bubbles in conjunction with ultrasound matrix imaging could be a relevant tool to track the resonance frequency of monodisperse microbubbles and indirectly the intra-arterial blood pressure [Fairbank, 1977; Tremblay-Darveau, 2014a].

3.4 Perspectives

Although these results are very promising, they need to be nuanced and further experiments should be performed to validate the whole method. First, the deconvolution step (4.15) is subject to a large uncertainty, since we are dividing by something close to zero at the edges of the bandwidth. To remove this uncertainty, we can examine microbubbles with a resonance frequency that fits better in the middle of the spectral bandwidth of the transducer than at the edges. Moreover, the physics of the bubbles depends on many parameters that we cannot

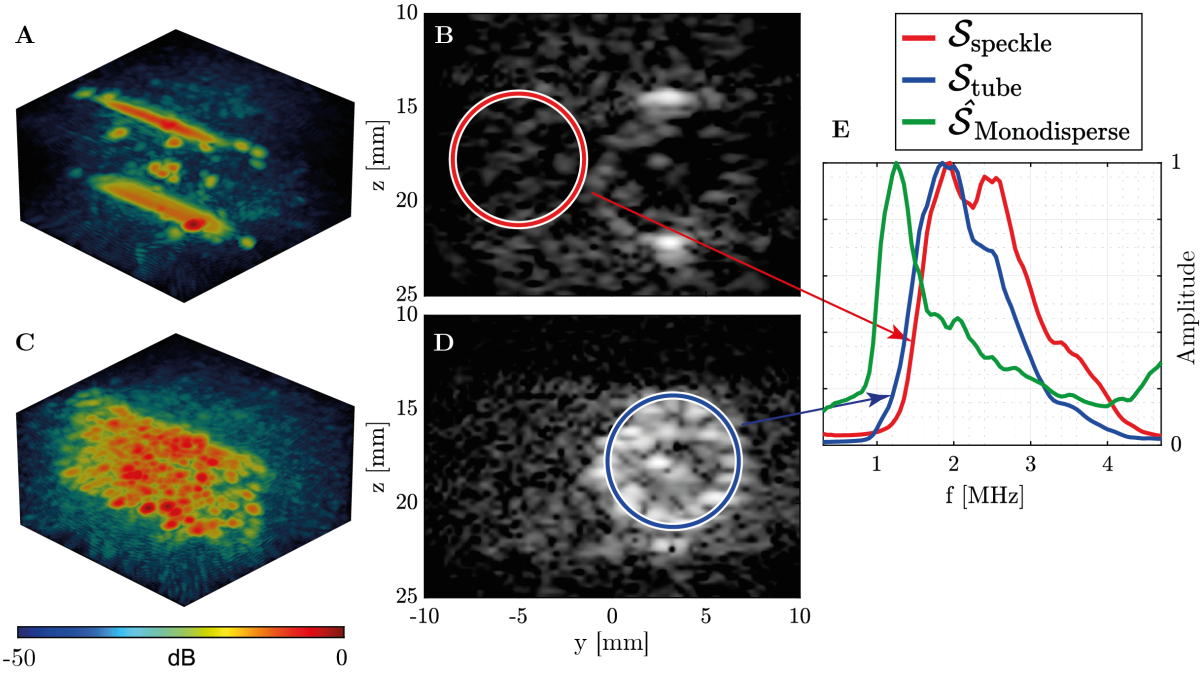

Figure 4.16: **Extraction of the resonance frequency of monodisperse microbubbles.** (**A, C**) 3D confocal volumes and (**B, D**) 2D cross-sections of $\mathcal{I}$ and $\mathcal{I}^{(\text{flow})}$, respectively. (**E**) Frequency spectrum associated to the phantom speckle (red curve) and the tube (blue curve). A deconvolution is performed to extract the resonance of the monodisperse bubbles (green curve).

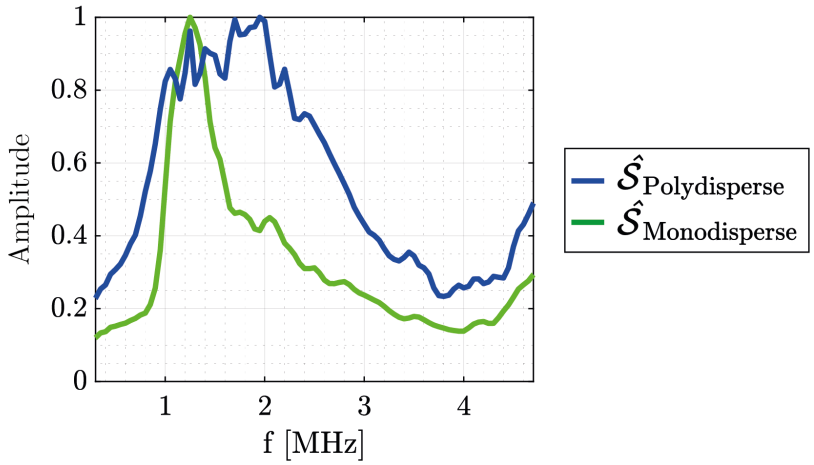

Figure 4.17: **Spectral analysis of poly- and mono-disperse microbubbles.** The green curve is the spectral analysis of the monodisperse PVA microbubbles whose production process is described in [Fig. 4.11]. The blue curve is assigned to the polydisperse Sonovue microbubbles.

properly control in this preliminary study:

– acoustic pressure, for example, can affect the nonlinear responses of the bubbles. In this experiment, the lowest possible voltage (10 Volts) was applied to the transducers, but the probe has not been yet calibrated, and therefore the corresponding acoustic pressure is not known;

- the presence of neighboring bubbles in such an experiment may lead to multiple scattering. Such effects could be exploited, for example, when considering isolated microbubbles in the tube rather than a bubble cloud as in this case. In addition, multiple scattering caused by microbubbles could be investigated by a complete acquisition of the **R**-matrix when the flow is stopped. Thus, a procedure similar to the one described in the previous chapter could be used to quantify the multiple scattering caused by microbubbles;
- the response of the bubbles may be altered by their local environment, *e.g.* by the presence of the vessel/tube surface [Versluis, 2020];
- the flow rate was not controlled in this experiment and its value was not known. The use of a syringe pump operating at a constant flow rate would eliminate this problem.

With all these considerations, new experiments could be performed to validate the method and possibly use it to track intra-arterial blood pressure.

4 Conclusion & Perspectives

In this chapter, we have shown that the time-dependence of the focused reflection matrix has been exploited for tracking the resonance frequency of monodisperse bubbles and indirectly the local pressure. This observation could be applied to intra-arterial measurements and would thus provide a new imaging method for the investigation and monitoring of cerebral vascular accidents.

Moreover, we show that other ultrasound imaging techniques, such as Ultrasound Localization Microscopy, can be easily combined with Matrix Imaging to at least partially compensate for aberrations. In this particular case, we have shown that matrix imaging was a real asset to detect a higher number of microbubbles, resulting not only in contrast enhancement of the ULM image, but also in elimination of artifacts caused by the skull (duplicated vessels, false detection of bubbles, etc.).

Even though transverse aberrations can be compensated for with the distortion matrix approach, the position of the scatterers in the image still depends on the speed-of-sound hypothesis assumed during beamforming. In the next chapter, we will now consider the effects of aberrations due to variations in the speed of sound in the axial dimension. Matrix imaging will be shown to provide the self-portrait of wave focusing at any point, including in the speckle. This key observation can then be used to extract a local map of the defocus across the ultrasound image. Such a map can then be leveraged for an axial compensation of aberrations.

Chapter 5

Matrix compensation of axial aberrations

Objectives

For a given speckle grain (fixed isochronous volume), we will examine the evolution of the RPSF not only in the transverse direction but also in the axial dimension. In this way, we will obtain a **self-portrait of the local focusing process**, from which we can determine a shift in the focal plane (defocus) at any point in the image. By correcting this focus shift, we can compensate for the axial aberrations of the ultrasound image. We will show that this method is particularly relevant for multilayered media.

Contents

1 Introduction

The reflection matrix approach considered until now is an appropriate tool to compensate for the transverse effects of aberrations, but the current formalism is not sufficient to account for the axial distortions of the ultrasound image. Indeed, axial variations of the speed-of-sound can lead to a mismatch between the focusing plane (where the wave is spatially focused) and the isochronous volume (area where singly-scattered echoes come from) at a given echo time t [Fig. 5.2A]. This phenomenon results in aberrations known as defocus in optics [Labiau, 2009] and to a bad scaling of the axial dimension of the ultrasound image.

In ultrasound, a compensation of a focus defect has already been realized in Ultrasound Localization Microscopy in presence of a strong and isolated scatterer [Diamantis, 2018]. Here we want to show how to perform this operation in ultrasonic speckle. To this end, we will exploit the principle of the RPSF presented in the previous chapters, but this time studying its axial dependence (and not only lateral).

In practice, this will be done by axially scanning the input and output focal points, for a given isochronous volume (*i.e.* working at a fixed echo time). The RPSF can be studied globally by averaging it incoherently over the field of view. The optimal focusing defect is then the one that minimizes the lateral extension of the RPSF, or equivalently maximizes the confocal signal, which also corresponds to an optimization of the **focal curvature** for a given speckle grain. However, it is also possible to combine the RPSFs in a coherent manner using a Singular Value Decomposition. One then obtains a self-portrait of the amplitude and phase of the focused wave. In particular, one can then take advantage of the Gouy phase jump [Feng, 2001], *i.e.* the sign change of the phase of a wave at the focal point, to produce an estimator that outperforms other intensity-based methods.

A global correction of the focus defect is valid through multi-layer media, which induce a constant focus defect. When the layer is homogeneous and translation invariant, this method appears to be simpler than existing refraction-based methods [Mozaffarzadeh, 2022; Greco De Sousa, 2007; Smith, 1986]. In a more general case where 3D spatially distributed aberrations occur, the defocus change for each point of the image and thus requires a local study of the RPSFs.

In addition to provide a significant improvement of the contrast and the resolution of the image, it makes it possible, in a multi-layered media, to measure absolute relative positions between the scatterers by re-scaling the z-axis of the image. Also, this step of compensation of axial aberrations can be seen as a preliminary step to the compensation of transverse aberrations [Fig. 5.2A].

In this chapter, we will first describe the different steps of the method using an experiment on an ultrasound phantom without aberrations. Then we will apply the method to the case of a multi-layered imaging experiments. We will show both theoretically and experimentally that the global correction of the focus defect allows correcting the aberrations of the image in the whole field of view. We will take advantage of this example to illustrate the fact that an axial compensation of aberrations allows making less restrictive the condition between the number of

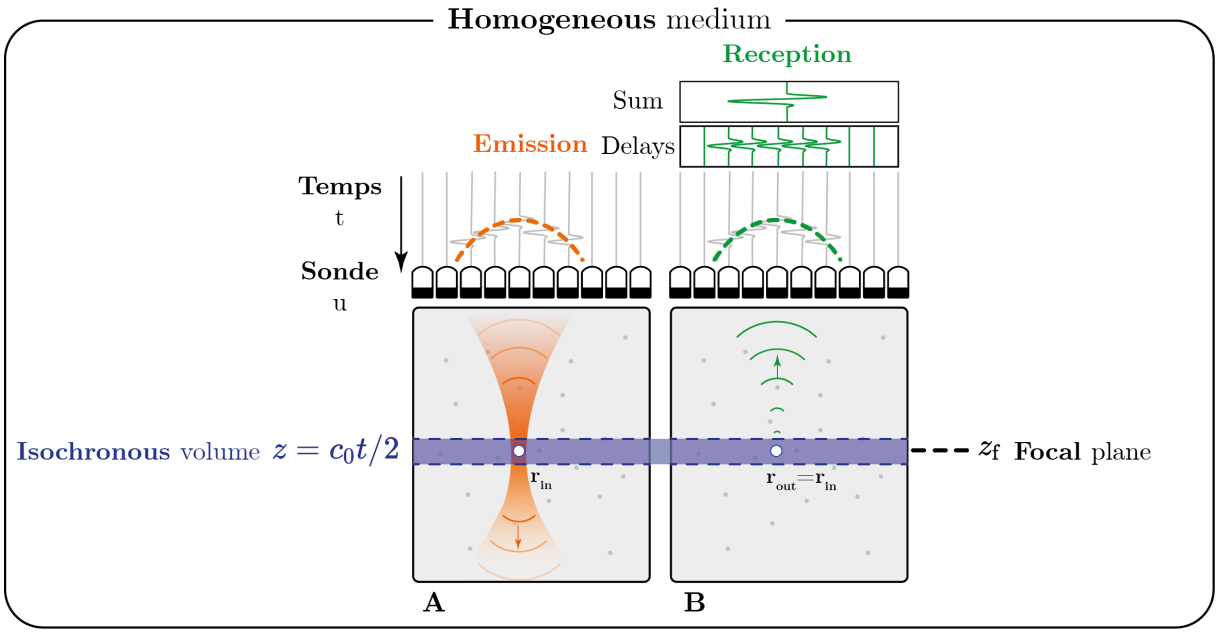

Figure 5.1: **Ultrasound imaging in a homogeneous medium.** Assuming that we know the constant speed-of-sound of the medium, (**A**) geometric time delays allow focusing on a given point at the input. (**B**) Echoes emanating from the same point can be similarly delayed so that the wavefronts can be aligned and thus coherently summed. In this case, the sum is optimal because the isochronous volume coincides with the focal plane.

insonifications and the level of aberrations. Finally, we will tackle the case of *in vivo* imaging by highlighting the need for a local study of RSPF and a local correction of a focus defect.

2 From transverse to axial aberrations

First, the differences between transverse and axial effects are examined. Suppose we know the speed of sound of a homogeneous medium [Fig. 5.1]. The application of geometric time-delays at both the input and the output allows the selection of echoes originating from the isochronous volume which matches the focal depth. A conventional delay and sum algorithm allows coherent summation of the individual channels, resulting in image resolution limited by diffraction.

However, if we consider a medium with spatially distributed aberrations [Fig. 5.2], the focusing process is severely affected at both the input and the output. First, the wavefront of the ultrasound wave is distorted as it passes through the aberrating layer, resulting in a degradation of the transverse PSF and thus a reduction in resolution. Even more, the imaging plane associated with the isochronous volume of the target point, no longer coincides with the focal plane [Fig. 5.2A]. The same considerations can be applied to the output, eventually leading to a global failure of the focusing process when a delay and sum algorithm is applied [Fig. 5.2B]. Such aberrations, due to the variation of the speed of sound in the axial direction, result in an image with incorrect positioning of the individual scatterers of the field of view.

We now consider a general procedure for beamforming the $\mathbf{R}-$matrix, in which the input and output focal spots are still located at the same depth ($z_{in} = z_{out}$), so that both experience

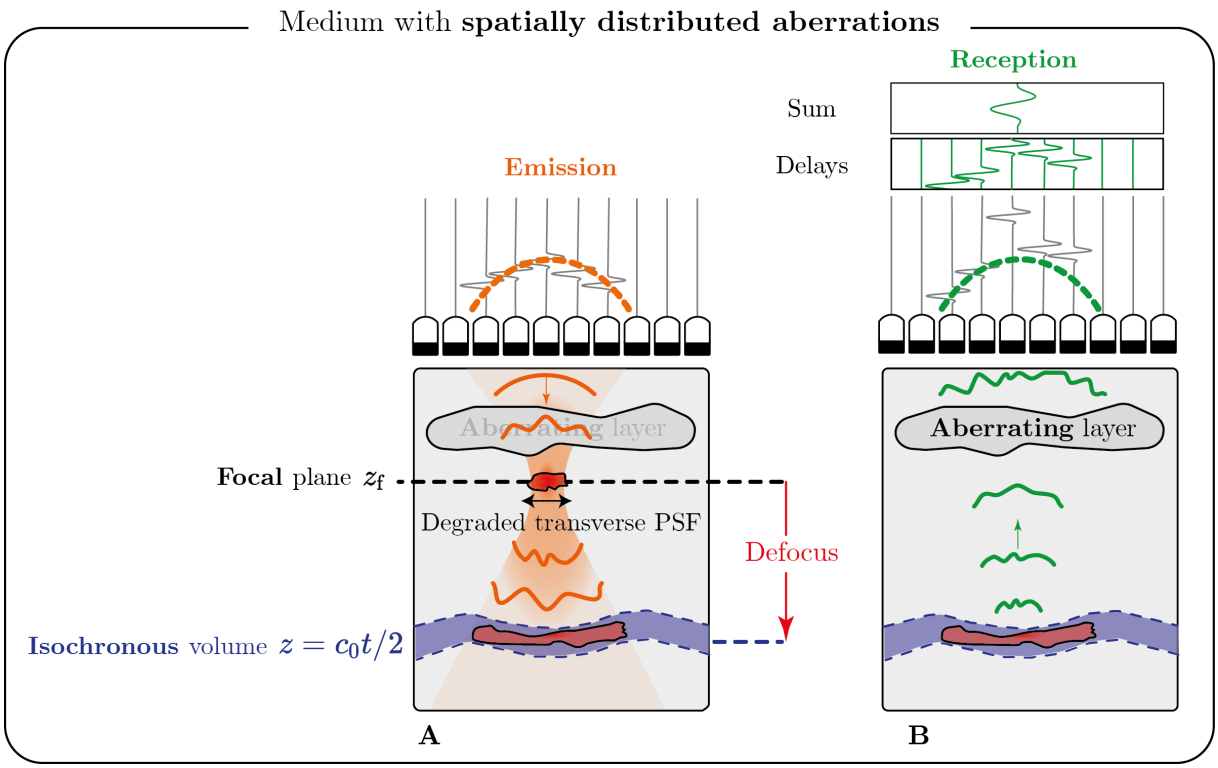

Figure 5.2: **Adverse effects of aberrations in ultrasound imaging.** We consider the case where spatial variations in the speed of sound affect the focusing process. (**A**) First, wavefronts are distorted due to the transverse variations in wave velocity, resulting in a degradation of the transverse PSF in the focal plane. In addition, axial variations in wave velocity lead to a mismatch between the position of the isochronous volume and the focal plane. Such axial aberrations effect leads to a shift in the true position of the scatterer under study. (**B**) The same considerations can be applied to reception, so that the delay and sum algorithm fails to coherently sum the targeted echoes from the isochronous volume.

the same transverse aberrations. Mathematically, it can be formulated for the general case of 3D imaging as follows:

$$R(\boldsymbol{\rho}_{\text{in}}, \boldsymbol{\rho}_{\text{out}}, z, t, c_0) = \sum_{\mathbf{i}_{\text{in}}} \sum_{\mathbf{u}_{\text{out}}} R\left(\mathbf{i}_{\text{in}}, \mathbf{u}_{\text{out}}, t + \Delta\tau(\mathbf{i}_{\text{in}}, \boldsymbol{\rho}_{\text{in}}, t, z, c_0) + \Delta\tau(\mathbf{u}_{\text{out}}, \boldsymbol{\rho}_{\text{out}}, t, z, c_0)\right), \tag{5.1}$$

where $\Delta\tau$ denotes a time delay, resulting from the difference between the calculated time-of-flight and the time to reach the focal depth:

$$\underbrace{\Delta\tau(\mathbf{i}_{\text{in}}/\mathbf{u}_{\text{out}}, \boldsymbol{\rho}, z, c_0)}_{\text{Time delays}} = \underbrace{\tau(\mathbf{i}_{\text{in}}/\mathbf{u}_{\text{out}}, \boldsymbol{\rho}, z, c_0)}_{\text{Time of flight}} - z/c_0, \tag{5.2}$$

where c_0 denotes the speed-of-sound hypothesis, which is considered constant in the following of this chapter. Its dependence is investigated in Chapter 6.

In conventional imaging, two considerations are then made to produce an image: (i) only the confocal signal is examined ($\boldsymbol{\rho}_{\text{in}} = \boldsymbol{\rho}_{\text{out}}$) and (ii) the imaging plane matches the coherence

volume (*i.e.* the isochronous volume) such that $z = c_0 t/2$. The extension of the first point has already been discussed earlier (see Chapters 2 and 3) by decoupling the input and output focal spots. Now we want to explore the decoupling between the imaging plane and the echo travel time to make the focal plane coincide with the coherence volume even in the presence of aberrations [Fig. 5.2]. To this end, three strategies can be explored:

- either by shifting the coherence volume ($t + \delta t$) in time to a fixed focal plane ($z = c_0 t/2$) [Fig. 5.3A]. This consideration is thus similar to the one presented in the previous chapter on bubble characterization;
- either by shifting the depth ($z + \Delta z$) to bring the focal plane to the fixed coherence volume ($t = 2z/c_0$), as shown in [Fig. 5.3B];
- either by scanning the speed of sound hypothesis (c_0) to bring the focal plane to the fixed coherence volume ($t = 2z/c_0$). This method will be presented in the next chapter.

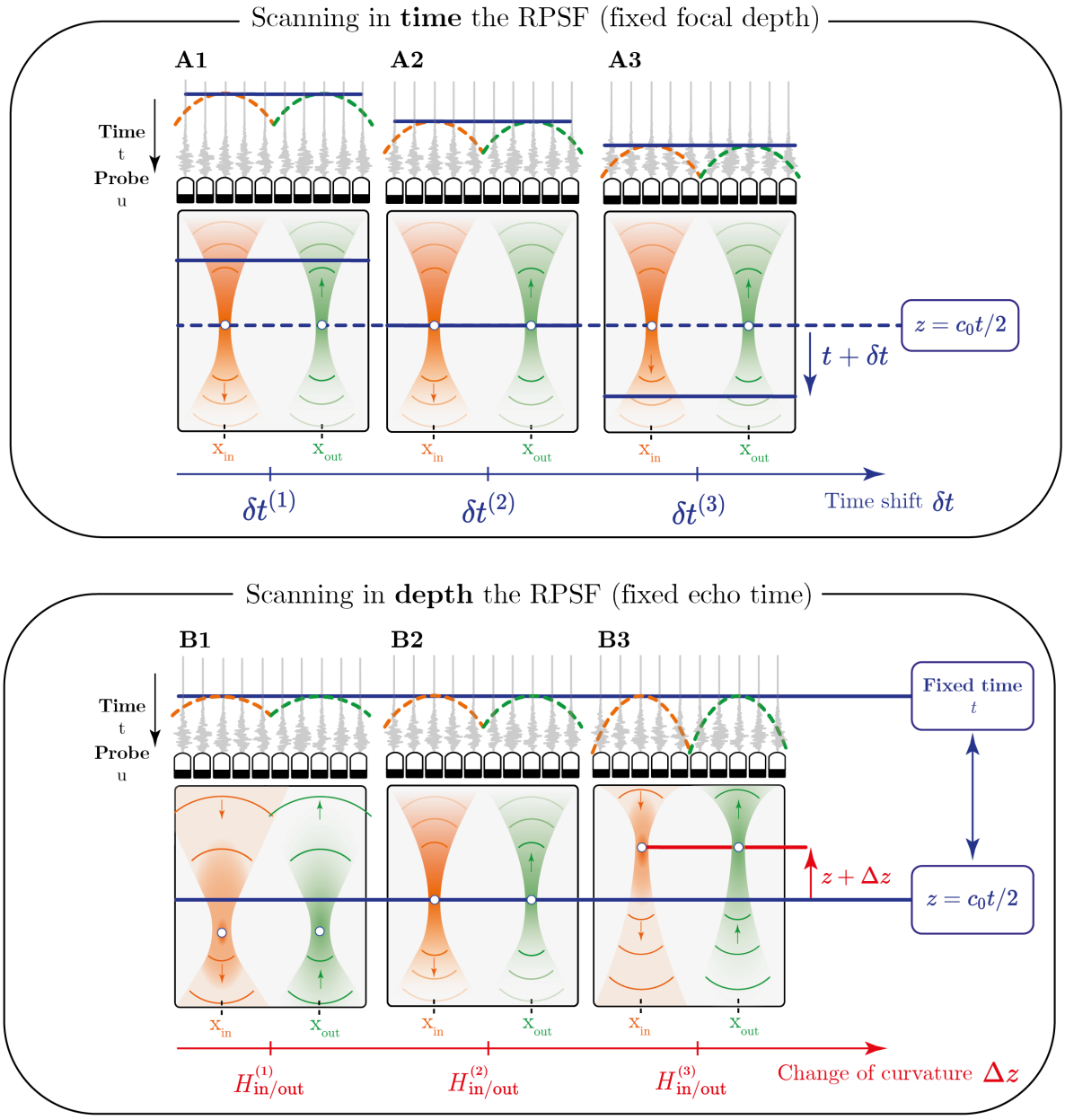

Figure 5.3: **Scanning in time or in depth the RPSF.** (**A**) The coherence volume ($t + \delta t$) is shifted by scanning the time-shift, δt, while the focal depth ($z = c_0 t/2$) is fixed (at both input and output). (**B**) The imaging plane ($z_i = z + \Delta z$) is shifted by scanning the focal depth Δz at fixed echo time ($t = 2z/c_0$). This second process is equivalent to scanning the focal curvature for a fixed echo time. Each column is associated with a different value of time shift δt or focal depth Δz. *Panel B is inspired by* [Perrot, 2021].

3 Scanning the axial dimension with time

First, we will examine the first option, which scans time. The time-dependent focused $\mathbf{R}-$matrix can be formed by considering an additional time shift δt with respect to the ballistic time, while

the focal depth is fixed at $z = c_0 t/2$, so that:

$$R(\boldsymbol{\rho}_{\text{in}}, \boldsymbol{\rho}_{\text{out}}, z = c_0 t/2, t + \delta t). \tag{5.3}$$

For the sake of clarity of notation, let us then consider the following change of variables:

$$[R_{\mathcal{D}}(\boldsymbol{\rho}, \boldsymbol{\Delta\rho}, z, \delta t)] = [R(\boldsymbol{\rho}_{\text{in}}, \boldsymbol{\rho}_{\text{out}}, c_0 t/2, \underbrace{t + \delta t}_{t_i})], \tag{5.4}$$

which can be expressed mathematically as follows:

$$\begin{bmatrix} \boldsymbol{\rho}_{\text{in}} \\ \boldsymbol{\rho}_{\text{out}} \\ z \\ t_i \end{bmatrix} \rightarrow \begin{bmatrix} \boldsymbol{\rho} \\ \boldsymbol{\Delta\rho} \\ z \\ \delta t \end{bmatrix} = \begin{bmatrix} \boldsymbol{\rho}_{\text{in}} \\ \boldsymbol{\rho}_{\text{out}} - \boldsymbol{\rho}_{\text{in}} \\ z \\ t_i - t \end{bmatrix}. \tag{5.5}$$

First, we consider the simple case of imaging an ultrasound phantom with a linear probe without an aberration layer [Fig. 5.4A1] with the parameters described in [Table. 2.1]. A line of the focused $\mathbf{R}-$matrix reshaped into $\mathbf{R}_{\mathcal{D}} = [R_{\mathcal{D}}(\{\boldsymbol{\rho}, z\}, \{\boldsymbol{\Delta\rho}, \delta t\})]$ defined in (Eq. 5.4) is shown [Fig. 5.4C1], *i.e.* for a speckle grain defined by its spatial coordinates $(\boldsymbol{\rho}, z)$. This panel represents nothing but a new visualization of the focused $\mathbf{R}$-matrix, where the transverse dimension refers to the de-scan variable $\boldsymbol{\Delta\rho}$ and the axial dimension refers to the time-shift δt with respect to ballistic time.

One can already see that the size of the transverse RPSF is minimized at the expected time $\delta t = 0$ μs. However, it exhibits some random fluctuations as other speckle grains contribute to the signal below and above the focal plane. A local incoherent spatial average (intensity) can be performed to smooth the speckle fluctuations [Fig. 5.4D_1] and the energy maximum occurs along the confocal signal ($\boldsymbol{\Delta\rho} = 0$ mm).

We now explore the possibility of extracting a defocus (or axial shift) that occurs in a multi-layered medium. To this end, a layer of water was added between the probe and the phantom [Fig. 5.4A2]. Similarly, an incoherent average allows smoothing the randomness of the individual speckle grains, and a maximum energy can be observed at a time other than $\delta t = 0$ μs. Thus, scanning in time the RPSF, or more generally the study of the time dependence of the focused $\mathbf{R}-$matrix allows us to construct a self-portrait of the focusing process, as the time shift with respect to the ballistic time is thus directly connected with the actual position of the focal plane $z_{\text{f}} = z + \Delta z$, where $\Delta z = c_0 \delta t/2$. Unfortunately, this approach, although very elegant, has two major drawbacks, namely the **attenuation** shown in [Fig. 5.4D] and the influence of neighboring strong reflectors. For these two reasons, scanning in time the RPSF is subject to severe limitations that makes it very limited and insufficient to properly estimate a defocus in biological tissues.

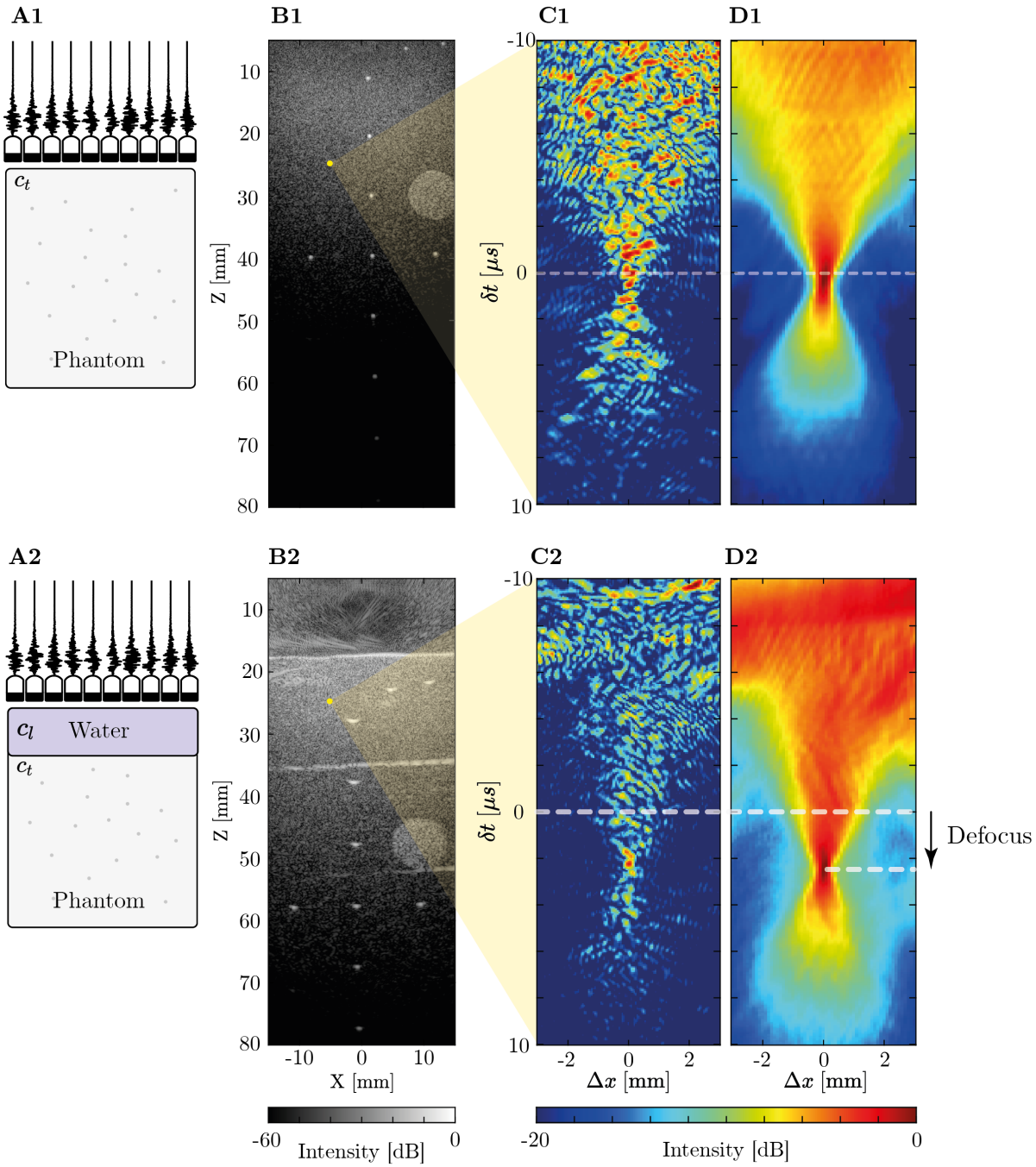

Figure 5.4: **Scanning in time the RPSF.** (**A**) Schematic representation of the experiment. (**B**) Conventional ultrasound image. (**C**) $R_{\mathcal{D}}(\{x, z\}, \{\Delta x, \delta t\})$ for a single speckle grain $(x, z) = (-5, 25)$ mm, shown as a yellow dot. (**D**) Incoherent average over multiple adjacent speckle grains, using a rectangular window of size $w_{\mathbf{r}} = 1$ mm. The first row corresponds to a phantom experiment with no aberrating layer. The second row corresponds to the case where there is a water layer between the probe and the phantom. The parameters of both acquisitions are identical and are described in [Table. 2.1].

4 Scanning in depth the RPSF

To overcome attenuation, we now investigate the second option, that consists in examining echoes backscattered at a **fixed echo time** t, corresponding to the ballistic depth $z_{\rm i} = c_0 t/2$ [see blue line in Fig. 5.3B]. The input and output focal spots are still located at the same depth ($z_{\rm in} = z_{\rm out} = z_{\rm i}$), so that they both experience the same transverse aberrations. An axial shift Δz of these focal spots is then considered with respect to the ballistic depth $z_{\rm i}$ such that the focused $\mathbf{R}-$matrix is expressed as follows:

$$R(\boldsymbol{\rho}_{\rm in}, \boldsymbol{\rho}_{\rm out}, z = c_0 t/2 + \Delta z, t). \tag{5.6}$$

Similarly than before, we consider the following change of variables:

$$[R_{\mathcal{D}}(\boldsymbol{\rho}, \boldsymbol{\Delta\rho}, \Delta z, t)] = [R(\boldsymbol{\rho}_{\rm in}, \boldsymbol{\rho}_{\rm out}, z, t)] \tag{5.7}$$

which can be expressed mathematically as follows:

$$\begin{bmatrix} \boldsymbol{\rho}_{\rm in} \\ \boldsymbol{\rho}_{\rm out} \\ z \\ t \end{bmatrix} \rightarrow \begin{bmatrix} \boldsymbol{\rho} \\ \boldsymbol{\Delta\rho} \\ \Delta z \\ t \end{bmatrix} = \begin{bmatrix} \boldsymbol{\rho}_{\rm in} \\ \boldsymbol{\rho}_{\rm out} - \boldsymbol{\rho}_{\rm in} \\ z - c_0 t/2 \\ t \end{bmatrix}. \tag{5.8}$$

Physically, scanning the focal depth z of the input and output focal spots can be seen as scanning the focal curvature on the RF data as depicted in [Fig. 5.3B]. Conventional imaging thus corresponds to confocal imaging ($\boldsymbol{\Delta\rho} = 0$) with the reference curvature ($\Delta z = 0$) such that:

$$\mathcal{I}_{\rm conf}(\boldsymbol{\rho}, t) = |R_{\mathcal{D}}(\boldsymbol{\rho}, \boldsymbol{\Delta\rho} = 0, \Delta z = 0, t)|^2. \tag{5.9}$$

Generally the time axis is converted into a depth axis $z_{\rm i} = c_0 t/2$ [blue axis in Fig. 5.3] but we have to keep in mind that the axial dimension of a conventional ultrasound image is dictated by the constant speed-of-sound hypothesis made during beamforming.

5 Spatial averaging

We study here the same phantom experiment described earlier in Chapter 2 [Table. 2.1]. One line of the focused $\mathbf{R}-$matrix reshaped in $\mathbf{RPSF} = [R_{\mathcal{D}}(\{\boldsymbol{\rho}, t\}, \{\boldsymbol{\Delta\rho}, \Delta z\})]$ defined in (Eq. 5.7) is shown [Fig. 5.5A], *i.e.* for a speckle grain defined by its spatio-temporal coordinates $(\boldsymbol{\rho}, t)$ (see Appendix 11). Even though the focusing process can be observed with an intensity maximum close to the reference point ($\Delta z = 0, \boldsymbol{\Delta\rho} = 0$), it still exhibits some fluctuations since other speckle grains contribute to the signal when the focal spot is enlarged at large defocus. As with the RPSF defined in the previous chapters, a local spatial average can be performed to smooth the speckle fluctuations and investigate quantitatively the focusing process.

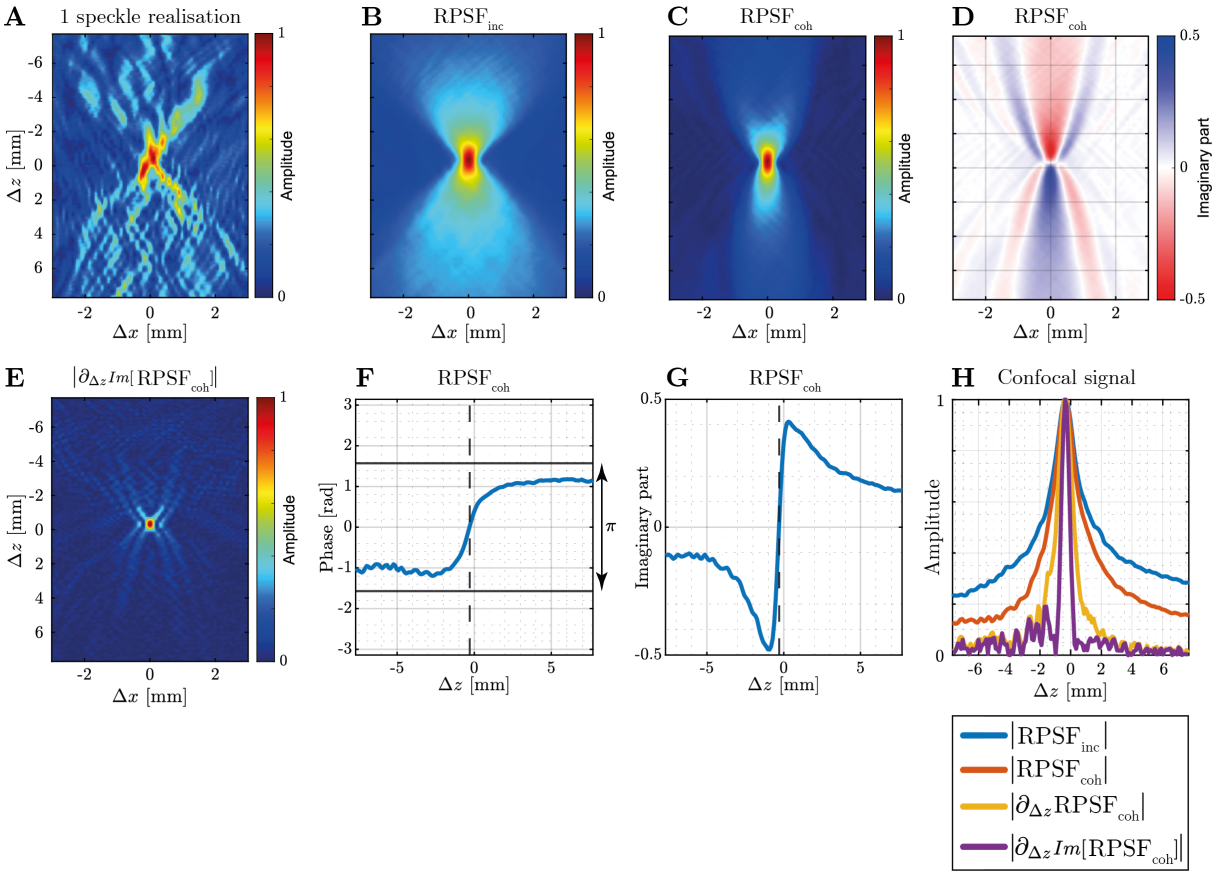

Figure 5.5: **Bi-dimensional RPSF in the speckle** (Tissue mimicking phantom experiment). **(A)** Modulus of RPSF for one speckle realization. **(B)** Incoherent mean $\mathbf{RPSF}_{\text{inc}}$. **(C, D)** Modulus and imaginary part of mean coherent $\mathbf{RPSF}_{\text{coh}}$, respectively. **(E)** Axial derivative of the imaginary part. **(F, G)** Phase and imaginary part of the confocal signal ($\Delta x = 0$ mm). **(H)** Axial evolution of the RPSFs.

5.1 Incoherent RPSF

The most direct way is to perform a local average of the intensity of the focused wave-field to obtain a bi-dimensional RPSF as follows:

$$\text{RPSF}_{\text{inc}}(\boldsymbol{\rho}, t, \boldsymbol{\Delta\rho}, \Delta z) = \sqrt{\langle |RPSF(\boldsymbol{\rho}', t', \boldsymbol{\Delta\rho}, \Delta z)|^2 \mathcal{W}(\boldsymbol{\rho}' - \boldsymbol{\rho}, t' - t)\rangle_{[\boldsymbol{\rho}', t']}}, \tag{5.10}$$

where $\mathcal{W}(\boldsymbol{\rho}' - \boldsymbol{\rho}) = 1$ for $|\boldsymbol{\rho}' - \boldsymbol{\rho}| < w_\rho/2$ and $|t' - t| < w_t/2$, and zero otherwise. An example of such an RSPF is shown in [Fig. 5.5B]. It is noteworthy that it has a more symmetrical shape in the axial dimension compared with time scanning method presented in the previous section [Fig. 5.4D$_1$]. This illustrates the robustness of a depth scan with respect to attenuation. A local defocus can then be extracted by finding the maximum of the RPSF [blue curve in Fig. 5.5H] for any point of the field of view:

$$\Delta\hat{z}_{\text{inc}}(\boldsymbol{\rho}, t) = \underset{[\Delta z, \boldsymbol{\Delta\rho}]}{\text{argmax}} \left\{ \text{RPSF}_{\text{inc}}(\boldsymbol{\Delta\rho}, \Delta z, \boldsymbol{\rho}, t) \right\}. \tag{5.11}$$

The $\Delta\hat{z}$ observed in [blue line in Fig. 5.5H] is close to 0 because we are in a reference experiment where the speed of sound considered in the propagation model corresponds to the speed of sound in the phantom. However, the RPSF has a significant background associated with multiple scattering that can occur before the focal plane. A coherent approach may be interesting to eliminate this incoherent background, as we will now see.

5.2 Coherent RPSF

Similar to the distortion matrix presented in Chapters 2 and 3, where an SVD is used to phase-align each focal point so that a coherent virtual guide star can be synthesized, here we take advantage of the SVD to phase-align each spatio-temporal focal point $(\boldsymbol{\rho}, t)$ so that we can extract what is coherent between each realization of disorder (assuming isoplanetism). Concretely, a coherent mean can be performed through a singular value decomposition of the reshaped matrix $\mathbf{RPSF} = [R_{\mathcal{D}}(\{\boldsymbol{\rho}, t\}, \{\boldsymbol{\Delta\rho}, \Delta z\})]$:

$$\mathbf{RPSF} = \mathbf{V}^{\dagger} \times \mathbf{\Sigma} \times \mathbf{U}, \tag{5.12}$$

which, in terms of matrix coefficients, writes

$$RPSF(\{\boldsymbol{\rho}, t\}, \{\boldsymbol{\Delta\rho}, \Delta z\}) = \sum_i V_i^*(\boldsymbol{\rho}, t)\sigma_i U_i(\boldsymbol{\Delta\rho}, \Delta z), \tag{5.13}$$

where $\mathbf{\Sigma}$ is a diagonal matrix containing the singular values σ_i in descending order: $\sigma_1 > \sigma_2 > .. > \sigma_N$. $\mathbf{U}$ and $\mathbf{V}$ are unitary matrices that contain the orthonormal set of output and input eigenvectors, $\mathbf{U}_i = [U_i(\boldsymbol{\Delta\rho}, \Delta z)]$ and $\mathbf{V}_i = [V_i(\boldsymbol{\rho}, t)]$. The first singular vector $\mathbf{U_1}$ directly provides an estimation of the coherent RPSF:

$$RPSF_{\text{coh}}(\boldsymbol{\Delta\rho}, \Delta z) \equiv U_1(\boldsymbol{\Delta\rho}, \Delta z). \tag{5.14}$$

It thus provides a lower background as shown in [Fig. 5.5C] than the incoherent RPSF [Fig. 5.5B] so that a local defocus can be extracted with a much better accuracy [orange curve on Fig. 5.5H]:

$$\Delta\hat{z}_{\text{coh}}(\boldsymbol{\rho}, t) = \underset{[\Delta z, \boldsymbol{\Delta\rho}]}{\text{argmax}} \{|RPSF_{\text{coh}}(\boldsymbol{\Delta\rho}, \Delta z, \boldsymbol{\rho}, t)|^2\}. \tag{5.15}$$

The uncertainty of this estimator $\Delta\hat{z}^{(\text{coh})}$ is given by the ratio between the depth of field of the imaging system $(2\lambda/NA^2)$ and the root square of the number of speckle grains $N_{\mathcal{W}}$ covered by the space-time window $\mathcal{W}$ (see Appendix 10):

$$\delta_{\Delta\hat{z}}^{(\text{coh})} \sim \frac{2\lambda}{(NA)^2\sqrt{N_{\mathcal{W}}}}, \tag{5.16}$$

with NA the numerical aperture of the imaging system. Thus, it is in the interest of the coherent RPSF to consider a very large number of independent speckle grains, but in practice $\mathcal{W}$ is limited by isoplanetism. Therefore, a trade-off between precision and resolution must be made in estimating Δz (the same trade-off as in estimating aberration laws in Chapter 3).

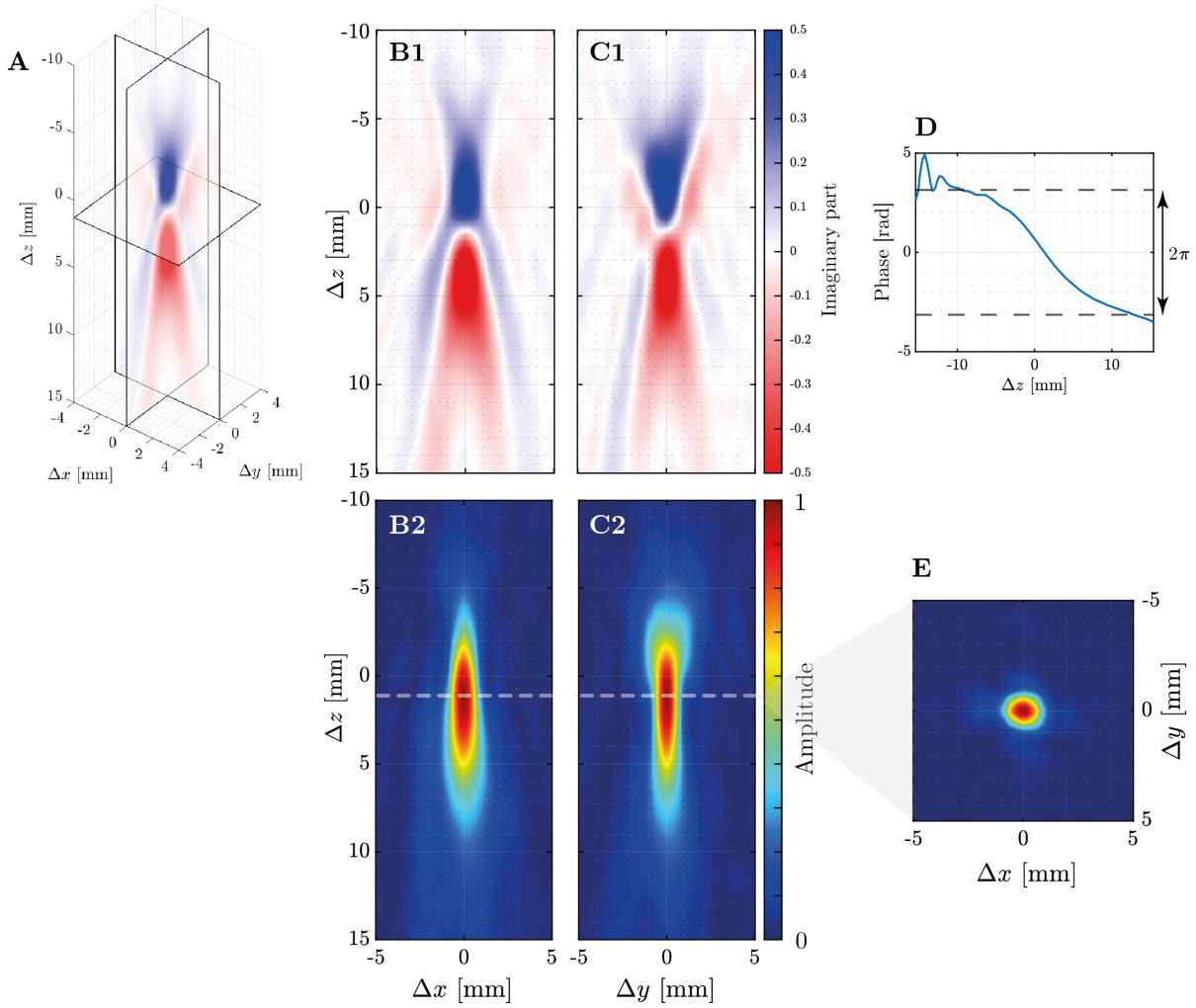

Figure 5.6: **Three-dimensional RPSF in the speckle** (Tissue mimicking phantom experiment). **(A)** 3D view and **(B, C)** 2D cross-sections of the coherent RPSF, respectively. "1" and "2" refers to the imaginary part and the amplitude of the RPSF, respectively. **(D)** Gouy phase jump of 2π. **(E)** Transverse cross-section of the RPSF at the focal plane.

5.3 Gouy phase jump

To obtain a more reliable estimator of $\Delta\hat{z}_{\text{coh}}$, one can also look at the phase of the coherent confocal spot [Fig. 5.5F]. The latter shows indeed a phase jump of π at the level of the focusing plane. The coherent confocal spot indeed cumulates the Gouy phase jumps ($\approx \pi/2$ in a 2D configuration) induced by the focusing processes at input and output. Interestingly, similar results can be obtained in 3D imaging using a matrix array of transducers ($\mathcal{P}_1$) and similar acquisition described in Chapter 3 (see Section 3), except that the Gouy phase jump reaches 2π as expected when adding one dimension to the problem [Fig. 5.6D]. Thus, the self-portrait of a three-dimensional wave in the speckle with an amplitude maximum supported by the Gouy phase jump can be extracted [Fig. 5.6A, B, C and E].

These Gouy phase jumps occur where the transverse confinement of the focused waves is minimal. It is therefore a more reliable estimator of the defocus than the axial evolution of the

incoherent RPSF [Fig. 5.5B] or the amplitude of the coherent PSF [Fig. 5.5C] which can be also sensitive to the geometric decay of the focused wave with depth. To increase the sensitivity of the method, one can also combine the two previous observables, modulus and phase of the RPSF, by examining the imaginary part of the latter [Fig. 5.5D]. Its point of inflection (*i.e.* the maximum of its axial derivative) provides a new estimator of the defocus [Fig. 5.5E]:

$$\Delta\hat{z}_{\text{gouy}}(\boldsymbol{\rho},t) = \underset{\Delta z}{\text{argmax}}\left\{|\partial_{\Delta z}\text{Im}[RPSF_{\text{coh}}(\boldsymbol{\Delta\rho}=0,\Delta z,\boldsymbol{\rho},t)]|\right\}. \tag{5.17}$$

The comparison between each estimator will be examined in more detail in the next chapter when the speed of sound will be examined instead of the axial shift Δz.

6 Application to imaging in multi-layered media

We will now present a first application of the extraction of such a defocus estimation in multi-layered media. Indeed, scanning the time-delay curvature through the focusing depth is particularly suitable for the following situation: Imaging a tissue whose sound velocity c is homogeneous and equal to the velocity model ($c = c_0$) but whose ultrasound image is degraded by the presence of several tissue layers of different velocity c_1 upstream of it.

6.1 Phantom experiments

The results of three *in vitro* experiments are now presented. The first experiment consists of a reference imaging experiment of an ultrasound phantom (CIRS, Model 050GSE) [Fig. 5.7B_1], previously described in Chapter 2 [Table 2.1]. In the second experiment, an aberrating water layer (c_1 = 1480 m.s^{-1}, Fig. 5.7B_2) is introduced between the probe and the phantom. The acquisition parameters are given in [Table 2.1]. In the third experiment, an aberrating Plexiglas plate (c_1 = 2690 m.s^{-1}, Fig. 5.7B_3) is examined. This last acquisition was performed with another ultrasound sequence described in [Table 5.1] which explains the decrease in resolution in the image [Fig. 5.7C3] compared to [Fig. 5.7C1 and C2].

Although the velocity model c_0 coincides well with the speed-of-sound in the phantom, the water layer degrades the resolution of the ultrasound image compared with the reference image, as evidenced by the impaired resolution of the bright spots and the poorer speckle contrast [Fig. 5.7C_2] compared to the reference image [Fig. 5.7C_1]. Due to a higher contrast between the phantom and Plexiglas in terms of speed-of-sound, compared to the phantom, the ultrasound image exhibits strong aberrations in the third experiment [Fig. 5.7C_3].

Local defocus are extracted using the estimator described in (Eq. 5.11) which is based on the study of the incoherent RPSF. Interestingly, it is homogeneous among the phantom layer [Fig. 5.7A]. Finally, a corrected image can be extracted in the target layer by compensating each point with the extracted defocus [Fig. 5.7D]:

$$\mathcal{I}_{\text{corr}}(\boldsymbol{\rho},t) = |\mathbf{R}_{\mathcal{D}}(\boldsymbol{\rho},t,\boldsymbol{\Delta\rho}=0,\Delta z=\Delta\hat{z}_{\text{layer}}|^2. \tag{5.18}$$

6.2 A constant defocus

To understand the nature of the aberration induced by a different sound velocity layer, and in particular the constant value of the defocus, we take up the analogy between beamforming and time-reversal experiment [Fig. 5.8]. A scatterer s at depth z_s is insonified by a plane wave [Fig. 5.8A] and associated with echo time [Fig. 5.8B]:

$$t_s = \frac{(z_s - z_1)}{c_0} + \frac{z_1}{c_1}. \tag{5.19}$$

It therefore appears at the depth z_i in the image [Fig. 5.8C]:

$$z_i = \frac{1}{2} c_0 t_s = z_s + z_1 \left(\frac{c_0}{c_1} - 1\right). \tag{5.20}$$

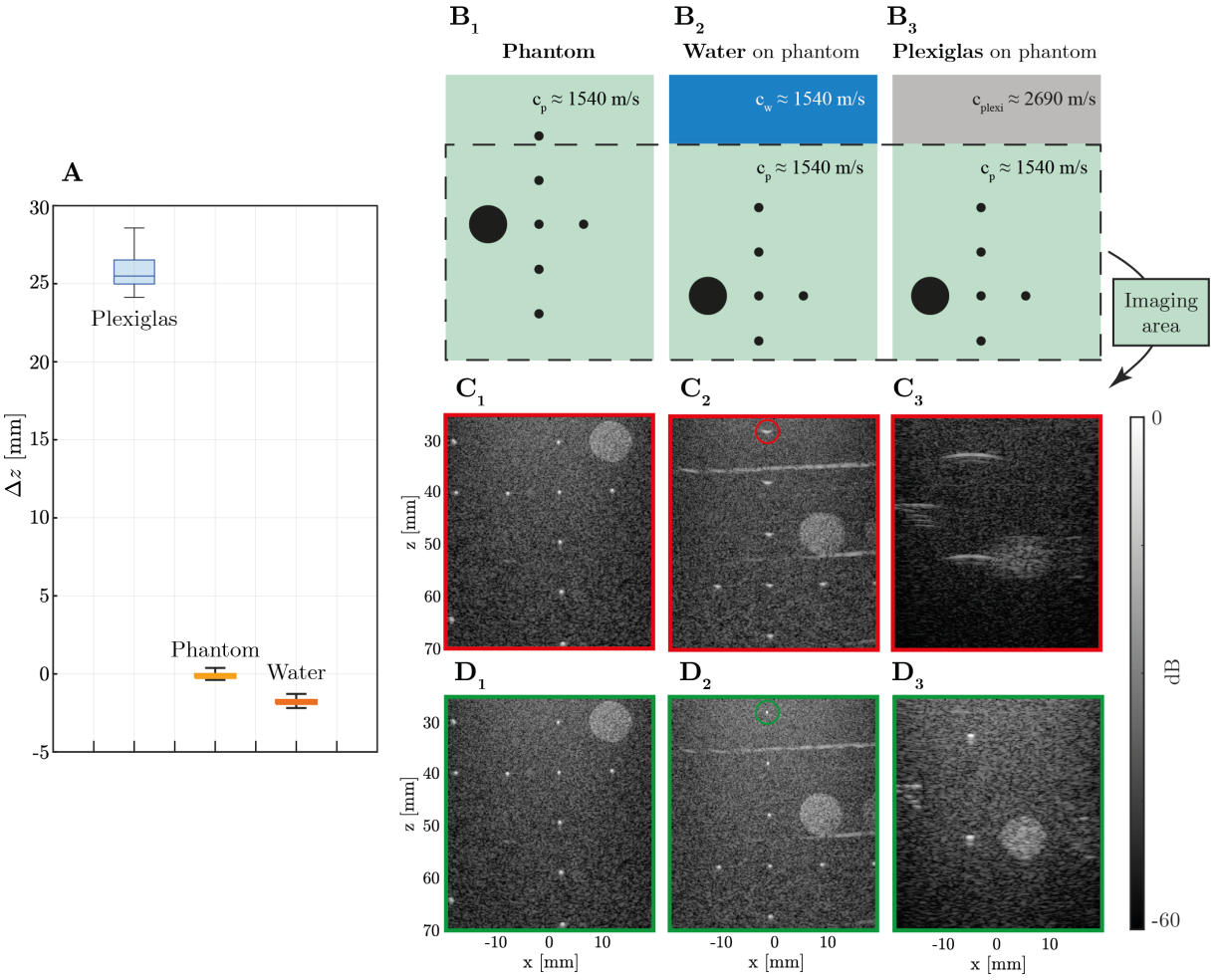

Figure 5.7: **Compensation of defocus in multi-layered media. (A)** Estimated defocus in **(B)** the three multilayered experiments. **(C, D)** Original and corrected image after compensation of the estimated defocus displayed in (**A**), respectively. The subscript "1", "2" and "3" account for the experiment number.

Parameters			Value
Probe	Type		Linear
	Number of transducers		$N_u = N_{\mathbf{u}_{\text{out}}} = 192$
	Transducer pitch		$\delta u = 0.2$ mm ($\approx \lambda$ at $c_0 = 1580$ m/s)
	Aperture		$\Delta u_x = 38.4$ mm
	Central frequency		$f_c = 5.625$ MHz
	Bandwidth		$\Delta f = [2 - 10]$ MHz
Acquisition	Electronic hardware		Aixplorer®, Supersonic Imagine
	Speed-of-sound hypothesis		$c_0 = 1540$ m/s
	Plane wave angles	Maximum	$\theta_{\text{in}} = 10°$ (calculated at c_0)
		Pitch	$\delta\theta_{\text{in}} = 1°$ (calculated at c_0)
		Number	$N_{\boldsymbol{\theta}_{\text{in}}} = 21$
	Emitted signal		Burst of three half periods of f_c
	Sampling frequency		$f_s = 22.5$ MHz
	Recording time		$\Delta t = 102$ μs

Table 5.1: **Acquisition of the reflection matrix, $\mathbf{R}_{\boldsymbol{\theta}\mathbf{u}}(t) \equiv [R(\boldsymbol{\theta}_{\text{in}}, \mathbf{u}_{\text{out}}, t)]$, when a Plexiglas plate is placed between the probe and a tissue mimicking phantom (CIRS, Model 054GS).**

Above all, the image of the scatterer is highly aberrated due to the mismatch between the velocity model and the sound velocity distribution upstream of the scatterer. Under a paraxial approximation, the position of the focusing plane is indeed given by:

$$z_f = z_i + \Delta z, \tag{5.21}$$

with

$$\Delta z = \left(\frac{c_l}{c_0} - \frac{c_0}{c_l} \right) z_l. \tag{5.22}$$

The parameter Δz can be seen as a defocus [Fig. 5.8C]. Remarkably, the defocus $\Delta \hat{z}_{\text{layer}}$ does not depend on the position z_s of the scatterer if $c_0 = c$, so that it is constant and can be easily estimated by spatially averaging all points located in the target medium.

6.3 An optimization step before the distortion matrix

Compensating a defocus can thus be seen as a first optimization step before targeting remaining transverse aberrations thanks to the distortion matrix approach [Fig. 5.2A]. We can now propose a general procedure to compensate for aberrations:

- (i) First, the concavity (Δz) at each spatio-temporal point $(\boldsymbol{\rho}, t)$ is optimized, allowing the compensation of low-order aberrations. We will see in the next chapter that concavity can also be optimized with the speed of sound hypothesis (c_0).
- (ii) Higher order aberrations, characterized by a much more complex shape, are then compensated for using the distortion matrix framework (see Chapters 2, 3 and 4).

This optimization step becomes crucial when dealing with a reduced set of insonifications,

i.e. a partial recording of the reflection matrix [Fig. 5.9].

To illustrate this assertion, the same Plexiglas experiment studied in a previous work [Lambert, 2020c] is investigated with a similar acquisition described in [Table. 2.1]. An incoherent RPSF is extracted in the echogenic structure indicated by the white box in panel A, either using 81 plane-waves [Fig. 5.9B] or with a down-sampled input basis with only 9 angles [Fig. 5.9C]. With this reduced set of insonifications, aliasing appears in the transverse direction (Δx) and the distortion matrix approach applied with a reference curvature ($\Delta z = 0$) would be hazardous. The application of a defocus allows avoiding aliasing induced by a reduced number of insonifications, before examining potential remaining transverse aberrations with the distortion matrix, for example.

This proof-of-concept is interesting from an academic point of view but remains quite limited as it only considers the case of a transverse invariant aberrating layer. In practice, this is never strictly the case. For example, in brain imaging, is characterized by porosity and skull thickness inhomogeneities. In liver imaging, ultrasound should propagate through an irregular

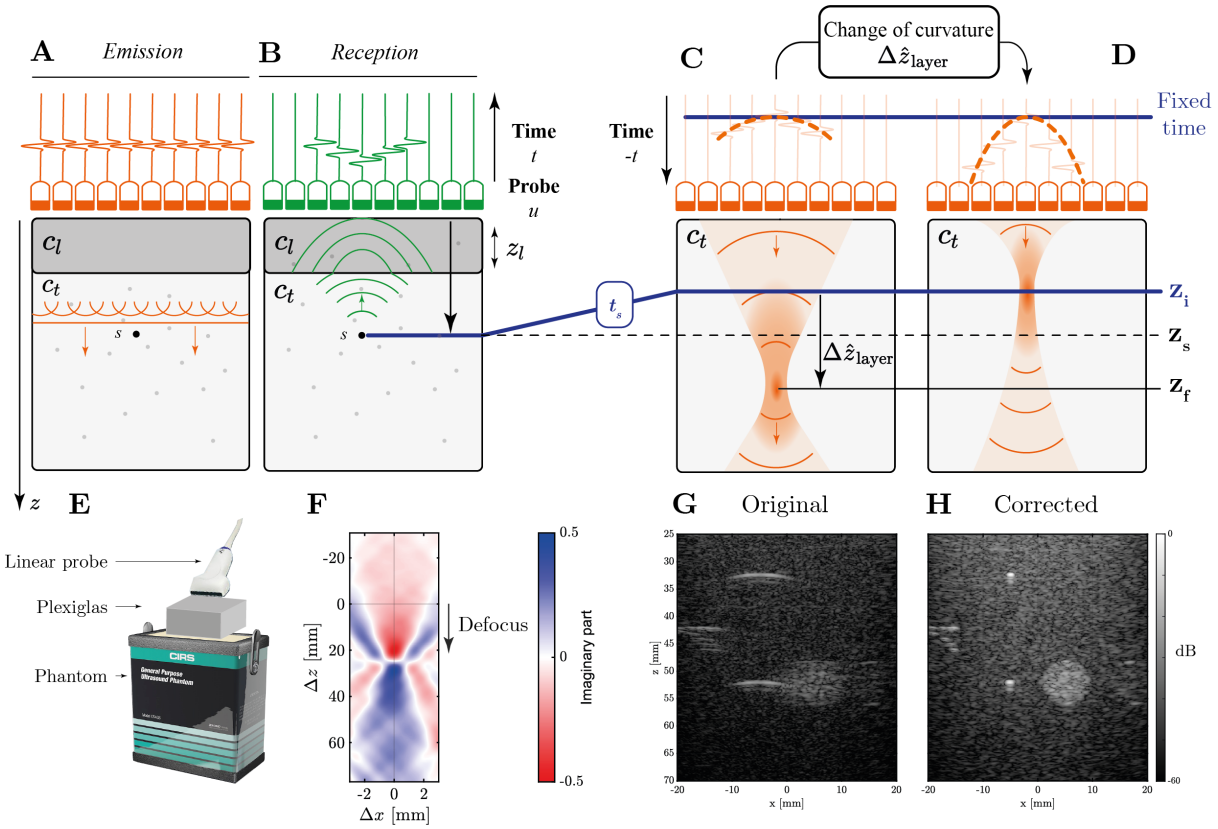

Figure 5.8: **A multilayered experiment** (Plexiglas on a tissue mimicking phantom). **(A)** Plane wave emission in a bilayer medium with speed of sound (c_l, c_t) **(B)** Recording of backscattered echoes associated to a strong reflector s **(C)** Time reversal in a medium of speed-of-sound c_t **(D)** Change of curvature on time-reversed signal so that the ballistic time matches the focus **(E)** Schematic of an experiment where a Plexiglas layer is placed between a tissue mimicking phantom and the probe. **(F)** RPSF in the tissue mimicking phantom **(G, H)** Original and corrected image after changing the focusing curvature, respectively.

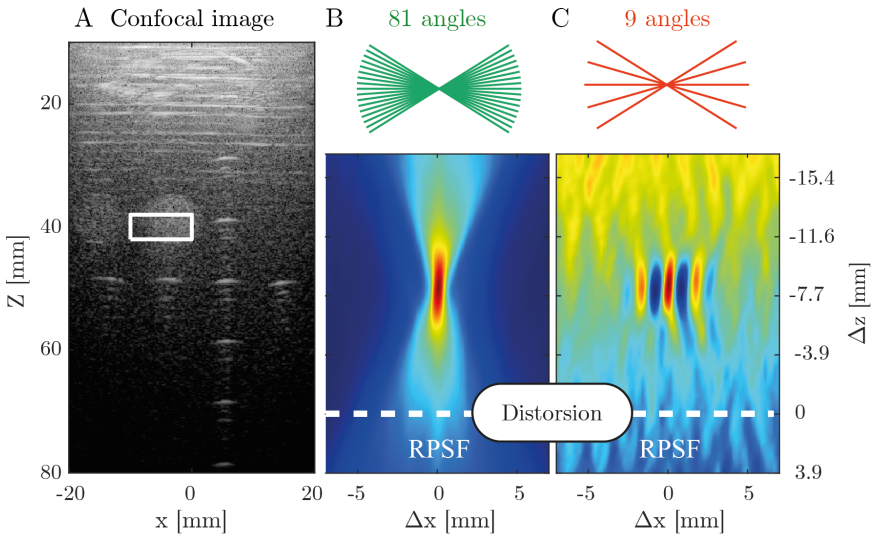

Figure 5.9: **Effect of a reduce set of insonifications on the RPSF. (A)** Confocal image. **(B, C)** Incoherent RPSF associated with the white box in panel (**A**) using 81 plane waves or 9 plane waves, respectively.

arrangement of adipose and muscle layers before reaching the organ.

7 Application to *in vivo* imaging

A single defocus is, however, not sufficient to compensate for spatially distributed aberrations that occur *in vivo*. Nevertheless, a local defocus map can be extracted and further used to apply a different axial shift for each focal point.

[Fig. 5.10] considers an *in vivo* ultrasound imaging experiment on a liver, in which an irregular arrangement of adipose and muscular tissues impairs the quality of the ultrasound image [Fig. 5.11A]. Ultrasound sequence parameters are described in [Table 5.2].

Parameters			**Value**
Probe	Type		Curve
	Curvature radius		$\mathcal{R}_u = 60$ mm
	Number of transducers		$N_u = N_{\mathbf{u}_{\text{out}}} = 192$
	Angular transducer pitch		$\delta\Theta_u = 0.32°$
	Aperture		$\Delta\Theta_u = 60°$
	Central frequency		$f_c = 3.5$ MHz
	Bandwidth		$\Delta f = [1-6]$ MHz
Acquisition	Electronic hardware		Aixplorer®, Supersonic Imagine
	Speed-of-sound hypothesis		$c_0 = 1540$ m/s
	Plane wave angles	Maximum	$\theta_{\text{in}} = 20°$ (calculated at c_0)
		Pitch	$\delta\theta_{\text{in}} = 1°$ (calculated at c_0)
		Number	$N_{\boldsymbol{\theta}_{\text{in}}} = 41$
	Sampling frequency		$f_s = 26.7$ MHz
	Recording time		$\Delta t = 235$ μs

Table 5.2: **Acquisition of the reflection matrix, $\mathbf{R}_{\boldsymbol{\theta}\mathbf{u}}(t) \equiv [R(\boldsymbol{\theta}_{\text{in}}, \mathbf{u}_{\text{out}}, t)]$, in a difficult-to-image patient liver.**

The method described above is extended to the case of a curved probe, which amounts to replacing the Cartesian coordinates (x, z) with polar coordinates $(\Theta, \mathcal{R})$, $\mathcal{R}$ playing the same role as the depth/curvature (z) with a linear array. The method is applied using the estimator described in (Eq. 5.11) which corresponds to the incoherent RPSF.

[Fig. 5.10B] shows the map of the estimated defocus at each point in the image. In contrast to previous academic experiments, this defocus is not homogeneous over the field of view. This is mainly due to the lateral variations of the sound velocity in the aberrating layers, which result in a rather large lateral variation of the focus defect. The axial variation of the focus defect in the liver is related to the mismatch between the velocity model c_0 and the velocity of sound $c(\mathbf{r})$ in the liver.

A corrected image can thus be obtained by compensating locally each defocus:

$$\mathcal{I}^{(\text{corr})}(\boldsymbol{\rho}, t) = |\mathbf{R}_{\mathcal{D}}(\boldsymbol{\rho}, t, \boldsymbol{\Delta\rho} = 0, \Delta\hat{z}(\boldsymbol{\rho}, t))|^2. \tag{5.23}$$

As a result, the confocal signal is largely enhanced with a speckle brightness improved of about 5 dB [Fig. 5.11A,B]. As a consequence, some structure appears more clearly, such as the muscle fibers [Fig. 5.11C] or the veins [Fig. 5.11D] inside the liver. Resolution enhancement can be

evaluated directly on the focused reflection matrix [Fig. 5.12A,B] at the ballistic time. The transverse RPSF shows a resolution enhancement of about a factor 2 [Fig. 5.12C].

Assuming an infinite probe, no refraction and under a paraxial approximation, the defocus map can even be translated into an integrated speed-of-sound imaging map [Lambert, 2020a]. However, a huge bias remains as it relies on strong assumptions. A more convenient method to map the speed-of-sound is proposed in the next Chapter.

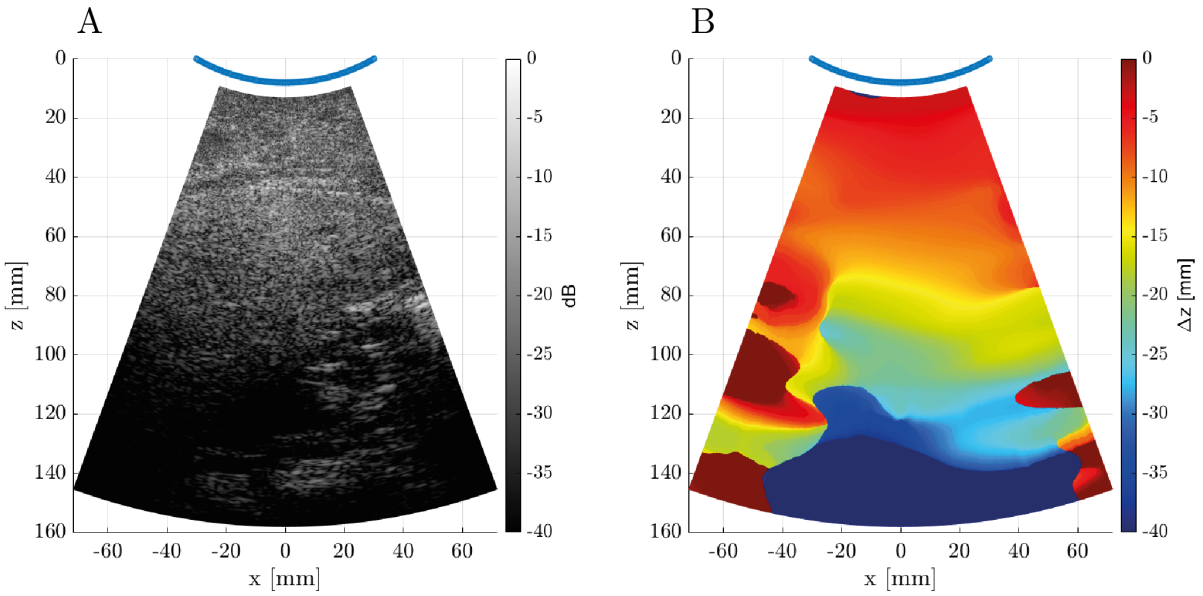

Figure 5.10: **Local defocus map in an *in vivo* imaging of a difficult-to-image patient liver. (A)** Confocal image and **(B)** local defocus map.

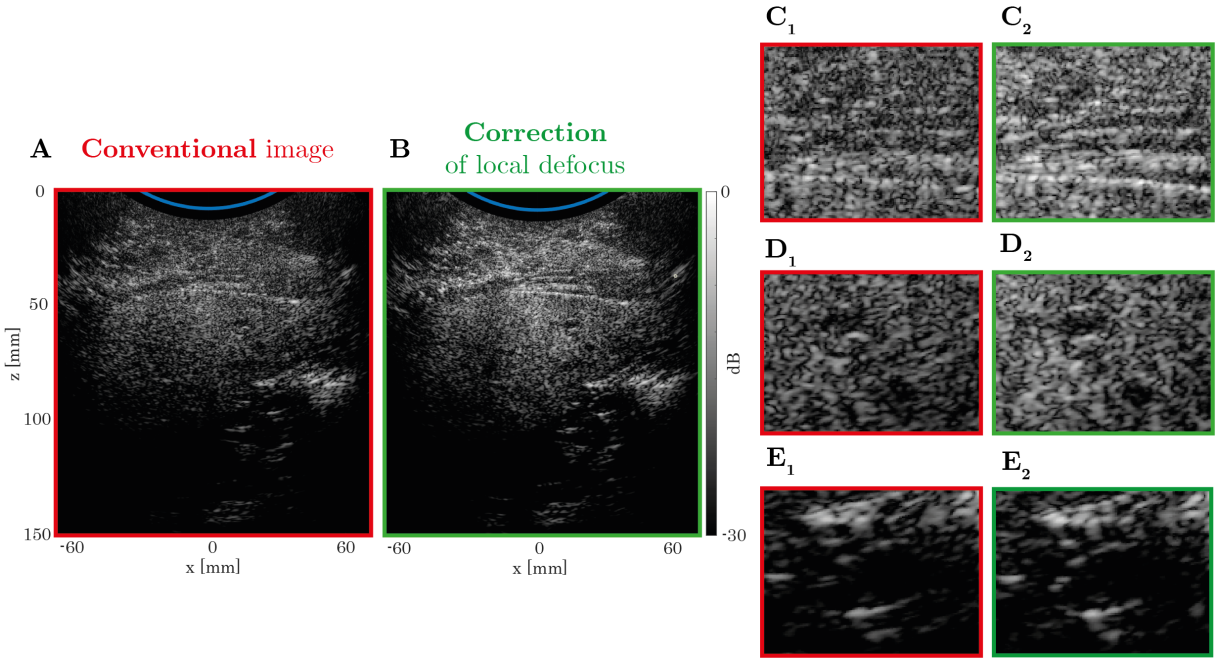

Figure 5.11: **Compensation of local defocus on the liver image of a difficult-to-image patient liver. (A, B)** Original and corrected image, respectively. **(C-E)** Zoom on specific areas of the field of view containing either muscle fibers or veins. The subscripts "1" and "2" stands for before and after local defocus correction, respectively. Ultrasound images are normalized by the global maximum between the two images.

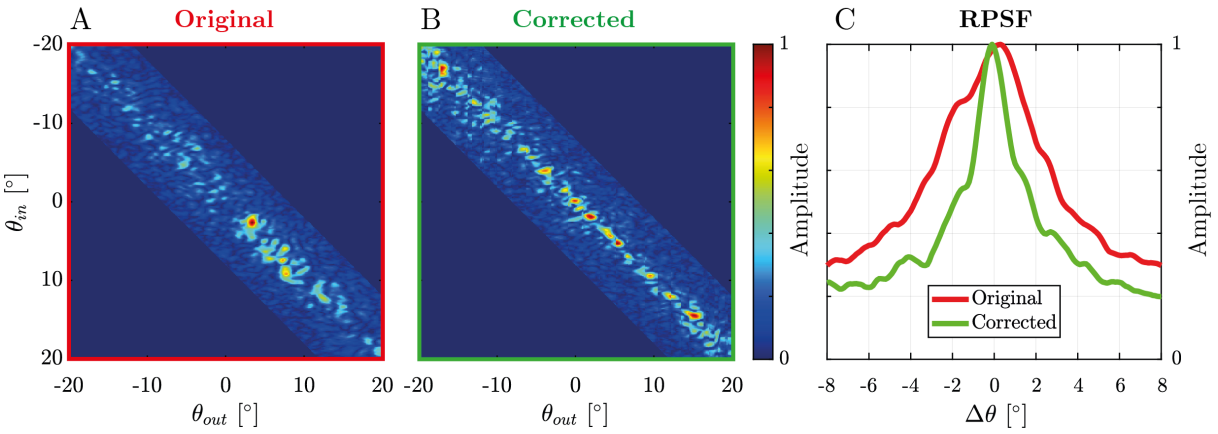

Figure 5.12: **Effect of local defocus compensation on transverse focused reflection matrices. (A, B)** Focused reflection matrix before and after correction (corresponding to $t = 77.9$ μs), respectively. **(C)** Spatial averaged anti-diagonals.

8 Conclusion & Perspectives

In this chapter, we have shown that it was possible to map a local defocus even in a random medium by finding the optimal focal curvature for each point in the field-of-view. The attenuation in the medium was overcome by scanning the depth of input and output focal points at each echo time. This appears to be particularly relevant for multi-layered media, where a single defocus can be compensated to produce a close to ideal image. In addition, we have presented

an application of local defocus correction in an *in vivo* imaging experiment of a difficult-to-image patient liver. Such a local compensation of defocus allows producing a better contrasted and resolved image than a conventional B-mode. This correction can be considered as a preliminary step before addressing the higher order aberrations through the distortion matrix approach.

In the next chapter, we will show that a similar method can be applied by scanning the speed-of-sound hypothesis instead of the focal depth. In this way, a map of the integrated speed-of-sound can be extracted. It results in an ultrasound image whose axial dimension is dictated by the true depth of scatterers and no longer by the echo time, as this is usually the case in conventional B-mode.

Chapter 6

Reflection matrix approach for speed-of-sound tomography

Objectives

Extending the method described in the previous chapter, the speed of sound at any point in the medium can now be estimated. Such a parameter is not only of interest as a **biomarker**, but its mapping can also be used to produce near-ideal images with **better accuracy on distance measurements**.

Contents

1 Introduction

Quantitative imaging goes beyond a simple image of medium reflectivity. It consists in mapping physical parameters that control wave propagation or scattering inside the medium. Examples include Doppler imaging, which quantifies the velocity of red-blood cells, or elastography [Bercoff, 2004], which measures the stiffness of tissues. In the latter, known as *shear wave elastography*, a shear wave is generated in the medium and its propagation is monitored by means of ultrafast imaging [Sandrin, 1999; Montaldo, 2009; Tanter, 2014]. From this movie of wave propagation, the shear wave velocity can be extracted locally. It provides a map of the shear modulus that describes the stiffness of soft tissues. This observable enables the detection of abnormalities such as malignant tumors [Samani, 2007; Fung, 1993].

Mapping the speed-of-sound of longitudinal waves used for ultrasound imaging is even a greater challenge and an active research topic. As shear wave velocity, older studies show that its quantification could be used as a bioindicator to detect abnormal soft tissues characteristics [Bamber, 1979; Sehgal, 1986] such as malignant tumors [Ozmen, 2015; Ruby, 2019] or hepatic steatosis [Imbault, 2017; Imbault, 2018; Dioguardi Burgio, 2019]. The latter occurs, for example, when fat droplets accumulate in the liver and reduce the effective speed-of-sound of the medium, since fat tissue has a lower sound velocity ($c_0 = 1480$ m/s) than liver tissue ($c_0 = 1600$ m/s) [Bamber, 1981; Chen, 1987; Duck, 1990]. However, it should be emphasized that an accuracy of at least 1% (≈ 10 m/s) must be achieved to provide quantitative results [Robinson, 1991].

Even more, retrieving the spatial variations of longitudinal wave velocity can be considered as **the holy grail of imaging**, since it allows the extraction of the optimal time-of-flight connecting each transducer to each point of the medium to produce a close-to-ideal image of the medium. In a transmission configuration, *Traditional Ultrasonic Computed Tomography* applies this concept in reverse by exploiting the ballistic time echoes, that can be used to minimize the eikonal equation using Fermat's principle, resulting in a tomography of the speed-of-sound of the medium [Duric, 2007; Hormati, 2010; Li, 2010; Huthwaite, 2011; Hu, 2022; Johnson, 2007; Perez-Liva, 2020; Greenleaf, 1975; Glover, 1977b; Greenleaf, 1975; Glover, 1977b; Duric, 2007; Wiskin, 2007; Lavarello, 2008; Lavarello, 2009; Hormati, 2010; Li, 2010; Huthwaite, 2011; Ali, 2019]. This method can be considered as a very similar problem to CT-scan reconstruction using the Radon transform, but here refraction must also be considered. However, such a method cannot be applied to a reflection configuration where only backscattered echoes are recorded.

Currently, there are two main groups of methods for determining the local speed-of-sound of longitudinal waves of an unknown medium in an epi-detection configuration. The first group of methods is based on the optimization of an image quality criterion with respect to the hypothesis of the speed-of-sound established during beamforming. Repeating this process for each point can lead to a map of the integrated speed-of-sound of the medium, that takes into account all heterogeneities between a point and the probe. Then, an inversion problem is formulated and solved to determine the local speed-of-sound [Jakovljevic, 2018]. A second group of methods estimates the local phase-shifts between different insonification directions [Jaeger, 2015a], assuming that each insonification direction is subject to different heterogeneities of the medium.

Again, an inverse problem is then solved to determine the local speed-of-sound of the medium. Such a map of local speed-of-sound can be used to correct aberrations [Stahli, 2021; Rau, 2019] or even for a more complex beamforming algorithm [Vyas, 2012; Augustin, 2021; Ali, 2022] to improve both the focusing quality and the estimation of the position of each scatterer, resulting in a near-ideal image.

In this chapter, we transfer the optimization-based method for extracting a local defocus described in the previous chapter to the local estimation of the integrated speed-of-sound of an unknown medium. In other words, instead of scanning the focal curvature through the depth of the focal spot, we directly scan the speed-of-sound hypothesis. This wealth of information is particularly interesting because it allows us not only to locally compensate for low-order transverse aberrations due to speed-of-sound errors at each point, but also to provide an ultrasound image whose axial dimension is no longer dictated by the echo time but by the depth itself. This feature may represent a major advance in ultrasound, since it allows a much more accurate measurement of distances in ultrasound images. Indeed, many ultrasound diagnoses rely on distance measurements, such as the monitoring of fetal growth or the detection of chromosomal abnormalities in obstetrics [Nicolaides, 1992].

After a more detailed presentation of the state of the art on the topic, the implications of an incorrect speed-of-sound hypothesis are explored in a phantom experiment to better explain the problem we face. Our method for extracting a speed-of-sound map is then validated in both numerical simulations and phantom experiments before being extended to **liver imaging of a difficult-to-image patient**.

2 State of the art

2.1 Pioneering works

The first studies dedicated to estimating the speed of sound measurements in reflection were obtained by placing several probes on the same side of the medium. It was noticed that any mismatch between the wave velocity model c_0 and the speed-of-sound distribution $c(\mathbf{r})$ induced a deterioration of the image, and more precisely, a shift of the objects as a function of the observation angle. [Carpenter, 1977; Robinson, 1982; Ophir, 1986; Kontonassios, 1987; Shattuck, 1989]. This displacement was then used to estimate the speed of sound in the medium. This method, called *crossed-beam tracking*, was later adapted using **synthetic apertures** within a single probe [Kondo, 1990; Krucker, 2004; Céspedes, 1992]. Another approach, using only a single transducer, was to study the time-of-flight shifts along the propagation axis when the medium is axially compressed [Ophir, 1990].

Inspired from tomographic methods in seismology, another approach is to estimate the time-of-flight directly from the raw RF signals by examining the correlations between the receiving channels. The speed of sound can then be estimated using a fit performed either in the spatial [Anderson, 1998] or temporal [Pereira, 2002] domain.

2.2 Integrated speed of sound

Thanks to the increasing capacity of data storage and computations, a much straightforward approach has been to optimize a given parameter of the medium as a function of the beamforming speed of sound hypothesis, resulting in an estimation of the effective speed-of-sound of the medium. Numerous set of parameters, such as the coherence factor [Imbault, 2017; Dioguardi Burgio, 2019], the speckle or strong reflector brightness [Benjamin, 2018; Zubajlo, 2018; Napolitano, 2006; Cho, 2009; Yoon, 2012; Yoon, 2011] or the deconvolution process with a given dataset of PSFs [Shin, 2010], have been studied. More recently, a local focusing criterion derived from the focused reflection matrix was optimized as a function of speed of sound [Lambert, 2020b] as described in Chapter 2.

All these methods can be used to determine the integrated speed of sound c_{int} (also called average, mean, effective, or global in previous works), which accounts for all spatial variations from the probe to a given focal point. It is very important to distinguish it from the local speed-of-sound of the medium, denoted c_{loc}, which directly accounts for the spatial dependence of the speed of sound.

1st order eikonal equation

In a multi-layered medium, $c_{\text{loc}}(z)$ and $c_{\text{int}}(z)$ can be related as follows:

$$\frac{z}{c_{\text{int}}(z)} = \int_0^z \frac{dz'}{c_{\text{loc}}(z')}. \tag{6.1}$$

2.3 Local speed-of-sound: an inverse problem

Since the goal is to determine the local speed of sound at any point in the field of view, several methods use the above indicators to first extract a map of the integrated speed of sound and then derive a map of the local speed of sound by formulating an inverse problem. In the case of multi-layered media, such an inverse problem is equivalent to a numerical differentiation of (Eq. 6.1). Jakovljevic et al. [Jakovljevic, 2018] used a gradient algorithm to estimate the local axial speed-of-sound in layered media from global estimates based on the indicator described by Anderson et al. [Anderson, 1998]. The method was then improved using the coherence factor to estimate global speed-of-sound [Ali, 2021; Telichko, 2022]. Byram et al. [Byram, 2012] use the indicator introduced by Anderson et al. [Anderson, 1998] to estimate the mean speed of sound. By calculating the time of flight between virtual detectors embedded in the medium, the local speed of sound can then be derived.

In parallel, the method of *crossed beam-tracking* [Kondo, 1990] has been generalized to the case of data acquired with linear and convex probes emitting a series of plane or diverging waves [Jaeger, 2015a; Jaeger, 2015b; Stähli, 2020; Rau, 2021; Sanabria, 2018a; Stahli, 2019; Jaeger, 2022; Sanabria, 2018b; Jaeger, 2022]. The method, namely *Computed Ultrasound Tomography in Echo mode (CUTE)*, consists in examining, for each point of the field-of-view, the phase shift $\delta\phi$ of each image pixel between different insonifications θ_{in}. Then, an inverse problem, relating

these phase-shifts to the local speed-of-sound, is formulated and solved. Although this method has already shown promising results, its main limitation lies in its inherent angular dependence [Podkowa, 2020], which limits its application mainly to the estimation of the speed of sound in the lateral direction. Furthermore, its robustness decreases, as the numerical aperture, with depth.

Regardless of the method used, the inverse problem to derive a map of the local speed-of-sound is ill-posed, as there are multiple solutions for a given phase-shift map or a given integrated speed-of-sound map. To circumvent this problem, a regularization method must be employed [Stahli, 2021; Ali, 2018; Ali, 2019; Sanabria, 2020].

It can be noticed, that most of the above-mentioned methods does not account for refraction events and thus assume a medium with relatively slow variations of speed-of-sound. When targeting more complex media such as transcranial imaging, refraction has to be taken into account in order to retrieve a spatially resolved map without artifacts. Beuret et al. [Beuret, 2020] have extended the CUTE method by taking into account refraction. More recently, Heriard et al. [Hériard-Dubreuil, 2023] have provided an angular-based method, that accounts for refraction, both at input and output.

At last, with the rapidly growing advances in artificial intelligence (AI), a new set of methods based on deep convolutional neural networks has emerged [Feigin, 2020]. The development of such algorithms requires a large training dataset, which can be generated using open-source software such as *Field II* [Jensen, 1991] or *k-wave* [Treeby, 2010]. However, it is important to keep in mind that even though the results of AI methods are very promising, it is a black box with an inherent bias due to the quality and the specificity of each training data set. In other words, it strongly depends on the accuracy with which a particular *in vivo* medium is numerically modelled.

3 Effects of an incorrect speed-of-sound hypothesis

Before presenting our new optimization-based estimator, we describe the effects of an incorrect speed-of-sound hypothesis on a reconstructed ultrasound image. For simplification, let us consider a homogeneous medium with velocity c. As in the previous chapter, an **analogy between numerical beamforming and a physical time-reversal experiment** is explored to illustrate these detrimental effects [Fig. 6.1]. Indeed, the beamforming process can be seen as the digital counterpart of a time reversal experiment in which one would try to refocus the backscattered wave of a scatterer s in a medium of speed-of-sound c in a new medium of speed-of-sound c_0:

- A plane wave ($\theta_{\text{in}} = 0°$) is emitted by an ultrasound probe at $t = 0$ μs in a medium of velocity c [Fig. 6.1A]. Its interaction with the scatterer s gives rise to a backscattered wave that propagates towards the probe and upon which the acoustic field is recorded from $t = 0$ μs [Fig. 6.1B] ;
- The recorded echoes are then time-reversed ($t \rightarrow -t$) and re-emitted either into a medium

of velocity $c_0 = c$ [Fig. 6.1C] or into a medium of velocity $c_0 > c$ [Fig. 6.1D].

In the first case ($c_0 = c$), the focusing of the re-emitted wave occurs at the ballistic time $t = \frac{2z_s}{c}$ and at the same spatial coordinates as the scatterer (z_s). In other words, the focusing plane z_f coincides with the imaging plane $z_i = c_0 t/2$ associated with the ballistic time t. Hence, in the second case where $c_0 > c$ (or $c_0 < c$), the focusing of the wave takes place upstream (or downstream) at a depth:

$$z_f = \frac{c}{c_0} z_s, \tag{6.2}$$

under the paraxial approximation, while the isochronous volume associated with the target's time-of-flight appears downstream (or upstream) of the focal plane:

$$z_i = \frac{1}{2} c_0 t = z_s \frac{c_0}{c}. \tag{6.3}$$

Thus, the ultrasound image makes the scatterer appear at the wrong depth ($z_i \neq z_s$) and its image is degraded because the focal plane does not match the imaging plane associated with the isochronous volume of the scatterer ($z_i \neq z_f$) [Fig. 6.1D]. This thought experiment shows that the mismatch between the model and real speed-of-sound induces a defocus. In optics, this corresponds to the case where the imaging plane (z_i) of the camera does not match the coherence plane (z_f) of the target object, resulting in a blurred image. Here, the impact of a velocity mismatch was considered at the output, but the same reasoning applies to the input by spatial reciprocity.

The phantom experiment previously described in Chapter 2 is examined to illustrate such detrimental effects [Fig. 6.1E], with sequence parameters described in [Table. 2.1]. [Fig. 6.1F] shows the ideal image obtained while assuming the correct speed-of-sound during beamforming ($c_0 = c$). [Fig. 6.1G] shows the image obtained while assuming an incorrect speed-of-sound $c_0 > c$ during beamforming. As describe before, the dissociation between the spatial focus (z_f) and the isochronous volume ($z_i = \frac{1}{2} c_0 t$) leads to a widened and distorted focal spot and thus a poor transverse resolution of each bright spot. Furthermore, scatterers appear at the wrong depth so that there is an uncertainty for each ultrasound image on the axial dimension of the image which is governed by the echo time t and which makes any distance measurement hazardous.

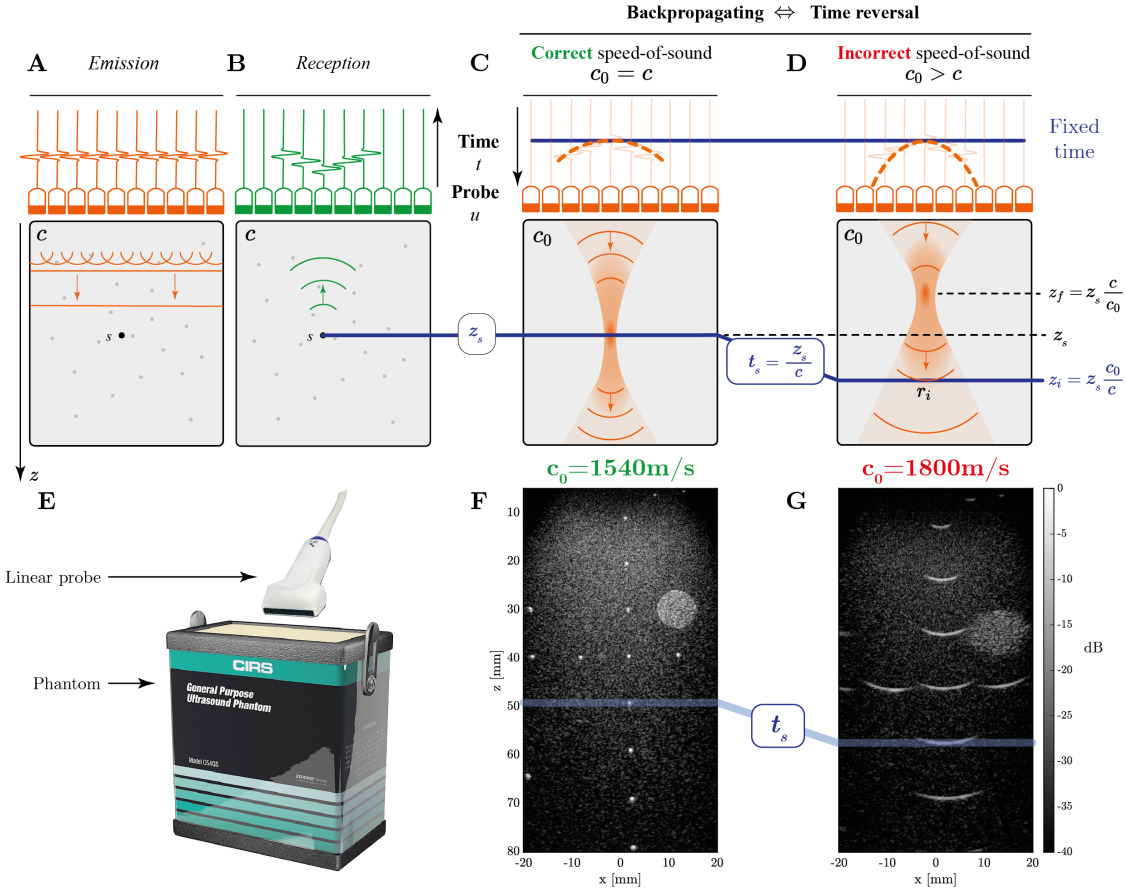

Figure 6.1: **Analogy between numerical beamforming and a physical time reversal experiment. (A)** Plane wave emission and **(B)** recording of backscattered echoes in a medium of velocity c_t. **(C, D)** Time reversal in a medium of same ($c_0 = c_t$) or different ($c_0 \neq c_t$) speed-of-sound, respectively. **(E)** Schematic of a tissue mimicking phantom experiment. **(F, G)** Beamforming with correct or incorrect speed-of-sound, respectively.

4 Scanning the speed-of-sound model

In the same spirit of the method described in the previous chapter, the focal curvature is now controlled directly via the velocity model c_0 to investigate the defocus described in [Fig. 6.1]. To this end, the focused $\mathbf{R}-$matrix is now built for a range of speed of sound models (c_0), while the emitted and received focal spots are considered at the expected ballistic depth ($z_{\text{in}} = z_{\text{out}} = c_0 t/2$) following (Eq. 5.1):

$$R_{\mathcal{D}}(\boldsymbol{\rho}, t, \boldsymbol{\Delta\rho}, c_0) = R(\boldsymbol{\rho}_{\text{in}}, \boldsymbol{\rho}_{\text{out}}, z = c_0 t/2, t, c_0). \tag{6.4}$$

The dependence of the focused $\mathbf{R}$-matrix on the speed of sound assumption is now explicit. The $\mathbf{R}$-matrix is now reshaped as a two-dimensional matrix as $\mathbf{RPSF} = [R_{\mathcal{D}}(\{\boldsymbol{\rho}, t\}, \{\boldsymbol{\Delta\rho}, c_0\})]$, where each line represents a realization of the RPSF as a function of the velocity model c_0 for a speckle grain characterized by its transverse position $\boldsymbol{\rho}$ and the echo time t, as shown in [Fig. 6.2A].

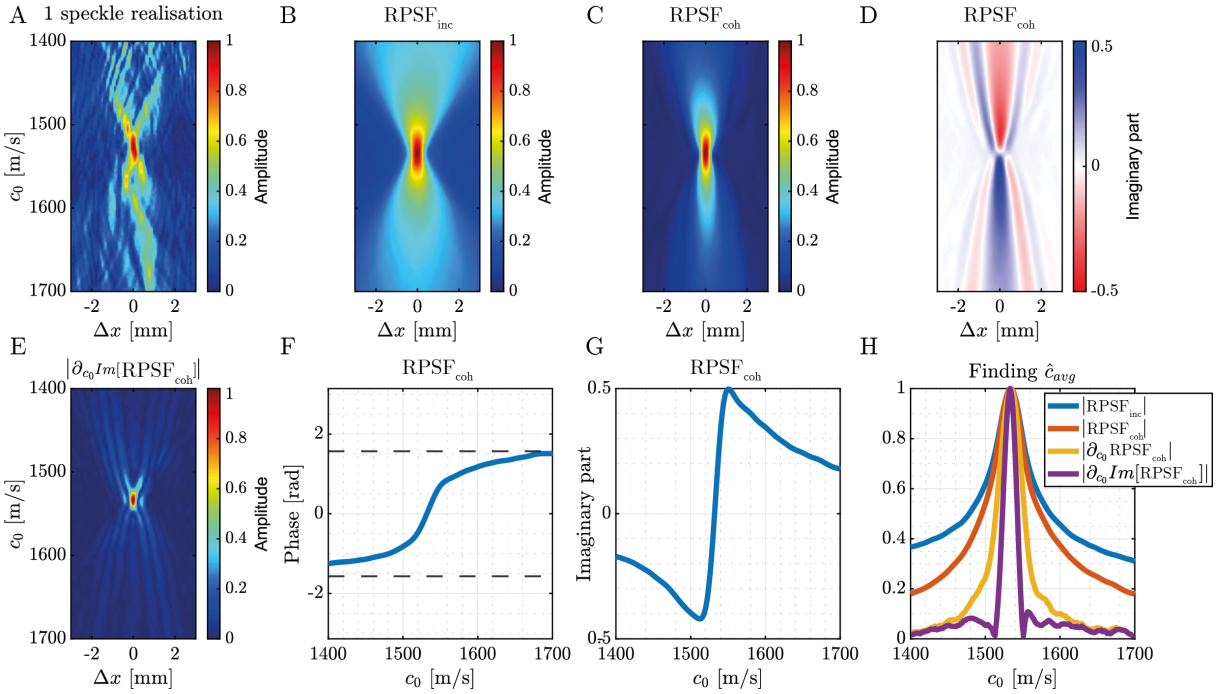

Figure 6.2: **Scan of the RPSF as a function of wave velocity model in ultrasound speckle** (Tissue mimicking phantom experiment). **(A)** Modulus of RPSF for one speckle realization at $(x, t) = (0$ mm, 42.9 μs). **(B)** Incoherent RPSF. **(C, D)** Modulus and imaginary part of the coherent RPSF, respectively. **(E)** Derivative of the imaginary part of the coherent RPSF. **(F, G)** Phase and imaginary part of the confocal component of the coherent RPSF ($\Delta x = 0$ mm). **(H)** Confocal component of each estimator. The blue curve is the incoherent RPSF. The orange curve is the modulus of the coherent RPSF. The yellow curve is the complex derivative of the coherent RPSF. The purple curve is the derivative of the imaginary part of the coherent RPSF. Spatial average is here performed with a window of size $(\mathcal{W}_x, \mathcal{W}_t) = (10$ mm, 1.3 μs).

Even though the focusing process can be observed with an intensity maximum close to the confocal point ($\boldsymbol{\Delta\rho} = 0$ mm) and a speed-of-sound value $c_0 = c_\mathrm{p}$, some fluctuations due to the random reflectivity of the sample emerge when we are out-of-focus ($c_0 \neq c_\mathrm{p}$).

5 Spatial averaging

As in the previous chapter, a local average of the RSPF can be performed in various ways to smooth out these fluctuations.

5.1 Incoherent

The most direct way is to perform an incoherent average of the RPSF around each point $(\boldsymbol{\rho}, t)$ of the image:

$$RPSF_\mathrm{inc}(\boldsymbol{\rho}, t, \boldsymbol{\Delta\rho}, c_0) = \sqrt{\langle |RPSF(\boldsymbol{\rho}', t', \boldsymbol{\Delta\rho}, c_0)|^2 \mathcal{W}(\boldsymbol{\rho}' - \boldsymbol{\rho}, t' - t)\rangle_{[\boldsymbol{\rho}', t']}}. \tag{6.5}$$

A direct estimation of the integrated speed-of-sound can be obtained by considering the value of c_0 that maximizes the incoherent RPSF at this point [Blue curve on Fig. 6.2H]:

$$\hat{c}_{\text{int}}^{(\text{inc})}(\boldsymbol{\rho}, t) = \underset{[c_0, \boldsymbol{\Delta\rho}]}{\text{argmax}} \left\{ RPSF_{\text{inc}}(\boldsymbol{\Delta\rho}, c_0, \boldsymbol{\rho}, t) \right\}. \tag{6.6}$$

Here, the speed-of-sound of the phantom is determined to be $\hat{c}_{\text{int}}^{(\text{inc})} = 1534$ m/s, which is a deviation of about 4% compared to the manufacturer's value ($c_{\text{p}} = 1540$ m/s).

When considering only the confocal component ($\boldsymbol{\Delta\rho} = 0$) of the RPSF, this estimator is quite similar to the one proposed by [Perrot, 2021]. However, the authors maximize this quantity for the whole field-of-view and only extracted a mean speed-of-sound. Yet, the speed-of-sound often display a complex distribution in soft tissues.

In practice, a speed-of-sound map is extracted using a spatio-temporal Gaussian kernel, whose size directly limits the computational time. In addition, faster computing can be reached when only investigating the confocal component of the RPSF ($\boldsymbol{\Delta\rho} = 0$). However, precision may be lower at the edges of the field-of-view because the focal spot may be tilted. The influence of the core size is investigated in an experiment where a layer of water is placed between the probe and the phantom [Fig. 6.3], with sequence parameters described in [Table. 2.1]. Without averaging [Fig. 6.3B], the reconstruction of the speed-of-sound map is quite noisy due to the speckle fluctuations [Fig. 6.2A]. By increasing the size of the kernel, this detrimental effect can be overcome, but the presence of strong reflectors can still bias the result in their vicinity [Fig. 6.3C$_1$]. Finally, with an empirical size of 5λ in this experiment [Fig. 6.3D$_2$], a continuous integrated speed-of-sound map can be extracted [Fig. 6.3D$_1$]. This map is an estimator of the effective speed-of-sound (not the local one), since it cumulates all the speed-of-sound inhomogeneities experienced by the wave as it travels from the probe to a given focal point. Even though this particular experiment is transversely invariant, the recovered map is two-dimensional and not restricted to the axial dimension, as we will see further.

5.2 Coherent

To improve the accuracy of our speed-of-sound estimator, a coherent RPSF can be extracted through a singular value decomposition of $\mathbf{RPSF} = [R_{\mathcal{D}}(\{\boldsymbol{\rho}, t\}, \{\boldsymbol{\Delta\rho}, c_0\})]$:

$$\mathbf{RPSF} = \mathbf{V}^{\dagger} \times \mathbf{\Sigma} \times \mathbf{U}, \tag{6.7}$$

where $\mathbf{\Sigma}$ is a diagonal matrix containing the singular values σ_i in descending order: $\sigma_1 > \sigma_2 > .. > \sigma_N$. $\mathbf{U}$ and $\mathbf{V}$ are unitary matrices that contain the orthonormal set of output and input eigenvectors, $\mathbf{U}_i = [U_i(\boldsymbol{\Delta\rho}, c_0)]$ and $\mathbf{V}_i = [V_i(\boldsymbol{\rho}, t)]$. The first singular vector thus constitutes the coherent RPSF [Fig. 6.2C,D]:

$$RPSF_{\text{coh}}(\boldsymbol{\Delta\rho}, c_0, \boldsymbol{\rho}, t) \equiv U_1(\boldsymbol{\Delta\rho}, c_0, \boldsymbol{\rho}, t). \tag{6.8}$$

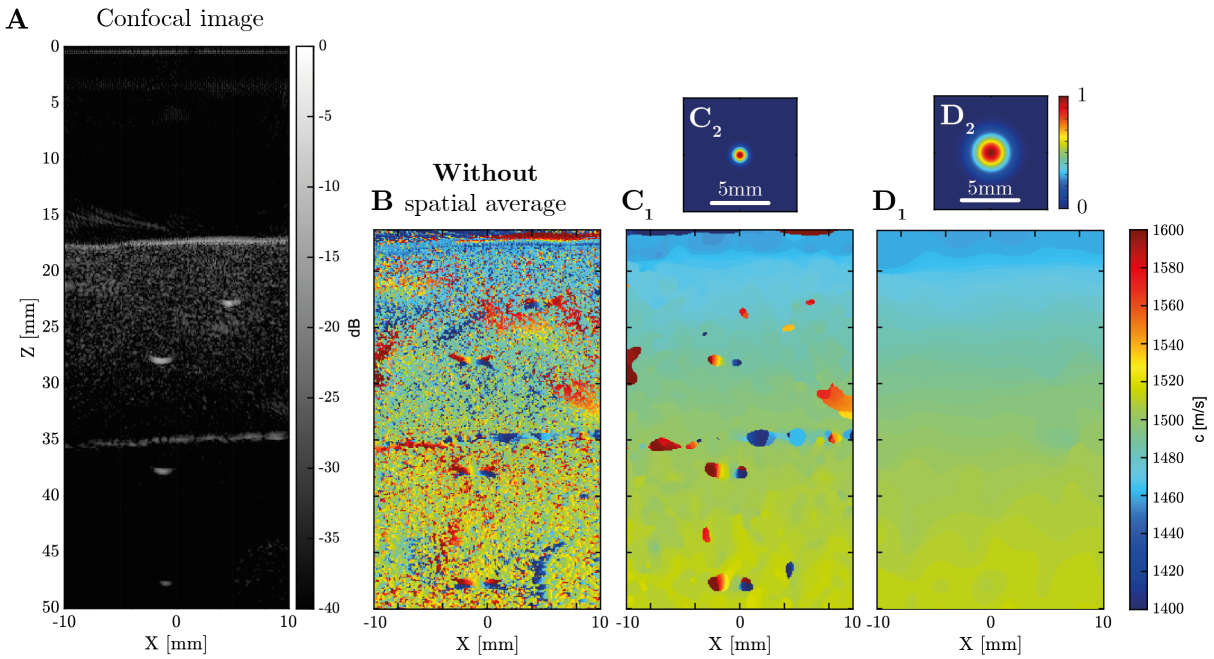

Figure 6.3: **Influence of spatial averaging on the estimation of the integrated speed-of-sound.** The results shown here correspond to an imaging experiment of a tissue mimicking phantom (c_p = 1540 m/s) through a layer of water ($c_\mathrm{w} \approx$ 1480 m/s). (**A**) Confocal image (**B, C, D**) Extracted speed-of-sound map from the incoherent RPSF without averaging and by averaging with a Gaussian kernel of standard deviation of 2 and 5 lambda, respectively.

An example of the coherent RPSF is presented in [Fig. 6.2C], which shows an amplitude with a much lower background than the incoherent RPSF [orange curve on Fig. 6.2H]. An estimation of the integrated speed-of-sound can thus be extracted by considering the speed-of-sound c_0 that maximizes the coherent RPSF:

$$\hat{c}_\mathrm{int}^{(\mathrm{coh})} = (\boldsymbol{\rho}, t) = \underset{[c_0, \boldsymbol{\Delta\rho}]}{\mathrm{argmax}} \left\{ |RPSF_\mathrm{coh}(\boldsymbol{\Delta\rho}, c_0, \boldsymbol{\rho}, t)| \right\}. \tag{6.9}$$

In the light of (equation 5.16), the coherent RPSF is expected to give a much better sensitivity than the incoherent RPSF for estimating the speed-of-sound.

Similar to the method described in the previous chapter, it is also possible to observe the double Gouy phase jump at the focus [Fig. 6.2F]. The origin of the Gouy phase shift lies in the transverse confinement of the focused wave-field [Feng, 2001], which therefore depends on the numerical aperture. The influence of the input numerical aperture is therefore studied in [Fig. 6.4]. For a single plane wave ($\theta_\mathrm{in} = 0°$), the estimation of the speed-of-sound fails with both the incoherent and coherent RPSF [red curve in Fig. 6.4A, C]. As the numerical aperture increases, the slope of the Gouy phase jump becomes steeper [Fig. 6.4B], resulting in a sharper peak when considering the coherent RPSF [green curve in Fig. 6.4C]. In addition, it is very likely that the variations observed in [Fig. 6.4C] in the estimate of the integrated sound velocity are due to the acoustic lens in front of the probe, whose velocity is much lower and to which the large angles would be more sensitive. Effects of the acoustic lens are described in more details in (Section

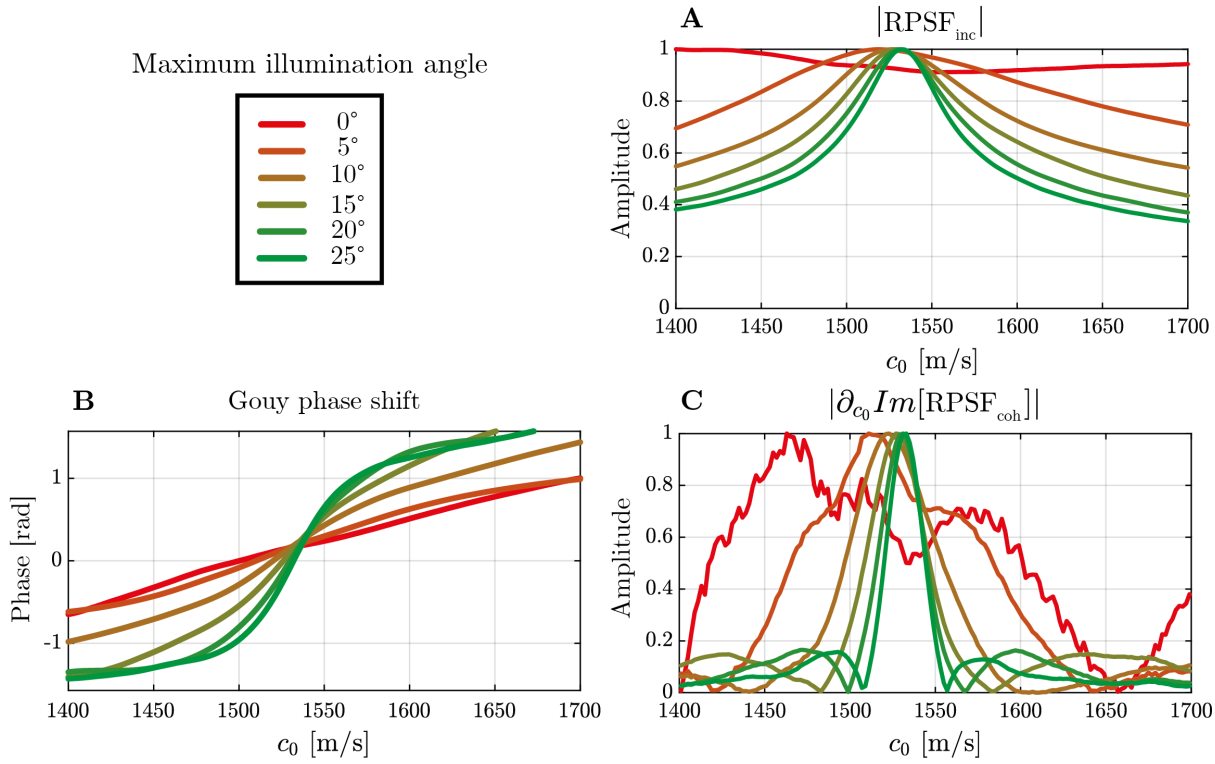

Figure 6.4: **Influence of the input numerical aperture on axial RPSFs.** (**A**) Amplitude of the confocal component of the incoherent RPSF. (**B**) Phase of the confocal component of the coherent RPSF. (**C**) Derivative of the imaginary part of the coherent RPSF. The three are shown as a function of the wave velocity model c_0. Numerical aperture increases from red to green. Results presented here are in a tissue mimicking phantom with parameters described in [Table. 2.1]. The selected point is located at (x,t)=(0 mm, 42.9 μs) and the average window is $(\mathcal{W}_x,\mathcal{W}_t)$=(20 mm, 2.6 μs).

6).

An even better estimator of c_{int} can thus be built by combining both the phase and the amplitude of the coherent RPSF. To this end, the axial derivative of the imaginary part [Fig. 6.2D] appear to be a relevant observable as its confocal component is characterized by a steep slope as shown in [Fig. 6.2G]. A new estimator can thus be constructed:

$$\hat{c}_{\text{int}}^{(\text{gouy})}(\boldsymbol{\rho},t) = \underset{c_0}{\text{argmax}}\left\{\left|\partial_{c_0}\text{Im}[RPSF_{\text{coh}}(\boldsymbol{\Delta\rho}=0,c_0,\boldsymbol{\rho},t)]\right|\right\}. \tag{6.10}$$

As it combines both an amplitude and phase information, it constitutes a sharp estimator of the position of the focal plane, as illustrated in [Fig. 6.2E].

5.3 Comparison between the different estimators

To compare all the estimators presented so far, we now consider only the confocal component, as shown in [Fig. 6.5]. Although the derivation of the imaginary part of the coherent RPSF [green line in Fig. 6.5] appears to be more accurate in this case, the singular value decomposition may introduce a bias with respect to the phase reference of the wave-field. To eliminate this

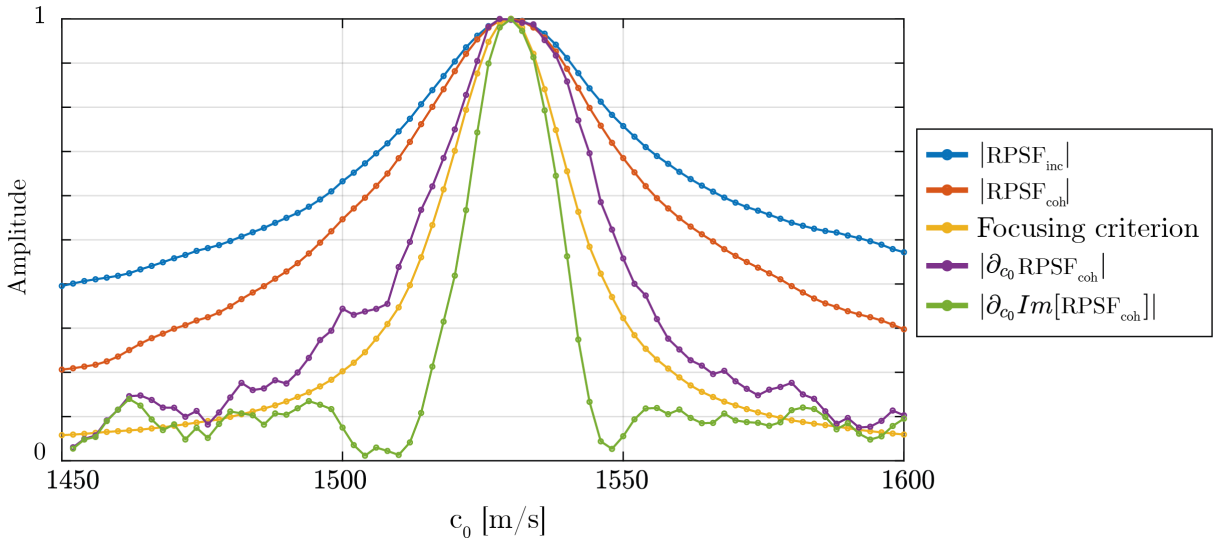

Figure 6.5: **Comparison of each speed-of-sound estimator.** Results presented here are obtained in the tissue mimicking phantom at (x, t) = (0 mm, 32.5 μs) and the average window is $(\mathcal{W}_x, \mathcal{W}_t)$=(15 mm, 0 μs). The blue curve refers to the amplitude of the incoherent RPSF. The orange curve refers to the amplitude of the coherent RPSF. The yellow curve refers to the square value of the focusing criterion, defined in (equation 2.43), as a function of the speed-of-sound hypothesis. The purple curve refers to the complex derivative of the coherent RPSF. The green curve refers to the derivative of the imaginary part of the coherent RPSF.

bias, the complex derivative of the coherent RPSF may be a solution [purple line in Fig. 6.5]. However, such numerical differentiation-based estimators also exhibit a larger noise background, which can be reduced by prior smoothing, but may also affect their accuracy. Therefore, a more in-depth study is needed to compare the robustness of each estimator with respect to noise. To this end, their behavior with respect to the number of resolution cells in each spatial window $\mathcal{W}$ has to be investigated.

Another important aspect is the time processing required for each estimator. First, only the confocal component can be studied to reduce the computational time. Second, as the coherent estimator is based on an SVD for each point, it appears drastically time-consuming, compared to the incoherent RPSF whose spatial average can be calculated in a quite fast way by spatial convolution. Although the study of the coherent RPSF takes much more time, it appears to be a more accurate estimator and can be relevant when one wants to extract a value of the speed of sound at a particular point with higher accuracy.

Finally, we now compare our estimator (Eq. 6.10) based on the Gouy phase shift and the estimator based on the normalized focusing criterion (Eq. 2.43) introduced in Chapter 2 [yellow line in Fig. 6.5]. Interestingly, the estimator based on the Gouy phase jump [green line in Fig. 6.5] is more accurate by a factor of about $\sqrt{2}$ than the focusing criterion. To compare the two on the same basis, the square of the focusing criterion was plotted. It can be emphasized that while the focusing criterion appears to be a robust and sensitive estimator of the speed of sound, it inherently requires the scanning of both the transverse axis ($\boldsymbol{\Delta\rho} \neq 0$) and the velocity model,

which is quite computational intensive.

6 A corrected image with better distances accuracy

Such a local map of the integrated speed-of-sound can be used directly for local correction of axial aberrations by optimizing the focusing law parametrized by c_0 so that the focal plane z_f coincides with the imaging plane $z_\mathrm{i} = c_0 t/2$ [Fig. 6.1C-D]:

$$\mathcal{I}_\mathrm{corr}(\boldsymbol{\rho}, t) = \left| R_\mathcal{D}(\boldsymbol{\rho}, \boldsymbol{\Delta\rho} = 0, t, c_0 = \hat{c}_\mathrm{int}^{(\mathrm{gouy})}(\boldsymbol{\rho}, t)) \right|^2. \tag{6.11}$$

Assuming no refraction, *i.e.* straight paths of wave propagation, the speed-of-sound map can finally be used to position each spatio-temporal point $\mathbf{r} = (\boldsymbol{\rho}, t)$ with better accuracy such that the estimation of their axial position is given by:

$$\hat{z}(\boldsymbol{\rho}, t) = \frac{1}{2} \hat{c}_\mathrm{int}(\boldsymbol{\rho}, t) t. \tag{6.12}$$

To validate the method, multi-layered experiments are now performed with a phantom, with parameters described in [Tab. 2.1]. In the first experiment, the probe is directly placed in contact with the tissue phantom (homogeneous medium) [Fig. 6.6A_1]. The integrated speed-of-sound shows a deviation at shallow depths compared to the manufacturer's value ($c_\mathrm{p} = 1540$ m/s) [Fig. 6.6B_1]. We attribute this difference to the acoustic lens of the probe, which needs to be taken into account for more robust measurements. In any case, (Eq. 6.11) can be used to obtain a corrected image showing an improvement in resolution at shallow depths, as indicated by the reflector marked with yellow arrows in [Fig. 6.6D_1].

Adding a layer of water between the probe and the tissue mimicking phantom [Fig. 6.6A_2] leads to an image presenting a small defocus and a degraded resolution when looking at its bright spots [Fig. 6.6C_2]. Integrated speed-of-sound can be estimated using (Eq. 6.6) based on the study of the incoherent RPSF [Fig. 6.6B_2]. As expected, the estimated speed-of-sound matches the water speed-of-sound ($c_w = 1480$ m/s) at first depth and then tends towards the speed-of-sound of the phantom as the depth increases. The corrected image shows a clear resolution enhancement and accuracy on distances is recovered as the distance between the two deepest strong reflectors matches the manufacturer value of 1 cm [Fig. 6.6D_2].

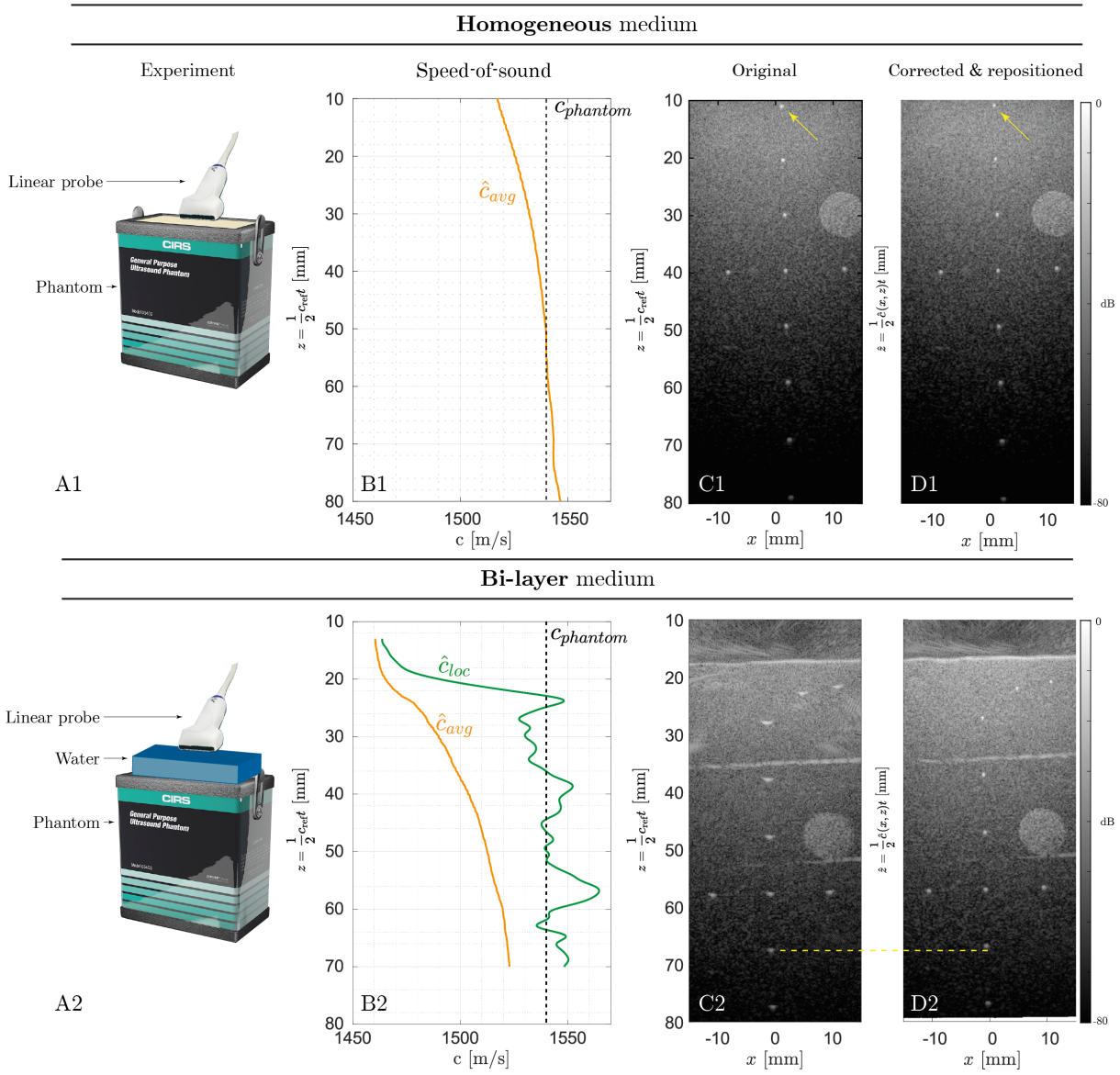

Figure 6.6: **Speed-of-sound estimation in two multilayered phantom experiments.** **(A)** Schematic of the experiments. **(B)** Speed-of-sound estimation as a function of the depth. **(C)** Original image displayed with a depth axis scaling as $z(t) = \frac{1}{2}c_0 t$ and with $c_0 = 1540$ m/s **(D)** Corrected image displayed with a corrected depth axis $\hat{z}(x,t) = \frac{1}{2}\hat{c}_{\text{int}}(x,t)t$. "1" refers to the experiment in which the probe is in contact with the phantom. "2" refers to the case where a layer of water is added between the two.

7 From an integrated to a local speed of sound map

The speed-of-sound map that we manage to extract refers to an integrated speed-of-sound c_{int}. In other words, it takes into account all the spatial variations of the local speed-of-sound c_{loc} seen from the probe to a given focal point. To recover the local speed-of-sound across the medium, we need to perform an inversion of (Eq. 6.1) and for this we take up the method developed in the following article by Jakovljevic et al. [Jakovljevic, 2018], which is described in (Appendix 6). Note that the above inversion method is based on a very strong approximation that the integrated speed of sound at a point $c_{\text{int}}(x, z)$ depends only on the upward axial values of the local velocity $c_{\text{loc}}(x, z' < z)$.

The local speed of sound can thus be extracted in the phantom experiment, as shown in [green curve in Fig. 6.6B$_2$]. However, this method is anything but optimal, as strong fluctuations around the expected phantom sound velocity can be observed. Here, the regularization of the inverse problem was performed by spatially smoothing the recovered integrated sound velocity map before estimating the local sound velocity. However, more robust regularization approaches can also be explored to obtain a more accurate local sound velocity map. Some of these approaches are presented by Ali et al. [Ali, 2019].

8 Numerical validation

The phantom experiments have made it possible to illustrate and qualitatively validate the method in the case of a homogeneous or multi-layered medium. However, there are some effects such as the acoustic lens that prevent quantitative validation. To fill this gap, we are now conducting a numerical study that allows quantitative validation and shows the limits of the method, especially in the case of transverse variations in the speed of sound.

Four multilayered media are simulated using the open-source *k-wave* software [Treeby, 2010] with the parameters described in [Tab. 6.1]. We then apply our method to retrieve the integrated speed of sound [Fig. 6.7B] based on the study of the incoherent RPSF and with average parameters described in [Table. 6.1]. The local speed-of-sound can be derived [Fig. 6.7C], resulting in corrected images with more accurate distances [Fig. 6.7E].

First, a control simulation is investigated in a homogeneous medium (see Appendix 9). The integrated and local speed-of-sound are found to be homogeneous, and the corrected image shows no enhancement as the original image is already close to optimal (*i.e.* diffraction limited resolution).

For a bi-layered medium with a horizontal interface [Fig. 6.7A], translating the integrated speed-of-sound [Fig. 6.7B] into an estimated local speed-of-sound [Fig. 6.7C] allows better definition of the separation between the two layers and more accurate determination of the speed-of-sound of the second layer. After averaging such map laterally, the axial evolution is also shown to better illustrate the accuracy of the method [Fig. 6.7F]. As previously described in the phantom experiment, the integrated speed of sound matches the value of the speed of sound of the first layer ($c = 1700$ m/s) at first depths and then tends to the speed-of-sound of the

Parameters			Value
Probe	Type		Linear
	Number of transducers		$N_u = N_{\mathbf{u}_{\text{out}}} = 376$
	Transducer pitch		$\delta u = 0.2$ mm ($< \lambda/2$ at c_0)
	Aperture		$\Delta u_x = 77$ mm
	Central frequency		$f_c = 3$ MHz
	Bandwidth		$\Delta f = [1.8 - 4.7]$ MHz
Acquisition	Speed-of-sound hypothesis		$c_0 = 1540$ m/s
	Plane wave angles	maximum	$\theta_{\text{in}} = 40°$ (calculated at c_0)
		pitch	$\delta\theta_{\text{in}} = 2°$ (calculated at c_0)
		number	$N_{\boldsymbol{\theta}_{\text{in}}} = 41$
Medium	Speed-of-sound map		see [Fig. 6.7A]
	Density	mean	$\langle\rho\rangle = 1$ kg.m^{-3}
		standard deviation	$\sigma_\rho = 0.01$ kg.m^{-3}
Analysis	Average window	lateral	$\mathcal{W}_x = 2.2$ mm
		axial	$\mathcal{W}_t = 2.9$ μs
	$\hat{c}_{\text{int}}$ estimator		Incoherent RPSF (Eq. 6.6)
Regularization	Smoothing of $\hat{c}_{\text{int}}$	lateral	$\mathcal{W}_x^{(s)} = 1.1$ mm
		axial	$\mathcal{W}_t^{(s)} = 1.4$ μs

Table 6.1: **Acquisition and analysis parameters of the numerical simulations.** The reflection matrix, $\mathbf{R}_{\boldsymbol{\theta}\mathbf{u}}(t) \equiv [R(\boldsymbol{\theta}_{\text{in}}, \mathbf{u}_{\text{out}}, t)]$, is generated using *K-wave* software.

second medium ($c = 1540$ m/s). Taking the corrected image according to (Eq. 6.11) leads to a diffraction-limited image. In addition, using (Eq. 6.12) to correctly position each pixel provides a better estimate of distances across the image, as seen by the slightly downshifted interface, which now perfectly matches the true sound speed map, as shown by the yellow dashed line in [Fig. 6.7D and E].

However, the integrated speed-of-sound map that we can obtain is two-dimensional and therefore contains much more information than just axial variations of the speed of sound. To demonstrate this point, we thus perform a numerical simulation, in which the interface is now titled [Fig. 6.8A1]. Such lateral variations can be captured by the RSPF, as shown by the lateral variation of the integrated speed-of-sound [Fig. 6.8B1]. Its inversion allows us to recover the tilted shape of the interface consistent with ground truth, as shown by the gray dashed lines [Fig. 6.8C1]. It can be emphasized that lateral variations can be extracted in the local speed of sound map even if the inversion model is based only on the axial derivative. This experiment demonstrates the wealth of information provided by the integrated speed of sound map. In addition, the corrected image [Fig. 6.8E1] shows both better resolution, as indicated by the strong reflectors, and better contrast than the original image [Fig. 6.8D1]. The left part of the interface cannot be reached because the reflection cannot be detected by the probe due to Snell-Descartes laws.

In a last case, we examine the limitations of our method by considering a medium with both a horizontal and a vertical interface [Fig. 6.8A2]. Even though the speed of sound map shows good agreement at the edges [Fig. 6.8C2], leading to a better estimation of the interface in the

corrected image [Fig. 6.8E2], our method fails in the middle due to the vertical interface [Fig. 6.8A2]. It should be noted, however, that this extreme case with a large lateral discontinuity is not very representative of the usual media studied in ultrasound imaging. In any case, this was to be expected, since our inversion approach is based only on axial variations of the integrated speed-of-sound. A more sophisticated inverse problem must be formulated to account for the oblique paths of wave propagation. Moreover, one can be guided by state-of-the-art methods that use insonifications from multiple angles to reconstruct the speed of sound map [Jaeger, 2015a]. In the future, it will be significant to extend our estimator to include the sub-aperture at emission and reception so that the angular dependence of the RPSF can be used to map the local speed-of-sound. Other, more sophisticated methods can account for the oblique trajectories and refraction phenomena of the incident and reflected waves. These can be used to invert the

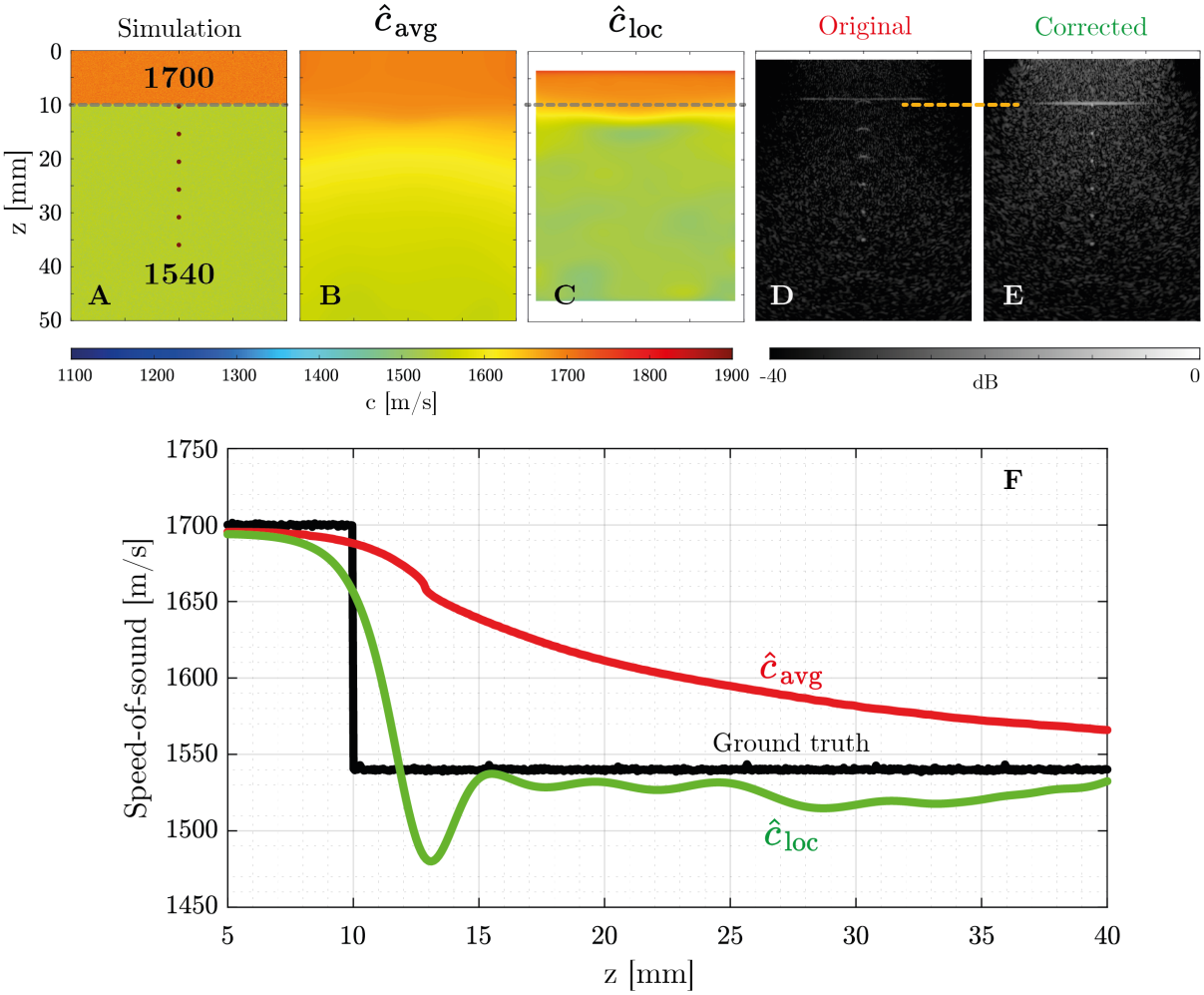

Figure 6.7: **Numerical simulation of a bi-layered medium using *K-wave* software.** (**A**) Speed-of-sound map simulated. (**B, C**) Integrated and local speed-of-sound estimation, respectively. (**D**) Original image. (**E**) Corrected image with each pixel reassigned to its estimated position. (**F**) Axial profile of the integrated and local speed of sound after lateral averaging of each map. Numerical simulations were performed using K-wave software with parameters described in [Table. 6.1].

integrated sound speed map obtained by our method.

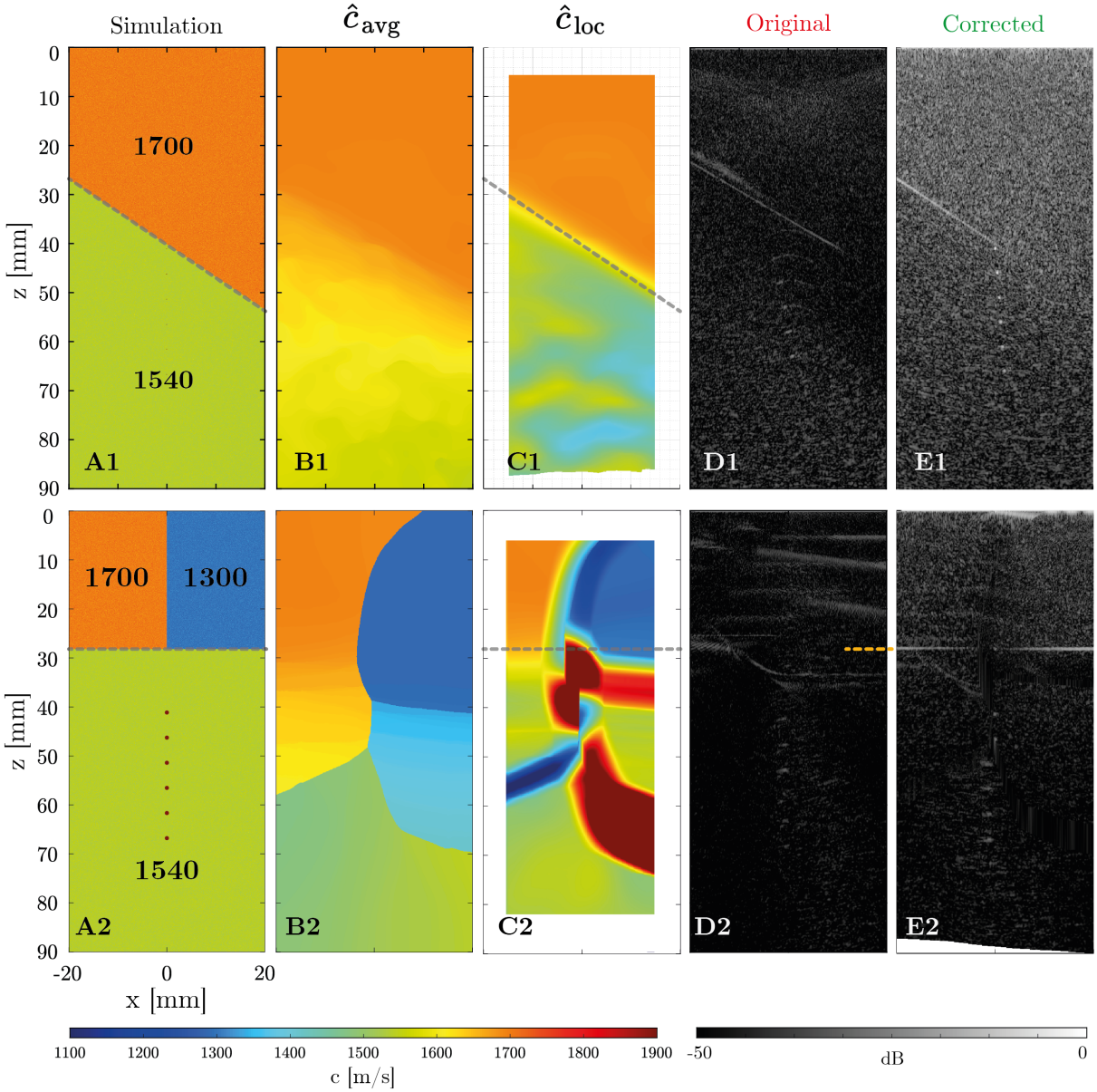

Figure 6.8: **Numerical simulations of a medium presenting lateral variations of the speed-of-sound.** (**A**) Speed-of-sound map simulated. (**B, C**) Integrated and local speed-of-sound estimation, respectively. (**D**) Original image. (**E**) Corrected image with each pixel reassigned to its estimated position. "1" refers to a bi-layered medium with an oblique interface. "2" refers to the extreme case of a medium presenting both lateral and axial variations of the speed of sound. Numerical simulations were performed using K-wave software with parameters described in [Table. 6.1].

9 Clinical application: a difficult to image patient liver

Now that our matrix method for speed-of-sound tomography has been investigated by means of numerical simulations and phantom experiments, we apply it to *in vivo* imaging. As a proof-of-concept, we consider a liver imaging experiment, as this is a multi-layered configuration in which our method is supposed to succeed. To show how interesting our method is for medical diagnosis, we test our approach on the patient's ultrasound data already processed in Chapter 5, whose acquisition sequence was described in [Table 5.2]. As this patient is potentially suffering from a steatosis, the measurement of the liver speed-of-sound is critical for diagnosis purpose [Imbault, 2017].

The conventional image ($c_0 = 1540$ m/s) is displayed in [Fig. 6.9A]. It shows a low contrast due to the huge layer of fat at shallow depths. The detection of a steatosis disease that may manifest as a bright speckle in absence of aberrations [Mehta, 2008; Dasarathy, 2009] is thus impossible from this ultrasound image.

An integrated speed-of-sound map $\hat{c}_{\text{int}}(\boldsymbol{\rho}, t)$ is obtained [Fig. 6.9C] from a local analysis of the incoherent RPSF whose parameters are given in [Tab. 6.2]. The speed of sound has a very low value in the first fat layer (~ 1400 m/s). At a depth of $z = 30$ mm, it suddenly increases, which is due to the presence of muscle fibers, as can be seen on the confocal image. The value of the integrated sound velocity remains constant inside the liver.

The integrated speed-of-sound can provide a corrected image [Fig. 6.9B] using (equation 6.11). The confocal signal is clearly enhanced, as a large improvement in speckle brightness can be observed. The interfaces between tissues exhibit much better lateral coherence, especially at shallow depths, where the variations in the speed of sound are most drastic and their effects on the image are most pronounced. The correction of axial aberrations is also accompanied by a drastic reduction in transverse aberrations, and thus a significant improvement in transverse

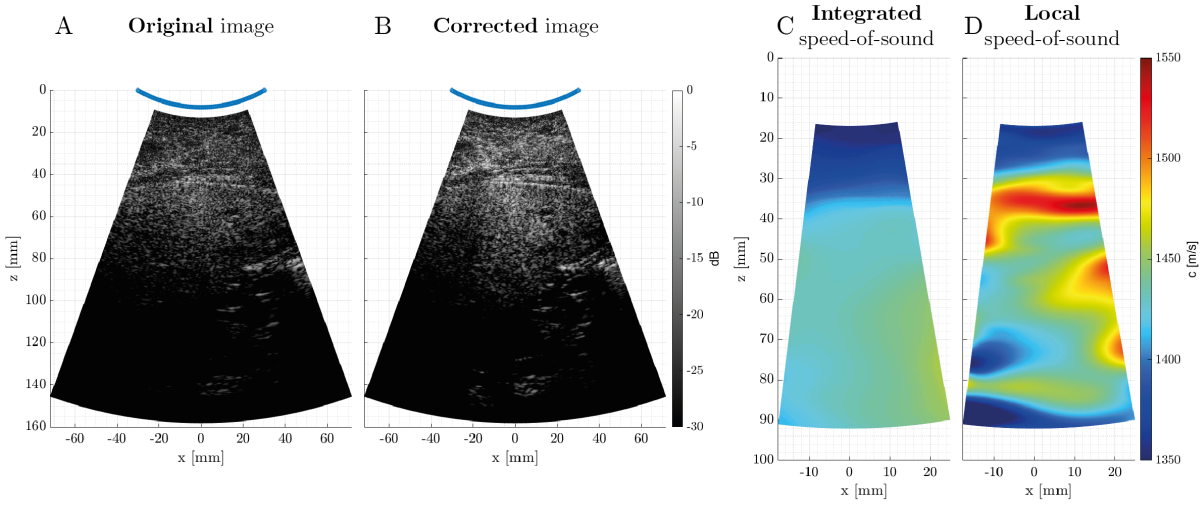

Figure 6.9: **Speed-of-sound mapping in an *in vivo* imaging experiment of a difficult-to-image patient liver. (A, B)** Original and corrected image, respectively. **(C)** Integrated and **(D)** local speed-of-sound reconstruction.

Parameters			Value
Analysis	Average window	lateral	$\mathcal{W}_\Theta = 6$ °
		axial	$\mathcal{W}_t = 7.8$ μs
	$\hat{c}_{\text{int}}$ estimator		Incoherent RPSF (Eq. 6.6)
Regularization	Smoothing of $\hat{c}_{\text{int}}$	lateral	$\mathcal{W}_\Theta^{(s)} = 2.4$ °
		axial	$\mathcal{W}_t^{(s)} = 2.3$ μs

Table 6.2: **Analysis parameters for extracting the speed-of-sound in an *in vivo* imaging experiment of a difficult-to-image patient liver.**

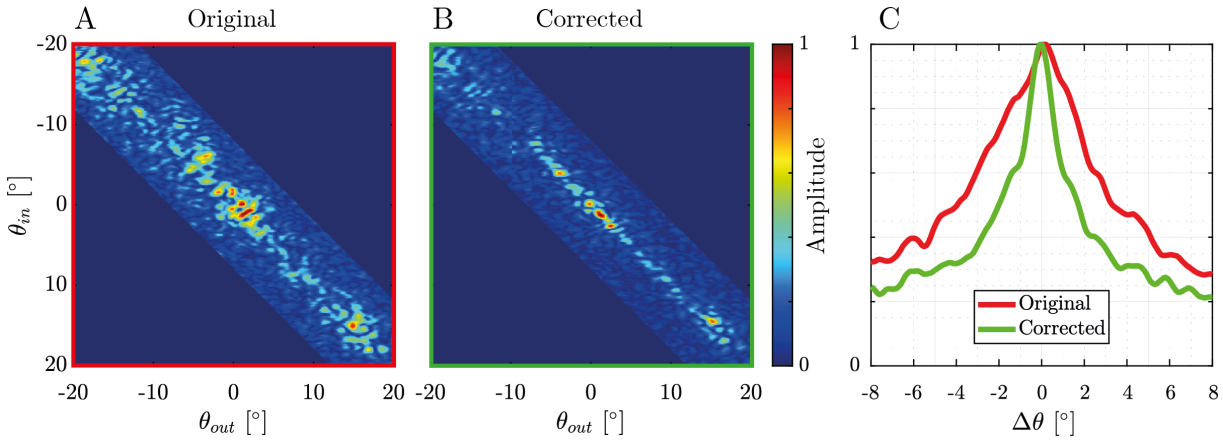

Figure 6.10: **Effect of speed-of-sound correction on transverse focused reflection matrices. (A, B)** Focused reflection matrix before and after correction (corresponding to $t = 90.9$ μs), respectively. **(C)** RPSF before (red curve) and after correction (green curve).

resolution and image contrast. This is confirmed when looking at the focused reflection matrix [Fig. 6.10A, B] that clearly shows that energy is brought back in the vicinity of the diagonal coefficients. An improvement in resolution by a factor of about two is emphasized by the transverse spreading of the RPSF [Fig. 6.10C]. The integrated speed-of-sound can also be used to reassign each pixel of the image to its true depth [Fig. 6.11]. As an example, we consider the distance between two speckle spots at the extremity of the red and green arrows in [Fig. 6.11 B and C], respectively. The distance between these two points was overestimated by 3 mm in the original image. This observation emphasizes the benefit that a reassignment of the pixels in depth could offer for ultrasound diagnosis.

Finally, the inversion of the integrated speed-of-sound $\hat{c}_{\text{int}}(\boldsymbol{\rho}, t)$ shown in [Fig. 6.9C] gives an estimator $\hat{c}_{\text{loc}}(\boldsymbol{\rho}, t)$ of the local sound velocity map $c(\mathbf{r})$ shown in [Fig. 6.9D]. This local sound velocity map shows the different tissue layers in the liver imaging experiment, especially the fat layer and the muscle tissue, which show particularly contrasted sound velocities. The measurement of sound velocity in the liver is crucial for the detection of diseases such as steatosis [Imbault, 2017]. The speed of sound measured here in the patient's liver is particularly low: $c \approx 1450$ m.s^{-1}. In a healthy liver, the value is around 1600 m.s^{-1}. This patient is therefore probably suffering from steatosis.

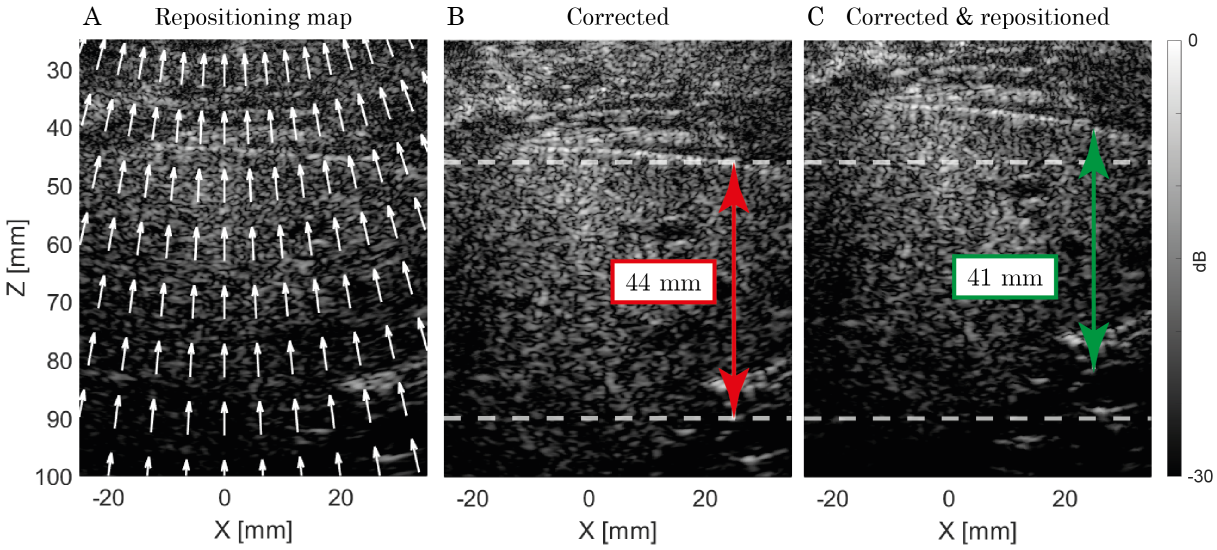

Figure 6.11: **Accurate distances in an *in vivo* imaging experiment of a difficult-to-image patient liver. (A)** Repositioning map based on integrated speed-of-sound map. **(B)** Corrected image only such that $\mathcal{R}_{\text{ref}}(t) = \frac{1}{2}c_{\text{ref}}t$. **(C)** Both re-positioned and corrected image such that $\hat{\mathcal{R}}(\Theta, t) = \frac{1}{2}c_{\text{int}}(\Theta, t)t$, where $(\mathcal{R}, \Theta)$ refers to polar coordinates.

10 Perspectives

In this work, sound velocity maps were obtained *in vivo* using the confocal component of the incoherent RPSF. The reason for this was mainly processing time, since a moving average window can be formulated quite easily by spatial convolution. Although the study of the coherent RPSF at each point takes much more time because it requires an SVD at each point, it is still a more accurate estimator and can be relevant when one wants to extract a value of the speed of sound at a particular point with higher accuracy.

This method is very similar to the method described in the previous chapter. Although the former method, which is based on the estimation of a defocus, seems to be relevant for multilayered media with constant axial defocus, the present method, which maps the speed of sound, seems to be more general since it directly provides a better estimate of the effective speed of sound, which directly leads to a higher accuracy in determining the position of the individual scatterers. Similarly, using the integrated sound velocity map for correction can be seen as an initial optimization method that corrects axial aberrations at each point before using the distortion matrix approach to capture the remaining higher order frequencies of the aberrations.

11 Conclusion

In this chapter, we have presented a new optimization-based method for extracting the integrated speed-of-sound map of an unknown medium. Our criterion is based on a self-portrait of the focusing process provided by the matrix imaging framework. The wave-field probed by virtual transducers at neighbor locations are combined through an SVD process to provide a coherent image of the local focusing process. The corresponding RPSF exhibits a Gouy phase shift and

a maximum amplitude when the wave velocity model is optimal. From this observable, an estimator of the integrated wave velocity has been built.

Besides directly generating images with better contrast and higher resolution, it allows positioning the depth of each scatterer with greater accuracy and thus to better evaluate the distance across ultrasound images. Even more, the differentiation of the integrated wave velocity allows an estimation of the local speed-of-sound. The method was validated by both simulations and phantom experiments before being applied in an *in vivo* clinical experiment that consisted in imaging the liver of a difficult-to-image patient. Our quantitative matrix imaging method allows better visualization of structures such as muscle fibers or veins, but also the measurement of an abnormally low speed-of-sound, characteristic of hepatic steatosis.

Although the coherent RPSF appears to be more accurate than its incoherent counterpart, it still needs to be precisely quantified and some additional studies need to be performed to determine both the robustness of each observable with respect to noise and their spatial resolution. In addition, the method must be compared to other state-of-the-art methods that optimize the speed of sound based on other quality criteria. The method described here is different from an angular approach that relies on phase mismatch between different insonification angles, *i.e.* distinct transverse wave vectors. The method described by Jaeger et al. [Jaeger, 2015a] is well suited for measuring lateral variations in the speed of sound, but it introduces a large bias on the absolute value of the measured velocity. Nevertheless, the latter method seems to complement our method, and it seems necessary to combine them. To this end, the matrix approach, which allows easy switching between the plane wave basis and the focused basis, seems to be an ideal tool for this fruitful combination. Moreover, the inversion of the problem could be both more accurate and more robust if oblique paths, refraction and a more robust regularization method were considered.

Finally, the perspective of this work will be to use the local speed-of-sound map as a new forward model to obtain a novel ultrasound image free of transverse and axial aberrations.

General Conclusion

The main goal of this work was to extend the study of the reflection matrix along several dimensions to finely compensate for aberrations and produce quantitative ultrasound images.

First, ultrasound matrix imaging was extended from 2D to 3D imaging using a matrix array of transducers. Experimental results in transcranial imaging were presented, providing an image with higher contrast and resolution, and a comparison with 2D imaging was made. It was then shown how matrix imaging can be easily combined with other imaging modalities in the specific case of *Ultrasound Localization Microscopy*. In this case, more bubbles can be detected and tracked, resulting in a higher contrast image with higher resolution and fewer reconstruction artifacts. These results were obtained *in vivo* in sheep. Second, the temporal degrees of freedom were used to characterize the acoustic response of monodisperse microbubbles, paving the way for a possible measurement of intra-arterial pressure *in vivo*. Last but not least, the spatio-temporal degrees of freedom of the focused reflection matrix have been used to optimize parameters such as the focal distance or the speed of sound, to correct axial aberrations (defocus) in ultrasound images, and map the speed of sound for quantitative imaging of biological tissues.

A first direct application of this work is the future integration of matrix imaging into Hologic's ultrasound platform. Although striking results were obtained in this manuscript, obtaining the same results in real time is a very different problem, as it requires a large amount of computing power. Even though 2D imaging is nearly real-time [Table 3.3], it is illusory today to transfer this method to real-time 3D imaging using a matrix array of transducers. To solve this problem, the use of sparse array or, more recently, RCA probes seems very promising, as they drastically reduce the number of channels and thus the required computational power. Another approach is to place a scattering medium directly behind the ultrasound probe to practically increase the effective aperture of the probe [Derode, 1995] and thus convert temporal degrees of freedom into spatial ones [Lemoult, 2010] for imaging large volumes with a limited number of transducers.

Another limitation of matrix imaging is the relatively long time required to acquire the fully sampled reflection matrix, while assuming a static medium. The method is therefore very sensitive to "undesirable" motion, such as operator-induced probe motion, out-of-plane motion, and also tissue motion (*e.g.* in cardiac imaging). Matrix imaging could therefore benefit from state-of-the-art methods to compensate for such movements.

If tissue motion can be considered a problem, it could also be considered a key parameter for obtaining biological information about the medium. Thus, a major challenge is to extend

matrix imaging to dynamic imaging. A first approach for using matrix imaging to capture the dynamics of biological tissue would be to reduce the number of insonifications, *i.e.* to perform ultrafast imaging by recording only a partial reflection matrix. However, this comes at the cost of aliasing artifacts in the focal plane [see Chapter 3, Section 3.3] and a break in symmetry between input and output. Such acquisitions directly affect the quality of several criteria presented in this thesis, *e.g.* for monitoring the convergence of the aberration law [see Chapter 3, Section 4.3.6] or for evaluating multiple scattering rates [see Chapter 3, Section 4.2.4]. Furthermore, since the degree of aberration through the skull is very important in transcranial imaging, the illumination base should be scanned almost completely if one wants to optimize the focusing process, which limits the compounded frame rate to a few hertz.

Still, in cases with fewer aberrations, we can imagine that matrix imaging could take advantage of ultrafast dynamic imaging to exploit, for example, fast decorrelation in vessels, leading to numerous realizations of the disorder at the same point [Osmanski, 2012a]. In other words, temporal averaging would replace spatial averaging. In principle, this could lead to an even more localized estimate of the transmission matrix, since no isoplanatic assumption would be made.

Another approach to extend matrix imaging to ultrafast *in vivo* imaging was presented in this work using successive insonification sequences [see Chapter 4, Section 2]. First, a static acquisition was performed to capture the fully sampled reflection matrix of the medium and extract local aberration laws. These estimates were then used to compensate for aberrations in a second ultrafast sequence, in which the insonification basis was drastically reduced to properly track microbubbles. In this particular case, the recording of the reflection matrix is actually much faster than the long recording time of several minutes required for microbubble tracking, and is therefore not a major limitation here. It should be emphasized that such a framework has been presented for the specific case of *Ultrasound Localization Microscopy*, but can be similarly applied to other ultrasound imaging modalities.

The results presented for characterizing bubbles seem promising, but require further investigation to validate them. Furthermore, the exploitation of temporal degrees of freedom can be used not only to characterize resonant objects, but also to tailor spatio-temporal focusing laws in order to compensate multiple reverberations that generally occur in transcranial brain imaging at shallow depths. This aspect is currently being investigated by Elsa Giraudat as part of her PhD thesis.

As for mapping the speed of sound, our method can be improved in various ways. First, the robustness of our new coherence-based estimators with respect to noise needs to be investigated. Then, the development of propagation models based on the speed-of-sound map is needed to refine the solution of the inverse problem and determine the local sound velocity from its integrated counterpart. Our method must be compared, or even combined, with the most modern methods of ultrasound imaging [Jaeger, 2015a] or even recent advances in applied mathematics [Borcea, 2023; Borcea, 2022a; Borcea, 2022b] used to determine the local speed-of-sound map of an unknown medium. In addition, our method can be combined with recent methods that generate high-resolution images from local speed-of-sound estimates [Ali, 2022]. Such a com-

bination could even be iterated to converge not only to an ideal image in terms of resolution, but also to better position each individual scatterer, leading to optimal distance measurements. This aspect will be explored in Emma Brenner's PhD thesis on the specific clinical case of breast imaging.

More generally, matrix imaging has been applied only to linear imaging. However, harmonic imaging is a great tool that is widely used in the clinic, for example, to better detect microbubbles or to achieve better contrast in cardiac imaging. In this context, the richness of the reflection matrix must be explored to extract all valuable information related to nonlinear wave propagation. For this reason, a matrix approach for harmonic imaging is currently being developed by Thibaud Vernier as part of his PhD thesis.

Last but not least, matrix imaging is a general framework that applies not only to ultrasound, but also to other fields of wave physics where a multi-element technology is used to study an unknown medium. It has already demonstrated its advantages in seismic imaging [Blondel, 2018; Touma, 2021; Giraudat, 2023], in optical imaging [Badon, 2020; Barolle, 2021; Najar, 2023; Balondrade, 2023], and is currently being investigated for radar imaging applications as part of Hussam Hanouni's PhD thesis. Given the ever-increasing computational and storage capabilities, matrix imaging has so far shown only a fraction of its potential in the field of wave imaging.

Scientific output

Peer-reviewed articles

– **Flavien Bureau**, Justine Robin, Arthur Le Ber, William Lambert, Mathias Fink and Alexandre Aubry. "Three-Dimensional Ultrasound Matrix Imaging". *Nature Communications, 2023*. DOI: 10.1038/s41467-023-42338-8.

International conferences

– **Flavien Bureau**, Elsa Giraudat, Arthur Le Ber, William Lambert, Mathias Fink and Alexandre Aubry. "In vivo speed-of-sound imaging using the spatiotemporal focused reflection matrix". Oral presentation at *IEEE International Ultrasonics Symposium, 2022*.

– **Flavien Bureau**, William Lambert, Arthur Le Ber, Mathias Fink and Alexandre Aubry. "3D Ultrasound Matrix Imaging for Aberration Correction over Multiple Isoplanatic Patches". Oral presentation at *IEEE International Ultrasonics Symposium, 2021*.

– **Flavien Bureau**, William Lambert, Laura Cobus, Thomas Frappart, Mathias Fink and Alexandre Aubry. "Matrix approach of aberration correction in medical ultrasound imaging". Oral presentation at *Forum Acusticum, 2020*.

– **Flavien Bureau**, William Lambert, Arthur Le Ber, Mathias Fink and Alexandre Aubry. "3D Matrix Approach for Aberration Correction in Random Scattering Media". Poster presentation at *IEEE International Ultrasonics Symposium, 2020*.

Appendix

1 Notations

Basis	Symbol	Adapted for
Acquisition basis	$\mathbf{R_{iu}}(t) = [R(\mathbf{i}_{\text{in}}, \mathbf{u}_{\text{out}}, t)]$	Data recording
Focused basis Common midpoint	$\mathbf{R}_{\boldsymbol{\rho\rho}}(z) = [R(\boldsymbol{\rho}_{\text{in}}, \boldsymbol{\rho}_{\text{out}}, z)]$ $\mathbf{R}_{\mathcal{M}}(z) = [R(\boldsymbol{\Delta\rho}, \boldsymbol{\rho}_{\text{m}}, z)]$	Focusing quality and multiple scattering quantification [Lambert, 2022b]
Dual basis (input)	$\mathbf{R_{cr}} = [R(\mathbf{c}_{\text{in}}, \mathbf{r}_{\text{out}})]$ $\mathbf{D_{cr}} = [D(\mathbf{c}_{\text{in}}, \mathbf{r}_{\text{out}})]$ $\mathbf{C}_{\text{in}} = [C(\mathbf{c}_{\text{in}}, \mathbf{c}'_{\text{in}})]$ $\hat{\mathbf{T}}_{\text{in}} = [\hat{T}(\mathbf{c}_{\text{in}}, \mathbf{r}_{\text{p}})]$	Local aberration compensation [Lambert, 2022a]
Dual basis (output)	$\mathbf{R_{rc}} = [R(\mathbf{r}_{\text{in}}, \mathbf{c}_{\text{out}})]$ $\mathbf{D_{rc}} = [D(\mathbf{r}_{\text{in}}, \mathbf{c}_{\text{out}})]$ $\mathbf{C}_{\text{out}} = [C(\mathbf{c}_{\text{out}}, \mathbf{c}'_{\text{out}})]$ $\hat{\mathbf{T}}_{\text{out}} = [\hat{T}(\mathbf{r}_{\text{p}}, \mathbf{c}_{\text{out}})]$	

Table 9.3: **Matrix notations.**

2 Fourier transform convention

The time Fourier transform is defined as follows :

$$R(\omega) = \int \mathrm{d}t R(t) \exp(+j\omega t), \tag{9.13}$$

$$R(t) = \int \mathrm{d}\omega R(\omega) \exp(-j\omega t). \tag{9.14}$$

The spatial Fourier transform is defined as follows:

$$R(\mathbf{k}) = \int \mathrm{d}\boldsymbol{\rho} R(\boldsymbol{\rho}) \exp(+j\mathbf{k}\boldsymbol{\rho}) = \int\int \mathrm{d}x\mathrm{d}y R(x,y) \exp(+j\left[k_x x + k_y y\right]), \tag{9.15}$$

$$R(\boldsymbol{\rho}) = \int \mathrm{d}\mathbf{k} R(\mathbf{k}) \exp(-j\mathbf{k}\boldsymbol{\rho}) = \int\int \mathrm{d}k_x\mathrm{d}k_y R(k_x,k_y) \exp(-j\left[k_x x + k_y y\right]). \tag{9.16}$$

3 Discrete Fourier transform

In practice, only discrete Fourier transform are performed numerically. This implies a good sampling of both real and **k**-space in order to define a unitary change of basis. Assuming a real sampling defined with a given gap (or pitch) and a given extension (or aperture), the **k**-space is defined as the inverse of these two quantities such that the extension dictates the pitch and inversely:

$$\text{Extension}: \Delta k = \frac{1}{\delta x}, \tag{9.17}$$

$$\text{Gap}: \delta k = \frac{1}{\Delta x}. \tag{9.18}$$

To define a unitary change of basis (*i.e.* no loss of information and no aliasing effects), the number of sampling points should be the same in both space, $N_x = N_k$ and the matrix that defines the change of basis should verify $\mathbf{G} \times \mathbf{G}^\dagger = \mathbf{G}^\dagger \times \mathbf{G} = \mathbf{I}$, $\mathbf{I}$ being the identity matrix.

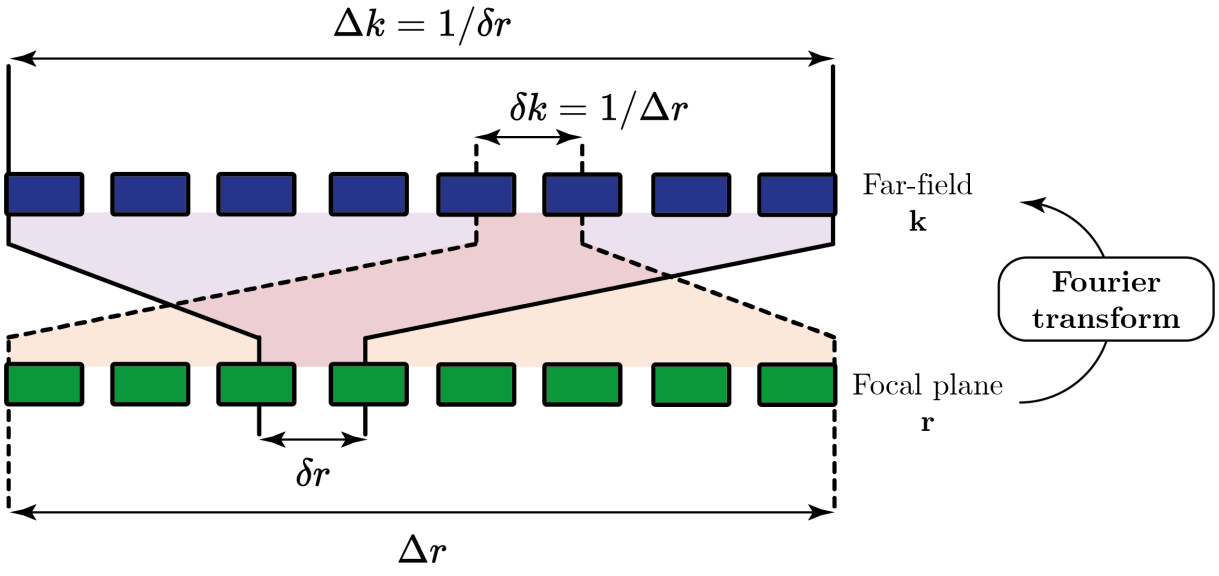

Figure 9.12: **Discrete Fourier transform.**

4 R−matrix in the focused basis

4.1 The general spatio-temporal focused reflection matrix

Projection in the focused basis consists in the following:

$$\mathbf{R_{rr}}(\delta t) = \sum_{\omega} \overbrace{\left[\mathbf{G}_0^* \times \mathbf{R_{uu}} \times \mathbf{G}_0^\dagger\right]}^{\text{at } \omega} \exp(-i\omega\delta t), \tag{9.19}$$

$$= \sum_{\omega} \left[\mathbf{G}_0^* \times \mathbf{G}_{\text{in}}^{\text{T}} \times \mathbf{\Gamma} \times \mathbf{G}_{\text{out}} \times \mathbf{G}_0^\dagger\right] \exp(-i\omega\delta t), \tag{9.20}$$

$$= \sum_{\omega} \left[\left(\mathbf{G}_{\text{in}} \times \mathbf{G}_0^\dagger\right)^\top \times \mathbf{\Gamma} \times \left(\mathbf{G}_{\text{out}} \times \mathbf{G}_0^\dagger\right)\right] \exp(-i\omega\delta t), \tag{9.21}$$

$$= \sum_{\omega} \left[\mathbf{H}_{\text{in}}^\top \times \mathbf{\Gamma} \times \mathbf{H}_{\text{out}}\right] \exp(-i\omega\delta t), \tag{9.22}$$

with $\mathbf{H}_{\text{in/out}} = \mathbf{G}_{\text{in/out}} \times \mathbf{G}_0^\dagger$ the input and output point spread function (PSF) and $\mathbf{G}_0$ is the homogeneous focusing matrices defined as follows:

$$\mathbf{G}_0^{(\text{in})} = A_{\text{in}}(i_{\text{in}}, \mathbf{r}_{\text{in}}) \exp(i\omega\tau(i_{\text{in}}, \mathbf{r}_{\text{in}}, c_0)), \tag{9.23}$$

$$\mathbf{G}_0^{(\text{out})} = A_{\text{out}}(u_{\text{out}}, \mathbf{r}_{\text{out}}) \exp(i\omega\tau(u_{\text{out}}, \mathbf{r}_{\text{out}}, c_0)). \tag{9.24}$$

In the canonical basis

$$G_0(\mathbf{u}, \mathbf{r}, c_0, \omega) = A(\mathbf{u}, \mathbf{r}) \exp\left(i\omega \frac{|\mathbf{u} - \mathbf{r}|}{c_0}\right). \tag{9.25}$$

In terms of coefficients it writes:

$$R(\mathbf{r}_{\text{in}}, \mathbf{r}_{\text{out}}, \delta t, c_0) = \int\int \mathrm{d}\omega \mathrm{d}\mathbf{r}' H_{\text{in}}(\mathbf{r}_{\text{in}}, \mathbf{r}', \omega, c_0) \gamma(\mathbf{r}') H_{\text{out}}(\mathbf{r}_{\text{out}}, \mathbf{r}', \omega, c_0) \exp(-i\omega\delta t), \tag{9.26}$$

$$= \int\int \mathrm{d}\omega \mathrm{d}\mathbf{r}' H_{\text{out}}(\mathbf{r}_{\text{out}}, \mathbf{r}', \omega, c_0) \gamma(\mathbf{r}') \exp(j\omega\delta t) \int \mathrm{d}t H_{\text{in}}(\mathbf{r}_{\text{in}}, \mathbf{r}', t, c_0) \exp(i\omega t), \tag{9.27}$$

$$= \int\int \mathrm{d}t \mathrm{d}\mathbf{r}' H_{\text{in}}(\mathbf{r}_{\text{in}}, \mathbf{r}', t, c_0) \gamma(\mathbf{r}') \int \mathrm{d}\omega H_{\text{out}}(\mathbf{r}_{\text{out}}, \mathbf{r}', t, c_0) \exp\left(-i\omega(\delta t - t)\right), \tag{9.28}$$

$$= \int\int \mathrm{d}t \mathrm{d}\mathbf{r}' H_{\text{in}}(\mathbf{r}_{\text{in}}, \mathbf{r}', t, c_0) \gamma(\mathbf{r}') H_{\text{out}}(\mathbf{r}_{\text{out}}, \mathbf{r}', \delta t - t, c_0), \tag{9.29}$$

$$R(\mathbf{r}_{\text{in}}, \mathbf{r}_{\text{out}}, \delta t, c_0) = \int \mathrm{d}\mathbf{r}' \gamma(\mathbf{r}') \left(H_{\text{in}} \overset{\delta t}{\circledast} H_{\text{out}}\right)(\mathbf{r}_{\text{in}}, \mathbf{r}_{\text{out}}, \mathbf{r}', c_0, \delta t). \tag{9.30}$$

General expression of the focused R-matrix

In a de-scan basis $(\mathbf{r}_{\text{in}}, \mathbf{r}_{\text{out}}) \to (\mathbf{r}, \mathbf{\Delta r})$, (Eq. 9.30) rewrites :

$$R_{\mathcal{D}}(\mathbf{r}, \mathbf{\Delta r}, \delta t, c_0) = \int \mathrm{d}\mathbf{r}' \gamma(\mathbf{r}') \left(H_{\text{in}} \overset{\delta t}{\circledast} H_{\text{out}}\right)(\mathbf{r}, \mathbf{\Delta r}, \mathbf{r}', c_0, \delta t) \tag{9.31}$$

4.2 Frequency or Time *beamforming*

In previous work [Lambert, 2020a] the focused $\mathbf{R}-$matrix was built in the frequency domain as follows:

$$\mathbf{R_{rr}}(\delta t) = \sum_{\omega} \underbrace{\left[\left[\mathbf{G}_0^{(\text{in})}\right]^* \times \mathbf{R_{iu}} \times \left[\mathbf{G}_0^{(\text{out})}\right]^\dagger\right]}_{\text{at } \omega} \exp(-i\omega\delta t). \tag{9.32}$$

In terms of matrix coefficients, (Eq. 9.32) becomes:

$$R(\mathbf{r}_{\text{in}}, \mathbf{r}_{\text{out}}, \delta t) = \sum_{\mathbf{i}_{\text{in}}} \sum_{\mathbf{u}_{\text{out}}} A(\mathbf{i}_{\text{in}}, \mathbf{r}_{\text{in}}, \mathbf{u}_{\text{out}}, \mathbf{r}_{\text{out}}) \sum_{\omega} R\left(\mathbf{i}_{\text{in}}, \mathbf{u}_{\text{out}}, \omega\right) \exp(-i\omega[\tau(\mathbf{i}_{\text{in}}, \mathbf{r}_{\text{in}}) + \tau(\mathbf{u}_{\text{out}}, \mathbf{r}_{\text{out}}) + \delta t]), \tag{9.33}$$

$$= \sum_{\mathbf{i}_{\text{in}}} \sum_{\mathbf{u}_{\text{out}}} \underbrace{A([\mathbf{i}_{\text{in}}, \mathbf{r}_{\text{in}}], [\mathbf{u}_{\text{out}}, \mathbf{r}_{\text{out}}])}_{\text{synthetic aperture}} R\left(\mathbf{i}_{\text{in}}, \mathbf{u}_{\text{out}}, \tau(\mathbf{i}_{\text{in}}, \mathbf{r}_{\text{in}}) + \tau(\mathbf{u}_{\text{out}}, \mathbf{r}_{\text{out}}) + \delta t\right), \tag{9.34}$$

which is nothing but a DAS algorithm where input and output focal spots have been decoupled.

4.3 RPSF expression

At the ballistic time ($\delta t = 0$ μs) and at a given depth and assuming isoplanetism, the focused $\mathbf{R}-$matrix can be expressed as follows :

$$R(\boldsymbol{\rho}_{\text{in}}, \boldsymbol{\rho}_{\text{out}}, z) = \int \mathrm{d}\boldsymbol{\rho} H_{\text{in}}(\boldsymbol{\rho} - \boldsymbol{\rho}_{\text{in}}, z)\gamma(\boldsymbol{\rho}, z)H_{\text{out}}(\boldsymbol{\rho} - \boldsymbol{\rho}_{\text{out}}, z). \tag{9.35}$$

4.3.1 Speckle regime

$$\left\langle |\mathbf{R}_{\rho\rho}|^2 \right\rangle = \langle \mathbf{R}_{\rho\rho}\mathbf{R}^*_{\rho\rho} \rangle, \tag{9.36}$$

$$= \int\int d\boldsymbol{\rho} d\boldsymbol{\rho}' H_{\text{in}}(\boldsymbol{\rho} - \boldsymbol{\rho}_{\text{in}}) H^*_{\text{in}}(\boldsymbol{\rho}' - \boldsymbol{\rho}_{\text{in}}) \underbrace{\langle \gamma(\boldsymbol{\rho})\gamma^*(\boldsymbol{\rho}') \rangle}_{\langle|\gamma|^2\rangle\delta(\boldsymbol{\rho}-\boldsymbol{\rho}')} H_{\text{out}}(\boldsymbol{\rho} - \boldsymbol{\rho}_{\text{out}}) H^*_{\text{out}}(\boldsymbol{\rho} - \boldsymbol{\rho}_{\text{out}}). \tag{9.37}$$

It comes:

$$\left\langle |\mathbf{R}_{\rho\rho}|^2 \right\rangle (\boldsymbol{\rho}_{\text{in}}, \boldsymbol{\rho}_{\text{out}}) \propto \int dx |H_{\text{in}}(\boldsymbol{\rho} - \boldsymbol{\rho}_{\text{in}})|^2 |H_{\text{out}}(\boldsymbol{\rho} - \boldsymbol{\rho}_{\text{out}})|^2. \tag{9.38}$$

A change of variable ($\boldsymbol{\rho}' = \boldsymbol{\rho} - \boldsymbol{\rho}_{\text{in}}$) leads to:

$$\left\langle |\mathbf{R}_{\rho\rho}|^2 \right\rangle (\boldsymbol{\rho}_{\text{in}}, \boldsymbol{\rho}_{\text{out}}) \propto \int dx |H_{\text{in}}(\boldsymbol{\rho})|^2 |H_{\text{out}}(x + \boldsymbol{\rho}_{\text{in}} - \boldsymbol{\rho}_{\text{out}})|^2. \tag{9.39}$$

Then by moving to a common midpoint basis, it comes:

$$\langle RPSF\rangle(\boldsymbol{\Delta\rho}) = \left\langle |\mathbf{R}_{\rho\rho}|^2 \right\rangle (\boldsymbol{\rho}_{\rm p} - \frac{\boldsymbol{\Delta\rho}}{2}, \boldsymbol{\rho}_{\rm p} + \frac{\boldsymbol{\Delta\rho}}{2}), \tag{9.40}$$

$$\langle RPSF\rangle(\boldsymbol{\Delta\rho}) \propto \int \mathrm{d}\boldsymbol{\rho} |H_{\rm in}(\boldsymbol{\rho})|^2 |H_{\rm out}(\boldsymbol{\rho} - \boldsymbol{\Delta\rho})|^2, \tag{9.41}$$

$$\langle RPSF\rangle(\boldsymbol{\Delta\rho}) \propto \left(|H_{\rm in}|^2 \overset{\boldsymbol{\Delta\rho}}{\circledast} |H_{\rm out}|^2 \right) (\boldsymbol{\Delta\rho}). \tag{9.42}$$

4.3.2 Specular regime

At a given depth, a specular reflector can be considered with a constant reflectivity γ such that:

$$R(\boldsymbol{\rho}_{\rm in}, \boldsymbol{\rho}_{\rm out}, z) = \gamma \int \mathrm{d}\boldsymbol{\rho} H_{\rm out}(\boldsymbol{\rho} - \boldsymbol{\rho}_{\rm out}, \boldsymbol{\rho}_{\rm in}, z) H_{\rm in}(\boldsymbol{\rho} - \boldsymbol{\rho}_{\rm in}, \boldsymbol{\rho}_{\rm in}, z), \tag{9.43}$$

$$= \gamma \left(H_{\rm in} \overset{\boldsymbol{\Delta\rho}}{\circledast} H_{\rm out} \right) (\boldsymbol{\Delta\rho}), \tag{9.44}$$

$$\tag{9.45}$$

which leads to:

$$\langle RPSF\rangle(\boldsymbol{\Delta\rho}) = |\gamma|^2 \left| \left(H_{\rm in} \overset{\boldsymbol{\Delta\rho}}{\circledast} H_{\rm out} \right) (\boldsymbol{\Delta\rho}) \right|^2. \tag{9.46}$$

4.4 Discriminate multiple scattering from electronic noise

We consider here the mean background of the de-scan focused reflection matrix for a given point $\mathbf{r}_{\rm p}$:

$$\mathrm{B}(\boldsymbol{\Delta\rho}, \mathbf{r}_{\rm p}) = \langle R(\boldsymbol{\Delta\rho}, \mathbf{r}) \mathcal{D}(\boldsymbol{\Delta\rho}) \mathcal{W}(\mathbf{r} - \mathbf{r}_{\rm p}) \rangle_{\mathbf{r}}, \tag{9.47}$$

where $\mathcal{D}(\Delta\boldsymbol{\rho})$ is a de-scan window function that eliminates the confocal peak and $\mathcal{W}$ is a spatial average window function around the targeted focal point $\mathbf{r}_{\rm p}$.

The background can be decomposed as the sum of a fully symmetric matrix associated to multiple scattering (due to spatial reciprocity) and a fully random matrix associated to the electronic noise as follows:

$$\underbrace{\mathbf{B}}_{\text{Background}} = \underbrace{\mathbf{M}}_{\text{Multiple scattering}} + \underbrace{\mathbf{N}}_{\text{Noise}}. \tag{9.48}$$

Projecting the $\mathbf{B}-$matrix onto its antisymmetric subspace directly holds the antisymmetric part of the electronic noise such that:

$$\mathbf{B}^{(\mathrm{A})} = \frac{\mathbf{B} - \mathbf{B}^\top}{2} = \mathbf{N}^{(\mathrm{A})}. \tag{9.49}$$

Assuming equipartition of the electronic noise onto its symmetric and antisymmetric subspace, it comes:

$$\|\mathbf{B}^{(\mathrm{A})}\|^2 = \|\mathbf{N}^{(\mathrm{A})}\|^2 = \frac{1}{2}\|\mathbf{N}\|^2. \tag{9.50}$$

The norm of the background can be expressed as follows:

$$\|\mathbf{B}\|^2 = \|\mathbf{M}\|^2 + \|\mathbf{N}\|^2 + 2\underbrace{\langle \mathbf{M}|\mathbf{N}\rangle}_{\sim 0}. \tag{9.51}$$

The multiple scattering rate α_M can be deduced by combining equations (9.50) & (9.51):

$$\alpha_M = \frac{\|\mathbf{M}\|^2}{\|\mathbf{B}\|^2} = 1 - 2\underbrace{\frac{\|\mathbf{B}^{(\mathrm{A})}\|^2}{\|\mathbf{B}\|^2}}_{\beta}, \tag{9.52}$$

with β the antisymmetric rate of the $\mathbf{B}-$matrix.

5 R−matrix in a dual basis

5.1 Time reversal analysis of the D−matrix

In this section, we recall the distortion formalism that was introduced by Lambert et al. [Lambert, 2020c; Lambert, 2020a]. At a given depth, the distortion matrix built in the plane wave basis ($\mathbf{c} = \mathbf{k}$) writes:

$$\mathbf{D_{xk}} = \mathbf{T}_0^* \circ \left[\mathbf{H}_{\text{in}}^{\text{T}} \times \mathbf{\Gamma} \times \mathbf{T}_{\text{out}}\right], \tag{9.53}$$

which can be written in terms of coefficients:

$$D(x_{\text{in}}, k_{\text{out}}) = \exp(-jk_{\text{in}}x_{\text{in}}) \int \mathrm{d}x H_{\text{in}}(x, x_{\text{in}})\gamma(x)\mathrm{G}_{\text{out}}(k_{\text{out}}, x), \tag{9.54}$$

$$= \int \mathrm{d}x H_{\text{in}}(x, x_{\text{in}})\gamma(x)\mathrm{G}_{\text{out}}(k_{\text{out}}, x - x_{\text{in}}). \tag{9.55}$$

Correlations are studied along the output focal spots $\mathbf{C_{kk}} = \mathbf{D}_{\mathbf{xk}}^{\dagger} \times \mathbf{D_{xk}}$. In terms of coefficients, it writes:

$$C(k_{\text{out}}, k'_{\text{out}}) = \int \mathrm{d}x_{\text{in}} D^*(x_{\text{in}}, k_{\text{out}})D(x_{\text{in}}, k'_{\text{out}}). \tag{9.56}$$

Assuming that the correlation matrix converges towards its ensemble average (*i.e.* a sufficient number of resolution cells are considered) and assuming a speckle regime (*i.e.* $\langle\gamma(x)\gamma(x')\rangle = \delta(x - x')$) the equation becomes:

$$\langle C(k_{\text{out}}, k'_{\text{out}})\rangle \propto \int\int \mathrm{d}x_{\text{out}}\mathrm{d}x \mathrm{G}^*_{\text{out}}(k_{\text{out}}, x - x_{\text{in}})|H_{\text{in}}(x, x_{\text{in}})|^2\mathrm{G}_{\text{out}}(k'_{\text{in}}, x - x_{\text{in}}). \tag{9.57}$$

Assuming isoplanetism, *i.e.* $H_{\text{in}}(x, x_{\text{in}}) = H_{\text{in}}(x - x_{\text{in}})$, it comes:

$$\langle C(k_{\text{out}}, k'_{\text{out}})\rangle \propto \int \mathrm{d}x \mathrm{G}^*_{\text{out}}(k_{\text{out}}, x)|H_{\text{in}}(x)|^2\mathrm{G}_{\text{out}}(k'_{\text{out}}, x), \tag{9.58}$$

that can be written in a matrix formalism as follows:

$$\langle \mathbf{C_{kk}} \rangle \propto \mathbf{G}_{\text{out}}^{\dagger} \times \mathbf{\Gamma}_{\mathbf{H}_{\text{in}}} \times \mathbf{G}_{\text{out}}, \tag{9.59}$$

where $\mathbf{\Gamma}_{\mathbf{H}_{\text{in}}}$ is a diagonal matrix whose coefficients are proportional to $|H_{\text{in}}(x)|^2$. $\langle \mathbf{C_{kk}} \rangle$ is equivalent to a reflection matrix associated with a virtual reflector of reflectivity $|H_{\text{in}}(x)|^2$.

In the simple case where we suppose a perfect input focal spot so that $\mathbf{H}_{\text{in}}(x) = \delta(x)$, it comes:

$$\langle C(k_{\text{out}}, k'_{\text{out}})\rangle \propto \int \mathrm{d}x \mathrm{T}^*_{\text{out}}(k_{\text{out}}, x)\mathrm{T}_{\text{out}}(k'_{\text{out}}, x). \tag{9.60}$$

And assuming a far field phase screen to describe the aberration, $\mathrm{G}_{\text{out}}(k_{\text{out}}, x) = \mathrm{G}_0(k_{\text{out}}, x)\mathrm{T}(k_{\text{out}})$, where $\mathbf{T}$ stands for the distortion part of the wavefront, the correlation matrix writes:

$$\langle C(k_{\text{out}}, k'_{\text{out}})\rangle \propto \mathrm{T}^*(k_{\text{out}})\mathrm{T}(k'_{\text{out}}), \tag{9.61}$$

or in a matrix formalism:

$$\langle \mathbf{C} \rangle \propto \mathbf{T}_{\text{out}}^{\dagger} \times \mathbf{\Gamma}_{\delta} \times \mathbf{T}_{\text{out}}. \tag{9.62}$$

In contrast to the matrix $\mathbf{\Gamma}_{\mathbf{H}_{\text{in}}}$, $\mathbf{\Gamma}_{\delta}$ is a diagonal matrix associated with a point-like (diffraction-limited) reflector at the origin. The correlation matrix associated with such a point-like reflector is of rank 1 so that the first singular vector of the correlation matrix holds the distorted wavefront $\mathrm{T}(k_{\text{out}}) = U_1(k_{\text{out}})$.

5.2 De-scan basis & distortion matrix

Considering the Fourier transform of the de-scan focused reflection matrix directly provides the distortion matrix in the plane wave basis:

$$\begin{aligned}
\mathcal{F}_{[\Delta x]}(\mathbf{R}_{\mathcal{D}}) &= \left[\mathrm{G}_0(k_{\text{out}}^{(x)}, \Delta x)\right] \times \left[R_{\mathcal{D}}(\Delta x, x_{\text{in}})\right], && (9.63)\\
&= \sum_{\Delta x} \exp(jk_{\text{out}}^{(x)} \Delta x) R_{\mathcal{D}}(\Delta x, x_{\text{in}}), && (9.64)\\
&= \sum_{x_{\text{out}}} \exp(jk_{\text{out}}^{(x)} [x_{\text{out}} - x_{\text{in}}]) R(x_{\text{out}}, x_{\text{in}}), && (9.65)\\
&= \exp(-jk_{\text{out}}^{(x)} x_{\text{in}}) \sum_{x_{\text{in}}} \exp(jk_{\text{out}}^{(x)} x_{\text{out}}) R(x_{\text{out}}, x_{\text{in}}), && (9.66)\\
&= \left[\mathrm{G}_0^*(k_{\text{out}}^{(x)}, x_{\text{in}})\right] \circ \left[R(k_{\text{out}}^{(x)}, x_{\text{in}}, z)\right], && (9.67)\\
&= \mathrm{D}(k_{\text{out}}^{(x)}, x_{\text{in}}). && (9.68)
\end{aligned}$$

5.3 Bias on $\hat{\mathbf{T}}$

In practice, the $\mathbf{T}-$matrix estimator is still impacted by the blurring of the synthesized guide star and the presence of diffusive background and/or noise. Therefore, the whole process shall be iterated at input and output in order to gradually refine the guide star and reduce the bias on our $\mathbf{T}-$matrix estimator. Moreover, the spatial window $\mathcal{W}$ over which the $\mathbf{C}-$matrix is computed shall be gradually decreased in order to address the high-order aberration components, the latter one being associated with smaller isoplanatic patches.

To understand the parameters controlling the bias $\delta\hat{\mathbf{T}}_{\text{out}}$ between $\hat{\mathbf{T}}_{\text{out}}$ and $\mathbf{T}_{\text{out}}$, one can express $\hat{\mathbf{T}}_{\text{out}}$ as follows:

$$\hat{\mathbf{T}}_{\text{out}} = \exp\left(j\arg\left\{\mathbf{C}_{\text{out}} \times \hat{\mathbf{T}}_{\text{out}}\right\}\right) = \frac{\mathbf{C}_{\text{out}} \times \hat{\mathbf{T}}_{\text{out}}}{||\mathbf{C}_{\text{out}} \times \hat{\mathbf{T}}_{\text{out}}||}. \tag{9.69}$$

$\hat{\mathbf{T}}_{\text{out}}$ can be expressed, at first order, as the sum of its expected value $\mathbf{T}_{\text{out}}$ and a perturbation term $\delta\hat{\mathbf{T}}_{\text{out}}$:

$$\hat{\mathbf{T}}_{\text{out}} = \underbrace{\frac{\langle \mathbf{C}_{\text{out}} \rangle \times \mathbf{T}_{\text{out}}}{||\langle \mathbf{C}_{\text{out}} \rangle \times \mathbf{T}_{\text{out}}||}}_{=\mathbf{T}_{\text{out}}} + \underbrace{\frac{\delta\mathbf{C}_{\text{out}} \times \mathbf{T}_{\text{out}}}{||\langle \mathbf{C}_{\text{out}} \rangle \times \mathbf{T}_{\text{out}}||}}_{\simeq\delta\hat{\mathbf{T}}_{\text{out}}}. \tag{9.70}$$

The bias intensity can be expressed as follows:

$$||\delta\hat{\mathbf{T}}_{\text{out}}||^2 = \frac{\mathbf{T}_{\text{out}}^{\dagger} \times \delta\mathbf{C}_{\text{out}}^{\dagger} \times \delta\mathbf{C}_{\text{out}} \times \mathbf{T}_{\text{out}}}{\mathbf{T}_{\text{out}}^{\dagger} \times \langle\mathbf{C}_{\text{out}}\rangle^{\dagger} \times \langle\mathbf{C}_{\text{out}}\rangle \times \mathbf{T}_{\text{out}}}. \tag{9.71}$$

The numerator of the last equation can be expressed as follows:

$$\mathbf{T}_{\text{out}}^{\dagger} \times \delta\mathbf{C}_{\text{out}}^{\dagger} \times \delta\mathbf{C}_{\text{out}} \times \mathbf{T}_{\text{out}} = N_u^2 \langle|\delta C(\mathbf{c},\mathbf{c}')|^2\rangle = N_u^2 |C(\mathbf{c},\mathbf{c})|^2 / N_{\mathcal{W}}, \tag{9.72}$$

with N_u the number of transducers. The denominator of (Eq. 9.71) can be expressed as follows:

$$\mathbf{T}_{\text{out}}^{\dagger} \times \langle\mathbf{C}_{\text{out}}\rangle^{\dagger} \times \langle\mathbf{C}_{\text{out}}\rangle \times \mathbf{T}_{\text{out}} = M^2 \left| \sum_{\mathbf{c}} T_{\text{in}} \overset{\mathbf{c}}{\circledast} T_{\text{in}}(\mathbf{c}) \right|^2. \tag{9.73}$$

The bias intensity is thus given by:

$$||\delta\hat{\mathbf{T}}_{\text{out}}(\mathbf{c})||^2 = \frac{\left| T_{\text{in}} \overset{\mathbf{c}}{\circledast} T_{\text{in}}(\mathbf{0}) \right|^2}{N_{\mathcal{W}} \left| \sum_{\mathbf{c}} T_{\text{in}} \overset{\mathbf{c}}{\circledast} T_{\text{in}}(\mathbf{c}) \right|^2}. \tag{9.74}$$

In the last expression, we recognize the ratio between the coherent intensity (energy deposited exactly at focus) and the mean incoherent input intensity. This quantity is known as the coherence factor in ultrasound imaging [Mallart, 1994; Robert, 2008a]:

$$C_{\text{in}} = \frac{\sum_{\mathbf{c}} T_{\text{in}} \overset{\mathbf{c}}{\circledast} T_{\text{in}}(\mathbf{c})}{T_{\text{in}} \overset{\mathbf{c}}{\circledast} T_{\text{in}}(\mathbf{0})} = \frac{|H_{\text{in}}(\boldsymbol{\rho}=\mathbf{0})|^2}{\Delta\rho_{\text{max}}^{-2} \int d\boldsymbol{\rho} |H_{\text{in}}(\boldsymbol{\rho})|^2}. \tag{9.75}$$

In the speckle regime and for a 2D probe, the coherence factor C ranges from 0, for strong aberrations and/or multiple scattering background, to 4/9 in the ideal case [Silverstein, 2001]. The bias intensity can thus be rewritten as:

$$||\delta\hat{\mathbf{T}}_{\text{out}}||^2 = \frac{1}{C_{\text{in}}^2 N_{\mathcal{W}}}. \tag{9.76}$$

This last expression justifies the multi-scale analysis proposed in Chapter 3. A gradual increase of the focusing quality, quantified by C, is required to address smaller spatial windows that scale as $N_{\mathcal{W}}$. Following this scheme, the bias made of our **T**−matrix estimator can be minimized.

5.4 Correction procedure workflow

[Fig. 9.13] shows a workflow summarising the various steps of the UMI procedure for performing adaptive focusing using the "distortion matrix approach".

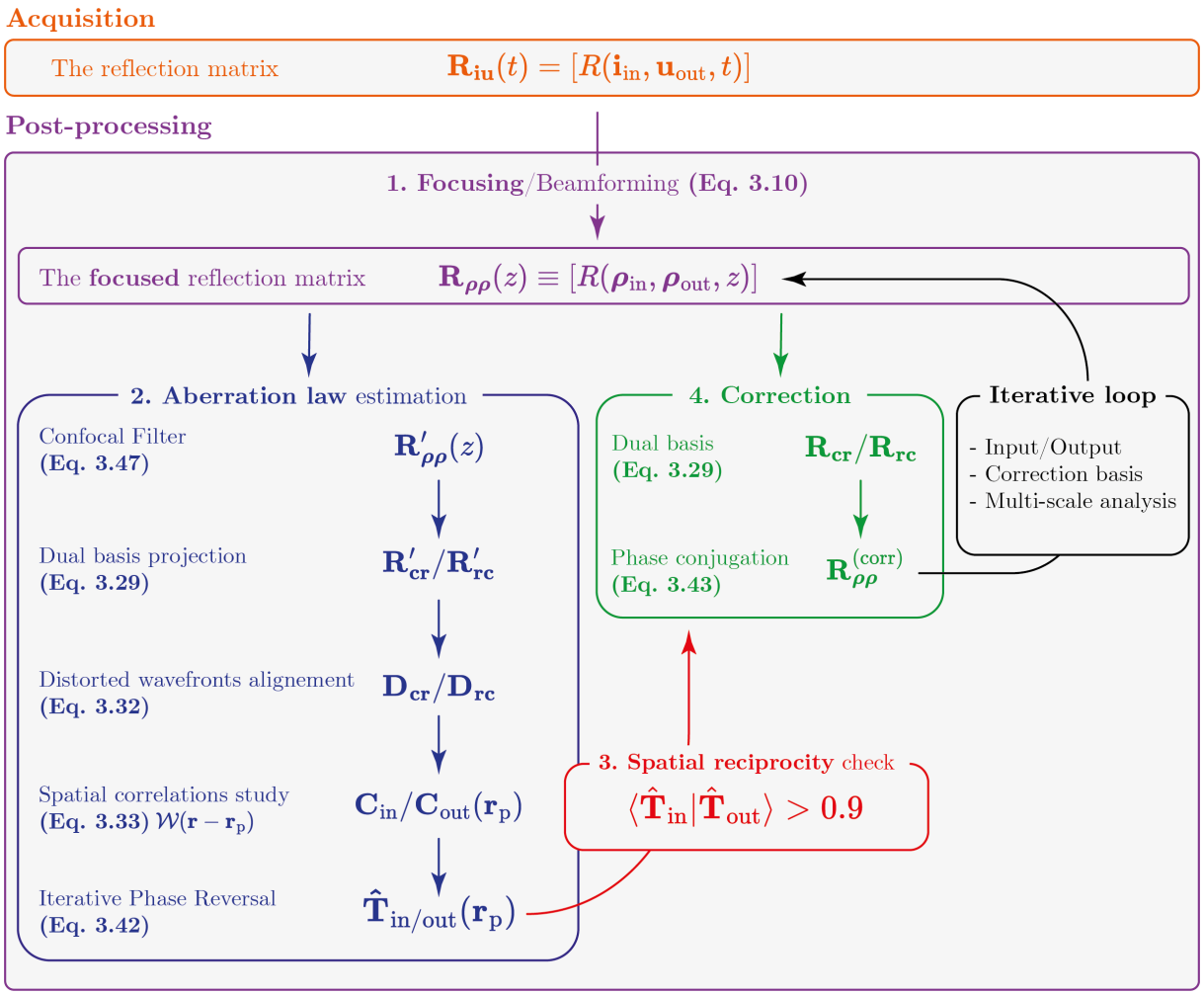

Figure 9.13: **Flowchart of the UMI process**.

5.5 Correcting random-phase artefacts

If the scattering distribution is too complex, the aberration law extracted with IPR or SVD may have a linear phase ramp that causes the associated field of view to shift laterally when correcting the $\mathbf{R}-$matrix [Lambert, 2020a]. To avoid such artifacts, the value of the linear phase ramp can be estimated by projecting the aberration law into the focal space. The lateral shift can be estimated and further used to compensate for such artifacts before the aberration law is used to correct the $\mathbf{R}-$matrix. Here, we show how such artifacts can be removed when the aberration law $\mathrm{T}(k_x)$ is extracted in the far-field basis ($\mathbf{k}$). First it is projected in the focal space by means of a Fourier transform:

$$H_{\mathbf{T}}(\Delta x) = \mathcal{F}_{[\Delta x]}(\mathrm{T}(k_x)) \tag{9.77}$$

$$= \sum_{k_x} \mathrm{T}(k_x) \exp(jk_x \Delta x). \tag{9.78}$$

Then, the maximum of its auto-convolution can be used to find the spatial shift associated with the phase-ramp:

$$\Delta x^{(\measuredangle)} = \text{argmax}\left(|H_{\text{T}} \overset{\Delta x}{\circledast} H_{\text{T}}|^2\right). \tag{9.79}$$

The aberration law can thus be updated as follows:

$$\text{T}'(k_x) = \text{T}(k_x)\exp(-jk_x\Delta x^{(\measuredangle)}), \tag{9.80}$$

with T' the aberration law free from any phase ramp artifact.

6 From the integrated to the local speed-of-sound

The obtained integrated speed-of-sound map, $\hat{c}_{\text{int}}$, can be used to estimate a local speed-of-sound map, $\hat{c}_{\text{loc}}$. To this end, we need to perform an inversion of (Eq. 6.1) and for this we take up the method developed in the following article by Jakovljevic et al. [Jakovljevic, 2018]. Under a paraxial approximation and assuming that the speed of sound is a piecewise constant function between discretized depths, such as $z_n = n\mathrm{d}z$ with $n \in \{0, 1, ..., N\}$, (Eq. 6.1) leads to:

$$z\sigma_{\text{int}}(z) = \int_0^z \sigma_{\text{loc}}(z')\mathrm{d}z', \tag{9.81}$$

$$\Rightarrow n\mathrm{d}z\sigma_{\text{int}}(z_n) = \sum_{i=1}^{n} \sigma_{\text{loc}}(z_i)\mathrm{d}z, \tag{9.82}$$

$$\Rightarrow \sigma_{\text{int}}(z_n) = \frac{1}{n}\sum_{i=1}^{n} \sigma_{\text{loc}}(z_i), \tag{9.83}$$

where $\sigma_{\text{loc}} = 1/\hat{c}_{\text{loc}}$ and $\sigma_{\text{int}} = 1/\hat{c}_{\text{int}}$ are the local and integrated slowness maps, respectively. (Eq. 9.83) defines the following system of equations for $n \in \{1, ..., N\}$:

$$\begin{cases} \sigma_{\text{int}}(z_1) = & \sigma_{\text{loc}}(z_1); \\ \sigma_{\text{int}}(z_2) = & \frac{1}{2}(\sigma_{\text{loc}}(z_1) + \sigma_{\text{loc}}(z_2)); \\ \sigma_{\text{int}}(z_3) = & \frac{1}{3}(\sigma_{\text{loc}}(z_1) + \sigma_{\text{loc}}(z_2) + \sigma_{\text{loc}}(z_3)); \\ ... & \\ \sigma_{\text{int}}(z_N) = & \frac{1}{N}\sum_{i=1}^{N} \sigma_{\text{loc}}(z_i), \end{cases} \tag{9.84}$$

which can be written in terms of matrix coefficients as follows:

$$\underbrace{\begin{pmatrix} 1 & 0 & 0 & ... & 0 \\ \frac{1}{2} & \frac{1}{2} & 0 & ... & 0 \\ \frac{1}{3} & \frac{1}{3} & \frac{1}{3} & ... & 0 \\ ... & ... & ... & ... & ... \\ \frac{1}{N} & \frac{1}{N} & \frac{1}{N} & ... & \frac{1}{N} \end{pmatrix}}_{\mathbf{A}} \times \underbrace{\begin{pmatrix} \sigma_{\text{loc}}(z_0) \\ \sigma_{\text{loc}}(z_1) \\ \sigma_{\text{loc}}(z_2) \\ ... \\ \sigma_{\text{loc}}(z_N) \end{pmatrix}}_{S_{\text{loc}}} = \underbrace{\begin{pmatrix} \sigma_{\text{int}}(z_0) \\ \sigma_{\text{int}}(z_1) \\ \sigma_{\text{int}}(z_2) \\ ... \\ \sigma_{\text{int}}(z_N) \end{pmatrix}}_{S_{\text{int}}}. \tag{9.85}$$

Since the **A**-matrix is triangular, its inversion is possible and leads to the following relation:

$$S_{\text{loc}} = \mathbf{A}^{-1} \times S_{\text{int}}. \tag{9.86}$$

The inversion of the **A**-matrix can be determined directly as follows:

$$\overbrace{\int_{z_{n-1}}^{z_n} \sigma_{\text{loc}}(z')\mathrm{d}z'}^{\text{Hypothesis : } \approx \mathrm{d}z\sigma_{\text{loc}}(z_n)} = \int_0^{z_n} \sigma_{\text{loc}}(z')\mathrm{d}z' - \int_0^{z_{n-1}} \sigma_{\text{loc}}(z')\mathrm{d}z'; \tag{9.87}$$

$$\Rightarrow \mathrm{d}z\sigma_{\text{loc}}(z_n) = n\sigma_{\text{int}}(z_n)\mathrm{d}z - (n-1)\sigma_{\text{int}}(z_{n-1})\mathrm{d}z; \tag{9.88}$$

$$\Rightarrow \sigma_{\text{loc}}(z_n) = -(n-1)\sigma_{\text{int}}(z_{n-1}) + n\sigma_{\text{int}}(z_n). \tag{9.89}$$

(Eq. 9.89) defines another system of equations:

$$\begin{cases} \sigma_{\text{loc}}(z_1) = & \sigma_{\text{int}}(z_1); \\ \sigma_{\text{loc}}(z_2) = & -\sigma_{\text{int}}(z_1) + 2\sigma_{\text{int}}(z_2); \\ \sigma_{\text{loc}}(z_3) = & -2\sigma_{\text{int}}(z_2) + 3\sigma_{\text{int}}(z_3); \\ ... & \\ \sigma_{\text{loc}}(z_N) = & -(N-1)\sigma_{\text{int}}(z_N - 1) + N\sigma_{\text{int}}(z_N). \end{cases} \tag{9.90}$$

which, in a matrix formalism, directly leads to (Eq. 9.86) with:

$$\mathbf{A}^{-1} = \begin{pmatrix} 1 & 0 & 0 & ... & 0 & 0 \\ -1 & 2 & 0 & ... & 0 & 0 \\ 0 & -2 & 3 & ... & 0 & 0 \\ ... & ... & ... & ... & ... & ... \\ 0 & 0 & 0 & ... & -(N-1) & N \end{pmatrix}. \tag{9.91}$$

.

It should be emphasized that (Eq. 9.89) shows that the local speed of sound can be found directly by knowing two successive values of the integrated speed of sound. In other words, it shows that the same inversion, *i.e.* the same matrix defined in (Eq. 9.91), can be used even if $z_0 \neq 0$.

Note that the above-mentioned inversion method relies on a very strong approximation that the integrated sound velocity at a point $c(x, z)$ depends only on the value of the local velocity $c(x, z' < z)$. More sophisticated methods can take into account the oblique trajectories and refraction phenomena of the incident and reflected waves.

7 IQ demodulation to compress the data

In ultrasound imaging, there are two main methods to capture the time dependence of the wave-field:

- either the sampling frequency is at least twice the maximum frequency of the spectral bandwidth. This mode is called RF and refers to radio-frequency signals;
- either the signal is demodulated before recording so that the spectral bandwidth is shifted towards the zero frequency [Fig. 9.14]. In this way, the sampling frequency can be drastically reduced, with a value at least equal to the spectral bandwidth. In this mode, the recorded signals are called IQ, where I stands for in-phase and Q for phase quadrature, and are directly complex values [Kirkhorn, 1999].

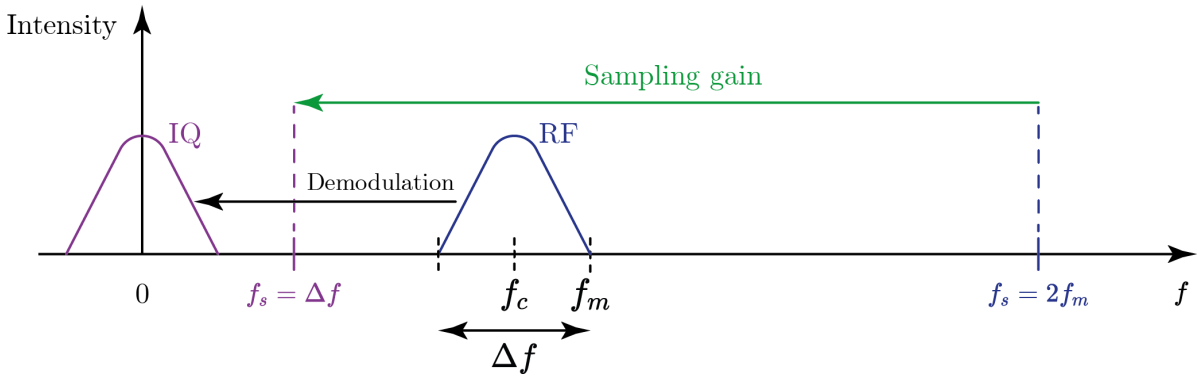

Figure 9.14: **Principle of IQ demodulation**.

8 Changing the assumed angles during beamforming

Assuming a set of N_{in} plane waves are generated by applying appropriate time delays $\Delta\tau(\theta_{\text{in}}, u_x)$ to each transducer u_x of the probe:

$$\Delta\tau(\theta_{\text{in}}, u_x) = \frac{u_x \sin(\theta_{\text{in}})}{c_{\text{acq}}}, \tag{9.92}$$

with c_{acq} the assumed speed-of-sound of the medium during the acquisition.

This set of acoustic responses is stored in a reflection matrix $\mathbf{R}_{\boldsymbol{\theta}\mathbf{u}}(t) \equiv [R(\theta_{\text{in}}, u_{\text{out}}, t)]$. Conventional *beamforming* consists in applying appropriate time-delays to focus at the same point both at the input and the output:

$$\mathcal{I}(\mathbf{r}) = \sum_{\theta_{\text{in}}^{(0)}} \sum_{u_{\text{out}}} \underbrace{A([\theta_{\text{in}}^{(0)}, u_{\text{out}}, \mathbf{r}])}_{\text{synthetic aperture}} R\left(\theta_{\text{in}}^{(0)}, u_{\text{out}}, \tau(\theta_{\text{in}}^{(0)}, \mathbf{r}, c_0) + \tau(u_{\text{out}}, \mathbf{r}, c_0)\right), \tag{9.93}$$

with $\tau(\theta, x, z)$ and $\tau(u_x, x, z)$ the cylindrical time-of-flights, A an apodization factor that limit the extent of the synthetic aperture and $\theta_{\text{in}}^{(0)}$ the assumed angles during beamforming (following Snell-Descartes law):

$$\theta_{\text{in}}^{(0)} = \arcsin\left(\frac{c_0}{c_{\text{acq}}} \sin(\theta_{\text{in}})\right), \tag{9.94}$$

with c_0 the speed-of-sound hypothesis made during beamforming.

9 Numerical simulation of a homogeneous medium

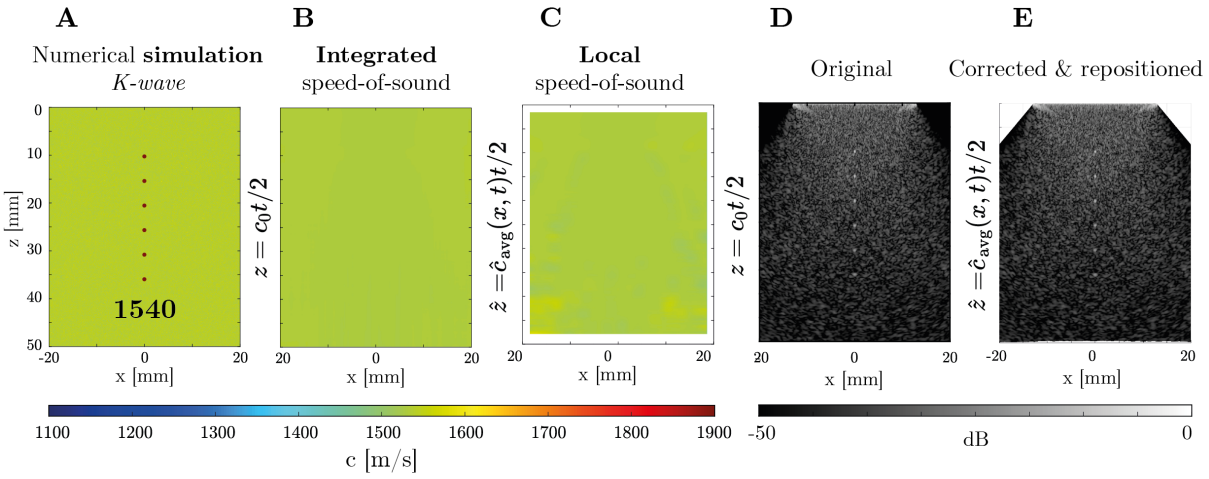

Figure 9.15: **Numerical simulation of a homogeneous medium. (A)** Speed-of-sound map simulated. **(B, C)** Integrated and local speed-of-sound estimation, respectively. **(D)** Original image. **(E)** Corrected image with each pixel reassigned to its estimated position. Numerical simulations were performed using *K-wave* software with parameters described in [Table. 6.1].

10 Uncertainty on the defocus estimation

To examine the bias of our estimator defined in (Eq. 5.17) in Chapter 5, we first decompose the RPSF evaluated at a given depth as follows:

$$|RPSF|(z) = |RPSF|(z=0) + \left(\frac{\partial^2 |RPSF|}{\partial z^2}\right)_{z=0} \frac{z^2}{2}. \tag{9.95}$$

From this equation, one can extract the incertitude of the estimation of the axial defocus:

$$\delta z = \sqrt{\frac{2\Delta|RPSF|}{\left|\frac{\partial^2|RPSF|}{\partial z^2}\right|_{z=0}}}. \tag{9.96}$$

The expression of the Gaussian beams can then be used to extract the uncertainty on our estimators:

$$|RPSF_{\text{coh}}|\text{: } \delta z^{(\text{coh})} = \frac{2z}{N_{\text{in}}^{1/4}}, \tag{9.97}$$

$$|\partial_{\Delta z} Im[RPSF_{\text{coh}}]|\text{: } \delta z^{(\text{Gouy})} = \sqrt{\frac{2}{3}}\frac{z}{N_{\text{in}}^{1/4}}, \tag{9.98}$$

where N_{in} is the number of focusing point considered for the spatial average.

11 Matrix representation

An example of restructuring a 4-dimensional matrix into a 2-dimensional matrix is shown in [Fig. 9.16].

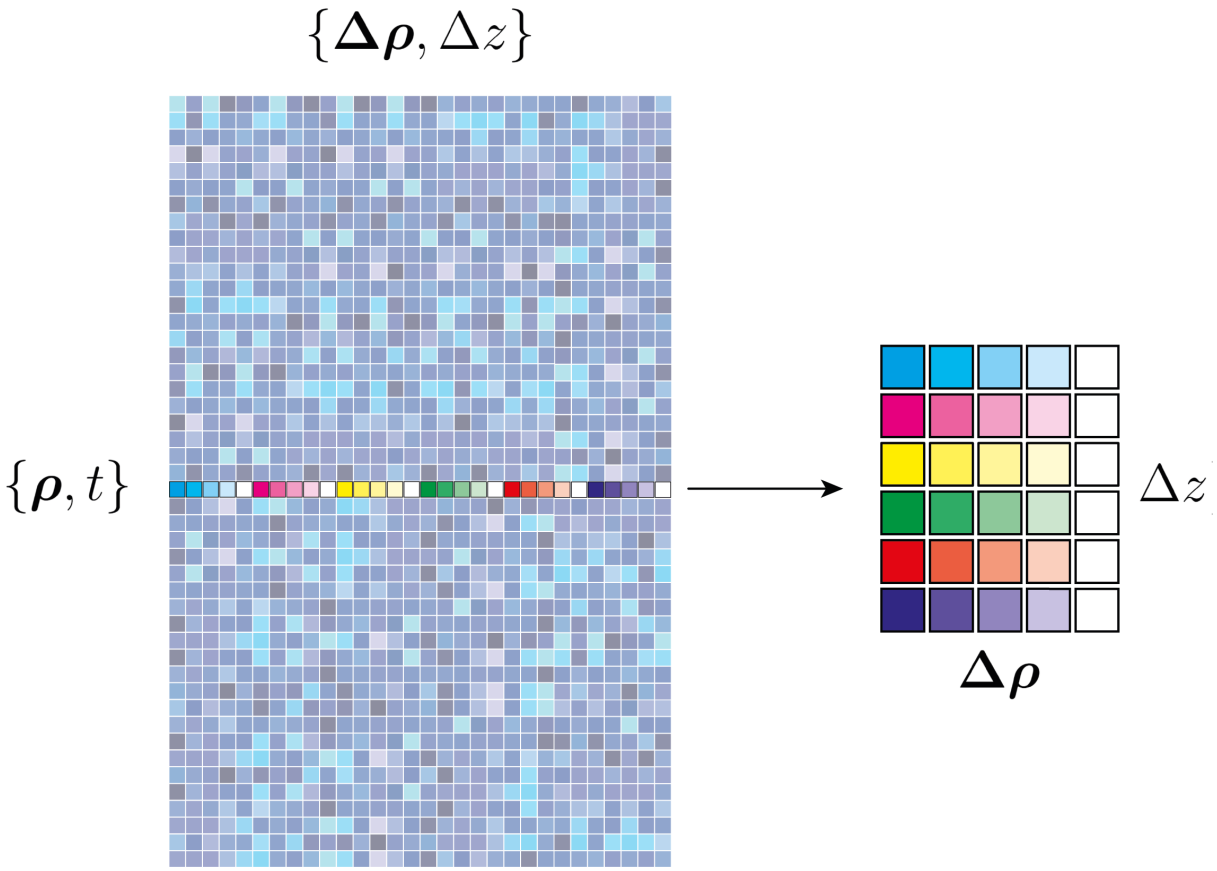

Figure 9.16: **Four-dimensional matrix representation.** A four-dimensional matrix $R_{\mathcal{D}}(\boldsymbol{\rho}, t, \boldsymbol{\Delta\rho}, \Delta z)$ is rearranged into a two-dimensional matrix $\mathbf{RPSF} = [R_{\mathcal{D}}(\{\boldsymbol{\rho}, t\}, \{\boldsymbol{\Delta\rho}, \Delta z\})]$ as given in (Chapter 5, Section 5). As shown in the colors, a line corresponds to the RPSF of a single spatio-temporal point $(\boldsymbol{\rho}, t)$ of the medium, which in turn can be rearranged in two dimensions $(\boldsymbol{\Delta\rho}, \Delta z)$ so that it can be visualized as an image.

12 Eigenvalue and Singular Value Decomposition

The relation between the singular value decomposition (SVD) of a rectangular matrix and the eigenvalue decomposition (EVD) of its left and right correlation matrices is shown in [Fig. 9.17].

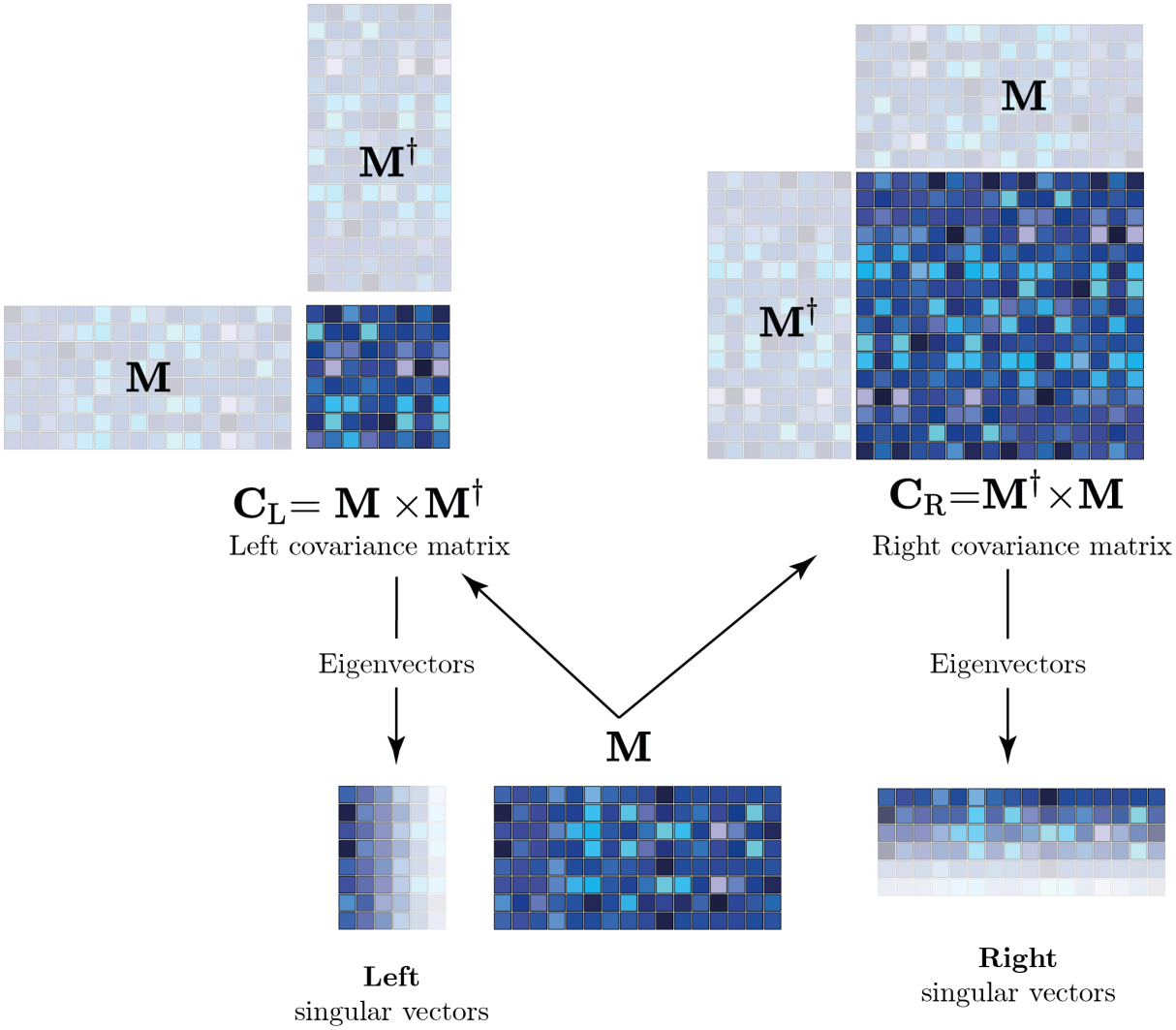

Figure 9.17: **Eigenvalue and Singular Value Decomposition.**

References

[Ali, 2022] Rehman Ali, Thurston Brevett, Dongwoon Hyun, Leandra L. Brickson, and Jeremy J. Dahl. "Distributed Aberration Correction Techniques Based on Tomographic Sound Speed Estimates". *IEEE Transactions on Ultrasonics, Ferroelectrics, and Frequency Control* 69.5 (2022), pp. 1714–1726. DOI: 10.1109/TUFFC.2022.3162836 (cit. on pp. 31, 155, 176).

[Ali, 2018] Rehman Ali, Jeremy J. Dahl, and Nick Bottenus. "Regularized Inversion Method for Frequency-Domain Recovery of the Full Synthetic Aperture Dataset from Focused Transmissions". *2018 IEEE International Ultrasonics Symposium (IUS)*. Kobe: IEEE, 2018, pp. 1–9. DOI: 10.1109/ULTSYM.2018.8580213 (cit. on p. 157).

[Ali, 2019] Rehman Ali, Scott Hsieh, and Jeremy Dahl. "Open-source Gauss-Newton-based methods for refraction-corrected ultrasound computed tomography". *Medical Imaging 2019: Ultrasonic Imaging and Tomography*. Vol. 10955. SPIE, 2019, pp. 39–52. DOI: 10.1117/12.2511319 (cit. on pp. 154, 157, 167).

[Ali, 2021] Rehman Ali, Arsenii V. Telichko, Huaijun Wang, Uday K. Sukumar, Jose G. Vilches-Moure, Ramasamy Paulmurugan, and Jeremy J. Dahl. "Local Sound Speed Estimation for Pulse-Echo Ultrasound in Layered Media". *IEEE Transactions on Ultrasonics, Ferroelectrics, and Frequency Control* (2021), pp. 1–1. DOI: 10.1109/TUFFC.2021.3124479 (cit. on pp. 106, 156).

[Anderson, 1998] Martin E. Anderson and Gregg E. Trahey. "The direct estimation of sound speed using pulse–echo ultrasound". *The Journal of the Acoustical Society of America* 104.5 (1998), pp. 3099–3106. DOI: 10.1121/1.423889 (cit. on pp. 25, 155, 156).

[Aubry, 2014] A. Aubry, L. A. Cobus, S. E. Skipetrov, B. A. van Tiggelen, A. Derode, and J. H. Page. "Recurrent Scattering and Memory Effect at the Anderson Localization Transition". *Physical Review Letters* 112.4 (2014), p. 043903. DOI: 10.1103/PhysRevLett.112.043903 (cit. on p. 43).

[Aubry, 2008a] Alexandre Aubry. "Approche matricielle de l'opérateur de propagation des ondes ultrasonores en milieu diffusant aléatoire". PhD Thesis. 2008 (cit. on pp. 42, 44, 66).

[Aubry, 2007] Alexandre Aubry and Arnaud Derode. "Ultrasonic imaging of highly scattering media from local measurements of the diffusion constant: Separation of coherent and incoherent intensities". *Physical Review E* 75.2 (2007), p. 026602. DOI: 10.1103/PhysRevE.75.026602 (cit. on p. 57).

[Aubry, 2009a] Alexandre Aubry and Arnaud Derode. "Detection and imaging in a random medium: A matrix method to overcome multiple scattering and aberration". *Journal of Applied Physics* 106.4 (2009), p. 044903. DOI: 10.1063/1.3200962 (cit. on pp. 42, 43).

[Aubry, 2009b] Alexandre Aubry and Arnaud Derode. "Random Matrix Theory Applied to Acoustic Backscattering and Imaging In Complex Media". *Physical Review Letters* 102.8 (2009), p. 084301. DOI: 10.1103/PhysRevLett.102.084301 (cit. on pp. 34, 41, 43).

[Aubry, 2011] Alexandre Aubry and Arnaud Derode. "Multiple scattering of ultrasound in weakly inhomogeneous media: application to human soft tissues". *The Journal of the Acoustical Society of America* 129.1 (2011), pp. 225–233. DOI: 10.1121/1.3506343 (cit. on p. 107).

[Aubry, 2008b] Alexandre Aubry, Arnaud Derode, and Frédéric Padilla. "Local measurements of the diffusion constant in multiple scattering media: Application to human trabecular bone imaging". *Applied Physics Letters* (2008), p. 4. DOI: https://doi.org/10.1063/1.2901379 (cit. on p. 22).

[Aubry, 2001] J.-F. Aubry, M. Tanter, J. Gerber, J.-L. Thomas, and M. Fink. "Optimal focusing by spatio-temporal inverse filter. II. Experiments. Application to focusing through absorbing and reverberating media". *The Journal of the Acoustical Society of America* 110.1 (2001), pp. 48–58. DOI: 10.1121/1.1377052 (cit. on pp. 28, 37).

[Aubry, 2003] J.-F. Aubry, M. Tanter, M. Pernot, J.-L. Thomas, and M. Fink. "Experimental demonstration of noninvasive transskull adaptive focusing based on prior computed tomography scans". *The Journal of the Acoustical Society of America* 113.1 (2003), pp. 84–93. DOI: 10.1121/1.1529663 (cit. on pp. 28, 46, 98).

[Augustin, 2021] Xenia Augustin, Lin Zhang, and Orcun Goksel. *Estimating Mean Speed-of-Sound from Sequence-Dependent Geometric Disparities*. 2021. DOI: 10.1109/IUS52206.2021.9593742 (cit. on pp. 31, 155).

[Austeng, 2002] Andreas Austeng and Sverre Holm. "Sparse 2-D arrays for 3-D phased array imaging–design methods". *IEEE transactions on ultrasonics, ferroelectrics, and frequency control* 49.8 (2002), pp. 1073–1086. DOI: 10.1109/tuffc.2002.1026019 (cit. on p. 70).

[Babcock, 1953] H. W. Babcock. "The possibility of compensating astronomical seeing". *Publications of the Astronomical Society of the Pacific* 65.386 (1953), pp. 229–236. DOI: 10.1086/126606 (cit. on pp. 27, 29).

[Badon, 2020] Amaury Badon, Victor Barolle, Kristina Irsch, A. Claude Boccara, Mathias Fink, and Alexandre Aubry. "Distortion matrix concept for deep optical imaging in scattering media". *Science Advances* (2020). DOI: 10.1126/sciadv.aay7170 (cit. on pp. 34, 49, 58, 59, 69, 177).

[Badon, 2016] Amaury Badon, Dayan Li, Geoffroy Lerosey, A Claude Boccara, Mathias Fink, and Alexandre Aubry. "Smart optical coherence tomography for ultra-deep imaging through highly scattering media". *Science Advances* (2016), p. 9. DOI: 10.1126/sciadv.1600370 (cit. on p. 34).

[Balondrade, 2023] Paul Balondrade, Victor Barolle, Nicolas Guigui, Emeric Auriant, Nathan Rougier, Claude Boccara, Mathias Fink, and Alexandre Aubry. *Multi-Spectral Reflection Matrix for Ultra-Fast 3D Label-Free Microscopy*. 2023. DOI: https://doi.org/10.48550/arXiv.2309.10951 (cit. on pp. 49, 177).

[Bamber, 2005] J. C. Bamber. "Attenuation and Absorption". *Physical Principles of Medical Ultrasonics*. Ed. by C. R. Hill, J. C. Bamber, and Gail R. Ter Haar. Chichester, UK: John Wiley & Sons, Ltd, 2005, pp. 93–166. DOI: 10.1002/0470093978.ch4 (cit. on p. 22).

[Bamber, 1979] J. C. Bamber and C. R. Hill. "Ultrasonic attenuation and propagation speed in mammalian tissues as a function of temperature". *Ultrasound in Medicine & Biology* 5.2 (1979), pp. 149–157. DOI: 10.1016/0301-5629(79)90083-8 (cit. on pp. 31, 154).

[Bamber, 1981] J.C. Bamber and C.R. Hill. "Acoustic properties of normal and cancerous human liver—I. Dependence on pathological condition". *Ultrasound in Medicine & Biology* 7.2 (1981), pp. 121–133. DOI: 10.1016/0301-5629(81)90001-6 (cit. on p. 154).

[Banjavic, 1978] R. A. Banjavic, J. A. Zagzebski, E. L. Madsen, and R. E. Jutila. "Ultrasonic Beam Sensitivity Profile Changes in Mammalian Tissue". *Ultrasound in Medicine: Volume 4*. Ed. by Denis White and E. A. Lyons. Boston, MA: Springer US, 1978, pp. 515–518. DOI: 10.1007/978-1-4613-4021-8_117 (cit. on p. 22).

[Baranger, 2018] Jerome Baranger, Bastien Arnal, Fabienne Perren, Olivier Baud, Mickael Tanter, and Charlie Demene. "Adaptive Spatiotemporal SVD Clutter Filtering for Ultrafast Doppler Imaging Using Similarity of Spatial Singular Vectors". *IEEE Transactions on Medical Imaging* 37.7 (2018), pp. 1574–1586. DOI: 10.1109/TMI.2018.2789499 (cit. on pp. 21, 125).

[Barolle, 2021] Victor Barolle, Victor Barolle, Jules Scholler, Jules Scholler, Pedro Mecê, Jean-Marie Chassot, Kassandra Groux, Mathias Fink, A. Claude Boccara, and Alexandre Aubry. "Manifestation of aberrations in full-field optical coherence tomography". *Optics Express* 29.14 (2021), pp. 22044–22065. DOI: 10.1364/OE.419963 (cit. on pp. 58, 177).

[Beenakker, 1997] C. W. J. Beenakker. "Random-matrix theory of quantum transport". *Reviews of Modern Physics* 69.3 (1997), pp. 731–808. DOI: 10.1103/RevModPhys.69.731 (cit. on pp. 34, 35).

[Bendjador, 2020] Hanna Bendjador, Thomas Deffieux, and Mickaël Tanter. "The SVD Beamformer: Physical Principles and Application to Ultrafast Adaptive Ultrasound". *IEEE Transactions on Medical Imaging* 39.10 (2020), pp. 3100–3112. DOI: 10.1109/TMI.2020.2986830 (cit. on pp. xiii, 61, 63, 69).

[Benjamin, 2018] Alex Benjamin, Rebecca E. Zubajlo, Manish Dhyani, Anthony E. Samir, Kai E. Thomenius, Joseph R. Grajo, and Brian W. Anthony. "A Novel Approach to the Quantification of the Longitudinal Speed of Sound and its Potential for Tissue Characterization (Part - I)". *Ultrasound in medicine & biology* 44.12 (2018), pp. 2739–2748. DOI: 10.1016/j.ultrasmedbio.2018.07.021 (cit. on p. 156).

[Bercoff, 2011] J Bercoff, G Montaldo, T Loupas, D Savery, Fabien Mézière, M Fink, and M Tanter. "Ultrafast compound doppler imaging: providing full blood flow characterization". *IEEE Transactions on Ultrasonics, Ferroelectrics and Frequency Control* 58.1 (2011), pp. 134–147. DOI: 10.1109/TUFFC.2011.1780 (cit. on p. 17).

[Bercoff, 2003] J. Bercoff, S. Chaffai, M. Tanter, L. Sandrin, S. Catheline, M. Fink, J.L. Gennisson, and M. Meunier. "In vivo breast tumor detection using transient elastography". *Ultrasound in Medicine & Biology* 29.10 (2003), pp. 1387–1396. DOI: 10.1016/S0301-5629(03)00978-5 (cit. on pp. 17, 46).

[Bercoff, 2004] Jeremy Bercoff, Mickaël Tanter, and Mathias Fink. "Supersonic Shear Imaging: a new technique for soft tissue elasticity mapping". *IEEE transactions on ultrasonics, ferroelectrics, and frequency control* 51 (2004), pp. 396–409. DOI: 10.1109/TUFFC.2004.1295425 (cit. on pp. 17, 46, 154).

[Bertolo, 2021] Adrien Bertolo, Mohamed Nouhoum, Silvia Cazzanelli, Jeremy Ferrier, Jean-Charles Mariani, Andrea Kliewer, Benoit Belliard, Bruno-Félix Osmanski, Thomas Deffieux, Sophie Pezet, Zsolt Lenkei, and Mickaël Tanter. "Whole-Brain 3D Activation and Functional Connectivity Mapping in Mice using Transcranial Functional Ultrasound Imaging". *Journal of Visualized Experiments* (2021). DOI: 10.3791/62267 (cit. on pp. 106, 111).

[Betzig, 2006] Eric Betzig, George H. Patterson, Rachid Sougrat, O. Wolf Lindwasser, Scott Olenych, Juan S. Bonifacino, Michael W. Davidson, Jennifer Lippincott-Schwartz, and Harald F. Hess. "Imaging intracellular fluorescent proteins at nanometer resolution". *Science (New York, N.Y.)* 313.5793 (2006), pp. 1642–1645. DOI: 10.1126/science.1127344 (cit. on pp. 110, 111).

[Beuret, 2020] Samuel Beuret, Dimitris Perdios, and Jean-Philippe Thiran. "Refraction-Aware Integral Operator for Speed-of-Sound Pulse-Echo Imaging". *2020 IEEE International Ultrasonics Symposium (IUS)*. 2020, pp. 1–4. DOI: 10.1109/IUS46767.2020.9251601 (cit. on p. 157).

[Bjaerum, 2002] S. Bjaerum, H. Torp, and K. Kristoffersen. "Clutter filter design for ultrasound color flow imaging". *IEEE Transactions on Ultrasonics, Ferroelectrics and Frequency Control* 49.2 (2002), pp. 204–216. DOI: 10.1109/58.985705 (cit. on p. 20).

[Blaak, 2009] S. Blaak, Z. Yu, G.C.M. Meijer, C. Prins, C.T. Lancée, J.G. Bosch, and N. de Jong. "Design of a micro-beamformer for a 2D piezoelectric ultrasound transducer". *2009 IEEE International Ultrasonics Symposium*. 2009, pp. 1338–1341. DOI: 10.1109/ULTSYM.2009.5441534 (cit. on p. 70).

[Blondel, 2018] Thibaud Blondel, Julien Chaput, Arnaud Derode, Michel Campillo, and Alexandre Aubry. "Matrix Approach of Seismic Imaging: Application to the Erebus Volcano, Antarctica". *Journal of Geophysical Research : Solid Earth* 123.12 (2018), pp. 10, 936–10, 950. DOI: 10.1029/2018jb016361 (cit. on pp. 34, 49, 69, 177).

[Borcea, 2022a] Liliana Borcea, Josselin Garnier, Alexander V. Mamonov, and Jörn Zimmerling. *Waveform inversion via reduced order modeling*. 2022. DOI: https://doi.org/10.48550/arXiv.2202.01824 (cit. on p. 176).

[Borcea, 2022b] Liliana Borcea, Josselin Garnier, Alexander V. Mamonov, and Jörn Zimmerling. *Waveform inversion with a data driven estimate of the internal wave*. 2022. DOI: https://doi.org/10.48550/arXiv.2208.11051 (cit. on p. 176).

[Borcea, 2023] Liliana Borcea, Josselin Garnier, Alexander V. Mamonov, and Jörn Zimmerling. *When data driven reduced order modeling meets full waveform inversion*. 2023. DOI: https://doi.org/10.48550/arXiv.2302.05988 (cit. on p. 176).

[Born, 1926] Max Born. "Quantenmechanik der Stoßvorgänge". *Zeitschrift für Physik* 38.11 (1926), pp. 803–827. DOI: 10.1007/BF01397184 (cit. on pp. 22, 39).

[Bruneel, 1977] C. Bruneel, R. Torguet, K. M. Rouvaen, E. Bridoux, and B. Nongaillard. "Ultrafast echotomographic system using optical processing of ultrasonic signals". *Applied Physics Letters* 30.8 (1977), pp. 371–373. DOI: 10.1063/1.89436 (cit. on pp. 12, 17).

[Brütt, 2022] Cécile Brütt, Alexandre Aubry, Benoît Gérardin, Arnaud Derode, and Claire Prada. "Weight of single and recurrent scattering in the reflection matrix of complex media". *Physical Review E* 106.2 (2022), p. 025001. DOI: 10.1103/PhysRevE.106.025001 (cit. on pp. 39, 43, 49, 107).

[Byram, 2012] Brett C. Byram, Gregg E. Trahey, and Jørgen A. Jensen. "A Method for Direct Localized Sound Speed Estimates Using Registered Virtual Detectors". *Ultrasonic imaging* 34.3 (2012), pp. 159–180. DOI: 10.1177/0161734612455576 (cit. on p. 156).

[Campillo, 2003] Michel Campillo and Anne Paul. "Long-Range Correlations in the Diffuse Seismic Coda". *Science* 299.5606 (2003), pp. 547–549. DOI: 10.1126/science.1078551 (cit. on p. 38).

[Carpenter, 1977] D. Carpenter, G. Kossoff, W. J. Garrett, K. Daniel, and P. Boele. "The UI Octoson — A New Class of Ultrasonic Echoscope". *Australasian Radiology* 21.1 (1977), pp. 85–89. DOI: 10.1111/j.1440-1673.1977.tb02948.x (cit. on p. 155).

[Céspedes, 1992] Ignacio Céspedes, Jonathan Ophir, and Yijun Huang. "On the feasibility of pulse-echo speed of sound estimation in small regions: Simulation studies". *Ultrasound in Medicine & Biology* 18.3 (1992), pp. 283–291. DOI: 10.1016/0301-5629(92)90097-T (cit. on p. 155).

[Chaput, 2012] J. A. Chaput, D. Zandomeneghi, R. C. Aster, H. Knox, and P. R. Kyle. "Imaging of Erebus volcano using body wave seismic interferometry of Strombolian eruption coda". *Geophysical Research Letters* 39.7 (2012). DOI: 10.1029/2012GL050956 (cit. on p. 38).

[Chau, 2019] Gustavo Chau, Marko Jakovljevic, Roberto Lavarello, and Jeremy Dahl. "A Locally Adaptive Phase Aberration Correction (LAPAC) Method for Synthetic Aperture Sequences". *Ultrasonic Imaging* 41.1 (2019), pp. 3–16. DOI: 10.1177/0161734618796556 (cit. on pp. xiii, 30).

[Chavignon, 2022] Arthur Chavignon, Vincent Hingot, Cyrille Orset, Denis Vivien, and Olivier Couture. "3D transcranial ultrasound localization microscopy for discrimination between ischemic and hemorrhagic stroke in early phase". *Scientific Reports* 12.1 (2022), pp. 1–11. DOI: 10.1038/s41598-022-18025-x (cit. on pp. 106, 113, 122).

[Chen, 1987] C.F. Chen, D.E. Robinson, L.S. Wilson, K.A. Griffiths, A. Manoharan, and B.D. Doust. "Clinical Sound Speed Measurement in Liver and Spleen in Vivo". *Ultrasonic Imaging* 9.4 (1987), pp. 221–235. DOI: 10.1177/016173468700900401 (cit. on p. 154).

[Cho, 2009] M. H. Cho, L. H. Kang, J. S. Kim, and S. Y. Lee. "An efficient sound speed estimation method to enhance image resolution in ultrasound imaging". *Ultrasonics* 49.8 (2009), pp. 774–778. DOI: 10.1016/j.ultras.2009.06.005 (cit. on p. 156).

[Čižmár, 2012] Tomáš Čižmár and Kishan Dholakia. "Exploiting multimode waveguides for pure fibre-based imaging". *Nature Communications* 3.1 (2012), p. 1027. DOI: 10.1038/ncomms2024 (cit. on p. 34).

[Clement, 2004] G. T. Clement, P. J. White, and K. Hynynen. "Enhanced ultrasound transmission through the human skull using shear mode conversion". *The Journal of the Acoustical Society of America* 115.3 (2004), pp. 1356–1364. DOI: 10.1121/1.1645610 (cit. on p. 98).

[Colombi, 2014] Andrea Colombi, Lapo Boschi, Philippe Roux, and Michel Campillo. "Green's function retrieval through cross-correlations in a two-dimensional complex reverberating medium". *The Journal of the Acoustical Society of America* 135.3 (2014), pp. 1034–1043. DOI: 10.1121/1.4864485 (cit. on p. 38).

[Coudert, 2023] Antoine Coudert. "Développement de la microscopie de localisation ultrasonore (ULM) volumétrique et transcrânienne adaptée pour l'humain". PhD thesis. 2023 (cit. on pp. 111, 113).

[Couture, 2012] O. Couture, M. Fink, and M. Tanter. "Ultrasound contrast plane wave imaging". *IEEE Transactions on Ultrasonics, Ferroelectrics and Frequency Control* 59.12 (2012), p. 6373790. DOI: 10.1109/TUFFC.2012.2508 (cit. on p. 17).

[Couture, 2009] Olivier Couture, Souad Bannouf, Gabriel Montaldo, Jean-François Aubry, Mathias Fink, and Mickael Tanter. "Ultrafast Imaging of Ultrasound Contrast Agents". *Ultrasound in Medicine & Biology* 35.11 (2009), pp. 1908–1916. DOI: 10.1016/j.ultrasmedbio.2009.05.020 (cit. on p. 17).

[Couture, 2011] Olivier Couture, Estelle Dransart, Sabrina Dehay, Fariba Nemati, Didier Decaudin, Ludger Johannes, and Mickael Tanter. "Tumor Delivery of Ultrasound Contrast Agents Using Shiga Toxin B Subunit". *Molecular Imaging* 10.2 (2011), p. 7290.2010.00030. DOI: 10.2310/7290.2010.00030 (cit. on p. 17).

[Couture, 2018] Olivier Couture, Vincent Hingot, Baptiste Heiles, Pauline Muleki-Seya, and Mickael Tanter. "Ultrasound Localization Microscopy and Super-Resolution: A State of the Art". *IEEE Transactions on Ultrasonics, Ferroelectrics, and Frequency Control* 65.8 (2018), pp. 1304–1320. DOI: 10.1109/TUFFC.2018.2850811 (cit. on p. 112).

[Dabrowski, 2001] W. Dabrowski, J. Dunmore-Buyze, H. N. Cardinal, and A. Fenster. "A real vessel phantom for flow imaging: 3-D Doppler ultrasound of steady flow". *Ultrasound in Medicine & Biology* 27.1 (2001), pp. 135–141. DOI: 10.1016/s0301-5629(00)00277-5 (cit. on p. 70).

[Dahl, 2005] J.J. Dahl, M.S. Soo, and G.E. Trahey. "Spatial and temporal aberrator stability for real-time adaptive imaging". *IEEE Transactions on Ultrasonics, Ferroelectrics, and Frequency Control* 52.9 (2005), pp. 1504–1517. DOI: 10.1109/TUFFC.2005.1516023 (cit. on pp. 29, 102).

[Dasarathy, 2009] Srinivasan Dasarathy, Jaividhya Dasarathy, Amer Khiyami, Rajesh Joseph, Rocio Lopez, and Arthur J. McCullough. "Validity of real time ultrasound in the diagnosis of hepatic steatosis: A prospective study". *Journal of Hepatology* 51.6 (2009), pp. 1061–1067. DOI: 10.1016/j.jhep.2009.09.001 (cit. on p. 171).

[Davidsen, 1993] R.E. Davidsen and S.W. Smith. "Sparse geometries for two-dimensional array transducers in volumetric imaging". *1993 Proceedings IEEE Ultrasonics Symposium*. Baltimore, MD, USA: IEEE, 1993, 1091–1094 vol.2. DOI: 10.1109/ULTSYM.1993.339598 (cit. on p. 70).

[Davros, 1985] W J Davros, E L Madsen, and J A Zagzebski. "Breast mass detection by US: a phantom study." *Radiology* 156.3 (1985), pp. 773–775. DOI: 10.1148/radiology.156.3.3895293 (cit. on p. 25).

[Deffieux, 2018] Thomas Deffieux, Charlie Demene, Mathieu Pernot, and Mickael Tanter. "Functional ultrasound neuroimaging: a review of the preclinical and clinical state of the art". *Current Opinion in Neurobiology.* Neurotechnologies 50 (2018), pp. 128–135. DOI: 10.1016/j.conb.2018.02.001 (cit. on p. 111).

[Delabays, 1995] A. Delabays, N. G. Pandian, Q. L. Cao, L. Sugeng, G. Marx, A. Ludomirski, and S. L. Schwartz. "Transthoracic real-time three-dimensional echocardiography using a fan-like scanning approach for data acquisition: methods, strengths, problems, and initial clinical experience". *Echocardiography (Mount Kisco, N.Y.)* 12.1 (1995), pp. 49–59. DOI: 10.1111/j.1540-8175.1995.tb00521.x (cit. on p. 70).

[Delannoy, 1979] B. Delannoy, R. Torguet, C. Bruneel, E. Bridoux, J. M. Rouvaen, and H. Lasota. "Acoustical image reconstruction in parallel-processing analog electronic systems". *Journal of Applied Physics* 50.5 (1979), pp. 3153–3159. DOI: 10.1063/1.326397 (cit. on p. 17).

[Demene, 2015] Charlie Demene, Thomas Deffieux, Mathieu Pernot, Bruno-Felix Osmanski, Valerie Biran, Jean-Luc Gennisson, Lim-Anna Sieu, Antoine Bergel, Stephanie Franqui, Jean-Michel Correas, Ivan Cohen, Olivier Baud, and Mickael Tanter. "Spatiotemporal Clutter Filtering of Ultrafast Ultrasound Data Highly Increases Doppler and fUltrasound Sensitivity". *IEEE Transactions on Medical Imaging* 34.11 (2015), pp. 2271–2285. DOI: 10.1109/TMI.2015.2428634 (cit. on pp. 20, 125).

[Demené, 2017] Charlie Demené, Jérome Baranger, Miguel Bernal, Catherine Delanoe, Stéphane Auvin, Valerie Biran, Marianne Alison, Jérôme Mairesse, Elisabeth Harribaud, Mathieu Pernot, Mickaël Tanter, and Olivier Baud. "Functional ultrasound imaging of brain activity in human newborns". *Science Translational Medicine* 9 (2017), eaah6756. DOI: 10.1126/scitranslmed.aah6756 (cit. on p. 111).

[Demené, 2014] Charlie Demené, Mathieu Pernot, Valérie Biran, Marianne Alison, Mathias Fink, Olivier Baud, and Mickaël Tanter. "Ultrafast Doppler Reveals the Mapping of Cerebral Vascular Resistivity in Neonates". *Journal of Cerebral Blood Flow & Metabolism* 34.6 (2014), pp. 1009–1017. DOI: 10.1038/jcbfm.2014.49 (cit. on p. 21).

[Demené, 2021] Charlie Demené, Justine Robin, Alexandre Dizeux, Baptiste Heiles, Mathieu Pernot, Mickael Tanter, and Fabienne Perren. "Transcranial ultrafast ultrasound localization microscopy of brain vasculature in patients". *Nature Biomedical Engineering* 5.3 (2021), pp. 219–228. DOI: 10.1038/s41551-021-00697-x (cit. on pp. 98, 106, 110, 112, 113).

[Demeulenaere, 2022] Oscar Demeulenaere, Zulma Sandoval, Philippe Mateo, Alexandre Dizeux, Olivier Villemain, Romain Gallet, Bijan Ghaleh, Thomas Deffieux, Charlie Deméné, Mickael Tanter, Clément Papadacci, and Mathieu Pernot. "Coronary Flow Assessment Using 3-Dimensional Ultrafast Ultrasound Localization Microscopy." *JACC. Cardiovascular imaging* 15.7 (2022), pp. 1193–1208. DOI: 10.1016/j.jcmg.2022.02.008 (cit. on pp. 110, 112, 113).

[Dennison, 1953] A. T. Dennison. "THE DESIGN OF ELECTROMAGNETIC GEOPHONES*". *Geophysical Prospecting* 1.1 (1953), pp. 3–28. DOI: 10.1111/j.1365-2478.1953.tb01128.x (cit. on p. 34).

[Derode, 2003a] Arnaud Derode, Eric Larose, Mickael Tanter, Julien de Rosny, Arnaud Tourin, Michel Campillo, and Mathias Fink. "Recovering the Green's function from field-field correlations in an open scattering medium (L)". *The Journal of the Acoustical Society of America* 113.6 (2003), p. 2973. DOI: 10.1121/1.1570436 (cit. on p. 38).

[Derode, 1995] Arnaud Derode, Philippe Roux, and Mathias Fink. "Robust Acoustic Time Reversal with High-Order Multiple Scattering". *Physical Review Letters* 75.23 (1995), pp. 4206–4209. DOI: 10.1103/PhysRevLett.75.4206 (cit. on p. 175).

[Derode, 2003b] Arnaud Derode, Arnaud Tourin, Julien De Rosny, Mickaël Tanter, Sylvain Yon, and Mathias Fink. "Taking Advantage of Multiple Scattering to Communicate with Time-Reversal Antennas". *Physical Review Letters* 90.1 (2003), p. 014301. DOI: 10.1103/PhysRevLett.90.014301 (cit. on pp. 34, 35).

[Desailly, 2015] Yann Desailly, Juliette Pierre, Olivier Couture, and Mickael Tanter. "Resolution limits of ultrafast ultrasound localization microscopy". *Physics in Medicine and Biology* 60.22 (2015), pp. 8723–8740. DOI: 10.1088/0031-9155/60/22/8723 (cit. on p. 111).

[Diamantis, 2018] Konstantinos Diamantis, Alan H. Greenaway, Tom Anderson, Jorgen Arendt Jensen, Paul A. Dalgarno, and Vassilis Sboros. "Super-Resolution Axial Localization of Ultrasound Scatter Using Multi-Focal Imaging". *IEEE Transactions on Biomedical Engineering* 65.8 (2018), pp. 1840–1851. DOI: 10.1109/TBME.2017.2769164 (cit. on p. 133).

[Diarra, 2013] Bakary Diarra, Marc Robini, Piero Tortoli, Christian Cachard, and Herve Liebgott. "Design of Optimal 2-D Nongrid Sparse Arrays for Medical Ultrasound". *IEEE Transactions on Biomedical Engineering* 60.11 (2013), pp. 3093–3102. DOI: 10.1109/TBME.2013.2267742 (cit. on p. 70).

[Dioguardi Burgio, 2019] Marco Dioguardi Burgio, Marion Imbault, Maxime Ronot, Alex Faccinetto, Bernard E. Van Beers, Pierre-Emmanuel Rautou, Laurent Castera, Jean-Luc Gennisson, Mickael Tanter, and Valérie Vilgrain. "Ultrasonic Adaptive Sound Speed Estimation for the Diagnosis and Quantification of Hepatic Steatosis: A Pilot Study". *Ultraschall in der Medizin - European Journal of Ultrasound* 40.06 (2019), pp. 722–733. DOI: 10.1055/a-0660-9465 (cit. on pp. 31, 154, 156).

[Dorokhov, 1984] O.N. Dorokhov. "On the coexistence of localized and extended electronic states in the metallic phase". *Solid State Communications* 51.6 (1984), pp. 381–384. DOI: 10.1016/0038-1098(84)90117-0 (cit. on p. 35).

[Downey, 1996] D. B. Downey, D. A. Nicolle, M. F. Levin, and A. Fenster. "Three-dimensional ultrasound imaging of the eye". *Eye (London, England)* 10 (Pt 1) (1996), pp. 75–81. DOI: 10.1038/eye.1996.11 (cit. on p. 70).

[Duck, 1990] Francis A. Duck. "Acoustic Properties of Tissue at Ultrasonic Frequencies". *Physical Properties of Tissues*. Elsevier, 1990, pp. 73–135. DOI: 10.1016/B978-0-12-222800-1.50008-5 (cit. on pp. 6, 22, 154).

[Duric, 2007] Nebojsa Duric, Peter Littrup, Lou Poulo, Alex Babkin, Roman Pevzner, Earle Holsapple, Olsi Rama, and Carri Glide. "Detection of breast cancer with ultrasound tomography: First results with the Computed Ultrasound Risk Evaluation (CURE) prototype". *Medical Physics* 34.2 (2007), pp. 773–785. DOI: 10.1118/1.2432161 (cit. on p. 154).

[Dussik, 1942] Karl Dussik. "Uber die Möglichkeit, hochfrequente mechanische Sehwingungen als diagnostisehes Hilfsmittel zu verwertenl." *Gesellschaft für Neurol. und Psychiatr.* (1942). DOI: https://doi.org/10.1007/BF02877929 (cit. on p. 3).

[Ekroll, 2013] Ingvild Kinn Ekroll, Abigail Swillens, Patrick Segers, Torbjorn Dahl, Hans Torp, and Lasse Lovstakken. "Simultaneous quantification of flow and tissue velocities based on multi-angle plane wave imaging". *IEEE Transactions on Ultrasonics, Ferroelectrics, and Frequency Control* 60.4 (2013), pp. 727–738. DOI: 10.1109/TUFFC.2013.2621 (cit. on p. 17).

[Errico, 2015] Claudia Errico, Juliette Pierre, Sophie Pezet, Yann Desailly, Zsolt Lenkei, Olivier Couture, and Mickael Tanter. "Ultrafast ultrasound localization microscopy for deep super-resolution vascular imaging". *Nature* 527.7579 (2015), pp. 499–502. DOI: 10.1038/nature16066 (cit. on pp. 20, 110–112).

[Fairbank, 1977] William M. Fairbank and Marlan O. Scully. "A New Noninvasive Technique for Cardiac Pressure Measurement: Resonant Scattering of Ultrasound from Bubbles". *IEEE Transactions on Biomedical Engineering* BME-24.2 (1977), pp. 107–110. DOI: 10.1109/TBME.1977.326112 (cit. on pp. 110, 123, 129).

[Fatemi, 2019] Ali Fatemi, Erik Andreas Rye Berg, and Alfonso Rodriguez-Molares. "Studying the Origin of Reverberation Clutter in Echocardiography: In Vitro Experiments and In Vivo Demonstrations". *Ultrasound in Medicine & Biology* 45.7 (2019), pp. 1799–1813. DOI: 10.1016/j.ultrasmedbio.2019.01.010 (cit. on p. 22).

[Favre, 2022] Hugues Favre, Mathieu Pernot, Mickael Tanter, and Clément Papadacci. "Boosting transducer matrix sensitivity for 3D large field ultrasound localization microscopy using a multi-lens diffracting layer: a simulation study". *Physics in Medicine & Biology* 67.8 (2022), p. 085009. DOI: 10.1088/1361-6560/ac5f72 (cit. on p. 122).

[Favre, 2023] Hugues Favre, Mathieu Pernot, Mickael Tanter, and Clément Papadacci. "Transcranial 3D ultrasound localization microscopy using a large element matrix array with a multi-lens diffracting layer: an in vitro study". *Physics in Medicine & Biology* 68.7 (2023), p. 075003. DOI: 10.1088/1361-6560/acbde3 (cit. on p. 122).

[Feigin, 2020] Micha Feigin, Daniel Freedman, and Brian W. Anthony. "A Deep Learning Framework for Single-Sided Sound Speed Inversion in Medical Ultrasound". *IEEE Transactions on Biomedical Engineering* 67.4 (2020), pp. 1142–1151. DOI: 10.1109/TBME.2019.2931195 (cit. on p. 157).

[Feng, 1988] Shechao Feng, Charles Kane, Patrick A. Lee, and A. Douglas Stone. "Correlations and Fluctuations of Coherent Wave Transmission through Disordered Media". *Physical Review Letters* 61.7 (1988), pp. 834–837. DOI: 10.1103/PhysRevLett.61.834 (cit. on p. 43).

[Feng, 2001] Simin Feng and Herbert G. Winful. "Physical origin of the Gouy phase shift". *Optics Letters* 26.8 (2001), p. 485. DOI: 10.1364/OL.26.000485 (cit. on pp. 133, 162).

[Fernandez, 2003] A.T. Fernandez, K.L. Gammelmark, J.J. Dahl, C.G. Keen, R.C. Gauss, and G.E. Trahey. "Synthetic elevation beamforming and image acquisition capabilities using an 8 /spl times/ 128 1.75D array". *IEEE Transactions on Ultrasonics, Ferroelectrics, and Frequency Control* 50.1 (2003), pp. 40–57. DOI: 10.1109/TUFFC.2003.1176524 (cit. on p. 70).

[Fink, 1992] Mathias Fink. "Time reversal of ultrasonic fields. I. Basic principles". *IEEE Transactions on Ultrasonics, Ferroelectrics, and Frequency Control* 39.5 (1992), pp. 555–566. DOI: 10.1109/58.156174 (cit. on pp. 9, 27).

[Fink, 1997] Mathias Fink and Christian Dorme. "Aberration correction in ultrasonic medical imaging with time-reversal techniques". *International Journal of Imaging Systems and Technology* 8.1 (1997), pp. 110–125. DOI: 10.1002/(SICI)1098-1098(1997)8:1<110::AID-IMA13>3.0.CO;2-6 (cit. on p. 29).

[Flax, 1988] S.W. Flax and M. O'Donnell. "Phase-aberration correction using signals from point reflectors and diffuse scatterers: basic principles". *IEEE Transactions on Ultrasonics, Ferroelectrics, and Frequency Control* 35.6 (1988), pp. 758–767. DOI: 10.1109/58.9333 (cit. on p. 27).

[Flesch, 2017] M Flesch, M Pernot, J Provost, G Ferin, A Nguyen-Dinh, M Tanter, and T Deffieux. "4D in vivo ultrafast ultrasound imaging using a row-column addressed matrix and coherently-compounded orthogonal plane waves". *Physics in Medicine and Biology* 62.11 (2017), pp. 4571–4588. DOI: 10.1088/1361-6560/aa63d9 (cit. on p. 70).

[Foschini, 1998] G.J. Foschini and M.J. Gans. "On Limits of Wireless Communications in a Fading Environment when Using Multiple Antennas". *Wireless Personal Communications* 6.3 (1998), pp. 311–335. DOI: 10.1023/A:1008889222784 (cit. on pp. 34, 35).

[Foster, 1979] F.Stuart Foster and John W. Hunt. "Transmission of ultrasound beams through human tissue—focussing and attenuation studies". *Ultrasound in Medicine & Biology* 5.3 (1979), pp. 257–268. DOI: 10.1016/0301-5629(79)90017-6 (cit. on p. 22).

[Freiburger, 1992] P. D. Freiburger, D. C. Sullivan, B. H. LeBlanc, S. W. Smith, and G. E. Trahey. "Two dimensional ultrasonic beam distortion in the breast: in vivo measurements and effects". *Ultrasonic Imaging* 14.4 (1992), pp. 398–414. DOI: 10.1177/016173469201400406 (cit. on p. 25).

[Freund, 1988] Isaac Freund, Michael Rosenbluh, and Shechao Feng. "Memory Effects in Propagation of Optical Waves through Disordered Media". *Physical Review Letters* 61.20 (1988), pp. 2328–2331. DOI: 10.1103/PhysRevLett.61.2328 (cit. on p. 43).

[Fry, 1978] F. J. Fry and J. E. Barger. "Acoustical properties of the human skull". *The Journal of the Acoustical Society of America* 63.5 (1978), pp. 1576–1590. DOI: 10.1121/1.381852 (cit. on p. 6).

[Fung, 1993] Yuan-Cheng Fung. *Biomechanics*. New York, NY: Springer, 1993. DOI: 10.1007/978-1-4757-2257-4 (cit. on p. 154).

[Gauss, 1997] R.C. Gauss, M.S. Soo, and G.E. Trahey. "Wavefront distortion measurements in the human breast". *1997 IEEE Ultrasonics Symposium Proceedings. An International Symposium (Cat. No.97CH36118)*. Vol. 2. 1997, 1547–1551 vol.2. DOI: 10.1109/ULTSYM.1997.663290 (cit. on p. 25).

[Gauss, 2001] Roderick C. Gauss, Gregg E. Trahey, and Mary S. Soo. "Wavefront estimation in the human breast". Ed. by Michael F. Insana and K. Kirk Shung. San Diego, CA, 2001, pp. 172–181. DOI: 10.1117/12.428194 (cit. on pp. 25, 30).

[Gérardin, 2014] Benoît Gérardin, Jérôme Laurent, Arnaud Derode, Claire Prada, and Alexandre Aubry. "Full Transmission and Reflection of Waves Propagating through a Maze of Disorder". *Physical Review Letters* 113.17 (2014), p. 173901. DOI: 10.1103/PhysRevLett.113.173901 (cit. on p. 35).

[Gilja, 1995] Odd Helge Gilja, Alf Inge Smievoll, Nils Thune, Knut Matre, Trygve Hausken, Svein Ødegaard, and Arnold Berstad. "In vivo comparison of 3D ultrasonography and magnetic resonance imaging in volume estimation of human kidneys". *Ultrasound in Medicine and Biology* 21.1 (1995), pp. 25–32. DOI: 10.1016/0301-5629(94)00082-4 (cit. on p. 70).

[Giraudat, 2023] Elsa Giraudat, Arnaud Burtin, Jean-Christophe Komorowski, Mathias Fink, and Alexandre Aubry. "Unveiling the deep plumbing system of a volcano by a reflection matrix approach of seismic noise". *Work to be published* (2023) (cit. on pp. 122, 177).

[Glover, 1977a] G. H. Glover. "Computerized time-of-flight ultrasonic tomography for breast examination". *Ultrasound in Medicine & Biology* 3.2 (1977), pp. 117–127. DOI: https://doi.org/10.1016/0301-5629(77)90064-3 (cit. on p. 38).

[Glover, 1977b] G.H. Glover and J.C. Sharp. "Reconstruction of Ultrasound Propagation Speed Distributions in Soft Tissue: Time-Of-Flight Tomography". *IEEE Transactions on Sonics and Ultrasonics* 24.4 (1977), pp. 229–234. DOI: 10.1109/T-SU.1977.30936 (cit. on pp. 38, 154).

[Goetschy, 2013] A. Goetschy and A. D. Stone. "Filtering Random Matrices: The Effect of Incomplete Channel Control in Multiple Scattering". *Physical Review Letters* 111.6 (2013), p. 063901. DOI: 10.1103/PhysRevLett.111.063901 (cit. on p. 35).

[Goïcoechea, 2023] Antton Goïcoechea, Cécile Brütt, Flavien Bureau, Arthur Le Ber, Claire Prada, and Alexandre Aubry. "Local measurement of the scattering mean free path in reflection". *Work to be published* (2023) (cit. on p. 23).

[Goss, 1978] S. A. Goss, R. L. Johnston, and F. Dunn. "Comprehensive compilation of empirical ultrasonic properties of mammalian tissues". *The Journal of the Acoustical Society of America* 64.2 (1978), pp. 423–457. DOI: 10.1121/1.382016 (cit. on p. 80).

[Greco De Sousa, 2007] Ana Greco De Sousa, Wagner De Albuquerque Pereira, and Joao Machado. "An ultrasonic theoretical and experimental approach to determine thickness and wave speed in layered media". *IEEE Transactions on Ultrasonics, Ferroelectrics and Frequency Control* 54.2 (2007), pp. 386–393. DOI: 10.1109/TUFFC.2007.252 (cit. on p. 133).

[Greenleaf, 1975] J. F. Greenleaf, S. A. Johnson, W. F. Samayoa, and F. A. Duck. "Algebraic Reconstruction of Spatial Distributions of Acoustic Velocities in Tissue from Their Time-of-Flight Profiles". *Acoustical Holography: Volume 6*. Ed. by Newell Booth. Boston, MA: Springer US, 1975, pp. 71–90. DOI: 10.1007/978-1-4615-8216-8_4 (cit. on p. 154).

[Greenleaf, 1987] James F. Greenleaf, Juha Ylitalo, and John J. Gisvold. "Ultrasonic Computed Tomography for Breast Examination". *IEEE Engineering in Medicine and Biology Magazine* 6.4 (1987), pp. 27–32. DOI: 10.1109/MEMB.1987.5006465 (cit. on p. 38).

[Guo, 1996] Z. Guo and A. Fenster. "Three-dimensional power Doppler imaging: a phantom study to quantify vessel stenosis". *Ultrasound in Medicine & Biology* 22.8 (1996), pp. 1059–1069. DOI: 10.1016/s0301-5629(96)00125-1 (cit. on p. 70).

[Gustafsson, 2000] M. G. L. Gustafsson. "Surpassing the lateral resolution limit by a factor of two using structured illumination microscopy". *Journal of Microscopy* 198.2 (2000), pp. 82–87. DOI: 10.1046/j.1365-2818.2000.00710.x (cit. on p. 19).

[Halliwell, 1978] M. Halliwell. "Ultrasonic Beam Distortion by the Normal Human Breast In Vivo". *Ultrasound in Medicine: Volume 4*. Ed. by Denis White and E. A. Lyons. Boston, MA: Springer US, 1978, pp. 555–556. DOI: 10.1007/978-1-4613-4021-8_121 (cit. on p. 22).

[Hansen, 2009] K. Hansen, J. Udesen, F. Gran, J. Jensen, and M. Bachmann Nielsen. "In-vivo Examples of Flow Patterns With The Fast Vector Velocity Ultrasound Method". *Ultraschall in der Medizin - European Journal of Ultrasound* 30.05 (2009), pp. 471–477. DOI: 10.1055/s-0028-1109572 (cit. on p. 17).

[Hara, 2005] K. Hara, J. Sakano, M. Mori, S. Tamano, R. Sinomura, and K. Yamazaki. "A New 80V 32x32ch Low Loss Multiplexer LSI for a 3D Ultrasound Imaging System". *Proceedings. ISPSD '05. The 17th International Symposium on Power Semiconductor Devices and ICs, 2005.* 2005, pp. 359–362. DOI: 10.1109/ISPSD.2005.1488025 (cit. on pp. 71, 113).

[Heiles, 2019] Baptiste Heiles. "Microscopie par Localisation Ultrasonore en 3D". PhD Thesis. 2019 (cit. on p. 120).

[Hériard-Dubreuil, 2023] Baptiste Hériard-Dubreuil, Adrien Besson, Frédéric Wintzenrieth, Claude Cohen-Bacrie, and Jean-Philippe Thiran. "Refraction-Based Speed of Sound Estimation in Layered Media: an Angular Approach". *IEEE Transactions on Ultrasonics, Ferroelectrics, and Frequency Control* (2023), pp. 1–1. DOI: 10.1109/TUFFC.2023.3261541 (cit. on p. 157).

[Hirama, 1982] Makoto Hirama, Osamu Ikeda, and Takuso Sato. "Adaptive ultrasonic array imaging system through an inhomogeneous layer". *The Journal of the Acoustical Society of America* 71.1 (1982), pp. 100–109. DOI: 10.1121/1.387336 (cit. on p. 27).

[Hollman, 1999] K.W. Hollman, K.W. Rigby, and M. O'Donnell. "Coherence factor of speckle from a multirow probe". *1999 IEEE Ultrasonics Symposium. Proceedings. International Symposium (Cat. No.99CH37027)*. Vol. 2. Caesars Tahoe, NV, USA: IEEE, 1999, pp. 1257–1260. DOI: 10.1109/ULTSYM.1999.849225 (cit. on p. 26).

[Hölscher, 2008] Thilo Hölscher, Wilko G. Wilkening, Sven Molkenstruck, Heinz Voit, and Christian Koch. "Transcranial Sound Field Characterization". *Ultrasound in Medicine & Biology* 34.6 (2008), pp. 973–980. DOI: 10.1016/j.ultrasmedbio.2007.11.016 (cit. on p. 98).

[Hormati, 2010] A. Hormati, I. Jovanovic, O. Roy, and M. Vetterli. "Robust ultrasound travel-time tomography using the bent ray model". *Medical Imaging*. 2010. DOI: 10.1117/12.844693 (cit. on p. 154).

[Hsu, 2017] Chia Wei Hsu, Seng Fatt Liew, Arthur Goetschy, Hui Cao, and A. Douglas Stone. "Correlation-enhanced control of wave focusing in disordered media". *Nature Physics* 13.5 (2017), pp. 497–502. DOI: 10.1038/nphys4036 (cit. on p. 35).

[Hu, 2022] Zhiming Hu, Mingchun Yang, Xiang Zhu, and Chao Tian. "Sound speed imaging of small animal organs by ultrasound computed tomography". *JUSTC* 52.1 (2022), pp. 8–7. DOI: 10.52396/JUSTC-2021-0113 (cit. on p. 154).

[Huang, 2017] Qinghua Huang and Zhaozheng Zeng. "A Review on Real-Time 3D Ultrasound Imaging Technology". *BioMed Research International* 2017 (2017), e6027029. DOI: 10.1155/2017/6027029 (cit. on p. 70).

[Huthwaite, 2011] P. Huthwaite and F. Simonetti. "High-resolution imaging without iteration: a fast and robust method for breast ultrasound tomography". *The Journal of the Acoustical Society of America* 130.3 (2011), pp. 1721–1734. DOI: 10.1121/1.3613936 (cit. on p. 154).

[Ilovitsh, 2018] Tali Ilovitsh, Asaf Ilovitsh, Josquin Foiret, Brett Z. Fite, and Katherine W. Ferrara. "Acoustical structured illumination for super-resolution ultrasound imaging". *Communications Biology* 1.1 (2018), p. 3. DOI: 10.1038/s42003-017-0003-5 (cit. on p. 19).

[Imbault, 2018] Marion Imbault, Marco Dioguardi Burgio, Alex Faccinetto, Maxime Ronot, Hanna Bendjador, Thomas Deffieux, Emma Ollivier Triquet, Pierre-Emmanuel Rautou, Laurent Castera, Jean-Luc Gennisson, Valérie Vilgrain, and Mickael Tanter. "Ultrasonic fat fraction quantification using *in vivo* adaptive sound speed estimation". *Physics in Medicine & Biology* 63.21 (2018), p. 215013. DOI: 10.1088/1361-6560/aae661 (cit. on pp. 31, 154).

[Imbault, 2017] Marion Imbault, Alex Faccinetto, Bruno-Félix Osmanski, Antoine Tissier, Thomas Deffieux, Jean-Luc Gennisson, Valérie Vilgrain, and Mickaël Tanter. "Robust sound speed estimation for ultrasound-based hepatic steatosis assessment". *Physics in Medicine and Biology* 62.9 (2017), pp. 3582–3598. DOI: 10.1088/1361-6560/aa6226 (cit. on pp. 31, 107, 154, 156, 171, 172).

[Ivancevich, 2008] Nikolas M. Ivancevich, Gianmarco F. Pinton, Heather A. Nicoletto, Ellen Bennett, Daniel T. Laskowitz, and Stephen W. Smith. "Real-time 3-D contrast-enhanced transcranial ultrasound and aberration correction". *Ultrasound in Medicine & Biology* 34.9 (2008), pp. 1387–1395. DOI: 10.1016/j.ultrasmedbio.2008.01.015 (cit. on p. 106).

[Jaeger, 2015a] Michael Jaeger, Gerrit Held, Sara Peeters, Stefan Preisser, Michael Grünig, and Martin Frenz. "Computed ultrasound tomography in echo mode for imaging speed of sound using pulse-echo sonography: proof of principle". *Ultrasound in Medicine & Biology* 41.1 (2015), pp. 235–250. DOI: 10.1016/j.ultrasmedbio.2014.05.019 (cit. on pp. 31, 107, 154, 156, 169, 174, 176).

[Jaeger, 2015b] Michael Jaeger, Elise Robinson, H Günhan Akarçay, and Martin Frenz. "Full correction for spatially distributed speed-of-sound in echo ultrasound based on measuring aberration delays via transmit beam steering". *Physics in Medicine and Biology* 60.11 (2015), pp. 4497–4515. DOI: 10.1088/0031-9155/60/11/4497 (cit. on p. 156).

[Jaeger, 2022] Michael Jaeger, Patrick Stähli, Naiara Korta Martiartu, Parisa Salemi Yolgunlu, Thomas Frappart, Christophe Fraschini, and Martin Frenz. "Pulse-echo speed-of-sound imaging using convex probes". *Physics in Medicine & Biology* 67.21 (2022), p. 215016. DOI: 10.1088/1361-6560/ac96c6 (cit. on pp. 106, 156).

[Jakovljevic, 2018] Marko Jakovljevic, Scott Hsieh, Rehman Ali, Gustavo Chau Loo Kung, Dongwoon Hyun, and Jeremy J. Dahl. "Local speed of sound estimation in tissue using pulse-echo ultrasound: Model-based approach". *The Journal of the Acoustical Society of America* 144.1 (2018), pp. 254–266. DOI: 10.1121/1.5043402 (cit. on pp. 31, 107, 154, 156, 167, 190).

[Jensen, 1991] J. A. Jensen. "A model for the propagation and scattering of ultrasound in tissue". *The Journal of the Acoustical Society of America* 89.1 (1991), pp. 182–190. DOI: 10.1121/1.400497 (cit. on p. 157).

[Jing, 2021] Bowen Jing and Brooks D. Lindsey. "Effect of Skull Porous Trabecular Structure on Transcranial Ultrasound Imaging in the Presence of Elastic Wave Mode Conversion at Varying Incidence Angle". *Ultrasound in Medicine & Biology* 47.9 (2021), pp. 2734–2748. DOI: 10.1016/j.ultrasmedbio.2021.05.010 (cit. on p. 98).

[Johnson, 2007] S.A. Johnson, T. Abbott, R. Bell, M. Berggren, D. Borup, D. Robinson, J. Wiskin, S. Olsen, and B. Hanover. "Non-Invasive Breast Tissue Characterization Using Ultrasound Speed and Attenuation". *Acoustical Imaging*. Ed. by Michael P. André et al. Acoustical Imaging. Dordrecht: Springer Netherlands, 2007, pp. 147–154. DOI: 10.1007/1-4020-5721-0_17 (cit. on p. 154).

[Kalsoum, 2014] E. Kalsoum, X. Leclerc, A. Drizenko, and J.-P. Pruvo. "Circle of Willis". *Encyclopedia of the Neurological Sciences*. Elsevier, 2014, pp. 803–805. DOI: 10.1016/B978-0-12-385157-4.01135-0 (cit. on p. 120).

[Kang, 2017] Sungsam Kang, Pilsung Kang, Seungwon Jeong, Yongwoo Kwon, Taeseok D. Yang, Jin Hee Hong, Moonseok Kim, Kyung–Deok Song, Jin Hyoung Park, Jun Ho Lee, Myoung Joon Kim, Ki Hean Kim, and Wonshik Choi. "High-resolution adaptive optical imaging within thick scattering media using closed-loop accumulation of single scattering". *Nature Communications* 8 (2017), p. 2157. DOI: 10.1038/s41467-017-02117-8 (cit. on pp. 34, 43, 69, 88).

[Katz, 2014] Ori Katz, Pierre Heidmann, Mathias Fink, and Sylvain Gigan. "Non-invasive single-shot imaging through scattering layers and around corners via speckle correlations". *Nature Photonics* 8.10 (2014), pp. 784–790. DOI: 10.1038/nphoton.2014.189 (cit. on p. 43).

[Kim, 2012] Moonseok Kim, Youngwoon Choi, Changhyeong Yoon, Wonjun Choi, Jaisoon Kim, Q-Han Park, and Wonshik Choi. "Maximal energy transport through disordered media with the implementation of transmission eigenchannels". *Nature Photonics* 6.9 (2012), pp. 581–585. DOI: 10.1038/nphoton.2012.159 (cit. on p. 34).

[Kirkhorn, 1999] Johan Kirkhorn. "Introduction to IQ-demodulation of RF-data" (1999), p. 13 (cit. on pp. 16, 192).

[Kondo, 1990] Masafumi Kondo, Kinya Takamizawa, Makoto Hirama, Kiyoshi Okazaki, Kazuhiro Iinuma, and Yasuaki Takehara. "An evaluation of an in vivo local sound speed estimation technique by the crossed beam method". *Ultrasound in Medicine & Biology* 16.1 (1990), pp. 65–72. DOI: 10.1016/0301-5629(90)90087-S (cit. on pp. 155, 156).

[Kontonassios, 1987] T. Kontonassios and J. Ophir. "Variance reduction of speed of sound estimation in tissues using the beam tracking method". *IEEE transactions on ultrasonics, ferroelectrics, and frequency control* 34.5 (1987), pp. 524–530. DOI: 10.1109/t-uffc.1987.26978 (cit. on p. 155).

[Krucker, 2004] J.F. Krucker, J.B. Fowlkes, and P.L. Carson. "Sound speed estimation using automatic ultrasound image registration". *IEEE Transactions on Ultrasonics, Ferroelectrics, and Frequency Control* 51.9 (2004), pp. 1095–1106. DOI: 10.1109/TUFFC.2004.1334842 (cit. on p. 155).

[Kruse, 2002] Dustin E Kruse and Katherine W Ferrara. "A New High Resolution Color Flow System Using an Eigendecomposition-Based Adaptive Filter for Clutter Rejection". *IEEE transactions on ultrasonics, ferroelectrics, and frequency control* 49.12 (2002). DOI: 10.1109/TUFFC.2002.1041080 (cit. on p. 20).

[Kwon, 2023] Yongwoo Kwon, Jin Hee Hong, Sungsam Kang, Hojun Lee, Yonghyeon Jo, Ki Hean Kim, Seokchan Yoon, and Wonshik Choi. "Computational conjugate adaptive optics microscopy for longitudinal through-skull imaging of cortical myelin". *Nature Communications* 14 (2023), p. 105. DOI: 10.1038/s41467-022-35738-9 (cit. on pp. 29, 43, 69, 106).

[Labeyrie, 1970] A. Labeyrie. "Attainment of Diffraction Limited Resolution in Large Telescopes by Fourier Analysing Speckle Patterns in Star Images". *Astronomy and Astrophysics* 6 (1970), p. 85 (cit. on pp. 27, 29).

[Labiau, 2009] S. Labiau, G. David, S. Gigan, and A. C. Boccara. "Defocus test and defocus correction in full-field optical coherence tomography". *Optics Letters* 34.10 (2009), p. 1576. DOI: 10.1364/OL.34.001576 (cit. on p. 133).

[Lacefield, 2002] James C. Lacefield, Wayne C. Pilkington, and Robert C. Waag. "Distributed aberrators for emulation of ultrasonic pulse distortion by abdominal wall". *Acoustics Research Letters Online* 3.2 (2002), pp. 47–52. DOI: 10.1121/1.1447562 (cit. on p. 102).

[Lambert, 2020a] William Lambert. "Matrix approach for ultrasound imaging and quantification". PhD thesis. 2020 (cit. on pp. 30, 49, 64, 76, 127, 150, 182, 185, 188).

[Lambert, 2022a] William Lambert, Laura Cobus, Mathias Fink, and Alexandre Aubry. "Ultrasound Matrix Imaging. II. The distortion matrix for aberration correction over multiple isoplanatic patches." (2022). DOI: 10.1109/TMI.2022.3199483 (cit. on pp. xiii, 29, 30, 35, 45, 49, 58, 59, 62, 63, 65, 66, 69, 84, 86, 90, 101, 102, 117, 179).

[Lambert, 2020b] William Lambert, Laura A. Cobus, Mathieu Couade, Mathias Fink, and Alexandre Aubry. "Reflection Matrix Approach for Quantitative Imaging of Scattering Media". *Physical Review X* 10.2 (2020), p. 021048. DOI: 10.1103/PhysRevX.10.021048 (cit. on pp. xiii, 26, 45, 49–52, 55, 56, 66, 69, 77, 78, 80, 107, 156).

[Lambert, 2020c] William Lambert, Laura A. Cobus, Thomas Frappart, Mathias Fink, and Alexandre Aubry. "Distortion matrix approach for ultrasound imaging of random scattering media". *Proceedings of the National Academy of Sciences* 117.26 (2020), pp. 14645–14656. DOI: 10.1073/pnas.1921533117 (cit. on pp. 28, 30, 34, 35, 45, 49, 59, 60, 62, 65, 66, 69, 84, 86, 102, 147, 185).

[Lambert, 2022b] William Lambert, Justine Robin, Laura A. Cobus, Mathias Fink, and Alexandre Aubry. "Ultrasound Matrix Imaging. I. The focused reflection matrix, the F -factor and the role of multiple scattering." *IEEE Transactions on Medical Imaging* (2022), pp. 1–1. DOI: 10.1109/TMI.2022.3199498 (cit. on pp. xiii, 23, 26, 27, 45, 48, 49, 51, 57, 58, 65, 66, 69, 82, 83, 90, 179).

[Langevin, 1920] Paul Langevin and Constantin Chilowski. "Procédés et appareils pour la production de signaux sous-marins dirigés et pour la localisation à distance d'obstacles sous-marins". 502 913. 1920 (cit. on pp. 3–5, 34).

[Lavarello, 2009] R.J. Lavarello and M.L. Oelze. "Tomographic Reconstruction of Three-Dimensional Volumes Using the Distorted Born Iterative Method". *IEEE Transactions on Medical Imaging* 28.10 (2009), pp. 1643–1653. DOI: 10.1109/TMI.2009.2026274 (cit. on p. 154).

[Lavarello, 2008] Roberto Lavarello and Michael Oelze. "A study on the reconstruction of moderate contrast targets using the distorted born iterative method". *IEEE Transactions on Ultrasonics, Ferroelectrics and Frequency Control* 55.1 (2008), pp. 112–124. DOI: 10.1109/TUFFC.2008.621 (cit. on p. 154).

[Ledoux, 1997] Léon A.F. Ledoux, Peter J. Brands, and Arnold P.G. Hoeks. "Reduction of the Clutter Component in Doppler Ultrasound Signals Based on Singular Value Decomposition: A Simulation Study". *Ultrasonic Imaging* 19.1 (1997), pp. 1–18. DOI: 10.1177/016173469701900101 (cit. on p. 20).

[Lemoult, 2010] Fabrice Lemoult, Geoffroy Lerosey, Julien De Rosny, and Mathias Fink. "Resonant Metalenses for Breaking the Diffraction Barrier". *Physical Review Letters* 104.20 (2010), p. 203901. DOI: 10.1103/PhysRevLett.104.203901 (cit. on p. 175).

[Li, 2010] Shengying Li, Marcel Jackowski, Donald P. Dione, Trond Varslot, Lawrence H. Staib, and Klaus Mueller. "Refraction corrected transmission ultrasound computed tomography for application in breast imaging". *Medical Physics* 37.5 (2010), pp. 2233–2246. DOI: 10.1118/1.3360180 (cit. on p. 154).

[Lindsey, 2014] Brooks D. Lindsey and Stephen W. Smith. "Refraction correction in 3D transcranial ultrasound imaging". *Ultrasonic Imaging* 36.1 (2014), pp. 35–54. DOI: 10.1177/0161734613510287 (cit. on p. 31).

[Liu, 1998] D.-L.D. Liu and R.C. Waag. "Estimation and correction of ultrasonic wavefront distortion using pulse-echo data received in a two-dimensional aperture". *IEEE Transactions on Ultrasonics, Ferroelectrics, and Frequency Control* 45.2 (1998), pp. 473–490. DOI: 10.1109/58.660157 (cit. on p. 29).

[Liu, 2014] Hao-Li Liu, Ching-Hsiang Fan, Chien-Yu Ting, and Chih-Kuang Yeh. "Combining Microbubbles and Ultrasound for Drug Delivery to Brain Tumors: Current Progress and Overview". *Theranostics* 4.4 (2014), pp. 432–444. DOI: 10.7150/thno.8074 (cit. on p. 110).

[Lok, 2018] U-Wai Lok and Pai-Chi Li. "Microbeamforming With Error Compensation". *IEEE Transactions on Ultrasonics, Ferroelectrics, and Frequency Control* 65.7 (2018), pp. 1153–1165. DOI: 10.1109/TUFFC.2018.2834411 (cit. on p. 70).

[Lovstakken, 2006] L. Lovstakken, S. Bjaerum, K. Kristoffersen, R. Haaverstad, and H. Torp. "Real-time adaptive clutter rejection filtering in color flow imaging using power method iterations". *IEEE Transactions on Ultrasonics, Ferroelectrics and Frequency Control* 53.9 (2006), pp. 1597–1608. DOI: 10.1109/TUFFC.2006.1678188 (cit. on p. 20).

[Lu, 1997] Jian-yu Lu. "2D and 3D High n a m e Rate Imaging with Limited Diffraction Beams". *IEEE Transactions on Ultrasonics, Ferroelectrics, and Frequency Control* (1997). DOI: 10.1109/58.655200 (cit. on pp. 12, 17).

[Mace, 2013] Emilie Mace, Gabriel Montaldo, Bruno-Felix Osmanski, Ivan Cohen, Mathias Fink, and Mickael Tanter. "Functional ultrasound imaging of the brain: theory and basic principles". *IEEE Transactions on Ultrasonics, Ferroelectrics and Frequency Control* 60.3 (2013), pp. 492–506. DOI: 10.1109/TUFFC.2013.2592 (cit. on p. 17).

[Macé, 2011] Emilie Macé, Gabriel Montaldo, Ivan Cohen, Michel Baulac, Mathias Fink, and Mickael Tanter. "Functional ultrasound imaging of the brain". *Nature Methods* 8.8 (2011), pp. 662–664. DOI: 10.1038/nmeth.1641 (cit. on p. 17).

[Mallart, 1994] Raoul Mallart and Mathias Fink. "Adaptive focusing in scattering media through sound-speed inhomogeneities: The van Cittert Zernike approach and focusing criterion". *The Journal of the Acoustical Society of America* 96.6 (1994), pp. 3721–3732. DOI: 10.1121/1.410562 (cit. on pp. 13, 14, 25, 27, 56, 90, 187).

[Mamo, 2015] Yohannes Mamo. "Cerebrovascular effects of vasoactive drugs: In vitro, in vivo and clinical investigations". PhD thesis. 2015 (cit. on p. 122).

[Marcus, 1975] Peter W. Marcus and Edwin L. Carstensen. "Problems with absorption measurements of inhomogeneous solids". *The Journal of the Acoustical Society of America* 58.6 (1975), pp. 1334–1335. DOI: 10.1121/1.380789 (cit. on p. 22).

[Måsøy, 2022] Svein-Erik Måsøy, Bastien Dénarié, Anders Sørnes, Espen Holte, Bjørnar Grenne, Torvald Espeland, Erik Andreas Rye Berg, Ole Marius Hoel Rindal, Wayne Rigby, and Tore Bjåstad. *Aberration correction in 2D echocardiography*. preprint. 2022. DOI: 10.36227/techrxiv.19739905.v1 (cit. on p. 30).

[Måsøy, 2005] Svein-Erik Måsøy, Trond Varslot, and Bjørn Angelsen. "Iteration of transmit-beam aberration correction in medical ultrasound imaging". *The Journal of the Acoustical Society of America* 117.1 (2005), pp. 450–461. DOI: 10.1121/1.1823213 (cit. on pp. 27, 29, 44, 61).

[Mast, 1997] T. Douglas Mast, Laura M. Hinkelman, Michael J. Orr, Victor W. Sparrow, and Robert C. Waag. "Simulation of ultrasonic pulse propagation through the abdominal wall". *The Journal of the Acoustical Society of America* 102.2 (1997), pp. 1177–1190. DOI: 10.1121/1.421015 (cit. on p. 22).

[Mast, 1998] T. Douglas Mast, Laura M. Hinkelman, Michael J. Orr, and Robert C. Waag. "The effect of abdominal wall morphology on ultrasonic pulse distortion. Part II. Simulations". *The Journal of the Acoustical Society of America* 104.6 (1998), pp. 3651–3664. DOI: 10.1121/1.423947 (cit. on p. 22).

[Mehta, 2008] Sanjeev R Mehta, E Louise Thomas, Jimmy D Bell, Desmond G Johnston, and Simon D Taylor-Robinson. "Non-invasive means of measuring hepatic fat content". *World Journal of Gastroenterology* 14.22 (2008), p. 3476. DOI: 10.3748/wjg.14.3476 (cit. on p. 171).

[Mertz, 2015] Jerome Mertz, Hari Paudel, and Thomas G. Bifano. "Field of view advantage of conjugate adaptive optics in microscopy applications". *Applied Optics* 54.11 (2015), p. 3498. DOI: 10.1364/AO.54.003498 (cit. on pp. 29, 59, 63).

[Minnaert, 1933] M. Minnaert. "XVI. On musical air-bubbles and the sounds of running water". *The London, Edinburgh, and Dublin Philosophical Magazine and Journal of Science* 16.104 (1933), pp. 235–248. DOI: 10.1080/14786443309462277 (cit. on pp. 110, 123).

[Mohanty, 2017] Kaustav Mohanty, John Blackwell, Thomas Egan, and Marie Muller. "Characterization of the Lung Parenchyma Using Ultrasound Multiple Scattering". *Ultrasound in Medicine & Biology* 43.5 (2017), pp. 993–1003. DOI: 10.1016/j.ultrasmedbio.2017.01.011 (cit. on pp. 22, 57).

[Montaldo, 2011] Gabriel Montaldo, Mickael Tanter, and Mathias Fink. "Time Reversal of Speckle Noise". *Physical Review Letters* 106.5 (2011), p. 054301. DOI: 10.1103/PhysRevLett.106.054301 (cit. on pp. 27, 29, 60).

[Montaldo, 2009] Gabriel Montaldo, Mickaël Tanter, Jérémy Bercoff, Nicolas Benech, and Mathias Fink. "Coherent plane-wave compounding for very high frame rate ultrasonography and transient elastography". *IEEE transactions on ultrasonics, ferroelectrics, and frequency control* 56.3 (2009), pp. 489–506. DOI: 10.1109/TUFFC.2009.1067 (cit. on pp. 17, 18, 73, 78, 99, 154).

[Montaldo, 2004] Gabriel Montaldo, Mickaël Tanter, and Mathias Fink. "Real time inverse filter focusing through iterative time reversal". *The Journal of the Acoustical Society of America* 115.2 (2004), pp. 768–775. DOI: 10.1121/1.1636462 (cit. on pp. 28, 37).

[Moustakas, 2000] Aris L. Moustakas, Harold U. Baranger, Leon Balents, Anirvan M. Sengupta, and Steven H. Simon. "Communication Through a Diffusive Medium: Coherence and Capacity". *Science* 287.5451 (2000), pp. 287–290. DOI: 10.1126/science.287.5451.287 (cit. on p. 34).

[Mozaffarzadeh, 2022] Moein Mozaffarzadeh, Dirk J. Eric Verschuur, Martin D. Verweij, Nico de Jong, and Guillaume Renaud. "Accelerated 2-D Real-Time Refraction-Corrected Transcranial Ultrasound Imaging". *IEEE Transactions on Ultrasonics, Ferroelectrics, and Frequency Control* 69.9 (2022), pp. 2599–2610. DOI: 10.1109/TUFFC.2022.3189600 (cit. on p. 133).

[Mozaffarzadeh, 2021] Moein Mozaffarzadeh, Martin D. Verweij, Verya Daeichin, Nico De Jong, and Guillaume Renaud. "Transcranial Ultrasound Imaging with Estimating the Geometry, Position and Wave-Speed of Temporal Bone". *2021 IEEE International Ultrasonics Symposium (IUS)*. 2021, pp. 1–4. DOI: 10.1109/IUS52206.2021.9593826 (cit. on pp. 98, 106).

[Muller, 1974] Richard A. Muller and Andrew Buffington. "Real-time correction of atmospherically degraded telescope images through image sharpening". *JOSA* 64.9 (1974), pp. 1200–1210. DOI: 10.1364/JOSA.64.001200 (cit. on pp. 27, 29).

[Müller, 2010] Claus B. Müller and Jörg Enderlein. "Image Scanning Microscopy". *Physical Review Letters* 104.19 (2010), p. 198101. DOI: 10.1103/PhysRevLett.104.198101 (cit. on p. 54).

[Najar, 2023] Ulysse Najar, Victor Barolle, Paul Balondrade, Mathias Fink, A. Claude Boccara, and Alexandre Aubry. *Non-invasive Retrieval of the Transmission Matrix for Optical Imaging Deep Inside a Multiple Scattering Medium*. 2023. DOI: https://doi.org/10.48550/arXiv.2303.06119 (cit. on pp. 49, 58, 69, 177).

[Napolitano, 2006] David Napolitano, Ching-Hua Chou, Glen McLaughlin, Ting-Lan Ji, Larry Mo, Derek DeBusschere, and Robert Steins. "Sound speed correction in ultrasound imaging". *Ultrasonics*. Proceedings of Ultrasonics International (UI'05) and World Congress on Ultrasonics (WCU) 44 (2006), e43–e46. DOI: 10.1016/j.ultras.2006.06.061 (cit. on p. 156).

[Nicolaides, 1992] K. H. Nicolaides, G. Azar, D. Byrne, C. Mansur, and K. Marks. "Fetal nuchal translucency: ultrasound screening for chromosomal defects in first trimester of pregnancy." *BMJ* 304.6831 (1992), pp. 867–869. DOI: 10.1136/bmj.304.6831.867 (cit. on pp. 3, 155).

[Nock, 1989] L. Nock, G. E. Trahey, and S. W. Smith. "Phase aberration correction in medical ultrasound using speckle brightness as a quality factor". *The Journal of the Acoustical Society of America* 85.5 (1989), pp. 1819–1833. DOI: 10.1121/1.397889 (cit. on pp. 25, 27).

[ODonnell, 1988] M. O'Donnell and S.W. Flax. "Phase-aberration correction using signals from point reflectors and diffuse scatterers: measurements". *IEEE Transactions on Ultrasonics, Ferroelectrics and Frequency Control* 35.6 (1988), pp. 768–774. DOI: 10.1109/58.9334 (cit. on pp. 28, 43, 45).

[Ogawa, 2013] Toshio Ogawa. "Acoustic Wave Velocity Measurement on Piezoelectric Ceramics". *Piezoelectric Materials and Devices - Practice and Applications*. IntechOpen, 2013. DOI: 10.5772/53117 (cit. on p. 6).

[Ophir, 1986] J. Ophir. "Estimation of the speed of ultrasound propagation in biological tissues: a beam-tracking method". *IEEE Transactions on Ultrasonics Ferroelectrics and Frequency Control* 33.4 (1986), pp. 359–368. DOI: 10.1109/t-uffc.1986.26843 (cit. on p. 155).

[Ophir, 1990] J. Ophir and Y. Yazdi. "A Transaxial Compression Technique (TACT) for Localized Pulse-Echo Estimation of Sound Speed in Biological Tissues". *Ultrasonic Imaging* 12.1 (1990), pp. 35–46. DOI: 10.1177/016173469001200103 (cit. on p. 155).

[Osmanski, 2012a] Bruno-Felix Osmanski, Gabriel Montaldo, Mickaël Tanter, and Mathias Fink. "Aberration correction by time reversal of moving speckle noise". *IEEE Transactions on Ultrasonics, Ferroelectrics and Frequency Control* 59.7 (2012), pp. 1575–1583. DOI: 10.1109/TUFFC.2012.2357 (cit. on pp. 122, 176).

[Osmanski, 2012b] Bruno-Felix Osmanski, Mathieu Pernot, Gabriel Montaldo, Alain Bel, Emmanuel Messas, and Mickael Tanter. "Ultrafast Doppler Imaging of Blood Flow Dynamics in the Myocardium". *IEEE Transactions on Medical Imaging* 31.8 (2012), pp. 1661–1668. DOI: 10.1109/TMI.2012.2203316 (cit. on p. 17).

[Ozmen, 2015] Neslihan Ozmen, Robin Dapp, Michael Zapf, Hartmut Gemmeke, Nicole V. Ruiter, and Koen W. A. Van Dongen. "Comparing different ultrasound imaging methods for breast cancer detection". *IEEE Transactions on Ultrasonics, Ferroelectrics, and Frequency Control* 62.4 (2015), pp. 637–646. DOI: 10.1109/TUFFC.2014.006707 (cit. on p. 154).

[Papadacci, 2014] Clement Papadacci, Mickael Tanter, Mathieu Pernot, and Mathias Fink. "Ultrasound backscatter tensor imaging (BTI): analysis of the spatial coherence of ultrasonic speckle in anisotropic soft tissues". *IEEE Transactions on Ultrasonics, Ferroelectrics, and Frequency Control* 61.6 (2014), pp. 986–996. DOI: 10.1109/TUFFC.2014.2994 (cit. on p. 108).

[Papadopoulos, 2012] Ioannis N. Papadopoulos, Salma Farahi, Christophe Moser, and Demetri Psaltis. "Focusing and scanning light through a multimode optical fiber using digital phase conjugation". *Optics Express* 20.10 (2012), p. 10583. DOI: 10.1364/OE.20.010583 (cit. on p. 34).

[Parthasarathy, 2012] Raghuveer Parthasarathy. "Rapid, accurate particle tracking by calculation of radial symmetry centers". *Nature Methods* 9.7 (2012), pp. 724–726. DOI: 10.1038/nmeth.2071 (cit. on p. 120).

[Pereira, 2002] Fernando R. Pereira, João C. Machado, and Wagner C. A. Pereira. "Ultrasonic wave speed measurement using the time-delay profile of rf-backscattered signals: Simulation and experimental results". *The Journal of the Acoustical Society of America* 111.3 (2002), pp. 1445–1453. DOI: 10.1121/1.1445787 (cit. on p. 155).

[Perez-Liva, 2020] Mailyn Perez-Liva, José Manuel Udías, Jorge Camacho, Elena Merčep, Xosé Luís Deán-Ben, Daniel Razansky, and Joaquín L. Herraiz. "Speed of sound ultrasound transmission tomography image reconstruction based on Bézier curves". *Ultrasonics* 103 (2020), p. 106097. DOI: 10.1016/j.ultras.2020.106097 (cit. on p. 154).

[Perrot, 2021] Vincent Perrot, Maxime Polichetti, François Varray, and Damien Garcia. "So you think you can DAS? A viewpoint on delay-and-sum beamforming". *Ultrasonics* 111 (2021), p. 106309. DOI: 10.1016/j.ultras.2020.106309 (cit. on pp. 50, 75, 137, 161).

[Pinton, 2012] Gianmarco Pinton, Jean-Francois Aubry, Emmanuel Bossy, Marie Muller, Mathieu Pernot, and Mickael Tanter. "Attenuation, scattering, and absorption of ultrasound in the skull bone". *Medical Physics* 39.1 (2012), pp. 299–307. DOI: 10.1118/1.3668316 (cit. on pp. 23, 98).

[Podkowa, 2020] Anthony S. Podkowa and Michael L. Oelze. "The convolutional interpretation of registration-based plane wave steered pulse-echo local sound speed estimators". *Physics in Medicine &amp$\mathsemicolon$ Biology* 65.2 (2020), p. 025003. DOI: 10.1088/1361-6560/ab6071 (cit. on p. 157).

[Popoff, 2011] S. M. Popoff, A. Aubry, G. Lerosey, M. Fink, A. C. Boccara, and S. Gigan. "Exploiting the Time-Reversal Operator for Adaptive Optics, Selective Focusing, and Scattering Pattern Analysis". *Physical Review Letters* 107.26 (2011), p. 263901. DOI: 10.1103/PhysRevLett.107.263901 (cit. on p. 34).

[Popoff, 2010a] S. M. Popoff, G. Lerosey, R. Carminati, M. Fink, A. C. Boccara, and S. Gigan. "Measuring the Transmission Matrix in Optics: An Approach to the Study and Control of Light Propagation in Disordered Media". *Physical Review Letters* 104.10 (2010), p. 100601. DOI: 10.1103/PhysRevLett.104.100601 (cit. on pp. 34, 37).

[Popoff, 2010b] Sébastien Popoff, Geoffroy Lerosey, Mathias Fink, Albert Claude Boccara, and Sylvain Gigan. "Image transmission through an opaque material". *Nature Communications* 1.1 (2010), p. 81. DOI: 10.1038/ncomms1078 (cit. on p. 34).

[Prada, 1994] Claire Prada and Mathias Fink. "Eigenmodes of the time reversal operator: A solution to selective focusing in multiple-target media". *Wave Motion* 20.2 (1994), pp. 151–163. DOI: 10.1016/0165-2125(94)90039-6 (cit. on pp. 41, 46).

[Prada, 1996] Claire Prada, Sébastien Manneville, Dimitri Spoliansky, and Mathias Fink. "Decomposition of the time reversal operator: Detection and selective focusing on two scatterers". *The Journal of the Acoustical Society of America* 99.4 (1996), pp. 2067–2076. DOI: 10.1121/1.415393 (cit. on pp. 34, 41).

[Prada, 2003] Claire Prada and Jean-Louis Thomas. "Experimental subwavelength localization of scatterers by decomposition of the time reversal operator interpreted as a covariance matrix". *The Journal of the Acoustical Society of America* 114.1 (2003), pp. 235–243. DOI: 10.1121/1.1568759 (cit. on p. 41).

[Provost, 2014] Jean Provost, Clement Papadacci, Juan Esteban Arango, Marion Imbault, Mathias Fink, Jean-Luc Gennisson, Mickael Tanter, and Mathieu Pernot. "3D ultrafast ultrasound imaging in vivo". *prada* 59.19 (2014), pp. L1–L13. DOI: 10.1088/0031-9155/59/19/L1 (cit. on pp. 46, 69, 74, 78).

[Provost, 2015] Jean Provost, Clement Papadacci, Charlie Demene, Jean-Luc Gennisson, Mickael Tanter, and Mathieu Pernot. "3-D ultrafast doppler imaging applied to the noninvasive mapping of blood vessels in Vivo". *IEEE Transactions on Ultrasonics, Ferroelectrics, and Frequency Control* 62.8 (2015), pp. 1467–1472. DOI: 10.1109/TUFFC.2015.007032 (cit. on p. 69).

[Ratsimandresy, 2002] L. Ratsimandresy, P. Mauchamp, D. Dinet, N. Felix, and R. Dufait. "A 3 MHz two dimensional array based on piezocomposite for medical imaging". *2002 IEEE Ultrasonics Symposium, 2002. Proceedings.* Vol. 2. Munich, Germany: IEEE, 2002, pp. 1265–1268. DOI: 10.1109/ULTSYM.2002.1192524 (cit. on pp. 69–71).

[Rau, 2019] Richard Rau, Dieter Schweizer, Valery Vishnevskiy, and Orcun Goksel. "Ultrasound Aberration Correction based on Local Speed-of-Sound Map Estimation". *2019 IEEE International Ultrasonics Symposium (IUS)* (2019), pp. 2003–2006. DOI: 10.1109/ULTSYM.2019.8926297 (cit. on p. 155).

[Rau, 2021] Richard Rau, Dieter Schweizer, Valery Vishnevskiy, and Orcun Goksel. "Speed-of-sound imaging using diverging waves". *International Journal of Computer Assisted Radiology and Surgery* 16.7 (2021), pp. 1201–1211. DOI: 10.1007/s11548-021-02426-w (cit. on p. 156).

[Renaudin, 2022] Noémi Renaudin, Charlie Demené, Alexandre Dizeux, Nathalie Ialy-Radio, Sophie Pezet, and Mickael Tanter. "Functional ultrasound localization microscopy reveals brain-wide neurovascular activity on a microscopic scale". *Nature Methods* 19.8 (2022), pp. 1004–1012. DOI: 10.1038/s41592-022-01549-5 (cit. on p. 112).

[Rigby, 2000] K.W. Rigby, C.L. Chalek, B.H. Haider, R.S. Lewandowski, M. O'Donnell, L.S. Smith, and D.G. Wildes. "Improved in vivo abdominal image quality using real-time estimation and correction of wavefront arrival time errors". *2000 IEEE Ultrasonics Symposium. Proceedings. An International Symposium (Cat. No.00CH37121).* Vol. 2. 2000, 1645–1653 vol.2. DOI: 10.1109/ULTSYM.2000.921639 (cit. on p. 30).

[Robert, 2005] J. Robert, A. T. Fernandez, and M. Burcher. "Aberration estimation using FDORT: insights and improved method for speckle signals". *IEEE Ultrasonics Symposium, 2005.* (2005). DOI: 10.1109/ULTSYM.2005.1603069 (cit. on pp. 28, 30, 43, 59).

[Robert, 2007] Jean-Luc Robert. "Estimation de fonctions de green dans les milieux complexes par décomposition de l'opérateur retournement temporel : application à l'imagerie médicale et à la correction d'aberration". PhD Thesis. 2007 (cit. on p. 43).

[Robert, 2008a] Jean-Luc Robert and Mathias Fink. "Green's function estimation in speckle using the decomposition of the time reversal operator: Application to aberration correction in medical imaging". *The Journal of the Acoustical Society of America* 123.2 (2008), pp. 866–877. DOI: 10.1121/1.2816562 (cit. on pp. 34, 69, 187).

[Robert, 2008b] Jean-Luc Robert and Mathias Fink. "The time-reversal operator with virtual transducers: Application to far-field aberration correction". *The Journal of the Acoustical Society of America* 124.6 (2008), pp. 3659–3668. DOI: 10.1121/1.3005560 (cit. on pp. 43, 45, 51).

[Robin, 2023] Justine Robin, Charlie Demené, Baptiste Heiles, Victor Blanvillain, Liene Puke, Fabienne Perren, and Mickael Tanter. "In vivo adaptive focusing for clinical contrast-enhanced transcranial ultrasound imaging in human". *Physics in Medicine & Biology* 68.2 (2023), p. 025019. DOI: 10.1088/1361-6560/acabfb (cit. on pp. 29, 102, 106, 112, 113, 120).

[Robinson, 1982] D. E. Robinson, F. Chen, and L. S. Wilson. "Measurement of velocity of propagation from ultrasonic pulse-echo data". *Ultrasound in Medicine & Biology*. Ultrasonic Mammography 8.4 (1982), pp. 413–420. DOI: 10.1016/S0301-5629(82)80009-4 (cit. on p. 155).

[Robinson, 1991] D.E. Robinson, J. Ophir, L.S. Wilson, and C.F. Chen. "Pulse-echo ultrasound speed measurements: Progress and prospects". *Ultrasound in Medicine & Biology* 17.6 (1991), pp. 633–646. DOI: 10.1016/0301-5629(91)90034-T (cit. on p. 154).

[Roddier, 1999] François Roddier, ed. *Adaptive Optics in Astronomy*. Cambridge: Cambridge University Press, 1999. DOI: 10.1017/CBO9780511525179 (cit. on pp. 27, 29).

[Rodriguez-Molares, 2017] Alfonso Rodriguez-Molares, Ali Fatemi, Lasse Lovstakken, and Hans Torp. "Specular Beamforming". *IEEE Transactions on Ultrasonics, Ferroelectrics, and Frequency Control* 64.9 (2017), pp. 1285–1297. DOI: 10.1109/TUFFC.2017.2709038 (cit. on p. 108).

[Rotter, 2017] Stefan Rotter and Sylvain Gigan. "Light fields in complex media: Mesoscopic scattering meets wave control". *Reviews of Modern Physics* 89.1 (2017), p. 015005. DOI: 10.1103/RevModPhys.89.015005 (cit. on p. 34).

[Roux, 2016] Emmanuel Roux, Alessandro Ramalli, Piero Tortoli, Christian Cachard, Marc C. Robini, and Hervé Liebgott. "2-D Ultrasound Sparse Arrays Multidepth Radiation Optimization Using Simulated Annealing and Spiral-Array Inspired Energy Functions". *IEEE Transactions on Ultrasonics, Ferroelectrics, and Frequency Control* 63.12 (2016), pp. 2138–2149. DOI: 10.1109/TUFFC.2016.2602242 (cit. on p. 70).

[Roux, 2018] Emmanuel Roux, François Varray, Lorena Petrusca, Christian Cachard, Piero Tortoli, and Hervé Liebgott. "Experimental 3-D Ultrasound Imaging with 2-D Sparse Arrays using Focused and Diverging Waves". *Scientific Reports* 8.1 (2018), p. 9108. DOI: 10.1038/s41598-018-27490-2 (cit. on p. 70).

[Ruby, 2019] Lisa Ruby, Sergio J. Sanabria, Katharina Martini, Konstantin J. Dedes, Denise Vorburger, Ece Oezkan, Thomas Frauenfelder, Orcun Goksel, and Marga B. Rominger. "Breast Cancer Assessment With Pulse-Echo Speed of Sound Ultrasound From Intrinsic Tissue Reflections: Proof-of-Concept". *Investigative Radiology* 54.7 (2019), pp. 419–427. DOI: 10.1097/RLI.0000000000000553 (cit. on p. 154).

[Rust, 2006] Michael J. Rust, Mark Bates, and Xiaowei Zhuang. "Stochastic optical reconstruction microscopy (STORM) provides sub-diffraction-limit image resolution". *Nature methods* 3.10 (2006), pp. 793–795. DOI: 10.1038/nmeth929 (cit. on pp. 110, 111).

[Samani, 2007] Abbas Samani, Judit Zubovits, and Donald Plewes. "Elastic moduli of normal and pathological human breast tissues: an inversion-technique-based investigation of 169 samples". *Physics in Medicine and Biology* 52.6 (2007), pp. 1565–1576. DOI: 10.1088/0031-9155/52/6/002 (cit. on p. 154).

[Sanabria, 2020] Sergio J Sanabria, Thurston Brevett, and Jeremy Dahl. "Anisotropic regularization of ultrasound pulse-echo tomography for reconstruction of speed-of-sound and tissue heterogeneity through abdominal layers". *2020 IEEE International Ultrasonics Symposium (IUS)*. 2020, pp. 1–4. DOI: 10.1109/IUS46767.2020.9251569 (cit. on p. 157).

[Sanabria, 2018a] Sergio J. Sanabria, Ece Ozkan, Marga Rominger, and Orcun Goksel. "Spatial domain reconstruction for imaging speed-of-sound with pulse-echo ultrasound: simulation and in vivo study". *Physics in Medicine and Biology* 63.21 (2018), p. 215015. DOI: 10.1088/1361-6560/aae2fb (cit. on p. 156).

[Sanabria, 2018b] Sergio J. Sanabria, Marga B. Rominger, and Orcun Goksel. "Speed-of-Sound Imaging Based on Reflector Delineation". *IEEE transactions on bio-medical engineering* (2018). DOI: 10.1109/TBME.2018.2881302 (cit. on p. 156).

[Sandrin, 1999] L Sandrin, S. Catheline, M. Tanter, X. Hennequin, and M. Fink. "Time-Resolved Pulsed Elastography with Ultrafast Ultrasonic Imaging". *Ultrasonic Imaging* 21.4 (1999), pp. 259–272. DOI: 10.1177/016173469902100402 (cit. on pp. 12, 17, 46, 154).

[Sandrin, 2002] L. Sandrin, M. Tanter, S. Catheline, and M. Fink. "Shear modulus imaging with 2-D transient elastography". *IEEE Transactions on Ultrasonics, Ferroelectrics and Frequency Control* 49.4 (2002), pp. 426–435. DOI: 10.1109/58.996560 (cit. on p. 46).

[Savord, 2003] B. Savord and R. Solomon. "Fully sampled matrix transducer for real time 3D ultrasonic imaging". *IEEE Symposium on Ultrasonics, 2003.* Honolulu, HI, USA: IEEE, 2003, pp. 945–953. DOI: 10.1109/ULTSYM.2003.1293556 (cit. on p. 70).

[Schneider, 1999] Michel Schneider. "Characteristics of SonoVue™". *Echocardiography* 16.s1 (1999), pp. 743–746. DOI: 10.1111/j.1540-8175.1999.tb00144.x (cit. on pp. 115, 123).

[Segers, 2018] Tim Segers, Pieter Kruizinga, Maarten P. Kok, Guillaume Lajoinie, Nico de Jong, and Michel Versluis. "Monodisperse Versus Polydisperse Ultrasound Contrast Agents: Non-Linear Response, Sensitivity, and Deep Tissue Imaging Potential". *Ultrasound in Medicine & Biology* 44.7 (2018), pp. 1482–1492. DOI: 10.1016/j.ultrasmedbio.2018.03.019 (cit. on pp. 110, 111, 123).

[Sehgal, 1986] Chandra M. Sehgal and James F. Greenleaf. "Correlative study of properties of water in biological systems using ultrasound and magnetic resonance". *Magnetic Resonance in Medicine* 3.6 (1986), pp. 976–985. DOI: 10.1002/mrm.1910030621 (cit. on pp. 31, 154).

[Shattuck, 1989] D. P. Shattuck, J. Ophir, G. W. Johnson, Y. Yazdi, and D. Mehta. "Correction of refraction and other angle errors in beam tracking speed of sound estimations using multiple tracking transducers". *Ultrasound in Medicine & Biology* 15.7 (1989), pp. 673–681. DOI: 10.1016/0301-5629(89)90175-0 (cit. on p. 155).

[Sheppard, 2013] Colin J. R. Sheppard, Shalin B. Mehta, and Rainer Heintzmann. "Superresolution by image scanning microscopy using pixel reassignment". *Optics Letters* 38.15 (2013), p. 2889. DOI: 10.1364/OL.38.002889 (cit. on p. 54).

[Shin, 2010] Ho-Chul Shin, Richard Prager, Henry Gomersall, Nick Kingsbury, Graham Treece, and Andrew Gee. "Estimation of average speed of sound using deconvolution of medical ultrasound data". *Ultrasound in Medicine & Biology* 36.4 (2010), pp. 623–636. DOI: 10.1016/j.ultrasmedbio.2010.01.011 (cit. on p. 156).

[Silverstein, 2001] S.D. Silverstein. "Ultrasound scattering model: 2-D cross-correlation and focusing criteria-theory, simulations, and experiments". *IEEE Transactions on Ultrasonics, Ferroelectrics, and Frequency Control* 48.4 (2001), pp. 1023–1030. DOI: 10.1109/58.935719 (cit. on p. 187).

[Silverstein, 2003] S.D. Silverstein and D.P. Ceperley. "Autofocusing in medical ultrasound: the scaled covariance matrix algorithm". *IEEE Transactions on Ultrasonics, Ferroelectrics, and Frequency Control* 50.7 (2003), pp. 795–804. DOI: 10.1109/TUFFC.2003.1214500 (cit. on p. 30).

[Smith, 1986] S.W. Smith, G.E. Trahey, and O.T. von Ramm. "Phased array ultrasound imaging through planar tissue layers". *Ultrasound in Medicine & Biology* 12.3 (1986), pp. 229–243. DOI: 10.1016/0301-5629(86)90314-5 (cit. on pp. 31, 133).

[Sommer, 2021] Tal I. Sommer and Ori Katz. "Pixel-reassignment in ultrasound imaging". *Applied Physics Letters* 119.12 (2021), p. 123701. DOI: 10.1063/5.0062716 (cit. on pp. 54, 69).

[Soulioti, 2020] Danai E. Soulioti, David Espindola, Paul A. Dayton, and Gianmarco F. Pinton. "Super-Resolution Imaging Through the Human Skull". *IEEE Transactions on Ultrasonics, Ferroelectrics, and Frequency Control* 67.1 (2020), pp. 25–36. DOI: 10.1109/TUFFC.2019.2937733 (cit. on pp. 106, 113).

[Soysal, 2022] Ugur Soysal, Pedro N. Azevedo, Flavien Bureau, Alexandre Aubry, Marcio S. Carvalho, Amanda C. S. N. Pessoa, Lucimara G. De La Torre, Olivier Couture, Arnaud Tourin, Mathias Fink, and Patrick Tabeling. "Freeze-Dried Microfluidic Monodisperse Microbubbles as a New Generation of Ultrasound Contrast Agents". *Ultrasound in Medicine & Biology* 48.8 (2022), pp. 1484–1495. DOI: 10.1016/j.ultrasmedbio.2022.03.011 (cit. on pp. 123–125).

[Stahli, 2019] Patrick Stahli, Martin Frenz, and Michael Jaeger. "Reflection-mode speed-of-sound imaging using soft-prior limits". *2019 IEEE International Ultrasonics Symposium (IUS)*. Glasgow, United Kingdom: IEEE, 2019, pp. 948–950. DOI: 10.1109/ULTSYM.2019.8925739 (cit. on p. 156).

[Stahli, 2021] Patrick Stahli, Martin Frenz, and Michael Jaeger. "Bayesian Approach for a Robust Speed-of-Sound Reconstruction Using Pulse-Echo Ultrasound". *IEEE Transactions on Medical Imaging* 40.2 (2021), pp. 457–467. DOI: 10.1109/TMI.2020.3029286 (cit. on pp. 155, 157).

[Stähli, 2020] Patrick Stähli, Maju Kuriakose, Martin Frenz, and Michael Jaeger. "Improved forward model for quantitative pulse-echo speed-of-sound imaging". *Ultrasonics* 108 (2020), p. 106168. DOI: 10.1016/j.ultras.2020.106168 (cit. on p. 156).

[Stern, 2019] Galya Stern and Ori Katz. "Noninvasive focusing through scattering layers using speckle correlations". *Optics Letters* 44.1 (2019), p. 143. DOI: 10.1364/OL.44.000143 (cit. on p. 43).

[Stride, 2020] Eleanor Stride, Tim Segers, Guillaume Lajoinie, Samir Cherkaoui, Thierry Bettinger, Michel Versluis, and Mark Borden. "Microbubble Agents: New Directions". *Ultrasound in Medicine & Biology* 46.6 (2020), pp. 1326–1343. DOI: 10.1016/j.ultrasmedbio.2020.01.027 (cit. on p. 110).

[Szabo, 2004] Thomas L. Szabo. *Diagnostic Ultrasound Imaging: Inside Out*. 2004 (cit. on p. 4).

[Tanter, 2001] M. Tanter, J.-F. Aubry, J. Gerber, J.-L. Thomas, and M. Fink. "Optimal focusing by spatio-temporal inverse filter. I. Basic principles". *The Journal of the Acoustical Society of America* 110.1 (2001), pp. 37–47. DOI: 10.1121/1.1377051 (cit. on pp. 34, 37).

[Tanter, 2014] Mickael Tanter and Mathias Fink. "Ultrafast imaging in biomedical ultrasound". *IEEE Transactions on Ultrasonics, Ferroelectrics, and Frequency Control* 61.1 (2014), pp. 102–119. DOI: 10.1109/TUFFC.2014.2882 (cit. on pp. 17, 46, 114, 154).

[Tanter, 2000] Mickaël Tanter, Jean-Louis Thomas, and Mathias Fink. "Time reversal and the inverse filter". *The Journal of the Acoustical Society of America* 108.1 (2000), pp. 223–234. DOI: 10.1121/1.429459 (cit. on p. 37).

[Tarighatnia, 2022] Ali Tarighatnia, Mohammad Reza Fouladi, Nader D. Nader, Ayuob Aghanejad, and Hossein Ghadiri. "Recent trends of contrast agents in ultrasound imaging: a review of the classifications and applications". *Materials Advances* 3.9 (2022), pp. 3726–3741. DOI: 10.1039/D1MA00969A (cit. on p. 110).

[Telichko, 2022] Arsenii V. Telichko, Rehman Ali, Thurston Brevett, Huaijun Wang, Jose G. Vilches-Moure, Sukumar U. Kumar, Ramasamy Paulmurugan, and Jeremy J. Dahl. "Noninvasive estimation of local speed of sound by pulse-echo ultrasound in a rat model of nonalcoholic fatty liver". *Physics in Medicine & Biology* 67.1 (2022), p. 015007. DOI: 10.1088/1361-6560/ac4562 (cit. on p. 156).

[Tiennot, 2019] Thomas Tiennot, Hermes A. S. Kamimura, Stephen A. Lee, Christian Aurup, and Elisa E. Konofagou. "Numerical modeling of ultrasound heating for the correction of viscous heating artifacts in soft tissue temperature measurements". *Applied Physics Letters* 114.20 (2019), p. 203702. DOI: 10.1063/1.5091108 (cit. on p. 98).

[Tong, 1996] S. Tong, D. B. Downey, H. N. Cardinal, and A. Fenster. "A three-dimensional ultrasound prostate imaging system". *Ultrasound in Medicine & Biology* 22.6 (1996), pp. 735–746. DOI: 10.1016/0301-5629(96)00079-8 (cit. on p. 70).

[Touma, 2021] Rita Touma, Thibaud Blondel, Arnaud Derode, Michel Campillo, and Alexandre Aubry. "A distortion matrix framework for high-resolution passive seismic 3-D imaging: application to the San Jacinto fault zone, California". *Geophysical Journal International* 226.2 (2021), pp. 780–794. DOI: 10.1093/gji/ggab133 (cit. on pp. 34, 49, 58, 59, 69, 177).

[Trahey, 1991] G. E. Trahey, P. D. Freiburger, L. F. Nock, and D. C. Sullivan. "In vivo measurements of ultrasonic beam distortion in the breast". *Ultrasonic Imaging* 13.1 (1991), pp. 71–90. DOI: 10.1177/016173469101300104 (cit. on p. 25).

[Treeby, 2010] Bradley E. Treeby and B. T. Cox. "k-Wave: MATLAB toolbox for the simulation and reconstruction of photoacoustic wave fields". *Journal of Biomedical Optics* 15.2 (2010), p. 021314. DOI: 10.1117/1.3360308 (cit. on pp. 157, 167).

[Tremblay-Darveau, 2014a] Charles Tremblay-Darveau, Ross Williams, and Peter N. Burns. "Measuring Absolute Blood Pressure Using Microbubbles". *Ultrasound in Medicine & Biology* 40.4 (2014), pp. 775–787. DOI: 10.1016/j.ultrasmedbio.2013.10.017 (cit. on pp. 110, 123, 129).

[Tremblay-Darveau, 2014b] Charles Tremblay-Darveau, Ross Williams, Laurent Milot, Matthew Bruce, and Peter N. Burns. "Combined perfusion and doppler imaging using plane-wave nonlinear detection and microbubble contrast agents". *IEEE Transactions on Ultrasonics, Ferroelectrics, and Frequency Control* 61.12 (2014), pp. 1988–2000. DOI: 10.1109/TUFFC.2014.006573 (cit. on p. 111).

[Varslot, 2004] Trond Varslot, Harald Krogstad, Eirik Mo, and Bjørn A. Angelsen. "Eigenfunction analysis of stochastic backscatter for characterization of acoustic aberration in medical ultrasound imaging". *The Journal of the Acoustical Society of America* 115.6 (2004), pp. 3068–3076. DOI: 10.1121/1.1736274 (cit. on pp. 44, 61).

[Velichko, 2020] Alexander Velichko. "Quantification of the Effect of Multiple Scattering on Array Imaging Performance". *IEEE Transactions on Ultrasonics, Ferroelectrics, and Frequency Control* 67.1 (2020), pp. 92–105. DOI: 10.1109/TUFFC.2019.2935811 (cit. on p. 34).

[Vellekoop, 2007] I. M. Vellekoop and A. P. Mosk. "Focusing coherent light through opaque strongly scattering media". *Optics Letters* 32.16 (2007), pp. 2309–2311. DOI: 10.1364/OL.32.002309 (cit. on p. 37).

[Versluis, 2020] Michel Versluis, Eleanor Stride, Guillaume Lajoinie, Benjamin Dollet, and Tim Segers. "Ultrasound Contrast Agent Modeling: A Review". *Ultrasound in Medicine & Biology* 46.9 (2020), pp. 2117–2144. DOI: 10.1016/j.ultrasmedbio.2020.04.014 (cit. on pp. 110, 131).

[Vignon, 2008] Francois. Vignon, William.T. Shi, Michael.R. Burcher, and Jeff.E. Powers. "Determination of temporal bone Isoplanatic Patch sizes for transcranial phase aberration correction". *2008 IEEE Ultrasonics Symposium*. Beijing, China: IEEE, 2008, pp. 1286–1289. DOI: 10.1109/ULTSYM.2008.0311 (cit. on p. 29).

[Vyas, 2012] Urvi Vyas and Douglas Christensen. "Ultrasound beam simulations in inhomogeneous tissue geometries using the hybrid angular spectrum method". *IEEE Transactions on Ultrasonics, Ferroelectrics and Frequency Control* 59.6 (2012), pp. 1093–1100. DOI: 10.1109/TUFFC.2012.2300 (cit. on pp. 31, 155).

[Weaver, 2002] Richard Weaver and Oleg Lobkis. "On the emergence of the Green's function in the correlations of a diffuse field: pulse-echo using thermal phonons". *Ultrasonics* 40.1-8 (2002), pp. 435–439. DOI: 10.1016/S0041-624X(02)00156-7 (cit. on p. 38).

[White, 1968] D. N. White, J. M. Clark, J. N. Chesebrough, M. N. White, and J. K. Campbell. "Effect of the skull in degrading the display of echoencephalographic B and C scans". *The Journal of the Acoustical Society of America* 44.5 (1968), pp. 1339–1345. DOI: 10.1121/1.1911266 (cit. on p. 22).

[White, 1978] D. N. White, G. R. Curry, and R. J. Stevenson. "The acoustic characteristics of the skull". *Ultrasound in Medicine & Biology* 4.3 (1978), pp. 225–252. DOI: 10.1016/0301-5629(78)90054-6 (cit. on pp. 22, 98).

[Wildes, 1997] D.G. Wildes, R.Y. Chiao, C.M.W. Daft, K.W. Rigby, L.S. Smith, and K.E. Thomenius. "Elevation performance of 1.25D and 1.5D transducer arrays". *IEEE Transactions on Ultrasonics, Ferroelectrics, and Frequency Control* 44.5 (1997), pp. 1027–1037. DOI: 10.1109/58.655628 (cit. on p. 70).

[Wiskin, 2007] J. Wiskin, D.T. Borup, S.A. Johnson, M. Berggren, T. Abbott, and R. Hanover. "Full-Wave, Non-Linear, Inverse Scattering". *Acoustical Imaging*. Ed. by Michael P. André et al. Acoustical Imaging. Dordrecht: Springer Netherlands, 2007, pp. 183–193. DOI: 10.1007/1-4020-5721-0_20 (cit. on p. 154).

[Xing, 2023] Paul Xing, Jonathan Porée, Brice Rauby, Antoine Malescot, Éric Martineau, Vinent Perrot, Ravi L. Rungta, and Jean Provost. "Phase Aberration Correction for in vivo Ultrasound Localization Microscopy Using a Spatiotemporal Complex-Valued Neural Network". *IEEE Transactions on Medical Imaging* (2023). DOI: 10.1109/TMI.2023.3316995 (cit. on pp. 112, 120).

[Yasuda, 2019] Jun Yasuda, Hideki Yoshikawa, and Hiroki Tanaka. "Phase aberration correction for focused ultrasound transmission by refraction compensation". *Japanese Journal of Applied Physics* 58.SG (2019), SGGE22. DOI: 10.7567/1347-4065/ab19aa (cit. on p. 31).

[Yiu, 2013] Billy Y.S. Yiu and Alfred C.H. Yu. "High-Frame-Rate Ultrasound Color-Encoded Speckle Imaging of Complex Flow Dynamics". *Ultrasound in Medicine & Biology* 39.6 (2013), pp. 1015–1025. DOI: 10.1016/j.ultrasmedbio.2012.12.016 (cit. on p. 17).

[Yoo, 2003] Yang Mo Yoo, Ravi Managuli, and Yongmin Kim. "Adaptive clutter filtering for ultrasound color flow imaging". *Ultrasound in Medicine & Biology* 29.9 (2003), pp. 1311–1320. DOI: 10.1016/S0301-5629(03)01014-7 (cit. on p. 20).

[Yoon, 2011] Changhan Yoon, Yuhwa Lee, Jin Ho Chang, Tai-Kyong Song, and Yangmo Yoo. "In vitro estimation of mean sound speed based on minimum average phase variance in medical ultrasound imaging". *Ultrasonics* 51.7 (2011), pp. 795–802. DOI: 10.1016/j.ultras.2011.03.007 (cit. on p. 156).

[Yoon, 2012] Changhan Yoon, Haijin Seo, Yuhwa Lee, Yangmo Yoo, Tai-Kyong Song, and Jin Ho Chang. "Optimal sound speed estimation using modified nonlinear anisotropic diffusion to improve spatial resolution in ultrasound imaging". *IEEE transactions on ultrasonics, ferroelectrics, and frequency control* 59.5 (2012), pp. 905–914. DOI: 10.1109/TUFFC.2012.2275 (cit. on p. 156).

[Yoon, 2020] Seokchan Yoon, Hojun Lee, Jin Hee Hong, Yong-Sik Lim, and Wonshik Choi. "Laser scanning reflection-matrix microscopy for aberration-free imaging through intact mouse skull". *Nature Communications* 11.1 (2020), p. 5721. DOI: 10.1038/s41467-020-19550-x (cit. on pp. 43, 62, 63, 65, 69, 92).

[Yu, 2010] Alfred Yu and Lasse Lovstakken. "Eigen-based clutter filter design for ultrasound color flow imaging: a review". *IEEE Transactions on Ultrasonics, Ferroelectrics and Frequency Control* 57.5 (2010), pp. 1096–1111. DOI: 10.1109/TUFFC.2010.1521 (cit. on p. 20).

[Zhang, 2018] Yingzhen N Zhang, Kathryn J Fowler, Gavin Hamilton, Jennifer Y Cui, Ethan Z Sy, Michelle Balanay, Jonathan C Hooker, Nikolaus Szeverenyi, and Claude B Sirlin. "Liver fat imaging—a clinical overview of ultrasound, CT, and MR imaging". *The British Journal of Radiology* 91.1089 (2018), p. 20170959. DOI: 10.1259/bjr.20170959 (cit. on p. 3).

[Zhao, 1992] D. Zhao, L. N. Bohs, and G. E. Trahey. "Phase aberration correction using echo signals from moving targets I: Description and theory". *Ultrasonic Imaging* 14.2 (1992), pp. 97–110. DOI: https://doi.org/10.1016/0161-7346(92)90001-C (cit. on p. 122).

[Zubajlo, 2018] Rebecca E. Zubajlo, Alex Benjamin, Joseph R. Grajo, Kanakaraju Kaliannan, Jing X. Kang, Atul K. Bhan, Kai E. Thomenius, Brian W. Anthony, Manish Dhyani, and Anthony E. Samir. "Experimental Validation of Longitudinal Speed of Sound Estimates in the Diagnosis of Hepatic Steatosis (Part II)". *Ultrasound in Medicine & Biology* 44.12 (2018), pp. 2749–2758. DOI: 10.1016/j.ultrasmedbio.2018.07.020 (cit. on p. 156).

RÉSUMÉ

L'échographie est une technique d'imagerie très utilisée en medecine, notamment car elle est non invasive. Elle consiste à insonifier un milieu avec une onde ultrasonore et à enregistrer les échos rétrodiffusés par les hétérogénéités du milieu au moyen d'une sonde ultrasonore. En appliquant des retards temporels appropriés à chaque canal d'émission et de réception, il est possible d'obtenir une image de la reflectivité du milieu. Cette approche repose sur des hypothèses fortes que sont une vitesse du son constante et un régime de diffusion simple. En pratique, ces hypothèses sont loin d'être vérifiées. En effet, les variations spatiales de la vitesse du son en tout point du champ de vision déforment le front d'onde, ce qui impacte considérablement le processus de focalisation et donc la résolution de l'image. Dans ce travail, ces limites fondamentales sont étudiées et résolues en enregistrant la matrice de réflexion du milieu, qui contient toute l'information disponible sur le milieu étudié. Alors que la génération d'une image ultrasonore est basée sur un processus de focalisation simultanée en entrée et en sortie sur chaque point de l'image, l'imagerie matricielle consiste à découpler les points focaux d'entrée et de sortie afin de pouvoir examiner les aberrations et la diffusion multiple en tout point. Plus précisément, l'objectif de cette étude est d'exploiter tous les degrés de liberté disponibles dans cette matrice pour étendre l'imagerie matricielle ultrasonore à plusieurs dimensions : (i) dans le domaine spatial en passant de l'imagerie 2D à l'imagerie 3D avec des applications à l'imagerie transcrânienne ; (ii) en exploitant les degrés de liberté temporels pour caracteriser la réponse spectrale d'objets résonants tel que les microbulles ; (iii) réaliser un autoportrait du processus de focalisation de l'onde en tout point du milieu ; (iv) exploiter la sensibilité du déphasage de Gouy au niveau du plan de focalisation pour sonder la défocalisation et compenser les aberrations axiales ; (v) cartographier la vitesse du son pour obtenir une image quantitative des tissus biologiques.

MOTS CLÉS

Imagerie ultrasonore ; Imagerie 3D ; Imagerie transcrânienne ; Imagerie matricielle ; Tomographie de la vitesse du son ; Focalisation adaptative ; Aberrations.

ABSTRACT

Ultrasound is a widely used imaging technique in medicine, especially because it is non-invasive. It consists in probing a medium with an ultrasonic wave and recording the echoes backscattered by the medium heterogeneities with an ultrasonic probe. By applying appropriate time delays to each transmit and receive channel, it is possible to obtain an image of the medium reflectivity. Ultrasound imaging relies on strong assumptions such as a constant speed of sound and only a single scattering regime. In practice, these assumptions are far from being fulfilled. The spatial variations in sound velocity distort the wavefront, which significantly impacts the focusing process and thus the image resolution. In this work, these fundamental limitations are addressed and solved by recording the reflection matrix, which contains all the information available on the medium of interest. While the generation of an ultrasound image is based on a process of simultaneous input and output focusing on each point of the image, matrix imaging consists in decoupling the input and output focal points in order to scan aberrations and multiple scattering. Specifically, the aim of this study is to exploit all the degrees of freedom available in this matrix to extend this approach in several dimensions: (i) in the spatial domain by moving from 2D to 3D imaging with applications to transcranial imaging; (ii) by exploiting the temporal degrees of freedom to characterize the spectral response of resonant objects such as microbubbles; (iii) by performing an auto-portrait of the wave focusing process at any point of the medium; (iv) by using the sensitivity of the Gouy phase shift at the focusing plane to probe the defocus and compensate for axial aberrations; (v) by mapping the speed-of-sound to obtain a quantitative image of biological tissues.

KEYWORDS

Ultrasound imaging; 3D imaging; Transcranial imaging; Matrix imaging; Speed-of-sound tomography; Adaptive focusing; Aberrations.